NEW CATALYST FORMULATIONS BASED ON GOLD AND MOLYBDENUM NITRIDES AND CARBIDES: APPLICATION IN SELECTIVE HYDROGENATION

Noémie PERRET

A dissertation submitted for the degree of Doctor of Philosophy

Heriot-Watt University

School of Engineering and Physical Sciences

Department of Chemical Engineering

November 2012

The development of selective heterogeneous catalytic systems is of fundamental importance for the realisation of sustainable green chemical processes. In this thesis, the hydrogenation of nitroarene, aldehyde and carboxylic acid compounds is examined in continuous gas phase operation, for the synthesis of a target functionalised aromatic amine and alcohol. Novel catalysts based on Mo nitride, carbide and supported Au have been synthesised and subjected to an array of complementary characterisation measurements that provide catalyst structure/performance correlations with detailed kinetic and mechanistic analysis.

The use of Mo_2N and Mo_2C as catalysts served to promote the selective hydrogenation of nitrobenzene to aniline and *p*-chloronitrobenzene to *p*-chloroaniline where the incorporation of nano-scale Au increased reaction rate. Activity has been correlated to hydrogen adsorption/release capacity, which shows a dependence on the degree of nitridation and crystallographic structure. In contrast, hydrogenation of benzaldehyde is limited by C=O activation, which is facilitated by the Mo component. Alumina supported Au has exhibited 100% selectivity in the hydrogenation of benzaldehyde and 4-nitrobenzaldehyde to the target alcohol, where Au particle size and surface Lewis acidity play crucial roles. The hydrogenation of benzoic acid over Au supported on a CeO_2-ZrO_2 mixed oxide has shown promising results with the possibility of a one step transformation to the alcohol.

The results presented in this thesis establish feasible catalytic routes to high value amines and alcohols where critical process optimisation is demonstrated in terms of catalyst composition/surface structure and reaction conditions.

Acknowledgements

First of all, I would especially like to thank my supervisor, Prof. Mark Keane, for the help, time, support and advices that he has given me over the last four years. Thanks for sharing your commitment to science and your knowledge with me.

I would also like to thank the staff in the chemical engineering department for their support, especially Ronald Millar, Marian Millar, Eileen M. McEvoy, Craig Bell, Curtis Abbott, Cameron Smith and Christina Graham (from chemistry). Ronnie, thanks for always having time to help me fixing my equipment; Marian and Eileen, our chats; Cameron, the one who can get stuff delivered quicker than in any other workshops I've dealt with!

This research project would have not been possible without the collaboration of Laurent Delannoy, Catherine Louis and Thomas Onfroy from the Université Pierre et Marie Curie (Paris); Fernando Cárdenas-Lizana and Lioubov Kiwi-Minsker from EPFL (Lausanne); Justin Hargreaves from the University of Glasgow, Russell Howe from the University of Aberdeen, Ross Blackley from the University of St Andrews; Serafin Bernal from the Universidad de Cádiz.
A special thanks to Laurent, Colin, Pressy, Christophe and Anne-Fe who made me feel very welcome during my 5 weeks placement in Paris, I had a great time!

Many thanks to my officemates, lab mates, colleagues and friends: Dalila, you've been here since the beginning, thanks for being there during the hard time, I'll remember you as the one who never give up. Yufen, I can't wait to see you ride that donkey at your wedding! Craig, you're the only one who listens to decent music in this building! Sydon & Nina: I'll remember some epic dinners. Fernando and Santi, thanks for bearing my non-existent English when I arrived. Thanks as well to Gregor (never angry, never stressed!), Aquino (for giving advices and sharing some of your knowledge about life!), Nathalia, Maoshuai, Anna, Riccardo and Panos.
Thanks to Dan, Graham, Ian and all the others who were always up for a pint at 5 p.m on Fridays; thanks to Rainer, Thomas and Marco who shared their passion of whisky with me.

I would like to thanks my sister Mylène and her husband Benjamin, my brother Ludovic, my parents and other members of my family, for their education and love. My friends in France who have known me since I was a teenager and who have seen me changed a lot over the past decade: Anne, Le Bapt, Burt, Mat, Soupi and Thyph.

Thanks to my friends and all the people I met over the last four year in Edinburgh. Thanks to my former flat mates: Mikel, for sharing your recipe of gazpacho; Claudia, who has been my personal "femininity coach" for the last few years; Robert, for whom anything in life is an amazing discovery or a new experience; Susana F. for your friendship; Jean-Baptist who managed to live with Amy and me for a year, which might not have been an easy task!

Thanks to the climbing crew: Andrew, Diego, Silvia and Alejandro. Thanks for initiating me, teaching me and sharing your "devotion" for such a great sport.

Many thanks as well to Billy, Christine, Emily, Karen (I hope you enjoy your new life in Germany), Marta (I'll remember your home-made vodka), Niklas (we had some nice time watching the rugby at Murrayfield), Ola, Oscar, Ross, Susana, Simon, Tibor, Will…

Last, but not least, I would like to thinks Amy. You are sometime calling yourself lazy while I admire your energy. Thanks for encouraging me to push myself to the limits.

Thanks everyone!

ACADEMIC REGISTRY
Research Thesis Submission

Name*:*	Noémie Perret		
School/PGI:	EPS		
Version: *(i.e. First, Resubmission, Final)*	Final	Degree Sought (Award **and** Subject area)	Doctor of Philosophy

Declaration

In accordance with the appropriate regulations I hereby submit my thesis and I declare that:

1) the thesis embodies the results of my own work and has been composed by myself
2) where appropriate, I have made acknowledgement of the work of others and have made reference to work carried out in collaboration with other persons
3) the thesis is the correct version of the thesis for submission and is the same version as any electronic versions submitted*.
4) my thesis for the award referred to, deposited in the Heriot-Watt University Library, should be made available for loan or photocopying and be available via the Institutional Repository, subject to such conditions as the Librarian may require
5) I understand that as a student of the University I am required to abide by the Regulations of the University and to conform to its discipline.

* *Please note that it is the responsibility of the candidate to ensure that the correct version of the thesis is submitted.*

Signature of Candidate*:*		Date:	21/11/12

Submission

Submitted By *(name in capitals):*	
Signature of Individual Submitting:	
Date Submitted:	

For Completion in the Student Service Centre (SSC)

Received in the SSC by *(name in capitals):*			
Method of Submission *(Handed in to SSC; posted through internal/external mail):*			
*E-thesis Submitted (**mandatory for final theses)***			
Signature:		Date:	

Please note this form should bound into the submitted thesis.

Updated February 2008, November 2008, February 2009, January 2011

Table of Contents

Lists of Tables

Lists of Figures

Glossary

Acronyms

AAS	Atomic Absorption Spectroscopy
AN	Aniline
BAC	Benzoic acid
BAD	Benzaldehyde
BE	Binding Energy
BET	S. Brunauer, P. H. Emmett and E. Teller theory; measurements of surface area
BOL	Benzyl alcohol
p-CAN	*para*-Chloroaniline
CB	Chlorobenzene
p-CNB	*para*-Chloronitrobenzene
CZ	$Ce_{0.62}Zr_{0.38}O_2$
m-DNB	*meta*-Dinitrobenzene
D-P	Deposition-Precipitation
FTIR	Fourier Transform Infrared Spectroscopy
GHSV	Gas Hourly Space Velocity
ICP-OES	Inductively Coupled Plasma-Optical Emission Spectrometry
JCPDS-ICDD	Joint Committee on Powder Diffraction Standards-International Centre for Diffraction Data
4-MBAD	4-Aminobenzaldehyde
MvK	Mars and Van Krevelen mechanism
m-NAN	*meta*-Nitroaniline
NB	Nitrobenzene
4-NBAD	4-Nitrobenzaldehyde
4-NBOL	4-Nitrobenzyl alcohol
OSC	Oxygen Storage Capacity
m-PDM	*meta*-Phenylenediamine
(HAADF) SEM	(High-Angle Annular Dark-Field) Scanning Electron Microscopy
TCD	Thermal Conductivity Detector
(HR)TEM	(High Resolution) Transmission Electron Microscopy
TOF	Turnover Frequency
TPD	Temperature Programmed Desorption
TPR	Temperature Programmed Reduction
UV-Vis	Ultraviolet-Visible Spectroscopy
XRD	Powder X-ray Diffraction
XPS	X-ray Photoelectron Spectroscopy

Symbols

a, c	Lattice parameter (Å)
A_{max}	Absorption band with maximum intensity in UV-Vis analysis (nm)
d, d_i, d_{hkl}	Metal particle size (nm)
D	Metal Dispersion (%)
dV/dr	Volume/diameter of pores ($cm^3\ g^{-1}\ Å^{-1}$)
F	Inlet molar feed rate ($mol\ h^{-1}$)
I_m (I_t)	Integrated intensity of the monoclinic (tetragonal) ZrO_2 planes
k	Pseudo-first order rate constant (h^{-1})
k'	Specific pseudo-first order rate constant ($mol\ m^{-2}\ h^{-1}$)
m	Mass of catalysts (g)
n	Number of moles (mol)
N_{BAD}, N_{BAC}, N_{BOL}	Molar fraction of benzaldehyde, benzoic acid and benzyl alcohol
N_A	Avogadro constant ($\approx 6.022\times10^{23}\ mol^{-1}$)
N_{Mo}	Mo surface density ($Mo\ m^{-2}$)
P_{CO}	Pressure of CO (Torr)
pH_{PCZ}	pH at the point of zero charge
S (S_0)	(Initial) Selectivity
SA_{TPR}, SA_{BET}	Surface area obtained from TPR and BET measurements ($m^2\ g^{-1}$)
T (T_{max})	(Maximum) Temperature
V_m	Fraction of monoclinic zirconia
X (X_0)	(Initial) Fractional conversion
X_m	Intensity ratio in XRD measurements
Y	Yield
β	Time scale fitting parameter
λ	Wavelength in FTIR analysis (Å)

Publications

1) N. Perret, F. Cárdenas-Lizana, D. Lamey, V. Laporte, L. Kiwi-Minsker and M. A. Keane, *Effect of crystallographic phase (β vs. γ) and surface area on gas phase nitroarene hydrogenation over Mo_2N*, Topics in Catalysis (2012) Accepted.

2) X. Wang, N. Perret and M. A. Keane, *The Role of hydrogen partial pressure in the gas phase hydrogenation of p-chloronitrobenzene over alumina supported Au and Pd: A consideration of reaction thermodynamics and kinetics*, Chemical Engineering Journal (2012) Accepted.

3) N. Perret, X. Wang, L. Delannoy, C. Potvin, C. Louis and M. A. Keane, *Enhanced selective nitroarene hydrogenation over Au supported on β-Mo_2C and β-Mo_2C/Al_2O_3*, Journal of Catalysis 286 (2012) 172-183.

4) F. Cárdenas-Lizana, D. Lamey, N. Perret, S. Gómez-Quero, L. Kiwi-Minsker and M. A. Keane, *Au/Mo_2N as a new catalyst formulation for the hydrogenation of p-Chloronitrobenzene in both liquid and gas phases*, Catalysis Communications 21 (2012) 46-51.

5) N. Perret, F. Cárdenas-Lizana and M. A. Keane, *Selective hydrogenation of benzaldehyde to benzyl alcohol over Au/Al_2O_3*, Catalysis Communications 16 (2011) 159-164.

6) F. Cárdenas-Lizana, S. Gómez-Quero, N. Perret, L. Kiwi-Minsker and M. A. Keane, *β-Molybdenum nitride: synthesis mechanism and catalytic response in the gas phase hydrogenation of p-chloronitrobenzene*, Catalysis Science & Technology 1 (2011) 794-801.

7) F. Cárdenas-Lizana, S. Gómez-Quero, N. Perret and M. A. Keane, *Gold catalysis at the gas–solid interface: role of the support in determining activity and selectivity in the hydrogenation of m-dinitrobenzene*, Catalysis Science & Technology 1 (2011) 652-661.

8) F. Cárdenas-Lizana, D. Lamey, S. Gómez-Quero, N. Perret, L. Kiwi-Minsker and M. A. Keane, *Selective three-phase hydrogenation of aromatic nitro-compounds over β-Mo_2N*, Catalysis Today 173 (2011) 53-61.

9) F. Cárdenas-Lizana, S. Gómez-Quero, N. Perret and M. A. Keane, *Support effects in the selective gas phase hydrogenation of p-chloronitrobenzene over gold*, Gold Bulletin 42 (2009) 124-132.

Oral Presentations

1) Presentation at SURCAT ECOSSE, 2009

2) Presentation at the Annual Heriot-Watt University Postgraduate Conference, 2009

Awards

1) 2nd year postgraduate research prize of the School of Engineering and Physical Sciences from Heriot-Watt University, 2010.

2) 1st year postgraduate research prize of the School of Engineering and Physical Sciences from Heriot-Watt University, 2009.

Chapter 1

Introduction and Scope of the Thesis

This Chapter presents a brief overview of the concept of green chemistry and introduces the catalysts and reactions investigated in this PhD research. The objectives of this project are also identified.

1.1 Green Chemistry

The response to the dual demands of environmentally friendly and economically competitive chemical processes has seen a concerted move towards the development of sustainable and green technologies over the past 15 years. Green chemistry is defined by 12 principles [1.1], which focus on the design of processes that promote the use of more environmental friendly feedstock, decrease the use of solvent, promoters and separation agents, involve fewer processing steps, lessen energy requirements and increase material efficiency. Moreover, the substances employed should be benign and limit the risks of accident and toxicity to human health. Selective catalytic systems can be designed to fulfil these guidelines. By preventing pollution at source, reducing or eliminating waste formation and circumventing waste treatment and disposal, heterogeneous catalysis represents a cornerstone of green chemistry.

Functionalised aromatic amines and alcohols are important intermediates in the production of several urea herbicides and insecticides, pharmaceuticals, agrochemicals, cosmetics, azo and leuco dyes, corrosion inhibitor and pigments [1.2,1.3]. The existing literature has mainly focused on the catalytic hydrogenation of nitro-compounds and aldehydes in batch liquid systems operated at elevated pressures [1.4,1.5]. However, selectivity in terms of targeted $-NO_2$ or C=O reduction in the presence of other reactive functional groups is challenging [1.6-8]. The drawback of traditional routes and the by-products associated with each reaction are assessed throughout this thesis. Synthesis routes often involve low product yield, low selectivity, toxic by-products and energy inefficiency. This is a system that requires reassessment in line with green chemistry principles in order to achieve sustainability in larger scale application.

1.2 Scope and Organisation of the Thesis

A review of the literature dealing with the formulation of novel catalysts for heterogeneous processes over the past 25 years revealed the development and use of interstitial nitrides and carbides of early transition metals (group 4-6) [1.9-12]. Not only have these materials exhibited catalytic activity similar to noble metals for a wide range of reactions but they are less expensive to produce [1.13]. They possess an electronic structure with a Fermi energy close to that of group VIII metals, which explain the similarities in term of catalytic behaviours [1.9]. Moreover, nitrides and carbides exhibit distinct kinetics and products selectivities, which have yet to be exploited [1.14]. The methods of preparation of molybdenum nitride and carbide have been developed and their application as hydrotreating catalysts is now established [1.10,1.12,1.15]. The literature on their use as catalysts for hydrogenation reactions is however limited.

The main focus of my PhD research is to develop novel catalysts that exhibit high selectivity to a target amine or alcohol. The hydrogenation of nitrobenzene (Chapter (**Chap.**) **5/6**), *para*(*p*)-chloronitrobenzene (**Chap. 2/3/4/5/6**) and *meta*-(*m*)-dinitrobenzene (**Chap. 4**) will be investigated as they can produce aniline, *p*-chloroaniline and *m*-nitroaniline, respectively, as three amines extensively used as raw material for dyestuff [1.16,1.17]. The production of an aromatic alcohol will be then considered from benzaldehyde (**Chap. 7**), 4-nitrobenzaldehyde (**Chap. 8**) and benzoic acid (**Chap. 9**). The reactions have been conducted in the gas phase, which facilitates continuous operation, offering advantages in terms of product/catalyst separation and economies of scale.

Catalyst optimisation can only be achieved through a coupling of characterisation with the observed catalytic response. This require a thorough understanding of (i) reaction mechanism, (ii) synthesis mechanism and (iii) characterisation of the critical (bulk and surface) properties. Firstly the synthesis mechanism and use of β-Mo_2N for the hydrogenation of *p*-chloronitrobenzene is investigated (**Chap. 2**). This is followed by a consideration of the effect(s) of varying surface area and Mo_2N crystallographic phase (β- and γ-) on the same reaction (**Chap. 3**). The work presented in **Chap. 6** will cover the effect of nitrogen incorporation on the catalytic response of Mo metal for the reduction of -NO_2 and C=O. The hydrogenation of nitroarenes promoted over Mo_2C (bulk and supported on Al_2O_3) is examined in **Chap 4**. Product yield is a crucial factor for industrial processes and can be improved by the

use of promoters. An increase in the activity of Mo based systems in methanol steam reforming, hydrodesulfurisation and hydrodenitrogenation has been reported with the addition of noble metals (Pd, Pt) [1.18] or the inclusion of Ni, Fe and Co [1.19]. With a view to enhancing overall catalyst performance, the incorporation of Au (**Chap. 2/3/4**) and the inclusion of Fe and Co (**Chap. 5**) as promoter have been considered.

It is clear from a series of comprehensive reviews [1.20-23], that interest in the use of supported Au catalysts is growing. Although work to date has largely focused on oxidation reactions in liquid phase, studies dealing with the hydrogenation of aldehydes to alcohols (*e.g.* crotonaldehyde, citral, acrolein) have shown promising results in terms of selectivity and stability [1.20,1.24]. **Chap. 7** will cover the selective hydrogenation of benzaldehyde to benzyl alcohol over Au/Al_2O_3. The catalytic response of hydrogenation reactions over supported Au depends mainly on (i) Au particle size and morphology [1.22,1.25,1.26] and (ii) nature of the support in terms of interaction with the metal, redox and acid-base properties [1.27-29]. These effects are probed for the hydrogenation of 4-nitrobenzaldehyde (**Chap 8**) and benzoic acid (**Chap. 9**). A schematic diagram of my PhD research is presented **Figure 1.1**.

Critical catalyst structural features are examined throughout this work by applying a range of techniques including:

- Determination of point of zero charge, surface area and pore size distribution.
- Adsorption/desorption dynamics of H_2, N_2 and O_2 investigated by flow chemisorption, temperature programmed reduction/desorption (TPR/TPD).
- Surface and bulk structural analysis: Elemental analysis, Atomic Absorption Spectroscopy (AAS), X-ray Diffraction (XRD), X-ray Photoelectron Spectroscopy (XPS), Scanning Electron Microscope (SEM), Transmission Electron Microscopes (TEM), Inductively Coupled Plasma Atom Emission Spectroscopy (ICP-AES), Fourier Transform Infrared Spectroscopy (FTIR) and Ultraviolet–Visible Spectroscopy (UV-Vis).

Each Chapter includes a comprehensive literature review of the topic under investigation, pertinent experimental details; results are coupled with discussion.

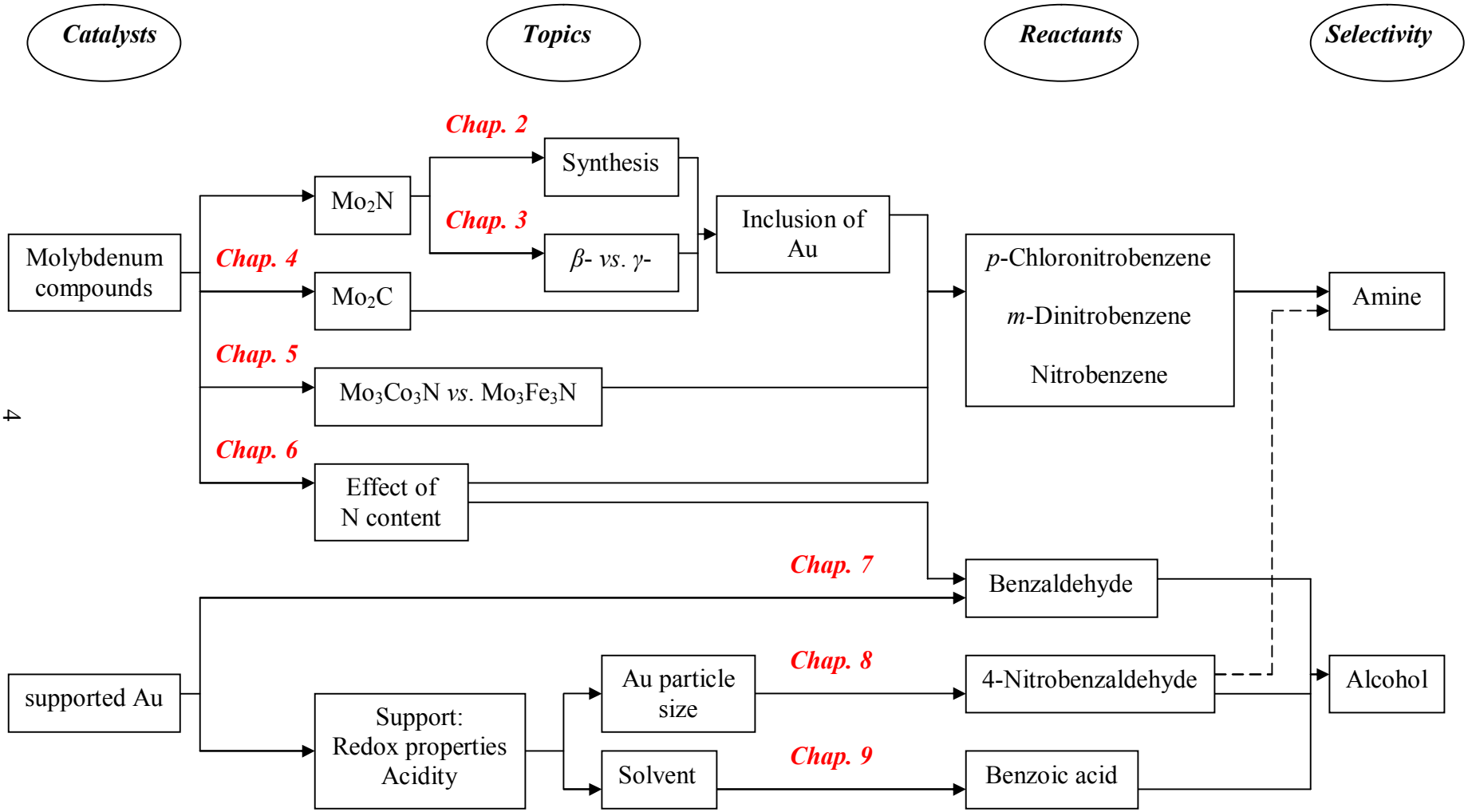

Figure 1.1: Scope of the studies undertaken in this thesis

The reader should note that some of the results presented in this thesis are the outcome of collaborations with,

Université Pierre et Marie Curie (France): Catherine Louis and Laurent Delannoy made the four catalysts used Chapter 4 (Mo_2C, Au/Mo_2C, Mo_2C/Al_2O_3 and Au/Mo_2C) while Claude Potvin conducted the XPS analysis (with associated curve fitting). Thomas Onfroy and Christophe Calers carried out the FTIR pyridine and XPS measurements, respectively, presented in Chapter 8.

University of Glasgow and Aberdeen (UK): Anne-Marie Alexander, S. M. Hunter, Peter Chung and Justin S.J. Hargreaves prepared Co_3Mo_3N and Fe_3Mo_3N catalysts and conducted SEM analysis while Russell Howe did the XPS measurements (with associated curve fitting) presented in Chapter 5.

Universidad de Cádiz (Spain): Serafin Bernal and Juan José Delgado synthesised the two Au supported catalysts used Chapter 9 and carried out the STEM and XPS analysis (with associated curve fitting).

Ecole Polytechnique Fédérale de Lausanne (Switzerland): Fernando Cárdenas-Lizana, Daniel Lamey and Lioubov Kiwi-Minsker synthesised γ-Mo_2N and conducted the SEM and XPS measurements Chapter 3 and Chapter 6. Fernando Cárdenas-Lizana also contributed to some of the results and writting of Chapter 2.

1.3 References

[1.1] P. T. Anastas, M. M. Kirchhoff and T. C. Williamson, *Catalysis as a foundational pillar of green chemistry*, Appl. Catal. A: General 221 (2001) 3-13.

[1.2] B. Nair, *Final report on the safety assessment of benzyl alcohol, benzoic acid, and sodium benzoate*, Int. J. Toxicol. 20 (2001) 23-50.

[1.3] H.-U. Blaser, H. Steiner and M. Studer, *Selective catalytic hydrogenation of fonctionalized nitroarenes: an update*, ChemCatChem 1 (2009) 210-221.

[1.4] R. A. Sheldon and R. S. Downing, *Heterogeneous catalytic transformations for environmentally friendly production*, Appl. Catal. A: General 189 (1999) 163-183.

[1.5] A. Corma and P. Serna, *Preparation of substituted anilines from nitro compounds by using supported gold catalysts*, Nat. Protoc. 1 (2006) 2590-2595.

[1.6] G. A. Somorjai and C. J. Kliewer, *Reaction selectivity in heterogeneous catalysis*, React. Kinet. Catal. Lett. 96 (2009) 191-208.

[1.7] P. Maki-Arvela, J. Hajek, T. Salmi and D. Y. Murzin, *Chemoselective hydrogenation of carbonyl compounds over heterogeneous catalysts*, Appl. Catal. A: General 292 (2005) 1-49.

[1.8] R. A. Sheldon, I. Arends and U. Hanefeld, *Green Chemistry and Catalysis*, Willey-VCH, Weinheim, 2007, pp. 92-104.

[1.9] S. T. Oyama, *The chemistry of transition metal carbides and nitrides*, Blackie Academic, Glasgow, 1996, pp. 14-15.

[1.10] A. M. Alexander and J. S. J. Hargreaves, *Alternative catalytic materials: carbides, nitrides, phosphides and amorphous boron alloys*, Chem. Soc. Rev. 39 (2010) 4388-4401.

[1.11] J. G. Chen, *Carbide and nitride overlayers on early transition metal surfaces: Preparation, characterization, and reactivities*, Chem. Rev. 96 (1996) 1477-1498.

[1.12] E. Furimsky, *Metal carbides and nitrides as potential catalysts for hydroprocessing*, Appl. Catal. A: General 240 (2003) 1-28.

[1.13] H. H. Hwu and J. G. Chen, *Surface chemistry of transition metal carbides*, Chem. Rev. 105 (2005) 185-212.

[1.14] S. T. Oyama, *Preparation and catalytic properties of transition metal carbides and nitrides*, Catal. Today 15 (1992) 179-200.

[1.15] M. Nagai, *Transition-metal nitrides for hydrotreating catalyst: Synthesis, surface properties and reactivities*, Appl. Catal. A: General 322 (2007) 178-190.

[1.16] S. W. Oh, M. N. Kang, C. W. Cho and M. W. Lee, *Detection of carcinogenic amines from Dyestuffs or dyed substrates*, Dyes Pigm. 33 (1997) 119-135.

[1.17] *SIDS Initial Assessment report for 4th SIAM*, *OECD SIDS*, *m-nitroaniline*, *CAS N° 99-09-2*, UNEP publications, 1995, pp. 73-78.

[1.18] W. Setthapun, S. K. Bej and L. T. Thompson, *Carbide and nitride supported methanol steam reforming catalysts: Parallel synthesis and high throughput screening*, Top. Catal. 49 (2008) 73-80.

[1.19] S. Alconchel, F. Sapina, D. Beltran and A. Beltran, *Chemistry of interstitial molybdenum ternary nitrides M_nMo_3N (M = Fe, Co, n = 3; M = Ni, n = 2)*, J. Mater. Chem. 8 (1998) 1901-1909.

[1.20] P. Claus, *Heterogeneously catalysed hydrogenation using gold catalysts*, Appl. Catal. A: General 291 (2005) 222-229.

[1.21] G. J. Hutchings, M. Brust and H. Schmidbaur, *Gold - an introductory perspective*, Chem. Soc. Rev. 37 (2008) 1759-1765.

[1.22] G. Bond, C. Louis and D. T. Thompson, *Catalysis by Gold in Catalytic Science Series*, G. J. Hutchings (Ed.), Imperial College Press, London, 2006, pp. 150-153.

[1.23] A. S. K. Hashmi and G. J. Hutchings, *Gold catalysis*, Angew. Chem. Int. Ed. 45 (2006) 7896-7936.

[1.24] B. Campo, C. Petit and M. A. Volpe, *Hydrogenation of crotonaldehyde on different Au/CeO_2 catalysts*, J. Catal. 254 (2008) 71-78.

[1.25] L. McEwan, M. Julius, S. Roberts and J.C.Q. Fletcher, *A Review of the use of gold catalysts in selective hydrogenation reactions*, Gold Bull. 43 (2010) 298-306.

[1.26] F. Cárdenas-Lizana, S. Gómez-Quero, N. Perret and M. A. Keane, *Support effects in the selective gas phase hydrogenation of p-chloronitrobenzene over gold*, Gold Bull. 42 (2009) 124-132.

[1.27] C. Milone, C. Crisafulli, R. Ingoglia, L. Schipilliti and S. Galvagno, *A comparative study on the selective hydrogenation of α,β unsaturated aldehyde and ketone to unsaturated alcohols on Au supported catalysts*, Catal. Today 122 (2007) 341.

[1.28] F. Cárdenas-Lizana, S. Gómez-Quero, N. Perret and M. A. Keane, *Gold catalysis at the gas–solid interface: role of the support in determining activity and selectivity in the hydrogenation of m-dinitrobenzene*, Catal. Sci. Tech. 1 (2011) 652-661.

[1.29] F. Cárdenas-Lizana, S. Gómez-Quero and M. A. Keane, *Exclusive production of chloroaniline from chloronitrobenzene over Au/TiO_2 and Au/Al_2O_3*, ChemSusChem 1 (2008) 215-221.

Chapter 2

Synthesis Mechanism and Catalytic Response of β-Mo_2N and Au/β-Mo_2N for the Gas Phase Hydrogenation of *p*-Chloronitrobenzene

In this Chapter, the synthesis mechanism of β-Mo_2N from a temperature programmed treatment of MoO_3 in flowing N_2+H_2 is investigated. Au is incorporated as a promoter and Au/Mo_2N is characterised. The catalytic actions of Mo_2N and Au/Mo_2N are examined in the continuous gas phase hydrogenation of *p*-chloronitrobenzene. The effect of the support (Mo_2N *vs* Al_2O_3) and metal (Au *vs* Pd) are also considered.

2.1 Introduction

Transition-metal nitrides in general, and Mo nitride in particular, exhibit a combination of properties that have resulted in multiple applications as coatings/structural components [2.1], high performance magnets [2.2], in electronic and optical devices [2.3] and as catalytic materials [2.4,2.5]. Conventional preparative routes have involved either (a) high temperature (1400-1900 K) reaction of the base metal and elemental nitrogen [2.6], (b) carbothermal nitridation of metal oxides [2.6] or (c) a self propagating high temperature synthesis [2.7]. Alternative methods that can operate under milder reaction conditions have drawn on controlled temperature programmed procedures. Examples include the reaction of MoO_3 with NH_3 [2.8-11] and N_2+H_2 [2.12,2.13], reaction of $MoCl_5$ with urea [2.14], reduction of MoO_2 with NH_4Cl [2.15], chemical vapour deposition of $MoCl_5$ (in the presence of NH_3) [2.16] and the thermal decomposition of $(HMT)_2(NH_4)_4Mo_7O_{24}$ [2.17,2.18]. A combination of NH_3+H_2 has been the most widely employed reacting gas in reduction-nitridation processes [2.4,2.19,2.20]. However, the use of a N_2+H_2 mixture circumvents the heat transfer problems associated with the endothermic NH_3 decomposition [2.12].

The methodologies applied to date have generated a combination of Mo_xN_y phases, principally metastable cubic (γ-Mo_2N) and hexagonal (δ-MoN) structures [2.6]. Although γ-Mo_2N is the most commonly synthesised form by thermal treatment of MoO_3 [2.9,2.12,2.19,2.21], there is also evidence in the literature for the formation of a body centred tetragonal β-nitride phase with a Mo/N ratio in the range 2.0-2.6 [2.13,2.22-26].

The literature dealing with the temperature programmed synthesis of Mo nitrides is still quite limited and a search through the literature did not reveal any comprehensive analysis of the mechanism(s) involved in the formation of *β*-Mo nitride from MoO_3. It is, however, worth noting a number of reports that deal (in part) with Mo nitride preparation [2.13,2.23,2.24,2.27-29], physical/chemical properties [2.6] and morphology [2.13,2.24]. Additional published studies are relevant in that the formation of partially reduced oxides (Mo_4O_{11} [2.30], MoO_2 [2.9]) or ordered bronzes (H_xMoO_3, $0.07 < x < 0.34$) [2.31] and/or Mo [2.22] have been observed during the reduction-nitridation process. Nagai *et al*. [2.23] recorded the formation of MoO_2, *γ*-Mo_2N, *β*-Mo_2N and Mo during treatment of MoO_3 with NH_3 up to 1173 K.

In terms of applications, it has been reported that group VI nitrides can exhibit comparable catalytic activity in hydrogen mediated reactions to that obtained with conventional metal catalysts [2.4,2.32]. This has been ascribed to a contraction of the *d*-band and modification of electron density due to the incorporation of N interstitially in the metal lattice [2.33], resulting in a capacity for H_2 adsorption [2.4]. Molybdenum nitrides have been successfully used to promote the hydrogenation of long chain alkadienes [2.34], CO [2.35] and ethylene [2.36], the hydrodenitrogenation of carbazole [2.23,2.28,2.37] and the hydrodesulfuration of thiophene [2.13,2.24] and dibenzothiophene [2.38]. Moreover, Mckay *et al*. [2.39], demonstrated in a recent study an enhanced catalytic response in ammonia synthesis for *β*-Mo_2N (prepared by MoO_3 treatment in H_2/N_2 at 973 K) when compared with *δ*-MoN and *γ*-Mo_2N. However, there are no studies in the open literature dealing with the hydrogenation of nitro-compounds over molybdenum nitride.

In this Chapter, the intermediates in *β*-Mo nitride synthesis are identified with the first application of this nitride in the catalytic hydrogenation of nitroarenes. The selective hydrogenation of *p*-chloronitrobenzene (*p*-CNB) to *p*-chloroaniline (*p*-CAN) has been selected as a model reaction. *p*-CAN is a high production volume compound [2.40], extensively used in the manufacture of a range of fine chemicals [2.41]. Existing routes to *p*-CAN involve high pressure batch liquid phase operations that generate toxic by-products with a low overall product yield [2.42] and there is now a pressing demand for alternative cleaner catalytic routes. In this study, the feasibility of *β*-Mo nitride as a catalytic material to promote the continuous gas phase hydrogenation of *p*-CNB to *p*-CAN is established.

A critical advancement in cleaner amine synthesis in batch operation using oxide supported Au catalysts has resulted from the work of Corma *et al*. [2.43], who demonstrated a preferential activation of -NO_2 with H_2 dissociation at low coordination Au sites by *in situ* IR spectroscopy and theoretical calculations. Previous work conducted in this laboratory [2.44,2.45] established -NO_2 hydrogenation chemoselectivity over Au in gas phase continuous operation. Studies to date have shown low hydrogenation activity for Au that can be ascribed to a restricted activation/dissociation of H_2 [2.46], which is dependent on chemisorption temperature [2.47] and Au particle size [2.48]. As Mo_2N can chemisorb hydrogen and Au is selective for nitro-group reduction, the combination of Au with Mo nitride is examined as a new catalyst formulation directed at elevating hydrogenation rate while maintaining chemo-selectivity. The catalytic action of Mo_2N and Au/Mo_2N are investigated in the gas phase hydrogenation of *p*-CNB. Au/Al_2O_3 (as benchmark [2.49]) is examined to probe a possible support effect, *i.e.* Mo_2N *vs.* Al_2O_3. Moreover, as Pd has shown enhanced activity in -NO_2 reduction [2.50], the catalytic performance of Pd/Mo_2N is also considered.

2.2 Experimental

2.2.1 Mo Nitride Synthesis

The MoO_3 (99.9995% w/w) precursor was obtained from Alfa Aesar and used as received. Mo nitride synthesis was conducted in a commercial CHEM-BET 3000 (Quantachrome) unit. The precursor (0.150 g MoO_3) was loaded in a U-shaped quartz cell (10 cm×3.76 mm i.d.) and heated in 15 cm^3 min^{-1} (GHSV = 7×10^3 h^{-1}, Brooks mass flow controlled) 15% v/v N_2/H_2 at 5 K min^{-1} to 933 K. The effluent gas passed through a liquid N_2 trap and changes in composition (consumption/release of H_2 and/or N_2) were monitored by a thermal conductivity detector (TCD) with data acquisition/manipulation using the TPR Win^{TM} software. The reaction was quenched by switching to a He flow (15 cm^3 min^{-1}), the temperature was maintained at 933 K for 3 h and the sample was cooled to room temperature. In order to independently analyse precursor reduction, the thermal treatment of MoO_3 in 15 cm^3 min^{-1} 15% v/v Ar/H_2 at 5 K min^{-1} to 933 K was also monitored. In addition, nitride decomposition, was examined by a controlled thermal treatment at 5 K min^{-1} in a flow (60 cm^3 min^{-1}, GHSV = 2×10^4 h^{-1}) of He to

1273 K. Samples for off-line analysis were passivated at room temperature in 1% v/v O_2/He; there was no detectable temperature increase during sample passivation.

A suspension of $HAuCl_4$ (300 cm^3, 3×10^{-4} M, Aldrich), aqueous urea (100 cm^3, 0.86 M) and Mo_2N was mixed (at 300 rpm) and heated (1 K min^{-1}) to 353 K (2.5 h). The solid was filtered and washed with distilled water until the wash water was Cl-free (based on $AgNO_3$ test), dried in He (45 cm^3 min^{-1}) at 383 K for 3 h, sieved into a batch of 75 μm average particle diameter and stored at 277 K under He in the dark. Pd/Mo_2N (2.5×10^{-4} M $Pd(NO_3)_2$, Aldrich) was synthesised following the same protocol. For comparison purposes, Au supported on Al_2O_3 (Puralox, Condea Vista Co.) was prepared by standard impregnation with $HAuCl_4$ as described elsewhere [2.51], dried and stored as above.

2.2.2 Sample Characterisation

Temperature programmed reduction (TPR) *post*-passivation, hydrogen chemisorption (at 290 K), surface area and pore volume measurements were conducted using the commercial CHEM-BET 3000 (Quantachrome) unit. Samples were activated in 17 cm^3 min^{-1} 5% v/v H_2/N_2 at 2 K min^{-1} to 493-673 ± 1 K (1 h), swept with 65 cm^3 min^{-1} N_2 (1.5 h) and cooled to room temperature. After TPR, the reduced samples were swept with a 65 cm^3 min^{-1} flow of N_2 for 1.5 h, cooled to room temperature and subjected to H_2 chemisorption using a pulse (10 μl) titration procedure. BET surface area was obtained from analysis in a 30% v/v N_2/He flow with ultra pure N_2 (> 99.99%, BOC) as internal standard. At least two cycles of nitrogen adsorption-desorption in the flow mode were employed using the standard single point BET method. Pore volume measurements were performed using the commercial Micromeritics Flowsorb II 2300 unit. Prior to analysis, the samples were outgassed at 423 K for 1 h and the total pore volume was obtained at a relative N_2 pressure of P/P_0 = 0.95. BET and pore volume measurements were reproducible to within ± 5%; the values quoted represent the mean.

Identification of the intermediate and final products was confirmed by XRD, employing a Bruker/Siemens D500 incident X-ray diffractometer using Cu Kα radiation. The samples were scanned at a rate of 0.02º $step^{-1}$ over the range $20º \leq 2\theta \leq 90º$ (scan time = 0.5 s $step^{-1}$). Diffractograms were identified by direct comparison with either commercial samples (MoO_3 (Aldrich, 99%) and Mo powder (Aldrich, ≥ 99.9%))

or the JCPDS-ICDD reference standards, *i.e.* MoO_3 (35-609), MoO_2 (32-0671), Mo (42-1120), *β*-Mo_2N (25-1368) and Au (04-0784)). Diffuse reflectance UV-Vis (DRS UV-Vis) measurements were conducted using a Perkin Elmer Lambda 35 UV-Vis Spectrometer with $BaSO_4$ powder as reference; absorption profiles were calculated from the reflectance data using the Kubelka-Munk function. Analysis by scanning electron microscopy (SEM) was carried out using a Hitachi S2700 field emission SEM unit operated at an accelerating voltage of 10 kV. The sample was deposited on a standard aluminium SEM holder and coated with gold. Elemental (nitrogen) analysis was determined using an Exeter CE-440 Elemental Analyser after sample combustion at *ca.* 1873 K.

The Au and Pd content (supported on *β*-Mo_2N or Al_2O_3 and in solution during reaction) was determined by atomic absorption spectrometry (Shimadzu AA-6650 spectrometer) using an air-acetylene flame. High resolution transmission electron microscopy (HRTEM) employed a JEOL JEM 2011 unit operated at an accelerating voltage of 200 kV using Gatan DigitalMicrograph 3.4 for data treatment. The specimens were prepared by dispersion in acetone and deposited on a holey carbon/Cu grid (300 Mesh). The mean metal (Au or Pd) particle size is given as surface area-weighted mean (*d*) [2.45] where over 200 individual metal particles were counted for each catalyst.

2.2.3 Hydrogenation of p-Chloronitrobenzene (p-CNB)

2.2.3.1 Catalytic System

The hydrogenation of *p*-CNB (Sigma-Aldrich, purity ≥ 99%) as a solution in ethanol (Sigma-Aldrich ≥ 99%) was carried out under atmospheric pressure at 493 K, *in situ* immediately after *β*-Mo_2N activation, in a fixed bed vertical glass reactor (l = 450 mm; i.d. = 15 mm). The catalytic reactor and operating conditions to ensure negligible heat/mass transport limitations have been fully described elsewhere [2.52] but some features, pertinent to this study, are given below. A layer of borosilicate glass beads served as preheating zone, ensuring that the organic reactant was vaporised and reached reaction temperature before contacting the catalyst. Isothermal conditions (± 1 K) were ensured by diluting the catalyst bed with ground glass (75 μm); the ground glass was mixed thoroughly with catalyst before insertion in the reactor. The reaction temperature was continuously monitored using a thermocouple inserted in a thermowell within the

catalyst bed. The *p*-CNB reactant in ethanol was delivered at a fixed calibrated flow rate to the reactor *via* a glass/teflon air-tight syringe and teflon line using a microprocessor controlled infusion pump (Model 100 kd Scientific). A co-current flow of *p*-CNB and ultra pure (> 99.99%, BOC) H_2 (< 1% v/v *p*-CNB in H_2) was maintained at GHSV = 330 min^{-1} with a catalyst mass to inlet *p*-CNB molar rate (*m*/*F*) in the range 8×10^3-8×10^4 g mol^{-1} min; H_2 content was well in excess of the stoichiometric requirement where the hydrogen flow rate was monitored using a Humonics (Model 520) digital flowmeter. In a series of blank tests, passage of *p*-CNB in a stream of H_2 through the empty reactor did not result in any detectable conversion. The reactor effluent was frozen in a liquid nitrogen trap for subsequent analysis.

2.2.3.2 Analytical Method and Activity/Selectivity Evaluation

The composition of the reaction/product(s) mixtures were determined using a Perkin-Elmer Auto System XL chromatograph equipped with a programmed split/splitless injector and a flame ionization detector, employing a DB-1 capillary column (i.d. = 0.33 mm, length = 30 m, film thickness = 0.20 μm). Data acquisition and manipulation were performed using the TotalChrom Workstation Version 6.1.2 (for Windows) chromatography data system and the overall reactant/product molar fractions were obtained using detailed calibration (not shown). Fractional hydrogenation ($X_{p\text{-CNB}}$) was obtained from

$$X_{p\text{ - CNB}} = \frac{[p-CNB]_{in} - [p-CNB]_{out}}{[p-CNB]_{in}} \tag{2.1}$$

where selectivity with respect to *p*-chloroaniline (*p*-CAN) is given by

$$S_{p\text{ - CAN}}(\%) = \frac{[p-CAN]_{out}}{[p-CNB]_{in} - [p-CNB]_{out}} \times 100 \tag{2.2}$$

Repeated reactions with different samples from the same batch of catalyst delivered conversion/selectivity values that were reproducible to within ± 7%.

2.3 Results and Discussion

2.3.1 β-Mo_2N Synthesis Mechanism

2.3.1.1 Temperature Programmed Synthesis

The commercial MoO_3 sample (as received), when subjected to a temperature programmed treatment in 15% v/v N_2/H_2 to 933 K, generated the profile presented in **Figure 2.1(A)**.

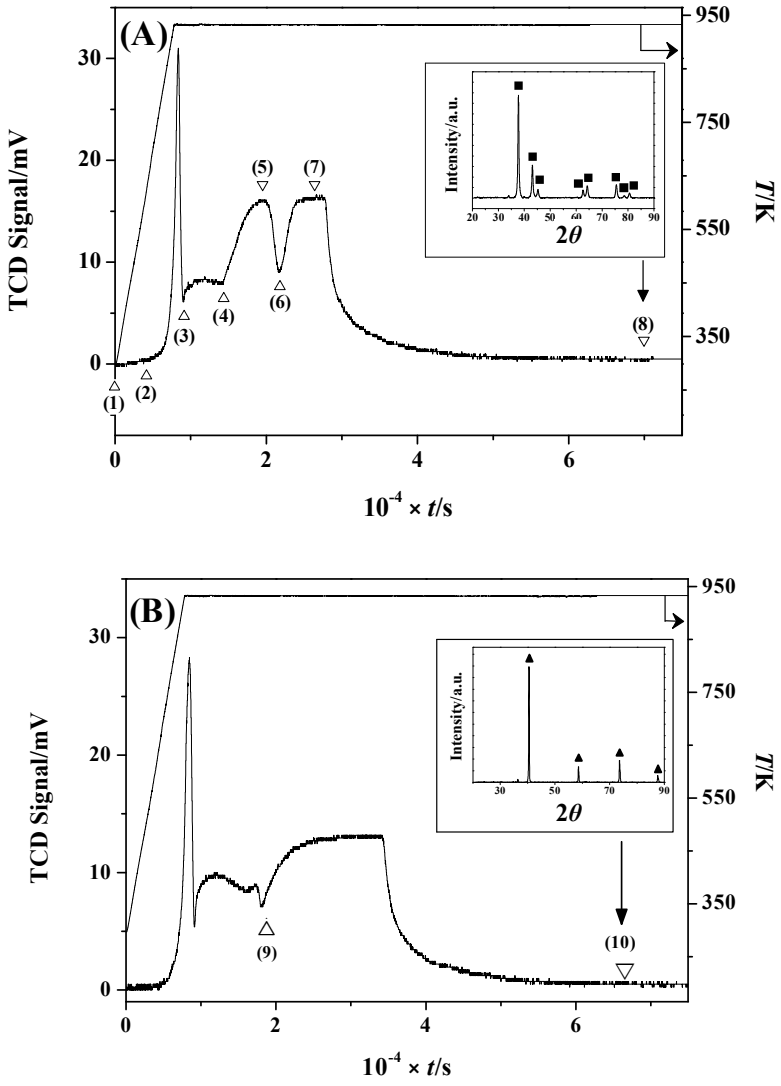

Figure 2.1: TCD response resulting from the temperature programmed nitridation of MoO_3 to 933 K (at 5 K min^{-1}) in (A) 15% v/v N_2/H_2 and (B) 15% v/v Ar/H_2. Insets: XRD patterns for the passivated products *post* thermal treatment. Note: peak assignments based on JCPDS-ICDD standards for (A) β-Mo_2N (25-1368, ■) and (B) Mo (42-1120, ▲).

The emergence of four positive (H_2 consumption) peaks suggests four separate reaction steps. To probe this response, the thermal treatment was repeated, stopping at different stages in order to generate eight samples for *ex situ* analysis, as identified in **Figure 2.1(A)**. Sample selection included starting material (1), final product (8) and intermediate samples (2-4 and 6) obtained *pre-* and *post-* a stage of significant H_2 consumption. Given the broadness of the two final peaks, samples 5 and 7 were taken at the peak maxima. Sample 2 was selected, although no significant response was noted, as there is some evidence in the literature [2.31] of a transition from MoO_3 to MoO_2 at this temperature (623 K). The associated time, temperature related peak maxima (T_{max}), BET surface area, total pore volume and phase composition associated with each sample are given in **Table 2.1**. Taking the profile in **Figure 2.1(A)**, intermediate(s) formation and conversion occurred during the final isothermal (933 K) hold, suggesting a kinetically controlled process. In contrast, previous studies have suggested that Mo nitride intermediate(s) formation was temperature dependant, *i.e.* thermochemically controlled: MoO_2 (613-773 K) [2.9,2.12,2.13,2.53]; H_xMoO_x (≤ 623 K) [2.31,2.53,2.54]; Mo_4O_{11} (673 K) [2.55]; γ-$Mo_2O_xN_{1-x}$ (773 K) [2.56]; Mo (900-1153 K) [2.13,2.55,2.57].

Table 2.1: Reaction time, temperature related TCD signal maximum (T_{max}), BET surface area (*SA*), total pore volume and % fraction of each phase associated with the passivated samples: see Figure 2.1.

Sample	Time (min)	T_{max} (K)	BET area (*SA*, $m^2\ g^{-1}$)	Pore Volume ($10^{-3}\ cm^3\ g^{-1}$)	% (Phase)
(1)	0	298	1	2	100 (MoO_3)
(2)	69	623	2	3	100 (MoO_3)
(3)	150	933	2	3	100 (MoO_2)
(4)	240	933	6	7	90 (MoO_2) 10 (Mo)
(5)	325	933	14	11	25 (Mo) 75 (β-Mo_2N)
(6)	365	933	14	10	20 (Mo) 80 (β-Mo_2N)
(7)	440	933	14	10	100 (β-Mo_2N)
(8)	1165	933	17	11	100 (β-Mo_2N)

2.3.1.2 XRD/Elemental Analysis/DRS UV-Vis

Powder XRD patterns of passivated samples obtained at points 1-8 are presented in **Figure 2.2**. It has been established previously [2.58] that the passivation step provides a protective oxide surface layer without deeper oxidation. In order to confirm the composition of each sample, the XRD patterns were compared with commercial samples (MoO_3 (A), MoO_2 (B) and Mo (C)) and the JCPDS-ICDD standards for MoO_3 (35-609), MoO_2 (32-0671), Mo (42-1120) and *β*-Mo_2N (25-1368, D). In **Figure 2.2**, each of the four columns represent the specific contribution at that stage of reduction and/or nitridation (1-8) due to (A) MoO_3, (B) MoO_2, (C) Mo and (D) *β*-Mo_2N and serves to illustrate the evolution of the MoO_3 reactant to *β*-Mo_2N product. The diffractogram of the final product shows peaks at 37.7°, 43.1°, 45.3°, 62.7°, 64.3°, 75.5°, 78.6° and 80.5° (**Figure 2.2,** profile 8-D), which are consistent with the (112), (200), (004), (220), (204), (312), (116) and (224) reflections of bulk *β*-Mo_2N. This result agrees with the findings of Gong *et al.* [2.13] who reported the formation of *β*-Mo_2N *via* temperature programmed treatment of MoO_3 with N_2+H_2 at 923-1023 K. In contrast, Nagai and co-workers [2.23,2.28] proposed that *β*-phase formation (from MoO_3 treatment in NH_3) required a higher synthesis temperature where the conversion of the (cubic) *γ*-phase to the *β*-form occurred at 1070 K (in He).

A decrease in the intensity of the characteristic signals for MoO_3 in **Figure 2.2** (comparing profiles 1-A with 2-A) suggests a transformation of the trioxide over the temperature range 298-623 K. While Ressler *et al.* [2.31] have proposed a transition of MoO_3 to MoO_2 at 623 K, we observed no detectable signals due to (bulk) MoO_2 associated with sample 2 (see profile 2-B). The sharp H_2 TPR consumption peak recorded at 933 K (between samples 2 and 3, see **Figure 2.1(A)**) can be attributed to the reduction of MoO_3 to MoO_2 as confirmed in profile 3-B (**Figure 2.2**). Moreover, the amount of H_2 associated with this signal matched that required for the oxide reduction (to within ± 10%), confirming the sole transition of trioxide to Mo dioxide.

The ill-defined positive peak between points 3 and 4 (**Figure 2.1(A)**) can be linked to a partial reduction of MoO_2 to Mo (**Figure 2.2**, profile 4-C and **Table 2.1**). The latter proceeds further from stage 4 to 5 (**Figure 2.1(A)**) where the XRD response for sample 5 shows only trace MoO_2. Nitrogen consumption generated a negative TCD signal (see **Figure 2.1(A)**) and the XRD profiles for samples 5 and 6 are consistent with the nitridation of Mo (profiles 5-D and 6-D in **Figure 2.2**). The nitridation process is

complete by stage 7, at which point there was no detectable Mo present (**Figure 2.2**, **Table 2.1**). Moreover, elemental analysis of samples 5 and 7 revealed an increase in nitrogen content (from 2.4 ± 0.3 to 5.7 ± 0.3% w/w), which can be attributed to the progressive nitridation of Mo. Samples 7 and 8 exhibited equivalent nitrogen contents, close to that for β-Mo_2N. The occurrence of a final positive signal (stage 6-8, **Figure 2.1(A)**) can be attributed to H_2 uptake on β-Mo_2N [2.4].

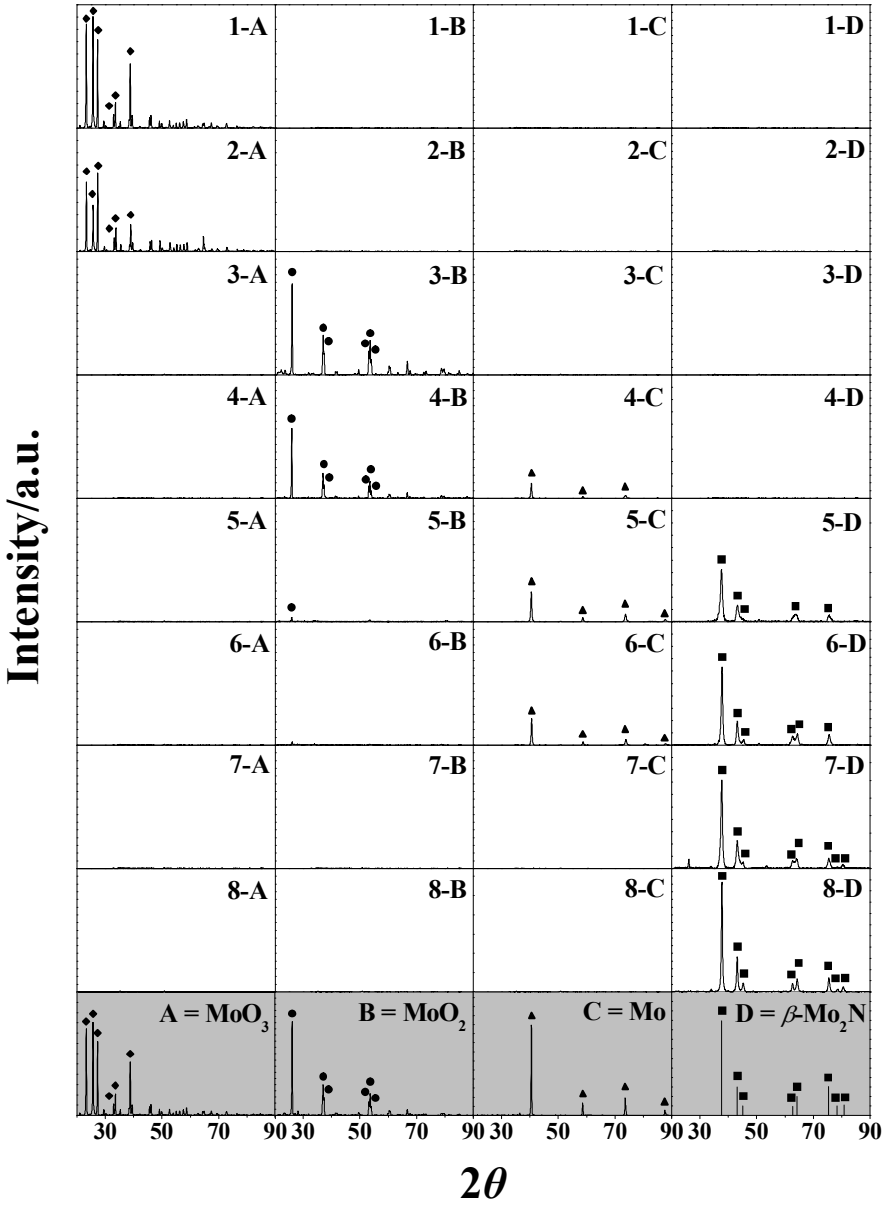

Figure 2.2: XRD profiles of samples 1-8 (see Figure 2.1) focusing on the contributions due to (A) MoO_3, (B) MoO_2, (C) Mo metal and (D) β-Mo_2N. Diffractograms for model samples and peak assignment based on JCPDS-ICDD reference data are denoted by A (MoO_3; Alfa Aesar, 99.9995%; 35-0609, ◆), B (MoO_2; Aldrich, 99%; 32-0671, ●), C (Mo; Aldrich, ≥ 99.9%; 42-1120, ▲) and D (JCPDS-ICDD β-Mo_2N standard (25-1368), ■).

Our results confirm that the reaction of MoO_3 with N_2+H_2 follows the sequence:

$$MoO_3 \xrightarrow[-H_2O]{+H_2} MoO_2 \xrightarrow[-H_2O]{+H_2} Mo \xrightarrow{+N_2} \beta - Mo_2N \qquad (2.3)$$

Previous studies have suggested the participation of MoO_2 [2.9,2.10,2.12,2.13,2.24], MoO_xH_y [2.31,2.53,2.54], Mo_4O_{11} [2.59,2.60] and Mo [2.13,2.24] as intermediates during the temperature programmed treatment of MoO_3 to form Mo nitride. Matsuda *et al.* [2.54] proposed the reduction pathway $MoO_3 \rightarrow H_xMoO_3 \rightarrow MoO_2$ for reaction at 623 K, Wise and Markel [2.12] suggested the steps $MoO_3 \rightarrow MoO_2 \rightarrow$ Mo at 773 K and Słoczyński [2.61] reported $MoO_3 \rightarrow Mo_4O_{11} \rightarrow MoO_2$ where $T < 823$ K.

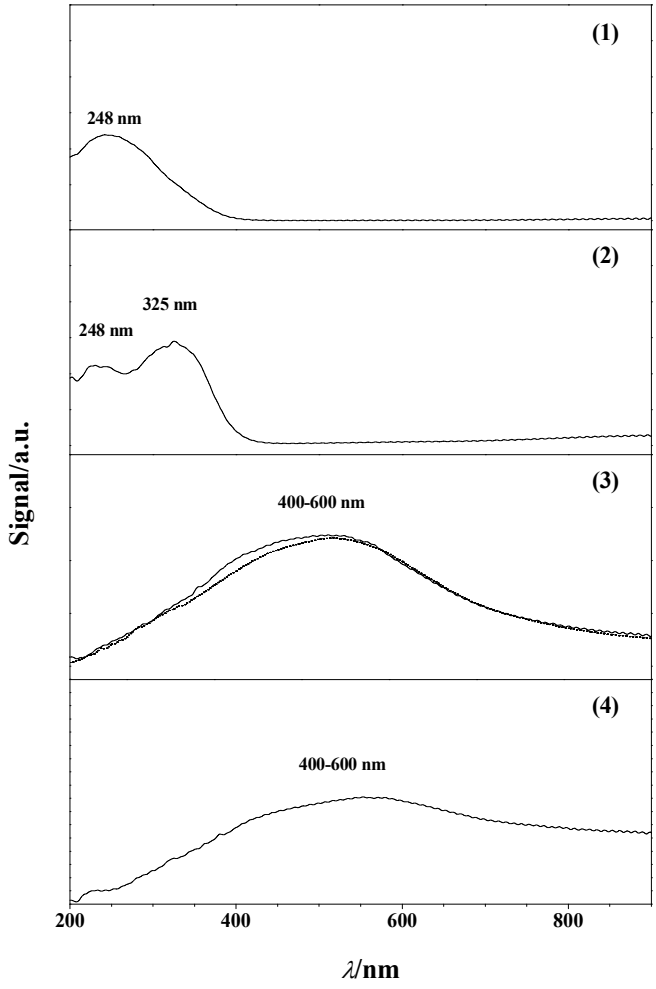

Figure 2.3: DRS UV-Vis spectra of samples 1-4 (see Figure 2.1(A)); dotted line in Profile (3) represents spectrum for a commercial MoO_2 (Aldrich, 99%).

In order to facilitate identification of the reaction intermediates, DRS UV-Vis measurements were also conducted (see **Figure 2.3**). Profiles 1 and 2 (representing samples 1 and 2, **Figure 2.1(A)**) exhibit bands centred at 248 and 325 nm. We can draw

on the literature [2.62] for MoO_3 where bands at 220-250 nm and 320 nm have been observed and attributed to tetrahedral Mo-O and octahedral Mo-O-Mo bridging, respectively. The appearance of the higher wavelength band (at 325 nm) in Profile 2 suggests a partial transition of Mo(VI) from tetrahedral to octahedral coordination, a result that is in line with findings reported by Aritani *et al*. [2.63]. The broad band over the 400-600 nm range for samples 3 and 4 suggests the formation of Mo(V) and/or Mo(IV) [2.64,2.65] and is consistent with our TPR (**Figure 2.1(A)**) and XRD (**Figure 2.2**) measurements, *i.e.* MoO_2 is produced at the final isothermal (933 K) hold (see **Table 2.1**). Indeed the UV-Vis spectrum associated with sample 3 coincides directly with that recorded for the commercial MoO_2 (dotted profile). The decrease in intensity of the MoO_2 signal for sample 4 (Profile 4) can be attributed to a partial reduction to Mo during steps 3 and 4 (see **Figures 2.1(A)** and **2.2**).

2.3.1.3 Stepwise Reduction/Nitridation and Denitridation

The results for the solid transformation of MoO_3 in N_2+H_2 to *β*-Mo_2N are consistent with the formation of MoO_2 and Mo as intermediates, *i.e.* a first stage that involves the conversion of MoO_3 to MoO_2 (sample 3 in **Figure 2.1(A)**) with subsequent reduction to metallic Mo. Nitrogen is then incorporated into the solid in a nitridation step. In order to decouple the reduction and nitridation steps and further confirm this reaction mechanism, the temperature programmed treatment of MoO_3 in H_2+Ar, *i.e.* in the absence of N_2, was monitored and delivered the profile shown in **Figure 2.1(B)**. The final product (at 933 K) in this instance was Mo as confirmed by XRD analysis (see inset in **Figure 2.1(B)**).

By comparing the profiles obtained for thermal treatment in N_2+H_2 (**Figure 2.1(A)**) with that in Ar+H_2 (**Figure 2.1(B)**), any observed differences can be attributed to the involvement of nitridation step(s) in the former. In both cases, the patterns coincide up to the point at which MoO_2 is partially reduced (sample 4 in **Figure 2.1(A)** and sample 9 in **Figure 2.1(B)**), where the associated XRD patterns are consistent with a mixture of MoO_2+Mo: see profiles 4B and 4C in **Figure 2.2** for thermal treatment in N_2+H_2, equivalent to that obtained in Ar+H_2. Additional hydrogen consumption in the Ar+H_2 treatment, *i.e.* positive signal (samples 9 and 10 in **Figure 2.1(B)**), can be attributed to H_2 uptake on Mo as has been reported elsewhere [2.66,2.67]. Further

treatment of the Mo sample in N_2+H_2 resulted in the sole formation of β-Mo_2N as confirmed by XRD analysis (diffractogram pattern not shown).

The reversibility of the nitridation step was also examined by considering a thermally (to 1273 K) induced denitridation of sample 8 (see **Figure 2.1(A)**). The resultant profile is shown in **Figure 2.4** where the amount of nitrogen released was consistent with the content in the starting sample. Nitride decomposition generated Mo as the sole product, which was confirmed by XRD analysis (see inset in **Figure 2.4**). This result finds support in the literature where the generation of Mo has been reported from γ-Mo_2N (*via* β-Mo_2N at 1073 K) for treatment (in He) at $T \geq 1153$ [2.23,2.57].

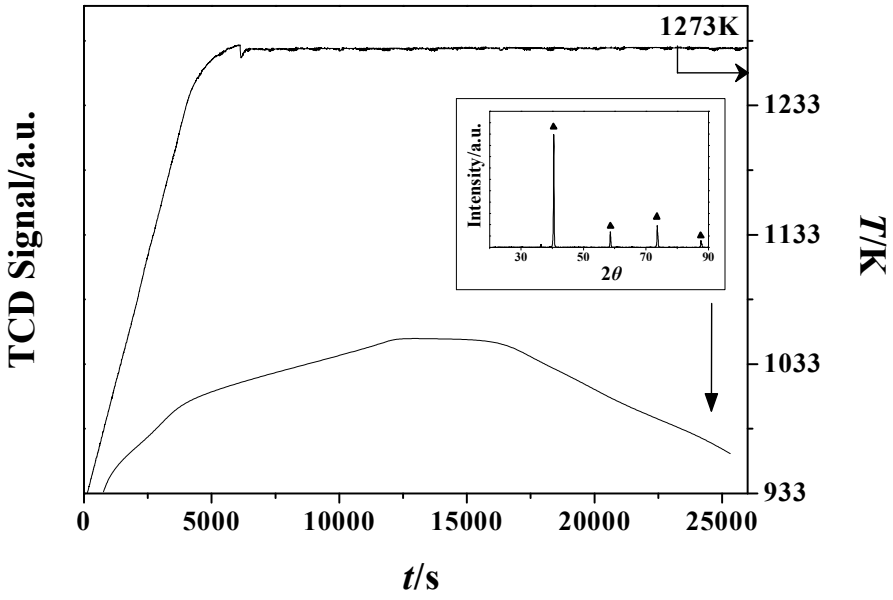

Figure 2.4: TCD response for the temperature programmed treatment of β-Mo_2N to 1273 K in He. Inset: XRD pattern for passivated product *post*-thermal treatment. Note: peak assignments based on the JCPDS-ICDD standard for Mo (42-1120, ▲).

2.3.1.4 SEM/BET/Pore Volume

A solid to solid transition can be termed topotactic if the structural atomic arrangement is conserved in terms of the relative position of the metal atoms [2.68]. It has been shown that Mo nitrides can be synthesized by controlled thermal treatment of MoO_3 with NH_3 [2.8,2.33,2.69] or N_2+H_2 [2.70] *via* a topotactic route where a continuous transformation through oxynitride(s) takes place [2.54]. A non-topotactic formation of β-Mo_2N has also been proposed in the literature [2.22,2.24] but without any explicit evidence to support this.

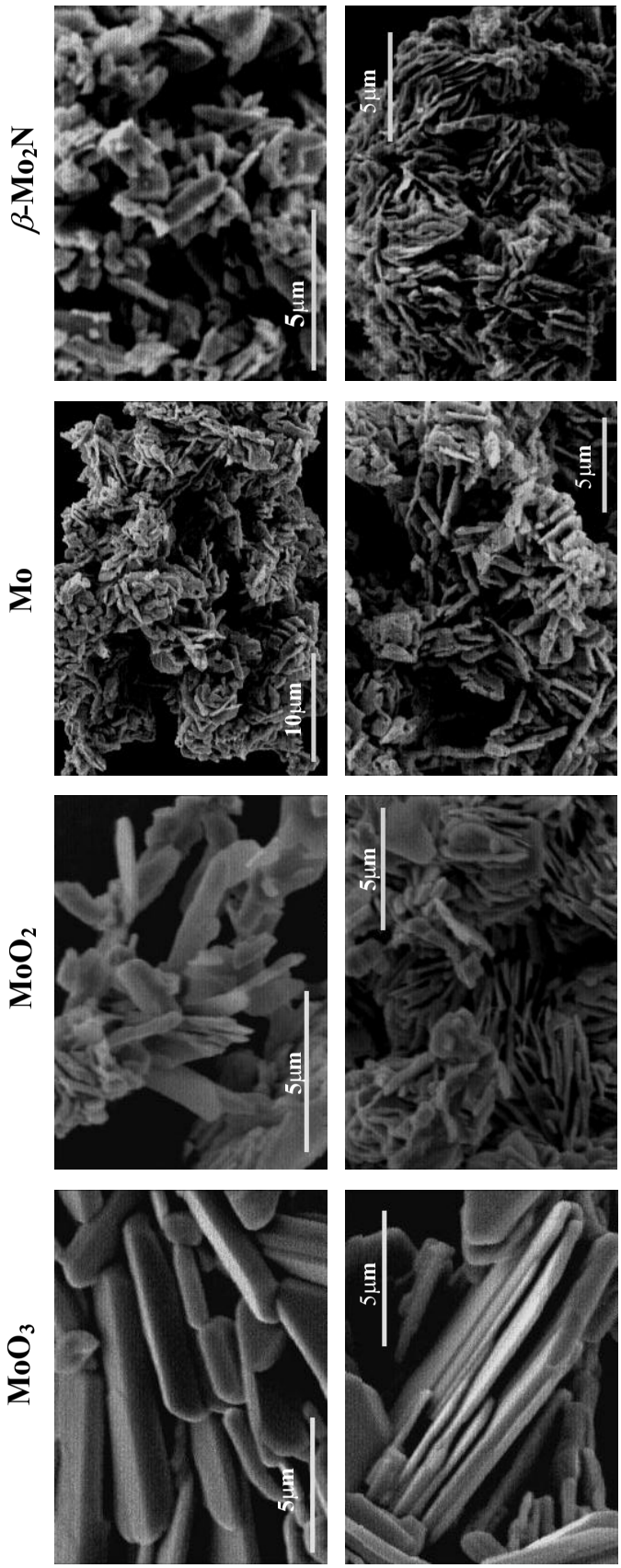

Figure 2.5: SEM micrographs of starting MoO_3 (sample 1, Figure 2.1(A); first row, Figure 2.2), passivated MoO_2 (sample 3, Figure 2.1(A); third raw Figure 2.2), Mo (sample 10, Figure 2.1(B)) and β-Mo_2N (sample 8, Figure 2.1(A); eighth row, Figure 2.2).

In order to consider the morphology and structural evolution of the solid during the preparation of β-Mo_2N, SEM analysis was conducted. The representative SEM images of the starting MoO_3, given in **Figure 2.5**, clearly show a platelet orthorhombic crystal structure, as reported elsewhere [2.6,2.71]. SEM analysis of the β-Mo_2N product (sample 8 in **Figure 2.1(A)**) indicates a non-topotactic transformation, *i.e.* disruption of the platelet morphology during the reduction-nitridation process. Moreover, the SEM micrographs of MoO_2 (sample 3 in **Figure 2.1(A)**) and Mo (sample 10 in **Figure 2.1(B)**) reveal a morphology similar to that of β-Mo_2N, suggesting that the disruption of the crystal configuration takes place during the $MoO_3 \rightarrow MoO_2$ reduction step. This is the first demonstrable evidence for a non-topotactic transformation, identifying the critical step(s) and intermediate(s).

The BET areas and total pore volume of the samples obtained during the reduction/nitridation process are given in **Table 2.1**. The starting MoO_3 (pale yellow crystalline powder) exhibited a negligible surface area (1 $m^2\ g^{-1}$) and low pore volume (2×10^{-3} $cm^3\ g^{-1}$). As reduction/nitridation proceeded, MoO_3 was transformed into a light gray (sample 2, **Figure 2.1(A)**), gray (samples 3-6) and ultimately a lustrous gray-black solid (β-Mo_2N). An increase in both BET ($1 \rightarrow 17$ $m^2\ g^{-1}$) and pore volume ($2\times10^{-3} \rightarrow 11\times10^{-3}$ $cm^3\ g^{-1}$) was observed with the transformation of MoO_3 into β-Mo_2N. Nagai *et al*. [2.23] recorded a surface area of 18 $m^2\ g^{-1}$ for β-Mo_2N synthesised from MoO_3 (1 $m^2\ g^{-1}$) in a temperature controlled reduction-nitridation using NH_3 while Gong *et al*. [2.13] achieved BET surface areas in the range 2-9 $m^2\ g^{-1}$ in N_2+H_2 under similar synthesis conditions. It should be noted that the most significant increase in surface area was associated with the reduction of MoO_2 to Mo (sample 3 to 4) and the subsequent nitridation to β-Mo_2N (sample 4 to 5). Schulmeyer and Ortner [2.72] reported that the conversion of MoO_2 (in H_2) to Mo was accompanied (on the basis of SEM analysis) by the formation of surface cracks and craters as a result of the stresses associated with oxygen removal, which can contribute to the higher BET value. There is no available data on pore volume changes during β-Mo_2N synthesis: the analysis here (**Table 2.1**) reveals an increase in total pore volume that was accompanied by a greater surface area.

2.3.2 Characterisation of β-Mo_2N

Nitride passivation *post*-synthesis (see Experimental section) was required to avoid sample autothermal oxidation upon contact with air [2.73]. The removal of the passivating layer was investigated by TPR and the result is presented in **Figure 2.6(I)**. The TPR profile exhibits a broad positive (hydrogen consumption) peak with T_{max} = 637 K, which can be ascribed to the reduction of the surface oxide layer with water release [2.74]. It should be noted that higher temperatures (by up to 400 K) are required for MoO_3 reduction [2.75], consistent with a more facile removal of the superficial passivating layer. Gong and co-workers [2.13] observed a single reduction peak (at 700 K) during the TPR of passivated β-Mo_2N while Colling *et al*. [2.20] reported the desorption of H_2O associated with the reduction of the passivated surface of γ-Mo_2N at T > 400 K. As the TPR signal returned to baseline in the final isothermal hold (see **Figure 2.6(I)**), a final temperature of 673 K was deemed to be sufficient for β-Mo_2N activation.

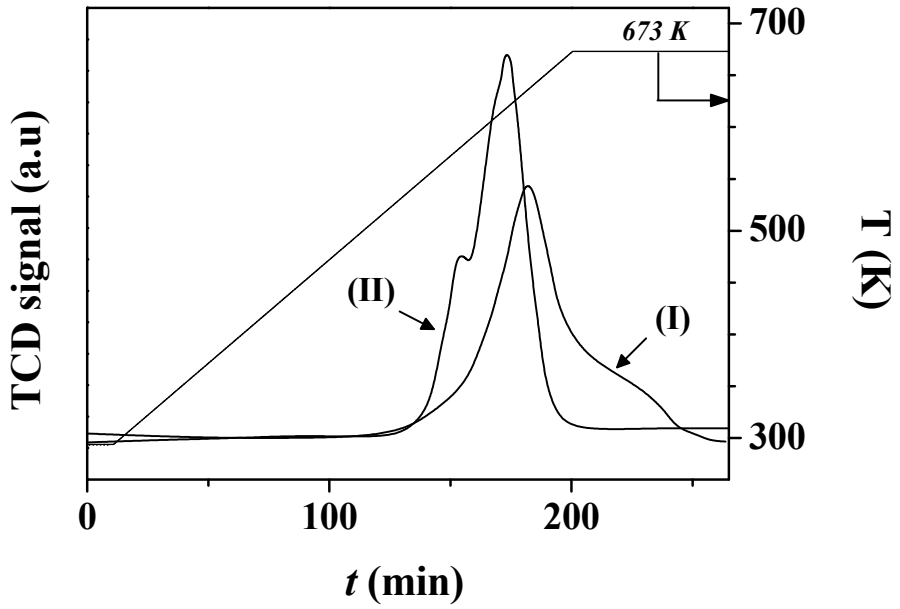

Figure 2.6: TPR profiles for passivated (I) β-Mo_2N and (II) Au/β-Mo_2N

Post-TPR, β-Mo_2N exhibited a measurable ambient temperature H_2 uptake (0.29 μmol g^{-1}, **Table 2.2**). There is no comparable measurement of H_2 chemisorption on β-Mo_2N in the literature. We should, however, flag the work of Li. *et al*. [2.76] who demonstrated room temperature hydrogen adsorption on Mo_2N, although the crystallographic phase was not identified. In addition, Saito and Anderson [2.77]

recorded an uptake of 14.3 μmol g^{-1} on γ-Mo_2N + Mo (BET = 7 m^2 g^{-1}). The dynamics of H_2 adsorption on group VI metal nitrides is still not well understood. Furimsky in his review [2.4] has considered H_2 activation on nitrogen deficient Mo-N sites, which leads to a heterolytic interaction with possible dissociative adsorption. The limited published work suggests a dependency of H_2 chemisorption capacity on temperature [2.78] and nitride surface area [2.79]. Li *et al.* [2.80], studying the H_2 adsorption on *β*-Mo_2N, recorded an order of magnitude greater uptake (from 12 to 173 μmol g^{-1}) with increasing temperature (308 K → 623 K) that they attributed to the formation of a stable hydride phase in the nitride sub-surface. Li *et al.* [2.76] suggested a surface dissociative adsorption on Mo-N pairs with migration from low to high energy sites. Moreover, Haddix and co-workers [2.81], using NMR to probe hydrogen interaction with Mo_2N, concluded that strongly bound hydrogen atoms can be generated at room temperature, occupying *ca.* 10% of the total (BET) surface area, suggesting adsorption at nitrogen deficient sites on the surface.

Table 2.2: Hydrogen chemisorption, metal (Au or Pd) particle size range and mean value (*d*) and rate (*k*) and specific rate (*k'*) constant associated with the hydrogenation of *p*-CNB.

Catalyst	Mo_2N	Au/Mo_2N	Au/Al_2O_3	Pd/Mo_2N
H_2 chemisorption (μmol g^{-1})	0.29	0.42 (32)[a]	0.21(4)[a]	0.51
Metal size range (nm)	-	2-14	1-20	1-7
d (nm)	-	8	8	2
k (μmol$_{p\text{-CNB}}$ g^{-1} min^{-1})	4.6	9.0	-	-
k' (mmol$_{p\text{-CNB}}$ mol_{metal}^{-1} min^{-1})	-	710	220	1140

[a]units : mmol mol_{Au}^{-1}

2.3.3 Au/β-Mo_2N synthesis and characterisation

The XRD pattern *pre-* and *post*-TPR (see **Figure 2.7(I)**) of Au/Mo_2N coincided (in term of peak position and relative intensities) to that recorded for *β*-Mo_2N (see **sample 8**, **Figure 2.2**). Any XRD signal due to metallic Au (2*θ* = 38.1°, JCPDS-ICDD 04-0784) was not visible as it overlaps with the main reflections for *β*-Mo_2N (112) at *ca.* 2*θ* = 37.6°. The TPR profile associated with Au/*β*-Mo_2N (**Figure 2.6**, **profile II**) is characterised by a main H_2 consumption peak (T_{max} = 603 K) where the incorporation of

Au (0.25% w/w) induced a shift in the main hydrogen consumption peak (by 34 K) to a lower temperature, demonstrating a more facile removal of the passivating oxygen due to the presence of Au. A similar effect has been noted in the literature [2.82] for the TPR of passivated Mo_2N with Ni addition. Chemisorption measurements have revealed a measurable increase in the amount of hydrogen uptake due to the inclusion of Au (**Table 2.2**).

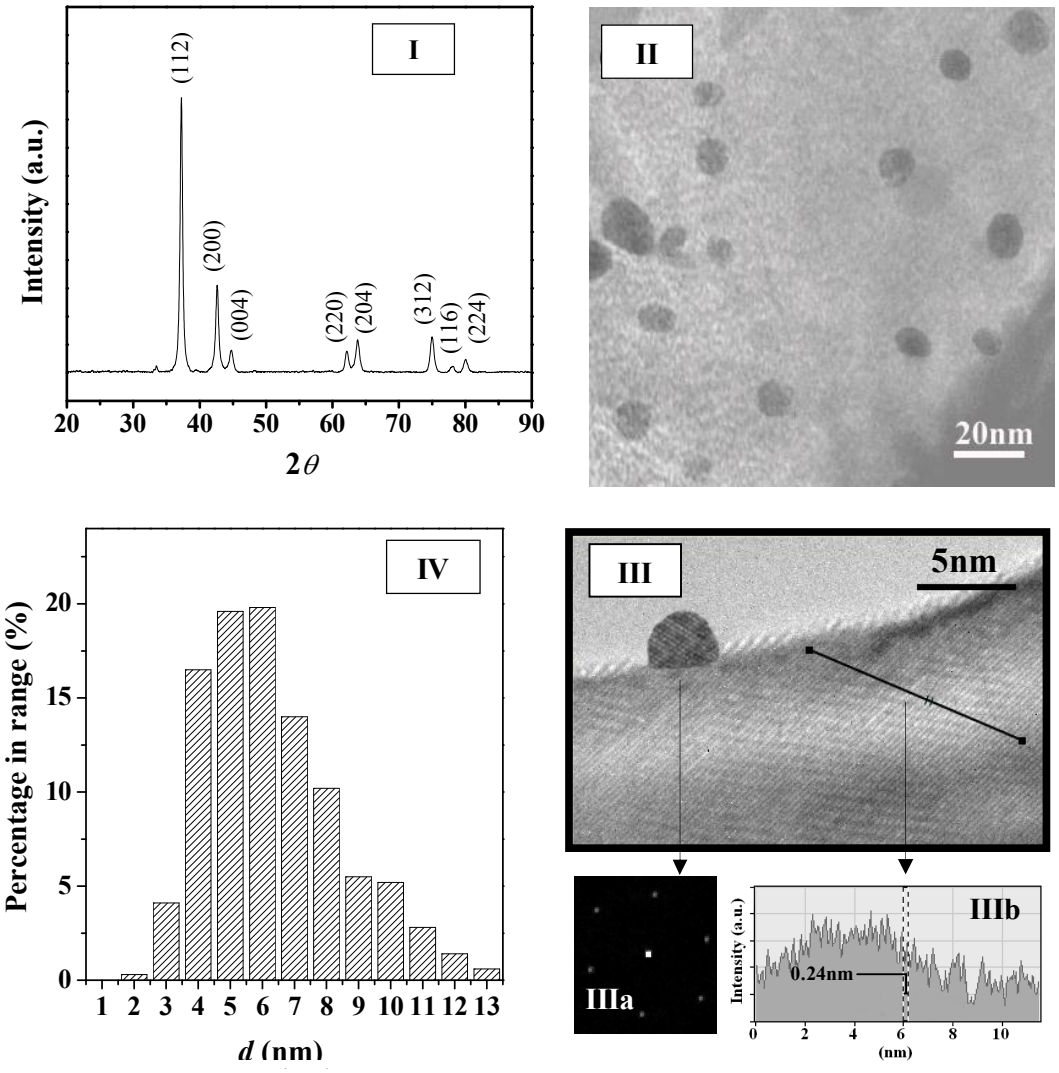

Figure 2.7: Au/β-Mo_2N: XRD pattern (I, including peak assignments based on JCPDS-ICDD 25-1368), representative medium (II) and high (III) resolution TEM images and metal particle size distribution (IV). Note: diffractogram pattern of isolated Au particle (IIIa) and intensity profile revealing distance between planes of the atomic lattice in the 12 nm segment marked on the nitride support (IIIb).

The representative TEM image **in Figure 2.7(II and III)** coupled with diffraction analysis (**IIIb**) establish a spacing of 0.24 nm between the planes in the atomic lattice that is characteristic of the *β*-Mo_2N (112) plane. The TEM image provided in **Figure 2.7(II)** serves to illustrate the nature of Au dispersion and morphology. The diffractogram pattern for an isolated Au particle (**Figure 2.7(IIIa)**) confirms the presence of metallic Au with associated *d*-spacings = 0.20/0.23 nm consistent with the (200) and (111) planes of Au^0 (JCPDS-ICDD 04-0784). The Au particles exhibit a pseudo-spherical morphology and a size distribution in the 2-13 nm range, as illustrated in the histogram given in **Figure 2.7(IV)**, with a mean particle size of (*d* =) 8 nm (**Table 2.2**). It should be noted that there is an appreciable component of Au particles with diameters ≤ 10 nm, *i.e.* the proposed critical Au size range for catalytic activity in hydrogen mediated reactions [2.83].

As the aim of this work is to explore the possibility of an enhanced selective hydrogenation rate over Mo nitride supported Au, Au/Al_2O_3 was adopted as a benchmark catalysts that has exhibited ultra-selectivity in $-NO_2$ group reduction [2.84]. It has been established [2.51] that the reference Au/Al_2O_3 shows the same mean Au particle size (*d* = 8 nm) as Au/Mo_2N. Given that nitroarene hydrogenation rate over supported Au is sensitive to dispersion [2.45], an explicit comparison of performance in terms of a support effect necessitates equivalence in terms of Au size. The synthesised Au/Mo_2N demonstrated an appreciably higher (by a factor of 8) level of hydrogen chemisorption (per mol Au) relative to Au/Al_2O_3 (see **Table 2.2**), which must be due to a contribution from both Au and Mo_2N components.

Since the catalytic action of Pd in $-NO_2$ reduction is well established [2.85], the reaction over Pd/Mo_2N was considered in order to evaluate the effect of incorporating a different metal with Mo_2N. Pd/Mo_2N was synthesised using an analogous procedure (with respect to Au/Mo_2N). The catalyst presented a uniform distribution of Pd nanoparticles (size range = 1-7 nm, *d* = 2 nm) and exhibited increased H_2 chemisorption (see **Table 2.2**) compared with the supported Au systems, as has been noted elsewhere [2.84].

2.3.4 Catalytic response in the gas phase hydrogenation of p-chloronitrobenzene

2.3.4.1 β-Mo_2N

The observed capacity of β-Mo_2N for hydrogen uptake suggests possible hydrogenation properties. This was tested in the gas phase hydrogenation of *p*-CNB where *p*-chloroaniline (*p*-CAN) was detected as the sole product. There was no evidence of further ring hydrogenation or hydrogenolysis of the -Cl or -NO_2 substituents. This ultra-selectivity with respect to -NO_2 group reduction is a significant result as the hydrogenation of *p*-CNB has been invariably accompanied by dechlorination and side-reactions resulting in the formation of azoxyderivates [2.86,2.87], aniline (AN) [2.88-90] and nitrobenzene (NB) [2.89-91]. This has been a feature of reaction over Ru-Ir/γ-Al_2O_3 [2.86], silica supported group VIII metals (Ag, Cu, Co, Fe and Ni) [2.87], $PtMO_x$ (M = Sm, Pr, Ce, Nd and La) supported on carbon nanotubes [2.89] and unsupported NiB alloys (as nanotubes (20-25 nm) [2.91] and nanoparticles (6-100 nm) [2.88]).

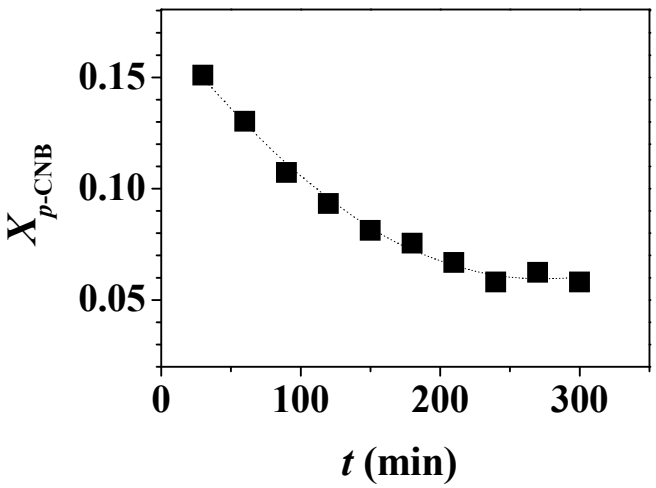

Figure 2.8: Variation of *p*-CNB fractional conversion ($X_{p\text{-CNB}}$) with time-on-stream; $m/F \approx 52500$ g mol^{-1} min; dotted line represents fit to eqn. (2.4).

The variation in fractional *p*-CNB conversion ($X_{p\text{-CNB}}$) as a function of time-on-stream is presented in **Figure 2.8**. An initial temporal decline in conversion is in evidence with a subsequent steady state at extended reaction times (> 250 min).

The temporal variation of conversion can be expressed in terms of the empirical relationship [2.92]

$$\frac{(X_{p\text{-CNB}} - X_0)}{(X_{300\text{min}} - X_0)} = \frac{t}{(\beta + t)} \tag{2.4}$$

where $X_{300\text{min}}$ corresponds to fractional conversion after 300 min on-stream and β is a time scale fitting parameter. Fit convergence (R^2 > 0.99) yields values for X_0 (initial conversion). **Figure 2.9(I;■)** represents the production of *p*-CAN per gram of β-Mo_2N for up to 1800 min. For reactor operation under plug-flow conditions where hydrogen was maintained far in excess, the following reactor/kinetic expression applies

$$\ln(1 - X_0)^{-1} = k\left(\frac{m}{F}\right) \tag{2.5}$$

where k (mol g^{-1} min^{-1}) is the pseudo-first order kinetic constant, m the mass of catalyst (g) and F the reactant flow rate (mol min^{-1}); m/F has the physical meaning of contact time. The associated linear relationship (forced through the origin, see **Figure 2.9(II;■)**) serves to validate our approach and the result k = 4.6 μmol g^{-1} min^{-1} is included **Table 2.2**.

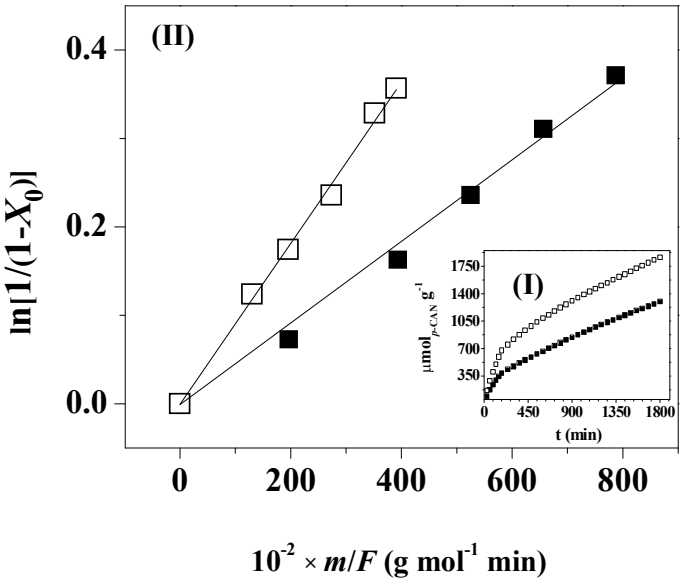

Figure 2.9: (I) time on-stream *p*-CAN production over Mo_2N (■) and Au/Mo_2N (□); (II) fractional initial conversion of *p*-CNB (X_0) as a function of m/F over Mo_2N (■) and Au/Mo_2N (□) where the lines represent fit to pseudo-first order kinetics.

2.3.4.2 Au/β-Mo_2N

100% selectivity to *p*-CAN extended to gas phase operation over Au/Mo_2N and the incorporation of Au was associated with an increased *p*-CAN production over Au/Mo_2N relative to Mo_2N as a function of time on-stream (see **Figure 2.9(I;□)**). The improved catalytic performance resulting from the combination of Au with Mo_2N is further demonstrated in the pseudo-first order kinetic plots presented in **Figure 2.9(II;□)**. the rate constant obtained (k, $\mu mol_{p\text{-}CNB}\ g^{-1}\ min^{-1}$, **Table 2.2**) corresponds to an increase by a factor of 2 compared to Mo_2N. This response can be linked to the increased hydrogen uptake on Au/Mo_2N (**Table 2.2**). Variations in surface hydrogen are known to influence the catalytic response in hydrogenation reactions where a concomitant increase in activity and surface hydrogen for molybdenum nitrides has also been reported elsewhere [2.93]. Zhang *et al*. [2.94], studying the hydrogenation of cyclohexene and the hydrodesulphurisation of thiophene over Mo_2N, associated with the higher activity with the incorporation of Zr to an increase in weakly bound hydrogen.

In order to compare Au/Mo_2N with the benchmark, specific rate constant (k') was defined per mol of metal. A major finding in this work is the appreciably greater activity (k', $mmol_{p\text{-}CNB}\ mol_{metal}^{-1}\ min^{-1}$) exhibited by Au/$Mo_2N$ relative to Au/Al_2O_3 (at a common mean Au particle size), which is demonstrated in **Figure 2.10** and **Table 2.2**. This can be taken as a demonstration of a surface cooperative effect involving Au and Mo_2N that results in a concomitant enhanced hydrogen uptake (**Table 2.2**) and catalytic efficiency. Blaser *et al*. [2.95] concluded that reaction at the gold-support interface can contribute to overall hydrogenation rate acceleration. Shimizu *et al*. [2.96] studied the effect of the carrier for supported Ag catalysts in nitroarene reduction and reported a synergy between Ag and Al_2O_3 that governed the rate-limiting H_2 dissociation to generate a H^+/H^- pair at the metal/support interface.

The hydrogenation rate can also be influenced by differences in *p*-CNB/surface interaction (-NO_2 activation) where the Au-Mo_2N interface may play a critical role. Corma and *co*-workers [2.97] have differentiated between -NO_2 group adsorption on the support and Au-support interface in terms of reactant activation, notably for Au/TiO_2. This effect can be probed by examining the catalytic action of Pd/Mo_2N where a higher *p*-CNB hydrogenation rate (**Figure 2.10**, **Table 2.2**) relative to Au/Mo_2N was recorded. These results are consistent with published literature where increased hydrogen

uptake/activity over supported Pd (relative to Au) has been reported [2.84]. In marked contrast to Au/Mo_2N and Au/Al_2O_3, at a common *p*-CNB conversion, Pd/Mo_2N promoted the formation of NB and AN as products of hydrodechlorination and hydrogenation (**Figure 2.10**). Interaction with Pd/Mo_2N serves to activate the C-Cl bond, which is then susceptible to hydrogenolytic cleavage. Use of Pd/Mo_2N in practical (industrial) application would require the incorporation of downstream separation and treatment units in order to extract the target *p*-CAN. This is circumvented in the case of Au/Mo_2N, which delivered the best performance in this study. Process efficiency can be further improved by operating multiple passes through the catalyst bed where the ultra-selectivity imposed by Au/Mo_2N can deliver complete conversion of the inlet *p*-CNB to *p*-CAN.

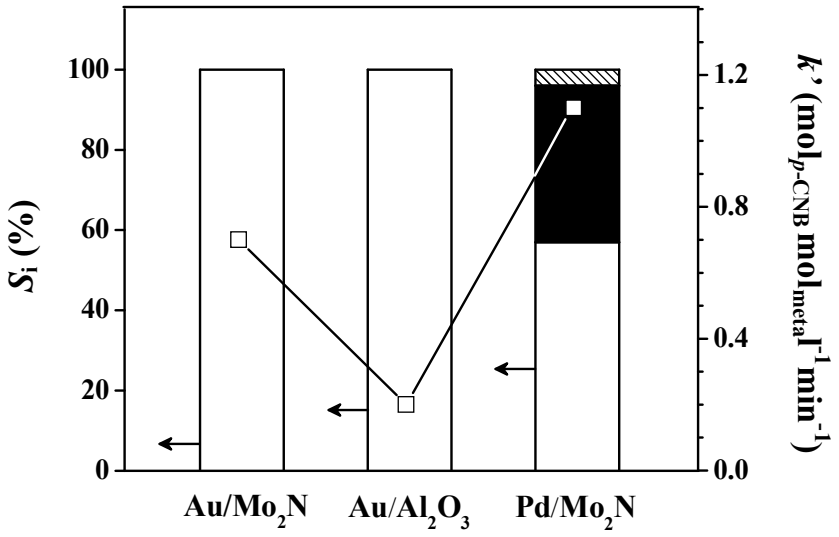

Figure 2.10: Specific activity with selectivity (S_i) to *p*-CAN (open bars), AN (hatched bars) and NB (solid bars) under conditions of equal fractional *p*-CNB conversion (X_0 ~ 0.2) over Au/Mo_2N, Au/Al_2O_3 and Pd/Mo_2N.

The results presented in this Chapter provide the first evidence of the combined catalytic action of Au and Mo_2N that serves to elevate surface hydrogen, resulting in an increased hydrogenation rate of *p*-CNB to the target *p*-CAN in gas phase operation. Further work must focus on structural modification of molybdenum nitride (*e.g.* crystallographic phase and/or surface area) and control over Au particle size to increase activity while retaining selectivity.

2.4 Conclusion

The results establish that the formation of *β*-Mo_2N by temperature programmed treatment (to 933 K) of MoO_3 in N_2/H_2 (15% v/v) occurs *via* a kinetically controlled stepwise reduction ($MoO_3 \rightarrow MoO_2 \rightarrow Mo$) and subsequent nitridation ($Mo \rightarrow$ *β*-Mo_2N). The transformation is non-topotactic with an increase in BET (from 1 to 17 $m^2 g^{-1}$) and total pore volume (from 2×10^{-3} to 11×10^{-3} $cm^3 g^{-1}$). H_2 chemisorption measurements have revealed a significant hydrogen content associated with the nitride.

This work has demonstrated, for the first time, the catalytic action of *β*-Mo_2N to promote the continuous gas phase hydrogenation of *p*-CNB where *p*-CAN was the sole product, *i.e.* 100% selective in terms of -NO_2 group reduction. Incorporation of Au with Mo_2N served to increase H_2 uptake with a four-fold higher hydrogenation rate relative to Mo_2N. Au/Mo_2N as a new catalyst formulation promotes the hydrogenation of *p*-CNB with 100% selectivity to *p*-CAN. Moreover, Au/Mo_2N outperformed a benchmark Au/Al_2O_3 catalyst that exhibited an equivalent mean Au particle size. Under the same reaction conditions, Pd/Mo_2N was non-selective and promoted a combined hydrodechlorination/ hydrogenation to give NB and AN. Moreover, the viability of Au/Mo_2N in the selective reduction of nitroarenes is established with versatility in gas phase operation. These findings can serve as the basis for the development of Au/Mo_2N materials as new catalysts for the cleaner production of commercially important aromatic amines with multiple applications in the fine chemical industry.

2.5 References

[2.1] V. P. Anitha, S. Vitta and S. Major, *Structure and properties of reactively sputtered gamma-Mo_2N hard coatings*, Thin Solid Films 245 (1994) 1-3.

[2.2] K. Machida, A. Nakamoto and G. Adachi, *Low-temperature synthesis of $NdFe_{11}TiC_XN_Y$ via plasma carbonitriding*, Chem. Lett. (1993) 1381-1384.

[2.3] V. P. Anitha, A. Bhattacharya, N. G. Patil and S. Major, *Study of sputtered molybdenum nitride as a diffusion barrier*, Thin Solid Films 236 (1993) 306-310.

[2.4] E. Furimsky, *Metal carbides and nitrides as potential catalysts for hydroprocessing*, Appl. Catal. A: General 240 (2003) 1-28.

[2.5] E. Furimsky, *Hydrodenitrogenation of petroleum*, Catal. Rev. Sci. Eng. 47 (2005) 297-489.

[2.6] S. T. Oyama, *The chemistry of transition metal carbides and nitrides*, Blackie Academic, Glasgow, 1996, pp. 14-15.

[2.7] P. Ronsheim, A. Mazza and A. N. Christensen, *Thermal plasma synthesis of transition metal nitrides and alloys*, Plasma. Chem. Plasma Process. 1 (1981) 135-147.

[2.8] L. Volpe and M. Boudart, *Compounds of molybdenum and tungsten with high specific surface-area. 1. Nitrides*, J. Solid State Chem. 59 (1985) 332-347.

[2.9] R. Kojima and K. Aika, *Molybdenum nitride and carbide catalysts for ammonia synthesis*, Appl. Catal. A: General 219 (2001) 141-147.

[2.10] R. N. Panda and S. Kaskel, *Synthesis and characterization of high surface area molybdenum nitride*, J. Mater. Sci. 41 (2006) 2465-2470.

[2.11] D. McKay, J. S. J. Hargreaves and R. F. Howe, *XPS evidence for molybdenum nitride formation in ZSM-5*, Catal. Lett. 112 (2006) 109-113.

[2.12] R. S. Wise and E. J. Markel, *Synthesis of high surface area molybdenum nitride in mixtures of nitrogen and hydrogen*, J. Catal. 145 (1994) 344-355.

[2.13] S. Gong, H. Chen, W. Li and B. Li, *Synthesis of beta-$Mo_2N_{0.78}$ hydrodesulfurization catalyst in mixtures of nitrogen and hydrogen*, Appl. Catal. A: General 279 (2005) 257-261.

[2.14] A. Gomathi, A. Sundaresan and C.N.R. Rao, *Nanoparticles of superconducting gamma-Mo_2N and delta-MoN*, J. Solid State Chem. 180 (2007) 291-295.

[2.15] X. Zhao and K.-J. Range, *High pressure synthesis of molybdenum nitride MoN*, J. Alloys Compd. 296 (2000) 72-74.

[2.16] S. L. Roberson, D. Finello and R. F. Davis, *Phase control of Mo_xN films via chemical vapor deposition*, Thin Solid Films 324 (1998) 30-36.

[2.17] S. Chouzier, P. Afanasiev, M. Vrinat, T. Cseri and M. Roy-Auberger, *One-step synthesis of dispersed bimetallic carbides and nitrides from transition metals hexamethylenetetramine complexes*, J. Solid State Chem. 179 (2006) 3314-3323.

[2.18] P. Afanasiev, *New single source route to the molybdenum nitride Mo_2N*, Inorg. Chem. 41 (2002) 5317-5319.

[2.19] R. C. V. McGee, S. K. Bej and L. T. Thompson, *Basic properties of molybdenum and tungsten nitride catalysts*, Appl. Catal. A: General 284 (2005) 139-146.

[2.20] C. W. Colling, J.-G. Choi and L. T. Thompson, *Molybdenum nitride catalysts II. H_2 temperature programmed reduction and NH_3 temperature programmed desorption*, J. Catal. 160 (1996) 35-42.

[2.21] G. S. Ranhotra, G. W. Haddix, A. T. Bell and J. A. Reimer, *Catalysis over molybdenum carbides and nitrides.1. Catalyst characterization*, J. Catal. 108 (1987) 24-39.

[2.22] S. Li, W. B. Kim and J. S. Lee, *Effect of the reactive gas on the solid-state transformation of molybdenum trioxide to carbides and nitrides*, Chem. Mater. 10 (1998) 1853-1862.

[2.23] M. Nagai, Y. Goto, A. Miyata, M. Kiyoshi, K. Hada, K. Oshikawa and S. Omi, *Temperature-programmed reduction and XRD studies of ammonia-treated molybdenum oxide and its activity for carbazole hydrodenitrogenation*, J. Catal. 182 (1999) 292-301.

[2.24] S. W. Gong, H. K. Chen, W. Li and B. Q. Li, *Catalytic behaviors of beta-$Mo_2N_{0.78}$ as a hydrodesulfurization catalyst*, Energy Fuels 20 (2006) 1372-1376.

[2.25] K. Inumaru, K. Baba and S. Yamanaka, *Synthesis and characterization of superconducting beta-Mo_2N crystalline phase on a Si substrate: An application of pulsed laser deposition to nitride chemistry*, Chem. Mater. 17 (2005) 5935-5940.

[2.26] H. J. Lee, J.-G. Choi, C. W. Colling, M. S. Mudholkar and L. T. Thompson, *TPD and decomposition of NH_3 over molybdenum nitride films*, Appl. Surf. Sci. 89 (1995) 121-130.

[2.27] M. Nagai, *Transition-metal nitrides for hydrotreating catalyst: Synthesis, surface properties and reactivities*, Appl. Catal. A: General 322 (2007) 178-190.

[2.28] M. Nagai, Y. Goto, A. Irisawa and S. Omi, *Catalytic activity and surface properties of nitrided molybdena-alumina for carbazole hydrodenitrogenation*, J. Catal. 191 (2000) 128-137.

[2.29] M. Nagai, Y. Goto, O. Uchino and S. Omi, *TPD study and carbazole hydrodenitrogenation activity of nitrided molybdena-alumina*, Catal. Today 45 (1998) 335-340.

[2.30] T. Ressler, R. E. Jentoft, J. Wienold, M. M. Günter and O. Timpe, *In situ XAS and XRD studies on the formation of Mo suboxides during reduction of MoO_3*, J. Phys. Chem. B 104 (2000) 6360-6370.

[2.31] T. Ressler, J. Wienold and R. E. Jentoft, *Formation of bronzes during temperature-programmed reduction of MoO_3 with hydrogen - an in situ XRD and XAFS study*, Solid State Ionics 141 (2001) 243-251.

[2.32] J. G. Chen, *Carbide and nitride overlayers on early transition metal surfaces: Preparation, characterization, and reactivities*, Chem. Rev. 96 (1996) 1477-1498.

[2.33] L. Volpe and M. Boudart, *Compounds of molybdenum and tungsten with high specific surface-area. 2. Carbides*, J. Solid State Chem. 59 (1985) 348-356.

[2.34] Y. Li, Y. Fan, J. He, B. Xu, H. Yang, J. Miao and Y. Chen, *Selective liquid hydrogenation of long chain linear alkadienes on molybdenum nitride and carbide modified by oxygen*, Chem. Eng. J. 99 (2004) 213-218.

[2.35] D. Liu, Y. Q. Liu, T. Zhou, C. G. Liu and G. H. Que, *In situ FT-IR study of CO hydrogenation on a molybdenum nitride catalyst*, Abstr. Pap. Am. Chem. Soc. 226 (2003) U530-U530.

[2.36] Y. Shigehara, *Ethylene hydrogenation catalyzed by molybdenum nitride*, Nippon Kagaku Kaishi (1977) 470-474.

[2.37] M. Nagai, Y. Goto, O. Uchino and S. Omi, *TPD and XRD studies of molybdenum nitride and its activity for hydrodenitrogenation of carbazole*, Catal. Today 43 (1998) 249-259.

[2.38] M. Nagai, Y. Goto, H. Ishii and S. Omi, *XPS and TPSR study of nitrided molybdena-alumina catalyst for the hydrodesulfurization of dibenzothiophene*, Appl. Catal. A: General 192 (2000) 189-199.

[2.39] D. McKay, J. S. J. Hargreaves, J. L. Rico, J. L. Rivera and X. L. Sun, *The influence of phase and morphology of molybdenum nitrides on ammonia synthesis activity and reduction characteristics*, J. Solid State Chem. 181 (2008) 325-333.

[2.40] G. Konnecker, A. Boehncke and S. Schmidt, *Ecotoxicological assessment of p-chloroaniline - Fate and effects in aquatic systems*, Fresenius Environ. Bull. 12 (2003) 589-593.

[2.41] P. F. Vogt and J. J. Gerulis, *Aromatic amines* in Ullmann's Encyclopedia of Industrial Chemistry, Wiley-VCH Verlag GmbH & Co. KGaA, Weinheim, 2005, pp.2-21.

[2.42] X. D. Wang, M. H. Liang, J. L. Zhang and Y. Wang, *Selective hydrogenation of aromatic chloronitro compounds*, Curr. Org. Chem. 11 (2007) 299-314.

[2.43] A. Corma, M. Boronat, S. González and F. Illas, *On the activation of molecular hydrogen by gold: a theoritical approximation to the nature of potential active sites*, Chem. Commun. 32 (2007) 3371-3373.

[2.44] F. Cárdenas-Lizana, S. Gómez-Quero, N. Perret and M. A. Keane, *Gold catalysis at the gas–solid interface: role of the support in determining activity and selectivity in the hydrogenation of m-dinitrobenzene*, Catal. Sci. Tech. 1 (2011) 652-661

[2.45] F. Cárdenas-Lizana, S. Gómez-Quero, H. Idriss and M. A. Keane, *Gold particle size effects in the gas-phase hydrogenation of m-dinitrobenzene over Au/TiO_2*, J. Catal. 268 (2009) 223-234.

[2.46] B. Hammer and J.K. Nørskov, *Why gold is the noblest of all the metals*, Nature 376 (1995) 238-240.

[2.47] E. Bus, J. T. Miller and J. A. van Bokhoven, *Hydrogen chemisorption on Al_2O_3-supported gold catalysts*, J. Phys. Chem. B 109 (2005) 14581-14587.

[2.48] C. Kartusch and J. A. van Bokhoven, *Hydrogenation over gold catalysts: The interaction of gold with hydrogen*, Gold Bull. 42 (2009) 343-347.

[2.49] F. Cárdenas-Lizana, S. Gómez-Quero, A. Hugon, L. Delannoy, C. Louis and M. A. Keane, *Pd-promoted selective gas phase hydrogenation of p-chloronitrobenzene over alumina supported Au*, J. Catal. 262 (2009) 235-243.

[2.50] J. Li, X.-Y. Shi, Y.-Y. Bi, J.-F. Wei and Z.-G. Chen, *Pd Nanoparticles in ionic liquid brush: A highly active and reusable heterogeneous catalytic assembly for solvent-free or on-water hydrogenation of nitroarene under mild conditions*, ACS Catal. 1 (2011) 657-664.

[2.51] N. Perret, F. Cárdenas-Lizana and M. A. Keane, *Selective hydrogenation of benzaldehyde to benzyl alcohol over Au/Al_2O_3*, Catal. Commun. 16 (2011) 159–164.

[2.52] G. Tavoularis and M. A. Keane, *The gas phase hydrodechlorination of chlorobenzene over nickel/silica*, J. Chem. Technol. Biotechnol. 74 (1999) 60-70.

[2.53] P. Delporte, F. Meunier, C. Phamhuu, P. Vennegues, M. J. Ledoux and J. Guille, *Physical characterization of molybdenum oxycarbide catalyst; TEM, XRD and XPS*, Catal. Today 23 (1995) 251-267.

[2.54] T. Matsuda, Y. Hirata, H. Itoh, H. Sakagami and N. Takahashi, *Effect of reduction temperature on the transformation of MoO_3 to MoO_x with a large surface area*, Micropor. Mesopor. Mater. 42 (2001) 337-344.

[2.55] H. Sakagami, Y. Asano, T. Ohno, N. Takahashi, H. Itoh and T. Matsuda, *Reduction of H_xMoO_3 with different amounts of hydrogen to high surface area molybdenum oxides*, Appl. Catal. A: General 297 (2006) 189-197.

[2.56] Y. J. Zhang, Q. Xin, I. Rodriguez-Ramos and A. Guerrero-Ruiz, *Simultaneous hydrodesulfurization of thiophene and hydrogenation of cyclohexene over dimolybdenum nitride catalysts*, Appl. Catal. A: General 180 (1999) 237-245.

[2.57] Z. B. Wei, Q. Xin, P. Grange and B. Delmon, *Surface species and the stability of gamma-Mo_2N*, Solid State Ionics 101 (1997) 761-767.

[2.58] A. de Lucas Consuegra, P. M. Patterson and M. A. Keane, *Use of unsupported and silica supported molybdenum carbide to treat chloroarene gas streams*, Appl. Catal. B: Environmental 65 (2006) 227-239.

[2.59] T. Ressler, *Reply to "kinetics and mechanism of MoO_3 reduction". Comments on "in situ XAS and XRD studies on the formation of Mo suboxides during reduction of MoO_3"*, J. Phys. Chem. B 106 (2002) 7719-7720.

[2.60] E. Lalik, W. I. F. David, P. Barnes and J. F. C. Turner, *Mechanisms of reduction of MoO_3 to MoO_2 reconciled?*, J. Phys. Chem. B 105 (2001) 9153-9156.

[2.61] J. Słoczyński, *Kinetics and mechanism of molybdenum(VI) oxide reduction*, J. Solid State Chem. 118 (1995) 84-92.

[2.62] G. Xiong, C. Li, Z. C. Feng, P. L. Ying, Q. Xin and J. K. Liu, *Surface coordination structure of molybdate with extremely low loading on gamma-alumina characterized by UV resonance Raman spectroscopy*, J. Catal. 186 (1999) 234-237.

[2.63] H. Aritani, T. Tanaka, T. Funabiki, S. Yoshida, K. Eda, N. Sotani, M. Kudo and S. Hasegawa, *Study of the local structure of molybdenum-magnesium binary oxides by means of Mo L_3-edge XANES and UV-Vis spectroscopy*, J. Phys. Chem. 100 (1996) 19495-19501.

[2.64] H. Prialiaud, *Proceeding of the Second International Conference on Chemistry and Uses of Molybdenum*, Climax Molybdenum Co. Ltd., London, 1996, pp.1-195.

[2.65] K. A. Vikulov, B. N. Shelimov and V. B. Kazansky, *IR and UV-Vis spectroscopic studies of the surface $Mo=CH_2$ and $Mo=CH-CH_3$ carbene*

complexes produced by methylcyclopropane chemisorption over photoreduced silica molybdena catalysts, J. Mol. Catal. 65 (1991) 393-402.

[2.66] G. Benítez, J. M. Heras and L. Viscido, *The interaction of duterium with polycrystalline molybdenum*, J. Phys. Condens. Matter 5 (1993) A221-A222.

[2.67] R. Bafrali and A. T. Bell, *Interactions of H_2 and NH_3 with Mo(100) and Mo(100)-c(2X2)N surfaces*, Surf. Sci. 278 (1992) 353-363.

[2.68] S. T. Oyama, *Preparation and catalytic properties of transition metal carbides and nitrides*, Catal. Today 15 (1992) 179-200.

[2.69] J. S. Lee, L. Volpe, F. H. Ribeiro and M. Boudart, *Molybdenum carbide catalysts .2. Topotactic synthesis of unsupported powders*, J. Catal. 112 (1988) 44-53.

[2.70] J. S. Lee, S. T. Oyama and M. Boudart, *Molybdenum carbide catalysts .1. Synthesis of unsupported powders*, J. Catal. 106 (1987) 125-133.

[2.71] C. Bouchy, I. Schmidt, J. R. Anderson, C. J. H. Jacobsen, E. G. Derouane and S. B. D.-A. Hamid, *Metastable fcc alpha-MoC_{1-x} supported on HZSM5: preparation and catalytic performance for the non-oxidative conversion of methane to aromatic compounds*, J. Mol. Catal. A: Chemical 163 (2000) 283-296.

[2.72] W. V. Schulmeyer and H. M. Ortner, *Mechanisms of the hydrogen reduction of molybdenum oxides*, Int. J. Refract. Hard Mater. 20 (2002) 261-269.

[2.73] G. H. Xie and Z. C. Jiang, *The first observation of Mo^{5+} in the passivation layer of Mo_2N*, Chin. Sci. Bull. 45 (2000) 1562-1564.

[2.74] Z. B. Wei, Q. Xin, P. Grange and B. Delmon, *TPD and TPR studies of molybdenum nitride*, J. Catal. 168 (1997) 176-182.

[2.75] J. R. Regalbuto and J.-W. Ha, *A corrected procedure and consistent interpretation for temperature programmed reduction of supported MoO_3* Catal. Lett. 29 (1994) 189-207.

[2.76] X. S. Li, Y. X. Chen, Y. J. Zhang, C. X. Ji and Q. Xin, *Temperature-programmed desorption and adsorption of hydrogen on Mo_2N*, React. Kinet. Catal. Lett. 58 (1996) 391-396.

[2.77] M. Saito and R. B. Anderson, *The activity of several molybdenum compounds for the methanation of CO*, J. Catal. 63 (1980) 438-446.

[2.78] Y. J. Zhang, Y. X. Li, C. Li and Q. Xin, *Adsorption and migration of hydrogen on different surface sites of gamma-Mo_2N catalyst*, Stud. Surf. Sci. Catal. 112 (1997) 457-464.

[2.79] A. Guerrero-Ruiz, Q. Xin, Y. J. Zhang, A. Maroto-Valiente and I. Rodriguez-Ramos, *Microcalorimetric study of H_2 adsorption on molybdenum nitride catalysts*, Langmuir 15 (1999) 4927-4929.

[2.80] X. S. Li, K. J. Zhang, Q. Xin, C. X. Ji, Y. F. Miao and L. Wang, *Irreversible hydrogen uptake on Mo_2N catalyst*, React. Kinet. Catal. Lett. 57 (1996) 177-182.

[2.81] G. W. Haddix, J. A. Reimer and A. T. Bell, *Characterization of H_2 adsorbed on gamma-Mo_2N by NMR-spectroscopy*, J. Catal. 108 (1987) 50-54.

[2.82] Y. H. Wang, W. Li, M. H. Zhang, N. J. Guan and K. Y. Tao, *Characterization and catalytic properties of supported nickel molybdenum nitrides for hydrodenitrogenation*, Appl. Catal. A: General 215 (2001) 39-45.

[2.83] P. Claus, *Heterogeneously catalysed hydrogenation using gold catalysts*, Appl. Catal. A: General 291 (2005) 222-229.

[2.84] F. Cárdenas-Lizana, S. Gómez-Quero and M. A. Keane, *Ultra-selective gas phase catalytic hydrogenation of aromatic nitro compounds over Au/Al_2O_3*, Catal. Commun. 9 (2008) 475-481.

[2.85] D. Q. Xu, Z. Y. Hu, W. W. Li, S. P. Luo and Z. Y. Xu, *Hydrogenation in ionic liquids: An alternative methodology toward highly selective catalysis of halonitrobenzenes to corresponding haloanilines*, J. Mol. Catal. A: Chemical 235 (2005) 137-142.

[2.86] Q. Xu, L. Wang, J. Chen, X. Li and R. Li, *Selective hydrogenation of p-chloronitrobenzene over Ru-Ir/gamma-Al_2O_3 catalyst modified by organic amines*, Chin. J. Catal. 28 (2007) 579-581.

[2.87] J. Ning, J. Xu, J. Liu, H. Miao, H. Ma, C. Chen, X. Li, L. Zhou and W. Yu, *A remarkable promoting effect of water addition on selective hydrogenation of p-chloronitrobenzene in ethanol*, Catal. Commun. 8 (2007) 1763-1766.

[2.88] B. Zhao, C.-J. Chou and Y.-W. Chen, *Hydrogenation of p-chloronitrobenzene on tungsten-modified NiCoB catalyst*, Ind. Eng. Chem. Res. 49 (2010) 1669-1676.

[2.89] X. X. Han, H. R. Li and R. M. Zhou, *Effect of rare earths on selective hydrogenation of p-chloronitrobenzene over $PtMO_x/CNTs$ catalysts*, Chin. Chem. Lett. 20 (2009) 96-98.

[2.90] H. Li, J. Zhang and H. Li, *Ultrasound-assisted preparation of a novel Ni-B amorphous catalyst in uniform nanoparticles for p-chloronitrobenzene hydrogenation*, Catal. Commun. 8 (2007) 2212-2216.

[2.91] M. Mo, L. Han, J. Lv, Y. Zhu, L. Peng, X. Guo and W. Ding, *Noncrystalline NiPB nanotubes for hydrogenation of p-chloronitrobenzene*, Chem. Commun. 46 (2010) 2268-2270.

[2.92] F. Cárdenas-Lizana, S. Gómez-Quero and M.A. Keane, *Clean production of chloroanilines by selective gas phase hydrogenation over supported Ni catalysts*, Appl. Catal. A: General 334 (2008) 199-206.

[2.93] J. G. Choi, J. R. Brenner, C. W. Colling, B. G. Demczyk, J. L. Dunning and L. T. Thompson, *Synthesis and characterization of molybdenum nitride hydrodenitrogenation catalysts*, Catal. Today 15 (1992) 201-222.

[2.94] Y. Zhang, Y. Li, R. Raval, C. Li, R. Zhai and Q. Xin, *Synthesis, characterization and catalytic properties of bimetallic $ZrMo_2N_x$-Mo_2N nitrides of high surface area*, J. Mol. Catal. A: Chemical 132 (1998) 241-253.

[2.95] H.-U. Blaser, H. Steiner and M. Studer, *Selective catalytic hydrogenation of fonctionalized nitroarenes: an update*, ChemCatChem 1 (2009) 210-221.

[2.96] K.-I. Shimizu, Y. Miyamoto and A. Satsuma, *Size- and support-dependent silver cluster catalysis for chemoselective hydrogenation of nitroaromatics*, J. Catal. 270 (2010) 86-94.

[2.97] M. Boronat, P. Concepción, A. Corma, S. González, F. Illas and P. Serna, *A molecular mechanism for the chemoselective hydrogenation of substituted nitroaromatics with nanoparticles of gold on TiO_2 catalysts: A cooperative effect between gold and the support*, J. Am. Chem. Soc. 129 (2007) 16230-16237.

Chapter 3

Effect of Crystallographic Phase (β *vs.* γ) and Surface Area on Gas Phase Nitroarene Hydrogenation over Mo_2N and Au/Mo_2N

In the previous Chapter, β-Mo_2N was found to exhibit 100% selectivity towards -NO_2 reduction in the gas phase hydrogenation of *p*-chloronitrobenzene. Moreover the incorporation of Au generated an increase in activity. In this Chapter, the effect of crystallographic phase (β *vs* γ) and surface area on the catalytic response are considered. The incorporation of Au by deposition-precipitation is investigated further.

3.1 Introduction

The application of transition metal nitrides as hydrotreating catalysts is now established [3.1-3]. The use of molybdenum nitrides to promote hydrogen mediated reactions has been considered to a limited extent with evidence of significant hydrogenation activity [3.4-9]. This has been ascribed to a contraction of the *d*-band and modification of electron density due to the interstitial incorporation of N in the metal lattice, which facilitates hydrogen adsorption/activation [3.10]. A distinct selectivity response has been observed for Mo nitride when compared with conventional supported metal (*e.g.* Pd or Pt) catalysts [3.5,3.6,3.8]. Indeed, the preferential formation of crotyl alcohol (from crotonaldehyde) [3.6] and ethene (from ethyne) [3.5] has been reported for reaction over Mo_2N with enhanced selectivities relative to Pd/Al_2O_3.

In the previous Chapter, the application of β-Mo_2N in the selective hydrogenation of *p*-chloronitrobenzene (*p*-CNB) to *p*-chloroaniline (*p*-CAN) was established. *p*-CAN is a high value chemical extensively used in the manufacture of fine chemicals but existing production routes exhibit serious drawbacks in terms of low selectivity and the generation of toxic waste [3.11]. In this Chapter the role of nitride crystallographic phase and surface area in gas phase hydrogenation is now considered.

In the synthesis of nitrides *via* temperature programmed reduction-nitridation, a number of factors have been proposed to influence the MoN_x phase, including the nature of the precursor [3.12] and preparation conditions [3.13-15], *i.e.* gas composition/space velocity, heating rate and final temperature. Cubic γ-Mo_2N has been

the most common crystallographic form obtained *via* thermal treatment of MoO_3 in NH_3 [3.12,3.13]. The use of H_2+N_2 mixtures can generate either (tetragonal) β-Mo_2N [3.16-18] or γ-Mo_2N [3.14,3.19,3.20]. Moreover, the formation of (hexagonal) δ-MoN from MoS_2+NH_3 has also been reported [3.21]. The synthesis of high surface area (up to 225 m^2 g^{-1}) Mo nitrides requires a low temperature ramp rate ($\leq$ 1 K min^{-1}) [3.14] and/or high gas space velocity (up to 150000 h^{-1}) [3.22] to circumvent hydrothermal sintering resulting from water released [3.20]. β-Mo_2N typically exhibits low surface areas (2-17 m^2 g^{-1}) [8,19,20] whereas higher values are characteristic of γ-Mo_2N (5-225 m^2 g^{-1}) [3.23-25].

The effect of the Mo nitride crystallographic phase in terms of hydrogenation applications has not been studied in a systematic manner. It is, however, worth noting that, in the case of ammonia synthesis [3.16] and carbazole hydrodenitrogenation [3.13], β-Mo_2N delivered a higher surface area normalised activity when compared with γ-Mo_2N and δ-MoN. A definitive correlation between catalytic activity and nitride area, irrespective of phase, has yet to be established. Hydrogen uptake, which is dependent on surface area and crystallographic phase [3.26-28], can play a critical role in determining hydrogenation rate. McKay and co-workers [3.16] have shown that specific activity (per m^2) for ammonia synthesis over β-Mo nitride was independent of surface area. In contrast, specific activities for thiophene desulfurisation [3.14] and pyridine hydrodenitrogenation [3.29] were found to decrease with increasing γ-Mo nitride area (from 4 to 193 m^2 g^{-1}).

In this Chapter, the independent effect(s) of varying surface area (7-66 m^2 g^{-1}) and Mo_2N crystallographic phase (β- and γ-) on *p*-CNB hydrogenation performance are considered for the first time. Moreover, with a view to enhancing overall catalyst performance, the role of Au as promoter is assessed. The use of promoters with Mo nitrides catalysts has not been addressed to any significant extent. It should be noted that an increase in activity has been demonstrated for methanol steam reforming (with lower CO_2 production) over Mo nitride with the addition of Pd, Pt and Ni [3.30] and thiophene hydrodesulfurisation due to the inclusion of Co [3.31].

3.2 Experimental

3.2.1 Mo nitride Synthesis

The MoO_3 (99.9995% w/w) precursor was obtained from Alfa Aesar. Mo nitride synthesis was conducted *via* temperature programmed treatment in H_2/N_2 or $H_2/N_2/Ar$ continuous flow at atmospheric pressure. β-Mo_2N synthesis was carried out in a commercial CHEM-BET 3000 (Quantachrome) unit. γ-Mo_2N preparation employed a fixed bed reactor. As Mo nitride powders produced in reducing gases are subject to self-ignition on contact with air [3.32], the samples were passivated at 293 K in 1% v/v O_2/He for *ex situ* analysis; there was no detectable temperature increase during passivation.

3.2.1.1 β-Mo_2N

The MoO_3 precursor was loaded in a quartz cell (3.76 mm i.d.) and contacted with 15 cm^3 min^{-1} (Brooks mass flow controlled; GHSV = 1500 h^{-1}) H_2/N_2, kept at 293 K for 1 h and then heated at 5 K min^{-1} to 933 K, maintaining the final temperature for 18 h. The reaction was quenched by switching to an Ar flow (65 cm^3 min^{-1}) and the sample was cooled to ambient temperature.

3.2.1.2 γ-Mo_2N

The MoO_3 precursor was placed in a horizontally mounted quartz reactor (i.d. = 10 mm), flushed with dry high purity Ar (99.9% v/v) at 400 cm^3 min^{-1} (GHSV = 24000 h^{-1}) for 4 h and heated to 623 K (at 5 K min^{-1}), which was maintained for 4 h. A 400 cm^3 min^{-1} flow of 8%/42%/50% v/v $N_2/H_2/Ar$ was then introduced and the temperature held constant for 2 h. Two γ-Mo_2N samples were prepared using different temperature ramping rates. The synthesis conditions were selected based on published literature [3.14] that has established a dependence of nitride surface area (34-101 m^2 g^{-1}) on heating rate (0.2-20 K min^{-1}). The temperature was raised from 623 K to 933 K at 0.3 K min^{-1} (sample denoted as γ-Mo_2N-a) or 0.1 K min^{-1} (γ-Mo_2N-b), maintaining the final isothermal hold for 2-13 h. The sample was quenched in Ar and rapidly (< 30 min) cooled to ambient temperature; the latter step was facilitated by contacting the reactor with an external high velocity air flow.

3.2.2 Au/Mo_2N Preparation and Activation

Au/β-Mo_2N, Au/γ-Mo_2N-a and Au/γ-Mo_2N-b (with a nominal Au loading = 1 mol %) were prepared by deposition-precipitation (D-P). A suspension of $HAuCl_4$ (300 cm^3, 3.32×10^{-4} M), aqueous urea (100 cm^3, 0.86 M) and the nitride support (2 g), were stirred (300 rpm) and heated (1 K min^{-1}) to 353 K, maintaining the final temperature for 2.5 h. The D-P process was performed in the dark in order to avoid formation of metallic colloids in solution by photoreduction of Au(III) [3.33]. It has been reported that a high residual chloride content (> 300 ppm) can induce the formation of large (> 20 nm) Au particles [3.34] while the chloride can poison the catalytically active sites [3.35]. In order to circumvent these negative effects, the catalyst precursor was filtered, washed with distilled water until the wash water was Cl-free (based on the $AgNO_3$ test), dried in He (45 cm^3 min^{-1}) at 383 K for 3 h and sieved into a batch of 75 μm average particle diameter. The samples were kept at 277 K under He in the dark in order to prevent Au agglomeration, which has been reported for storage in air and in the light [3.36].

3.2.3 Characterisation

The pH values associated with the point of zero charge (pH_{PZC}) of the nitrides were determined using the potentiometric mass titration technique. In each case, three different masses (0.025, 0.050 and 0.075 g) were immersed in 50 cm^3 0.1 M NaCl to which a known amount of NaOH (0.1 M) was added to adjust the pH to *ca.* 11. After stabilisation of the pH (*ca.* 1 h), titration of the samples was performed under continuous agitation in a He atmosphere with HCl (0.1 M). Temporal changes to pH were measured using a crystal-body electrode coupled to a data logging and collection system (Pico Technology Ltd.); calibration was performed with standard buffer solutions (pH 4 and 7).

Temperature programmed reduction (TPR), BET surface area, total pore volume, H_2 chemisorption and temperature programmed desorption (TPD) were determined using the commercial CHEM-BET 3000 (Quantachrome) unit. The samples were loaded into a U-shaped Quartz cell (3.76 mm i.d.) and heated in 17 cm^3 min^{-1} (Brooks mass flow controlled) 5% v/v H_2/N_2 at 2 K min^{-1} to 673 ± 1 K. The effluent gas passed through a liquid N_2 trap and changes in H_2 consumption were monitored by TCD

with data acquisition using the TPR Win^{TM} software. The activated samples were maintained at the final temperature in a constant flow of H_2/N_2 until return of the signal to baseline, swept with 65 cm^3 min^{-1} N_2 for 1.5 h and cooled to room temperature. The samples were then subjected to H_2 chemisorption using a pulse (10 μl) titration procedure, followed by H_2-TPD in N_2 (65 cm^3 min^{-1}) at 45 K min^{-1} to 933 K with an isothermal hold until the signal returned to the baseline. BET areas and pore volumes were determined, respectively, in 30% and 95% v/v N_2/He using undiluted N_2 as internal standard. At least 3 cycles of N_2 adsorption-desorption in the flow mode were employed to determine total area and pore volume using the standard single point method. The measurements were reproducible to within ± 8% and the values quoted represent the mean.

Powder X-ray diffractograms were recorded on a Bruker/Siemens D500 incident X-ray diffractometer with Cu Kα radiation. The samples were scanned at a rate of 0.02º $step^{-1}$ over the range $20º \leq 2\theta \leq 90º$. Diffractograms were identified using the JCPDS-ICDD reference standards, *i.e.* MoO_3 (35-609), *β*-Mo_2N (25-1368), *γ*-Mo_2N (25-1366) and Au (04-0784). Lattice parameters and residual error associated with the main planes for *β*-Mo_2N and *γ*-Mo_2N were determined using the TOPAS (version 3) software. Analysis by scanning electron microscopy (SEM) was conducted on a Philips FEI XL30-FEG equipped with an Everhart-Thornley secondary-electron (SE) detector, operated at an accelerating voltage of 10-15 kV and using NORAN System SIX (version 1.6) for data acquisition. Before analysis, the samples underwent a hydrocarbon decontamination treatment using a plasma-cleaner (EVACTRON). Elemental (nitrogen) analyses were conducted using an Exeter CE-440 Elemental Analyser after sample combustion at *ca.* 1873 K.

The Au content was measured by atomic absorption spectroscopy (AAS, Shimadzu AA-6650 spectrometer with an air-acetylene flame) from the diluted extract in aqua regia (25% v/v HNO_3/HCl). X-ray photoelectron spectroscopy (XPS) analyses were conducted on an Axis Ultra instrument (Kratos) using a monochromatic Al Kα X-ray source (1486.6 eV). Prior to analysis, the nitride sample was adhered to a conducting carbon tape, mounted in the sample holder and subjected to ultra-high vacuum conditions (< 10^{-8} Torr). The source power was maintained at 150 W and the emitted photoelectrons were sampled from a square area of 750×350 μm^2; the photoelectron take-off angle was 90°. The analyser pass energy was 80 eV for survey

spectra (0–1000 eV) and 40 eV for high resolution spectra (over the Mo $3d_{3/2}$ and Mo $3d_{5/2}$ binding energy (BE) range, 227-239 eV). Sputtering of the surface (for 1 min) with a 3 keV argon ion beam was employed to remove the passivating layer and reveal the sub-surface composition. The adventitious C 1*s* peak was calibrated at 284.5 eV and used as internal standard to compensate for any charging effects. The instrument work function was calibrated to give a BE of 84.00 eV for the Au $4f_{7/2}$ line of metallic gold (Metalor) and the spectrometer dispersion was adjusted to give a BE of 932.7 eV for the Cu $2p_{3/2}$ line of metallic copper (Metalor). Quantification of the XPS signal employed the CasaXPS software, using relative sensitivity factors provided by Kratos. High resolution transmission electron microscopy (HRTEM) analyses were performed on a JEOL JEM 2011 unit with a UTW energy dispersive X-ray detector (Oxford Instruments) operated at an accelerating voltage of 200 kV; Gatan DigitalMicrograph 3.4 was employed for data acquisition. Samples for analysis were prepared by dispersion in acetone and deposited on a holey carbon/Cu grid (300 Mesh). Up to 320 individual Au particles were counted for each catalyst and the mean metal particle sizes are quoted as the number average (*d*).

3.2.4 Catalysis Procedure

All the gases (H_2 and N_2, Ar, O_2 and He) employed were of ultra high purity (> 99.99, BOC). *p*-CNB (Sigma-Aldrich, ≥ 99%) reactant and solvent (ethanol, Sigma Aldrich, ≥ 99.8%) were used without further purification. The composition of the reactant/product mixtures was determined using a Perkin-Elmer Auto System XL chromatograph equipped with a programmed split/splitless injector and a flame ionisation detector, employing a DB-1 capillary column (i.d. = 0.33 mm, length = 30 m, film thickness = 0.20 μm). Data acquisition/manipulation was performed using the TotalChrom Workstation (Version 6.1.2 for Windows) chromatography data system. The overall reactant/product molar fractions were obtained using detailed calibrations (not shown).

The hydrogenation of *p*-CNB was carried out under atmospheric pressure at 493 K, *in situ* immediately after activation, in a fixed bed vertical glass reactor (i.d. = 15 mm). The catalytic reactor was operated under conditions that ensured negligible heat/mass transport limitations. A layer of borosilicate glass beads served as preheating zone where the organic reactant was vaporised and reached reaction temperature before

contacting the catalyst. Isothermal conditions (± 1 K) were maintained by diluting the catalyst bed with ground glass (75 μm); the ground glass was mixed thoroughly with catalyst before insertion in the reactor. The reaction temperature was continuously monitored using a thermocouple inserted in a thermowell within the catalyst bed. The reactant (*p*-CNB as a solution in ethanol) was delivered at a fixed calibrated flow rate to the reactor *via* a glass/teflon air-tight syringe and teflon line using a microprocessor controlled infusion pump (Model 100 kd Scientific). A co-current flow of *p*-CNB and H_2 (< 1% v/v *p*-CNB in H_2) was delivered at a GHSV = 330 min^{-1} with an inlet reactant molar flow (F) in the range 0.7-3.2 μmol min^{-1}. The H_2 flow rate was monitored using a Humonics (Model 520) digital flowmeter, where the H_2 content was maintained well in excess of the stoichiometric requirement. The mass of catalyst to inlet *p*-CNB molar feed rate (m/F) spanned the range 2.6×10^{-3}-7.9×10^{-2} g min μmol^{-1}. As a blank test, passage of *p*-CNB in a stream of H_2 through the empty reactor did not result in any detectable conversion. The reactor effluent was frozen in a liquid nitrogen trap for subsequent analysis. Fractional hydrogenation ($X_{p\text{-CNB}}$) was obtained from

$$X_{p\text{-CNB}} = \frac{[p-\text{CNB}]_{in} - [p-\text{CNB}]_{out}}{[p-\text{CNB}]_{in}} \tag{3.1}$$

and selectivity with respect to *p*-chloroaniline (*p*-CAN), as the target product, is given by

$$S_{p\text{-CAN}}\ (\%) = \frac{[p-\text{CAN}]_{out}}{[p-\text{CNB}]_{in} - [p-\text{CNB}]_{out}} \times 100 \tag{3.2}$$

Repeated reactions with different samples from the same batch of catalyst delivered conversion/selectivity values that were reproducible to within ± 7%.

3.3 Results and Discussion

3.3.1 Mo_2N

3.3.1.1 β-Mo_2N Characterisation

The XRD pattern of the MoO_3 precursor is shown **Figure 3.1(a)**. The reflections over the range 2θ = 23-49° correspond to the (110), (040), (021), (130), (101), (111), (041), (060), (150), (061) and (002) planes that are characteristic of orthorhombic α-MoO_3 (JCPDS-ICDD 35-609, see **Figure 3.1(e)**). The diffractogram for the passivated β-Mo_2N (**Figure 3.1(b)**) shows peaks at 2θ = 37.7°, 43.1°, 45.3°, 62.7°, 64.3°, 75.5°, 78.6° and 80.5° that can be associated, respectively, with the (112), (200), (004), (220), (204), (312), (116) and (224) planes of β-Mo_2N (JCPDS-ICDD 25-1368, **Figure 3.1(f)**).

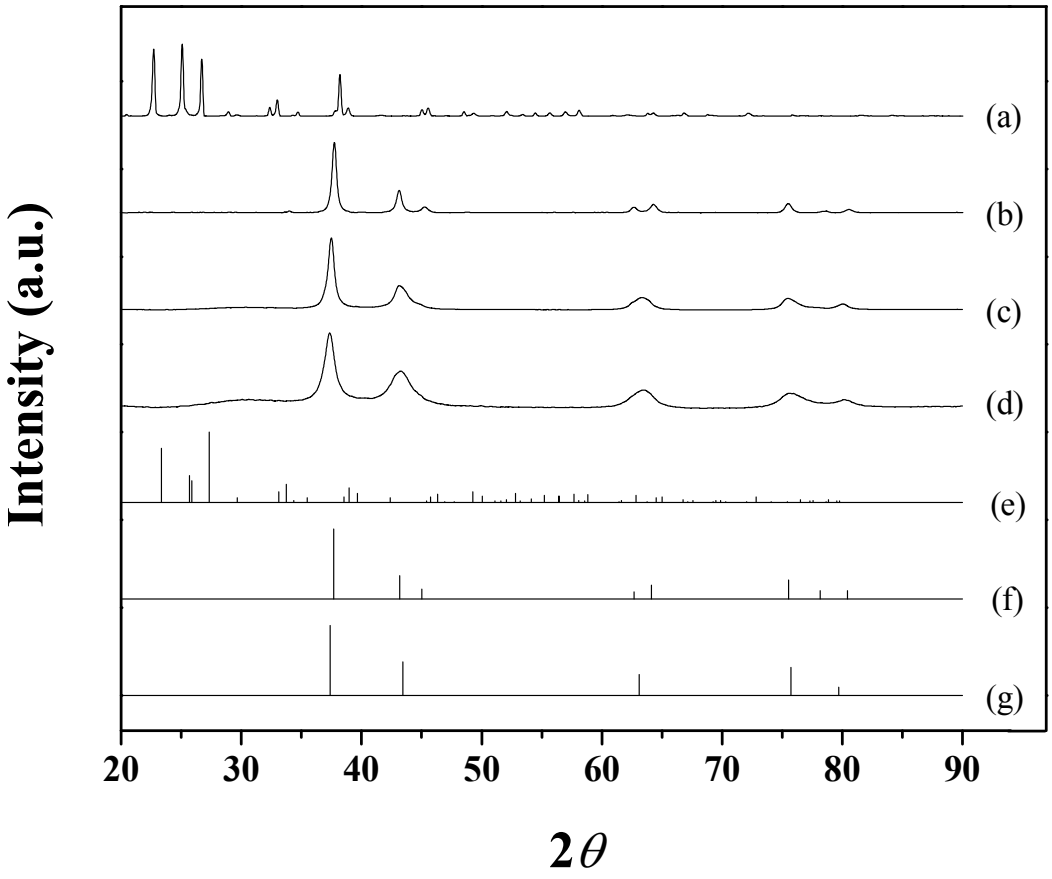

Figure 3.1: XRD patterns associated with (a) MoO_3, (b) β-Mo_2N, (c) γ-Mo_2N-a and (d) γ-Mo_2N-b with JCPDS-ICDD reference diffractograms for (e) MoO_3 (35-609), (f) β-Mo_2N (25-1368) and (g) γ-Mo_2N (25-1366).

Table 3.1: Lattice parameters and residual error associated with the main planes for γ-Mo_2N and β-Mo_2N in the analysis of Mo nitrides synthesised *via* temperature programmed treatment of MoO_3.

Cubic γ-Mo_2N				Tetragonal β-Mo_2N			
h k l	Residual Error (%)			h k l	Residual Error (%)		
	β-Mo_2N	γ-Mo_2N-a	γ-Mo_2N-b		β-Mo_2N	γ-Mo_2N-a	γ-Mo_2N-b
1 1 1	0.532	0.257	0.315	1 1 2	0.079	0.196	0.163
2 0 0	1.018	0.326	0.129	2 0 0	0.099	0.783	1.235
2 2 0	1.134	0.101	0.285	0 0 4	0.005	-	-
3 1 1	0.693	0.079	0.047	2 2 0	0.013	-	-
2 2 2	0.492	0.280	0.332	2 0 4	0.082	1.334	0.942
				3 1 2	0.008	0.601	0.727
				1 1 6	0.016	-	-
				2 2 4	0.035	0.171	0.793
Lattice Parameters (Å)	a = 4.198	a = 4.163	a = 4.156	Lattice Parameters (Å)	a = 4.205 c = 8.045	a = 4.172 c = 8.483	a = 4.162 c = 8.201
	a* = 4.163				a** = 4.188 c** = 8.048		

* for JCPDS-ICDD γ-Mo_2N reference (25-1366); ** for JCPDS-ICDD β-Mo_2N reference (25-1368)

It should be noted that there were no detectable signals due to Mo or oxide species, a result that confirms the complete transformation of MoO_3 to β-Mo_2N, where the passivation step served solely to provide a superficial oxide film without bulk oxidation [3.17].

In order to check for a possible γ-phase content, the sample was subjected to a single crystal analysis using the TOPAS software for lattice parameter optimisation and the results are presented in **Table 3.1**. The residual error obtained from adjusting the *d*-spacing to tetragonal β-Mo_2N was significantly lower when compared with that obtained for cubic γ-Mo_2N. The lattice parameters from the adjustment to the β-form (a = 4.205 Å; c = 8.045 Å) are very close to those for the JCPDS-ICDD standard (25-1368). Moreover, the nitrogen content (see **Table 3.2**: 5% w/w, bulk Mo/N = 2.7) is in good agreement with reported values of 2.6-2.7 [3.16,3.17,3.37,3.38] for β-Mo_2N.

The synthesised β-Mo_2N was examined by TEM and a representative image is shown in **Figure 3.2(1a)** where the intensity profile (see inset) yielded an average *d*-spacing of 0.24 nm, consistent with the (112) plane of β-Mo_2N. SEM analysis was also conducted to evaluate morphological features and the representative micrograph presented in **Figure 3.2(2a)** shows an aggregation of small crystallites (< 5 μm). A β-Mo_2N crystal structure containing ensembles of varying sizes (< 10 μm) has been reported elsewhere [3.12,3.16,3.18]. As the starting MoO_3 is characterised by a platelet morphology [3.39], the disruption of the orthorhombic precursor structure in the reduction/nitridation process ($MoO_3 \rightarrow MoO_2 \rightarrow Mo \rightarrow Mo_2N$) is the result of a non-topotactic transformation [3.8,3.12,3.17]. Cairns and co-workers [3.18] attributed the formation of small β-Mo_2N ensembles to water release/particle expansion during precursor reduction, following the model of Sloczynski and Bobinski [3.40].

It has been proposed [3.26] that passivation of Mo_2N results in the formation of one or two chemisorbed oxygen layers. Surface characterisation by XPS generated the spectra over the Mo 3*d* binding energy (BE) region for the MoO_3 precursor **(a)** and β-Mo_2N **(b)** presented in **Figure 3.3**. The XPS profile for MoO_3 is characterised by a sole spin-orbit doublet with a Mo $3d_{3/2}$ BE = 236.6 eV that is characteristic of Mo(VI) [3.41].

Table 3.2: Nitrogen content, Au loading, bulk and surface atomic Mo/N ratio, BET surface area, total pore volume, characteristic temperature programmed reduction (TPR) T_{max} with associated H_2 consumption, H_2 chemisorbed/desorbed (TPD), pH of the point of zero charge (pH_{PZC}), Au particle size range and mean value (*d*).

Catalyst	β-Mo_2N	Au/β-Mo_2N	γ-Mo_2N-a	Au/γ-Mo_2N-a	γ-Mo_2N-b	Au/γ-Mo_2N-b
Nitrogen content (% w/w)	5	-	6	-	6	-
Au loading (mol %)	-	0.26	-	0.54	-	0.59
Mo/N bulk ratio[a]; surface ratio after Ar ion sputtering[b]	2.7; 2.4	-	2.2; 1.4	-	2.2; 1.4	-
BET surface area ($m^2\ g^{-1}$)	7[c] (3)[d]	9[c] (5)[d]	36[c] (30)[d]	40[c] (33)[d]	66[c](60)[d]	82[c] (75)[d]
Pore volume ($cm^3\ g^{-1}$)	0.020	0.029	0.036	0.052	0.055	0.092
TPR T_{max} (K)	637	603	670	610	668	607
H_2 consumption during TPR ($\mu mol\ g^{-1}$)	303	373	732	777	1292	1454
H_2 chemisorption ($10^3\ \mu mol\ m^{-2}$)	42	45	16	20	16	18
TPD T_{max} (K)	806	746	827	795, 933	823	813, 933
H_2 desorbed ($\mu mol\ m^{-2}$)	0.4	1.4	0.2	0.7	0.2	0.5
pH_{PZC}	3.5	-	3.3	-	3.3	-
Au size range (nm)	-	2-13	-	1-8	-	1-8
d (nm)	-	7	-	4	-	4

[a]from elemental analysis; [b]from XPS measurements; [c]activated simple; [d]passivated simple

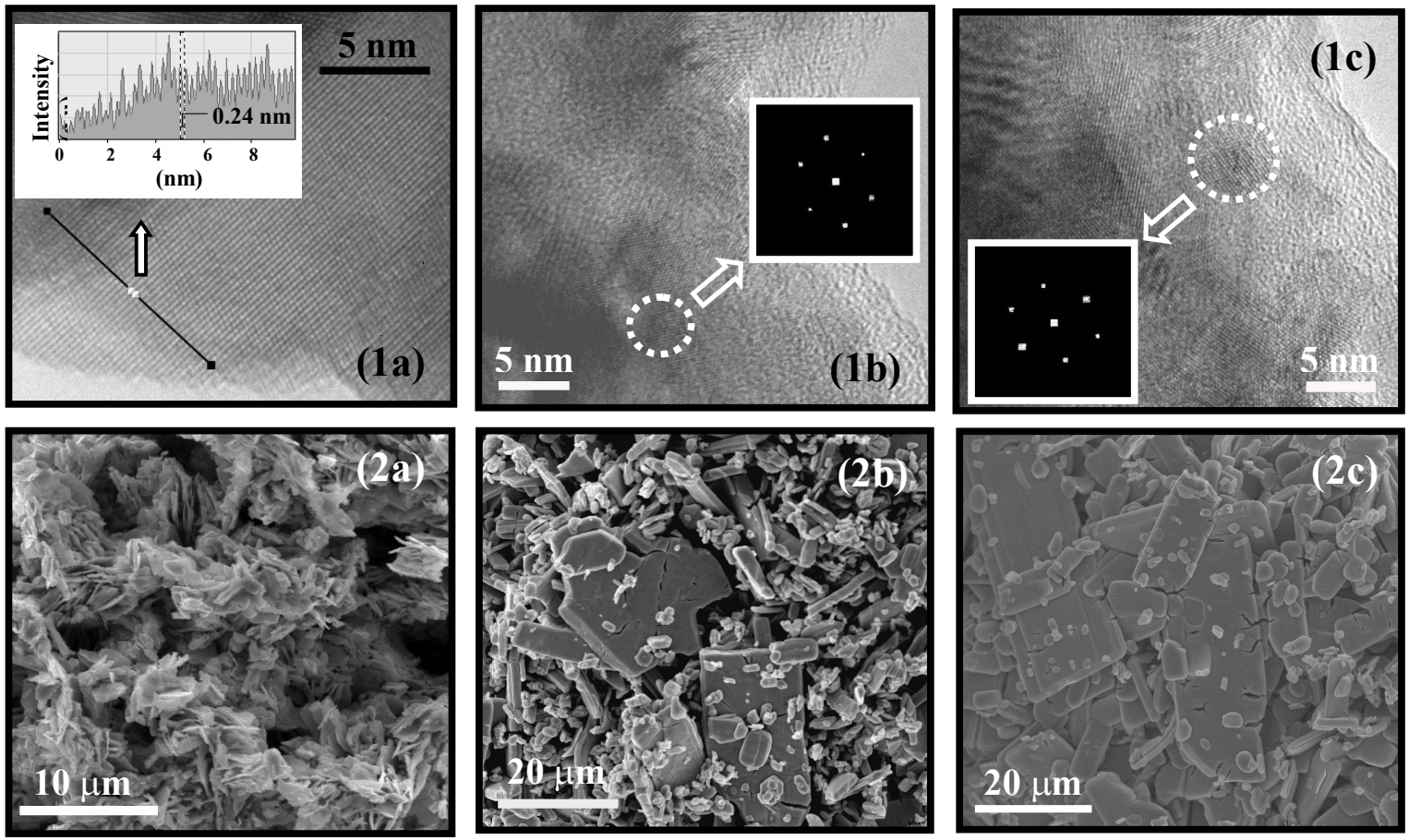

Figure 3.2: Representative (1) TEM images and (2) SEM micrographs of (a) *β*-Mo_2N, (b) *γ*-Mo_2N-a and (c) *γ*-Mo_2N-b. *Note*: Inset in (1a) shows the intensity profile, revealing the distance between the planes of the atomic lattice over the 10 nm segment that is marked on the TEM image; diffractogram patterns associated with the circled areas are included in (1b) and (1c).

Removal of the passivating oxide layer from Mo nitrides by Ar ion sputtering has been demonstrated elsewhere [3.41]. Sputtering was employed in this study to analyse the depth-profile composition of β-Mo_2N and mimic surface composition under reaction conditions. The XPS profile of the passivated sample (**Figure 3.3(b1)**) shows a principal XPS peak at BE = 228.7 eV that is characteristic of $Mo^{\delta+}$ ($2 \leq \delta < 4$) in passivated β-Mo_2N [3.42-44]. The occurrence of a detectable signal at 236.4 eV is consistent with a partial oxidation to Mo(VI) as a result of passivation [3.41]. While the hexavalent Mo signal in the precursor is strong and well defined, it is appreciably weaker for the Ar ion sputtered sample, demonstrating the near complete removal of the passivation layer (**Figure 3.3(b2)**).

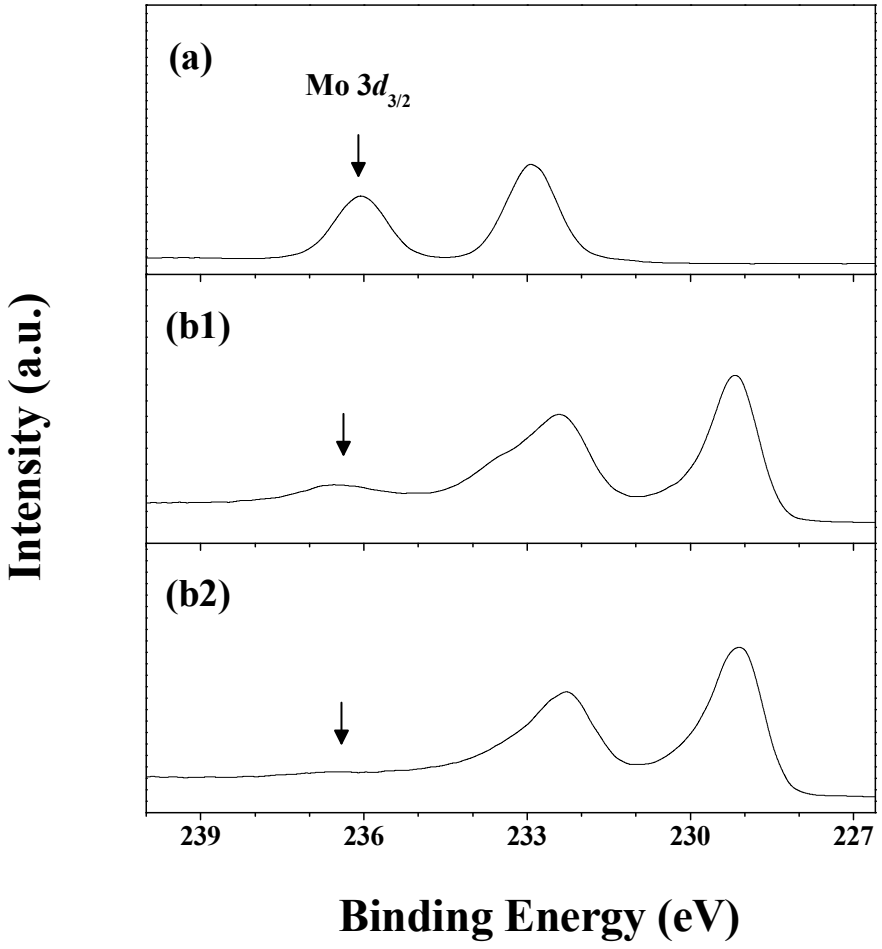

Figure 3.3: XPS spectra in the Mo 3*d* region of (a) MoO_3 and (b) β-Mo_2N (1) passivated and (2) after Ar ion sputtering. Note: Arrows illustrate the position of Mo $3d_{3/2}$ corresponding to Mo(VI).

The temperature requirements for the removal of this oxide overlayer were analysed by temperature programmed reduction (TPR) and the resultant profile, shown in **Figure 3.4(a1)**, is characterised by a positive peak with a maximum intensity at 637 K. Hydrogen consumption at temperatures over the range 637-740 K during TPR of passivated β-Mo_2N has been reported previously [3.17,3.26,3.45,3.46]. The H_2 consumed (303 μmol g^{-1}) is recorded in **Table 3.2** but we could not find any comparable measurement in the literature. The BET surface area falls within the range of values (2-17 m^2 g^{-1}) quoted previously for β-Mo_2N synthesised by temperature programmed reaction in N_2/H_2 [3.8,3.16,3.17]. The total area after passivation decreased (from 7 to 3 m^2 g^{-1}), as has been noted elsewhere [3.47].

A search through the literature has failed to unearth any study where quantitative measurements of H_2 chemisorption on β-Mo_2N are recorded. However, NMR [3.48] and IR [3.4] analyses suggest that H_2 can adsorb on Mo_2N at nitrogen deficient surface sites. Moreover, subsequent to adsorption, a heterolytic dissociation on Mo-N pairs (*via* the formation of Mo-H and N-H groups) has been proposed with migration to the sub-layers, which results in strong interactions [3.27,3.28,3.49]. A H_2 uptake of 42×10^{-3} μmol m^{-2} was recorded (**Table 3.2**) during pulse (ambient temperature) chemisorption analysis. Total surface hydrogen was evaluated by temperature programmed desorption (TPD) and the resultant profile is presented in **Figure 3.5(a1)**. The XRD pattern (not shown) of β-Mo_2N *post*-TPD was unchanged, demonstrating that the crystalline structure did not suffer any detectable alteration. Moreover, the nitrogen content (from elemental analysis) was unchanged; it has been established that loss of nitrogen from β-Mo_2N requires temperatures in excess of 1000 K [3.13]. The TPD profile is characterised by a broad peak (T_{max} = 806 K) where the H_2 released (0.4 μmol m^{-2}) is appreciably greater (by an order of magnitude) than that measured in the chemisorption step and must result from hydrogen uptake during TPR. Taking an overview of the limited available literature, the amount of H_2 desorbed (up to *ca.* 4 μmol m^{-2}) and associated T_{max} (370-800 K) appear to depend on nitride synthesis, *pre*-treatment and surface area [3.26,3.28]. High temperature (700-800 K) desorption has been associated with loss of H_2 from the bulk nitride as opposed to desorption from surface sites [3.28].

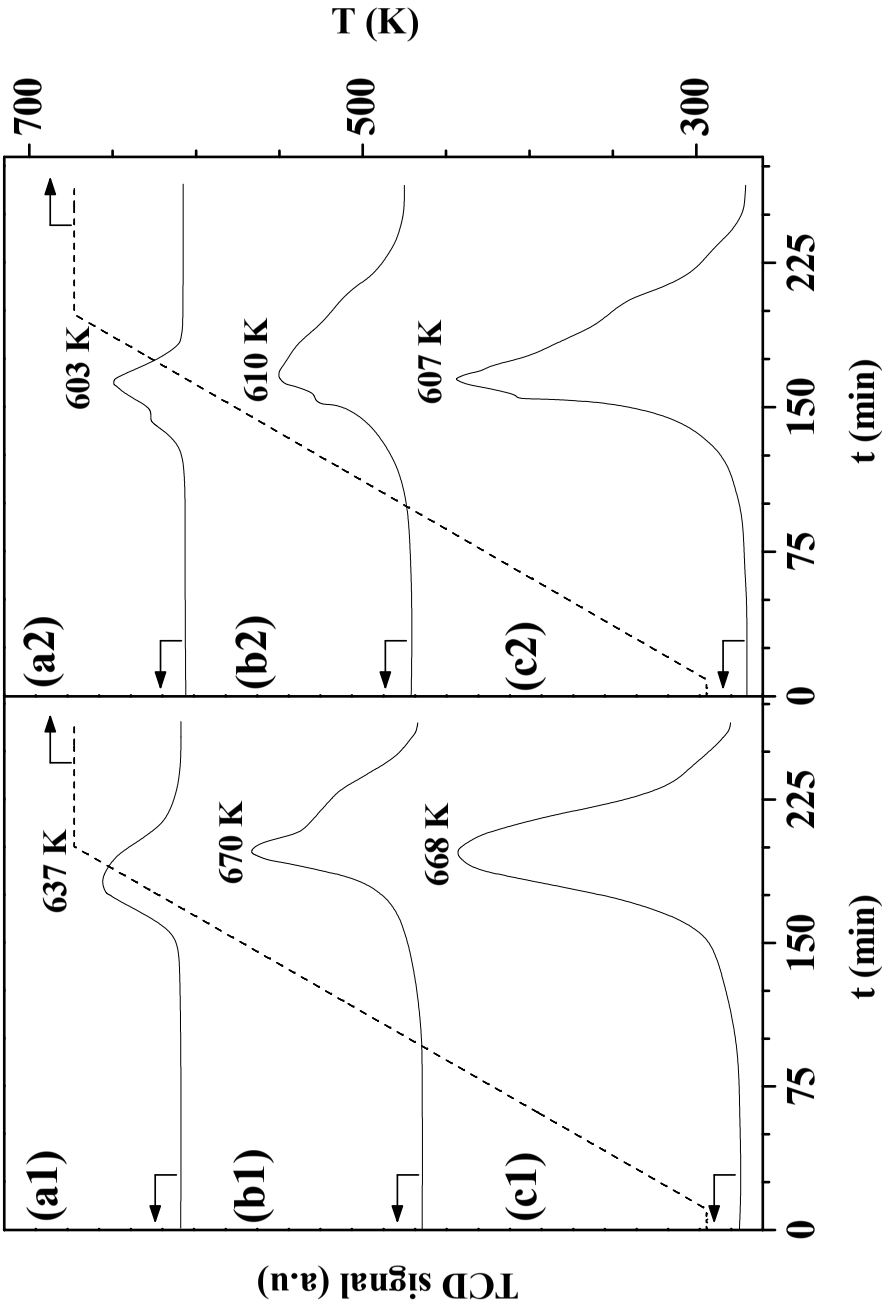

Figure 3.4: TPR profiles (solid line) with temperature ramp (dashed line) generated for passivated (a) *β*-Mo_2N, (b) *γ*-Mo_2N-a and (c) *γ*-Mo_2N-b (1) *pre-* and (2) *post-*Au incorporation.

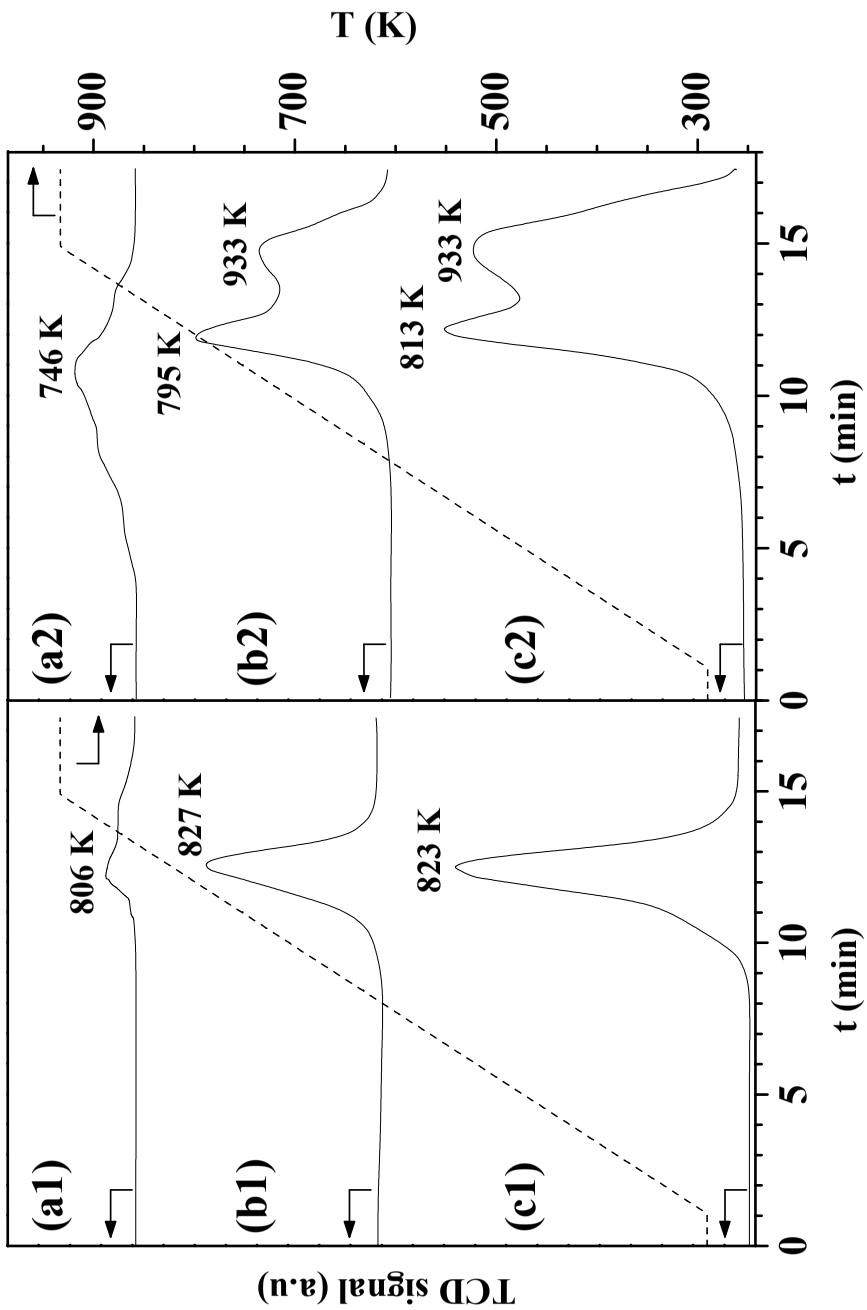

Figure 3.5: Hydrogen TPD response (solid line) with temperature ramp (dashed line) for (a) β-Mo_2N, (b) γ-Mo_2N-a and (c) γ-Mo_2N-b (1) *pre-* and (2) *post*-Au incorporation.

3.3.1.2 γ-Mo_2N Characterisation

Two γ-nitride (γ-Mo_2N-a and γ-Mo_2N-b) samples with different surface areas (**Table 3.2**) were synthesised by modifying the heating rate (see section 3.2.1.2). The total pore volumes are comparable to those quoted by Zhang and co-workers [3.50], *i.e.* 0.012 $cm^3\ g^{-1}$ (surface area = 17 $m^2\ g^{-1}$) and 0.060 $cm^3\ g^{-1}$ (surface area = 110 $m^2\ g^{-1}$). A reduction in surface area was observed after passivation, as noted for β-Mo_2N. The nitrogen content of both γ-Mo_2N samples (**Table 3.2**) was equivalent (6% w/w, bulk ratio Mo/N = 2.2) and agrees with values reported in the literature [3.44,3.50].

The XRD patterns for γ-Mo_2N-a **(c)** and γ-Mo_2N-b **(d)** (see **Figure 3.1**) coincide, presenting five main peaks at 2θ = 37.5°, 43.6°, 63.3°, 76.0° and 80.0° that can be matched to the (111), (200), (220), (311) and (222) planes of cubic γ-Mo_2N (JCPDS-ICDD 25-1366, profile **(g)**). Single crystal analysis generated lattice parameters consistent with the γ-Mo_2N JCPDS-ICDD standard; residual error < 0.4% (**Table 3.1**). Representative TEM images of γ-Mo_2N-a and γ-Mo_2N-b are presented in **Figure 3.2(1b)** and **Figure 3.2(1c)**, respectively, where the *d*-spacings (0.20 nm and 0.24 nm) are in agreement with the (200) and (111) planes of γ-Mo_2N. SEM analysis (see **Figure 3.2(2b)** and **2(2c)**) has revealed the predominance of large (*ca.* 15 μm×25 μm) platelet crystals with secondary, smaller (*ca.* 2 μm×10 μm) rod-like formations. This suggests a retention of the platelet morphology characteristic of MoO_3 and a topotactic $MoO_3 \rightarrow Mo_xN_yO_{1-y} \rightarrow$ γ-Mo_2N transformation [3.23,3.51]. The crystal size for both γ-Mo_2N samples is greater when compared with β-Mo_2N, as has been reported previously [3.16].

As in the case of β-Mo_2N, XPS analysis of γ-Mo_2N (not shown) confirmed a close to total removal of the passivation layer by Ar ion sputtering. A principal XPS signal at 228.3 eV was recorded that is within the range (228.2-230.0 eV) reported for passivated γ-Mo_2N [3.52-54] and attributed to $Mo^{\delta+}$ where $2 \leq \delta < 4$. In all three cases, bulk Mo/N exceeded the surface ratios (**Table 3.2**). Moreover, the surface Mo/N (1.4) for both sputtered γ-Mo_2N samples is significantly lower than that measured for β-Mo_2N (2.4).

The TPR profiles recorded for passivated γ-Mo_2N-a **(b1)** and γ-Mo_2N-b **(c1)** shown in **Figure 3.4** are characterised by a peak at 669 ± 1 K that falls within the values (590-855 K) recorded elsewhere [3.26,3.29,3.55,3.56]. A comparison of the TPR profiles for both γ-Mo_2N samples with that of β-Mo_2N reveals a shift in the reduction

peak to a higher temperature (by *ca.* 30 K) for γ-Mo_2N, suggesting differences in oxygen-nitride interactions. The hydrogen consumed during TPR can be associated with (i) removal of the passivation layer and (ii) surface adsorption of H_2, which can migrate to sub-layers. Hydrogen consumption (μmol g^{-1}, see **Table 3.2**) increases in the order: β-Mo_2N < γ-Mo_2N-a < γ-Mo_2N-b. The hydrogen required for reduction of the passivation layer should be proportional to nitride surface area and an equivalent amount of H_2 (per surface area) was recorded for the two γ-Mo_2N (= 20 μmol m^{-2}) samples. This value is within the range (5-20 μmol m^{-2}) reported in the literature for γ-Mo_2N with BET areas of 24-193 m^2 g^{-1} [3.29].

The significantly higher specific H_2 consumption for β-Mo_2N (= 43 μmol m^{-2}) relative to (both) γ-Mo_2N can be related to the crystallographic structure (β- *vs.* γ-) where difference in the exposed planes and surface composition can affect oxygen interaction with the nitride surface. Moreover, there is some consensus [3.27,3.48,3.49,3.57] that hydrogen uptake occurs at unsaturated surface Mo sites. Higher H_2 consumption can then be related to the greater nitrogen deficient surface character (higher Mo/N) exhibited by β-nitride, as confirmed by XPS. Specific (per m^2) H_2 chemisorption (**Table 3.2**) was the same on both γ-Mo_2N samples but was significantly lower (by a factor of 3) than that recorded for β-Mo_2N. In contrast, Choi and co-workers [3.28] found that H_2 uptake capacity increased in the order, β-$Mo_{16}N_7$ < δ-MoN < γ-$Mo_{16}N_7$. They attributed this to a reduced number of Mo atoms on the surface of β-$Mo_{16}N_7$. We observe the opposite effect with a higher Mo/N surface ratio for β-Mo_2N relative to γ-Mo_2N.

Hydrogen TPD from γ-Mo_2N-a **(b1)** and γ-Mo_2N-b **(c1)** generated the profiles presented in **Figure 3.5** with an equivalent H_2 release (0.2 μmol m^{-2}) at T_{max} = 825 ± 2 K, which is within the range (820-898 K) reported elsewhere [3.26,3.58]. The shift in H_2 desorption to a higher temperature (by *ca.* 20 K) for γ-Mo_2N relative to β-Mo_2N suggests stronger interaction. Total H_2 desorbed from γ-Mo_2N was lower (by a factor of 2) than that recorded for β-Mo_2N, where the latter exhibited greater H_2 consumption (per surface area) in the TPR and chemisorption measurements. These results suggest a dependence of surface hydrogen content on crystallographic phase that can be linked to surface Mo/N.

3.3.1.3 Catalytic Results

Selectivity is the key challenge in the hydrogenation of *p*-CNB, *i.e.* exclusive -NO_2 group reduction without C-Cl bond scission. Dechlorination results in the formation of nitrobenzene (NB) with subsequent hydrogenation to aniline (AN) as shown in **Figure 3.6**.

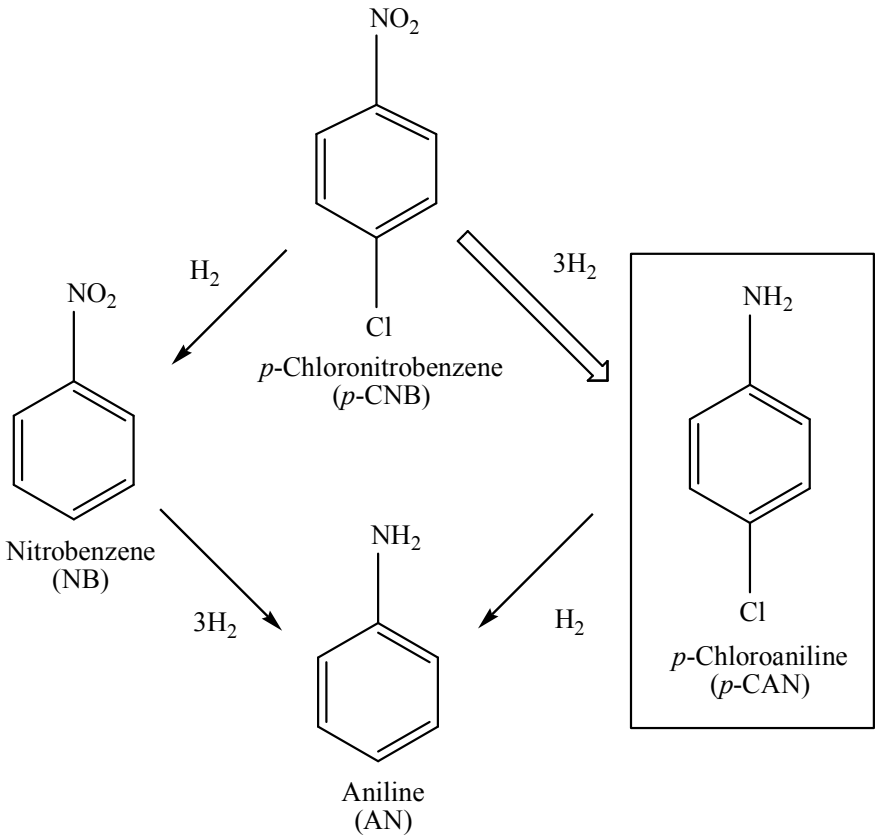

Figure 3.6: Main reaction pathways associated with the hydrogenation of *p*-CNB to the target (⇨) product (*p*-CAN) with non-selective (→) products resulting from hydrodechlorination/ hydrogenation.

Published articles [3.59-61] dealing with selective nitroarene hydrogenation have identified steps employed to improve selectivity, notably use of additives/promoters (*e.g.* NaHS and KOH) [3.62,3.63], support modifications (in terms of Lewis acid-base properties and formation of oxygen vacancies) [3.64,3.65] and metal dispersion [3.66]. Hydrogenation of *p*-CNB over β-Mo_2N, γ-Mo_2N-a and γ-Mo_2N-b generated *p*-CAN as the sole product, with no evidence of dechlorination. This finding

in itself is significant as composite hydrodechlorination/ hydrogenation (to form NB/AN) is a feature of reaction over conventional transition metal catalysts, *i.e.* Ni [3.67], Pt [3.68] and Ru [3.69]. Hydrogenation selectivity can be attributed to effective polarisation of the N=O group *via* surface interaction that renders the nitro function susceptible for hydrogen attack [3.70]. Indeed, $-NO_2$ adsorption-reduction on Mo has been demonstrated elsewhere [3.71,3.72] and Chen and Chen [3.67] have shown that the addition of Mo to nickel borides promoted selective nitro-group reduction while suppressing the dehalogenation step.

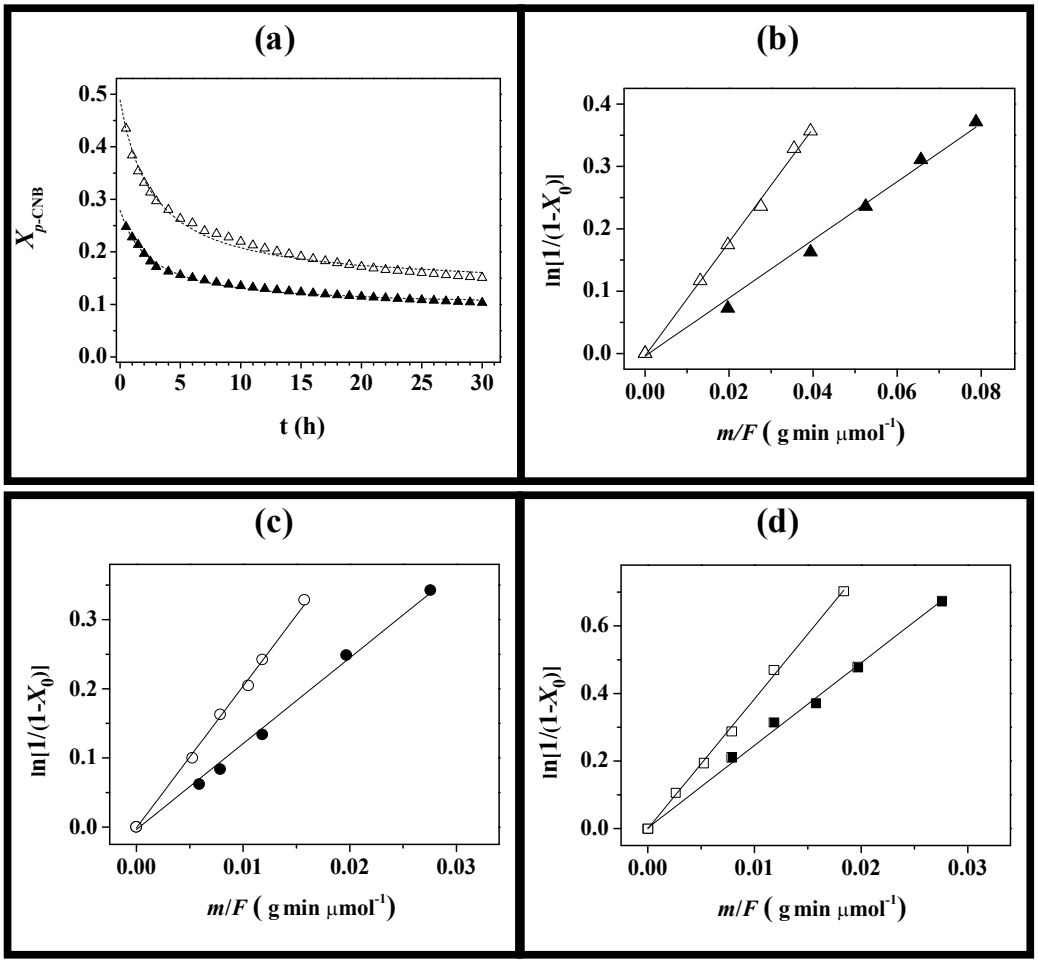

Figure 3.7 (a) Variation of *p*-CNB fractional conversion ($X_{p\text{-CNB}}$) with time-on-stream (m/F = 0.08 g min μmol^{-1}) for β-Mo_2N (▲) and Au/β-Mo_2N (Δ); lines represent fit to eqn. (3.3). Pseudo-first order kinetic plot for reaction over: (b) β-Mo_2N (▲) and Au/β-Mo_2N (Δ); (c) γ-Mo_2N-a (●) and Au/γ-Mo_2N-a (○); (d) γ-Mo_2N-b (■) and Au/γ-Mo_2N-b (□).

A temporal decrease in fractional *p*-CNB conversion ($X_{p\text{-CNB}}$) with time on-stream was observed, which can be expressed in terms of the empirical relationship [3.73]

$$\frac{(X_{p\text{-CNB}} - X_0)}{(X_{30\text{h}} - X_0)} = \frac{t}{(\beta + t)} \tag{3.3}$$

from which a value for the initial conversion (X_0) can be obtained, where $X_{30\text{h}}$ represents fractional conversion after 30 h on-stream and β is a time scale fitting parameter. A representative (β-Mo_2N) time on-stream response is shown in **Figure 3.7(a)** where it can be noted that a near steady state conversion was attained after *ca.* 15 h and maintained for 30 h of continuous operation. The applicability of a pseudo-first order kinetic treatment has been established for related catalyst systems [3.73]

$$\ln(1 - X_0)^{-1} = k\left(\frac{m}{F}\right) \tag{3.4}$$

where *m/F* corresponds to the mass of catalyst relative to inlet *p*-CNB molar feed rate. The pseudo-first order kinetic plots for β-Mo_2N, γ-Mo_2N-a and γ-Mo_2N-b are included in **Figure 3.7(b)-(d)**. The linear fit (passing through the origin) confirms adherence to the kinetic model. The extracted raw rate constants (k, μmol g^{-1} min^{-1}, **Table 3.3**) follow the order, γ-Mo_2N-b > γ-Mo_2N-a > β-Mo_2N.

In order to differentiate between the effect of surface area and crystal phase on the catalytic activity, the comparison must be based on specific rate (k', μmol m^{-2} min^{-1}, **Table 3.3**). Both γ-Mo_2N-a and γ-Mo_2N-b delivered an equivalent specific activity (35 ± 2×10^{-2} μmol m^{-2} min^{-1}) demonstrating that, for a given crystallographic phase, the intrinsic activity is independent of surface area. A significant finding is the appreciably higher specific rate recorded for β-Mo_2N. This can be correlated with the greater hydrogen content relative to γ-Mo_2N, which, in turn, is related to the increased number of nitrogen deficient (higher Mo/N, see **Table 3.2**) surface sites. The results demonstrate that *p*-CNB hydrogenation performance is sensitive to the nitride phase where rate is proportional to surface area.

Table 3.3: *p*-CNB hydrogenation rate constants (*k* and *k′*).

Catalyst	Rate constant k ($\mu mol\ g^{-1}\ min^{-1}$)	Specific rate constant k' ($\times 10^{-2}\ \mu mol\ m^{-2}\ min^{-1}$)
β-Mo_2N	4.6	66
γ-Mo_2N-a	12.2	34
γ-Mo_2N-b	24.5	37
Au/β-Mo_2N	9.0	100
Au/γ-Mo_2N-a	20.4	51
Au/γ-Mo_2N-b	38.4	47

3.3.2 Au/Mo_2N

3.3.2.1 Preparation and Characterisation

Catalyst supports, notably metal oxides, exhibit a characteristic pH-dependent surface charge [3.74]. The pH associated with the point of zero charge (pH_{PZC}) is a critical property that determines the solution pH requirements to ensure effective precursor-support interactions during catalyst preparation by deposition-precipitation (D-P) [3.75]. When pH < pH_{PZC}, the support bears a positive charge (due to protonation), favouring interaction with anionic species in solution and a pH in excess of pH_{PZC} results in a surface affinity for cationic species [3.76]. The pH_{PZC} depends on the chemical nature of the support rather than the crystallographic phase with equivalent values recorded for α- and γ-Al_2O_3, TiO_2-rutile and TiO_2-anastase, maghemite (γ-) and hematite (α-Fe_2O_3) [3.77]. The titration curves associated with pH_{PZC} measurements for β-Mo_2N **(1a)**, γ-Mo_2N-a **(1b)** and γ-Mo_2N-b **(1c)** are presented in **Figure 3.8**, yielding a similar value (3.4 ± 0.1) for the three nitrides. No measurements of pH_{PZC} for Mo_2N were found in the open literature.

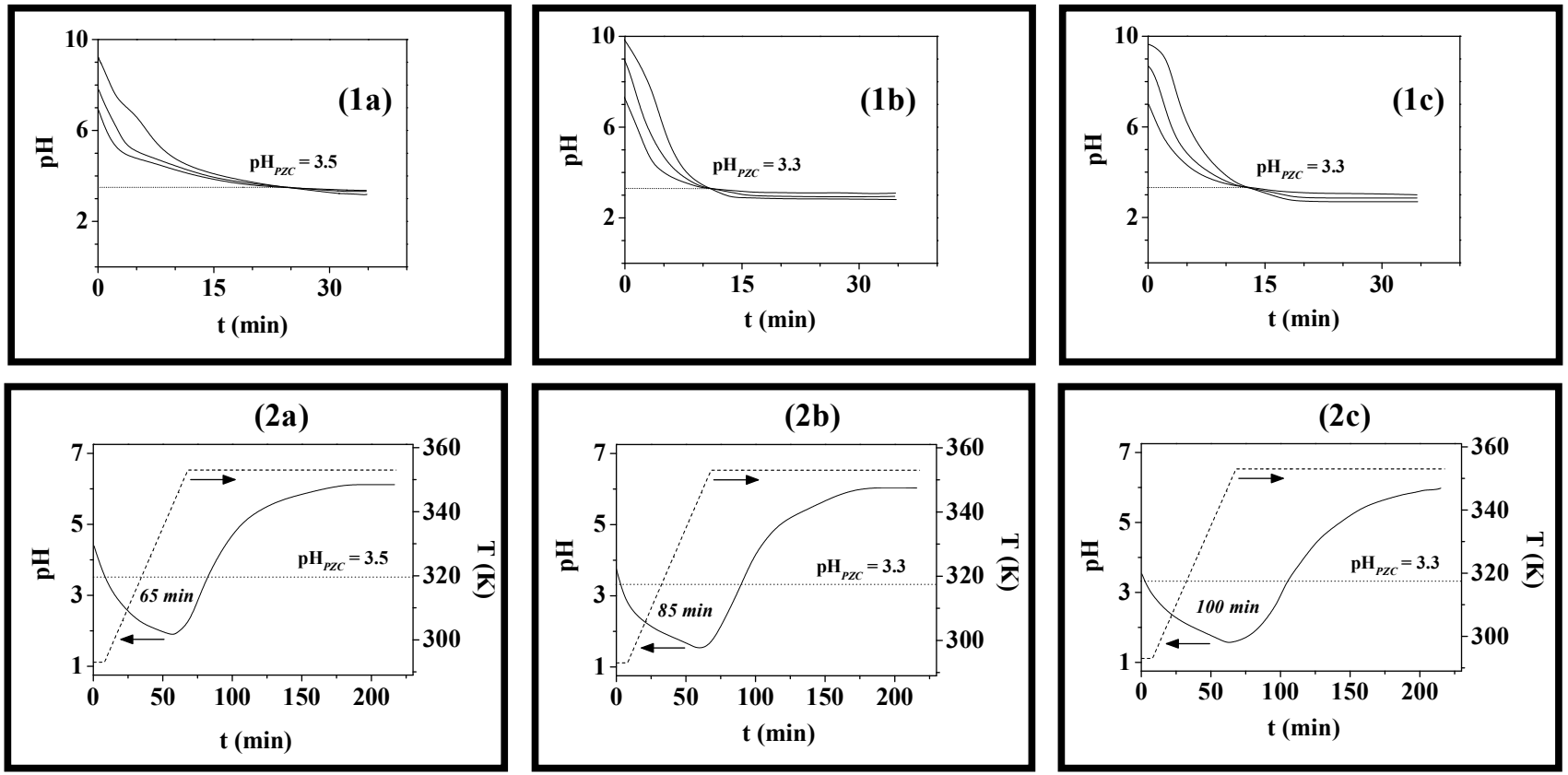

Figure 3.8: (1) pH profiles associated with the point of zero charge (pH_{PZC}) determination for (a) β-Mo_2N, (b) γ-Mo_2N-a and (c) γ-Mo_2N-b. (2) Temporal pH (solid line) and temperature (dashed line) variations in the preparation of (a) Au/β-Mo_2N, (b) Au/γ-Mo_2N-a and (c) Au/γ-Mo_2N-b. Note: Dotted line identifies the pH_{PZC} of the nitride; time during which pH < pH_{PZC} is given in italics.

The temporal pH variations during the preparation of Au/β-Mo_2N **(2a)**, Au/γ-Mo_2N-a **(2b)** and Au/γ-Mo_2N-b **(2c)** are also given in **Figure 3.8**. Initially, solution pH < pH_{PZC} and an electrostatic interaction between anionic gold species in solution ($HAuCl_4$ and/or $Au(OH)Cl_3^-$) and the positively charged support is favoured [3.36]. The surface sites act as nucleation centres for Au deposition [3.78]. The progressive decomposition of urea, as a result of the increase in temperature (up to 353 K), led to a gradual increase in solution pH where pH > pH_{PZC}. The support develops a negative surface charge resulting in an electrostatic repulsion with anionic gold species. A combination of chemical and electrostatic interactions between the precipitating species and the support are required to facilitate metal deposition [3.75]. Moreover, supports with a greater surface area can facilitate a more homogeneous nucleation, resulting in the formation of smaller supported Au ensembles.

The ultimate Au loadings (0.26–0.59 mol %, see **Table 3.2**) are below the nominal 1 mol %, which can be associated with the low pH_{PZC} that characterises the three nitride supports. A similar interpretation was proposed for a lower than expected Au content resulting from deposition on SiO_2 (pH_{PZC} = 2.2) [3.79]. The range of Au loadings obtained in this study can be correlated to the synthesis time where solution pH < pH_{PZC}, which was shortest (65 min) for β-Mo_2N, representing less favourable conditions for Au deposition resulting in the lowest metal content. The Au loading on both γ-Mo_2N supports with similar times at pH < 3.3 (pH_{PZC}) was essentially equivalent.

A concomitant increase in BET surface area and pore volume was observed after Au inclusion (**Table 3.2**). A similar phenomenon has been observed for the deposition of Pd and Au on boron nitride [3.80] and attributed to the development of nanopores during thermal treatment (drying and activation) with the release of water incorporated during deposition. The TPR profiles associated with Au/β-Mo_2N **(a2)**, Au/γ-Mo_2N-a **(b2)** and Au/γ-Mo_2N-b **(c2)** are presented **Figure 3.4**. Each is characterised by a principal H_2 consumption peak with T_{max} = 606 ± 4 K ascribed to passivating layer removal where the incorporation of Au resulted in a decrease in reduction temperature (by up to 60 K, see **Figure 3.4(a1)-(c1)**). A similar effect has been noted elsewhere [3.56] for the TPR of passivated Mo_2N, *i.e.* shift to lower temperature by up to 140 K, following Ni introduction. Moreover, the incorporation of Au on reducible carriers, *e.g.* Fe_2O_3 [3.81] and $Ce_xZr_{1-x}O_2$ [3.82] has resulted in a significant decrease (by up to 400 K) in the temperature required for partial reduction of the support. Reduction of

oxide supported gold ($Au^{3+} \rightarrow Au^0$) prepared by D-P has been reported to generate a TPR peak at $T < 500$ K [3.65]. This was not a feature of this study, suggesting a transformation of the Au precursor to metallic Au during preparation (*pre*-TPR). This has been reported previously [3.83], notably in the synthesis of iron oxide supported Au by co-precipitation. A reductive deposition of Au can occur on surface oxidised Mo species (*post*-passivation). The significantly lower standard redox potential of ionic Mo (*e.g.* E^0 for $H_2Mo^{VI}O_4/Mo^{IV}O_2$ = +0.65 V) compared with ionic Au (E^0 for $Au^{III}(OH)_3/Au^0$ = +1.32 V, E^0 for $Au^{III}Cl_4^-/Au^0$ = +1.00 V) [3.84] can act to reduce the Au precursor.

The incorporation of Au was accompanied by greater H_2 consumption during TPR (**Table 3.2**). This can be linked to (i) the increase in surface area and (ii) hydrogen spillover (from Au). It is known that H_2 chemisorption on supported Au is limited when compared with platinum group metals [3.85] but dissociative adsorption can proceed on low coordination Au sites, *i.e.* at edges and corners [3.86]. The three Au/nitride samples exhibited a measurable increase in H_2 chemisorption relative to the nitride support (**Table 3.2**). Hydrogen TPD generated the profiles shown in **Figure 3.5** for Au/β-Mo_2N **(a2)**, Au/γ-Mo_2N-a **(b2)** and Au/γ-Mo_2N-b **(c2)**. In each case, the incorporation of Au resulted in a significant increase in the amount of H_2 released (see **Table 3.2**). The TPD profiles present a principal peak (746-813 K) at a lower temperature (by up to 60 K) than that recorded for the nitride with an additional higher temperature (933 K) shoulder. These results indicate that the addition of Au results in greater capacity for hydrogen uptake (and subsequent release) with a distinct TPD response relative to the starting nitride.

Transmission electron microscopy was employed to obtain a measure of Au particle size. Representative **(1)** medium and **(2)** high magnification TEM images with particle size distributions **(3)** for **(a)** Au/β-Mo_2N, **(b)** Au/γ-Mo_2N-a and **(c)** Au/γ-Mo_2N-b are presented **Figure 3.9**. The images reveal a well dispersed Au phase in the form of quasi-spherical nano-scale particles.

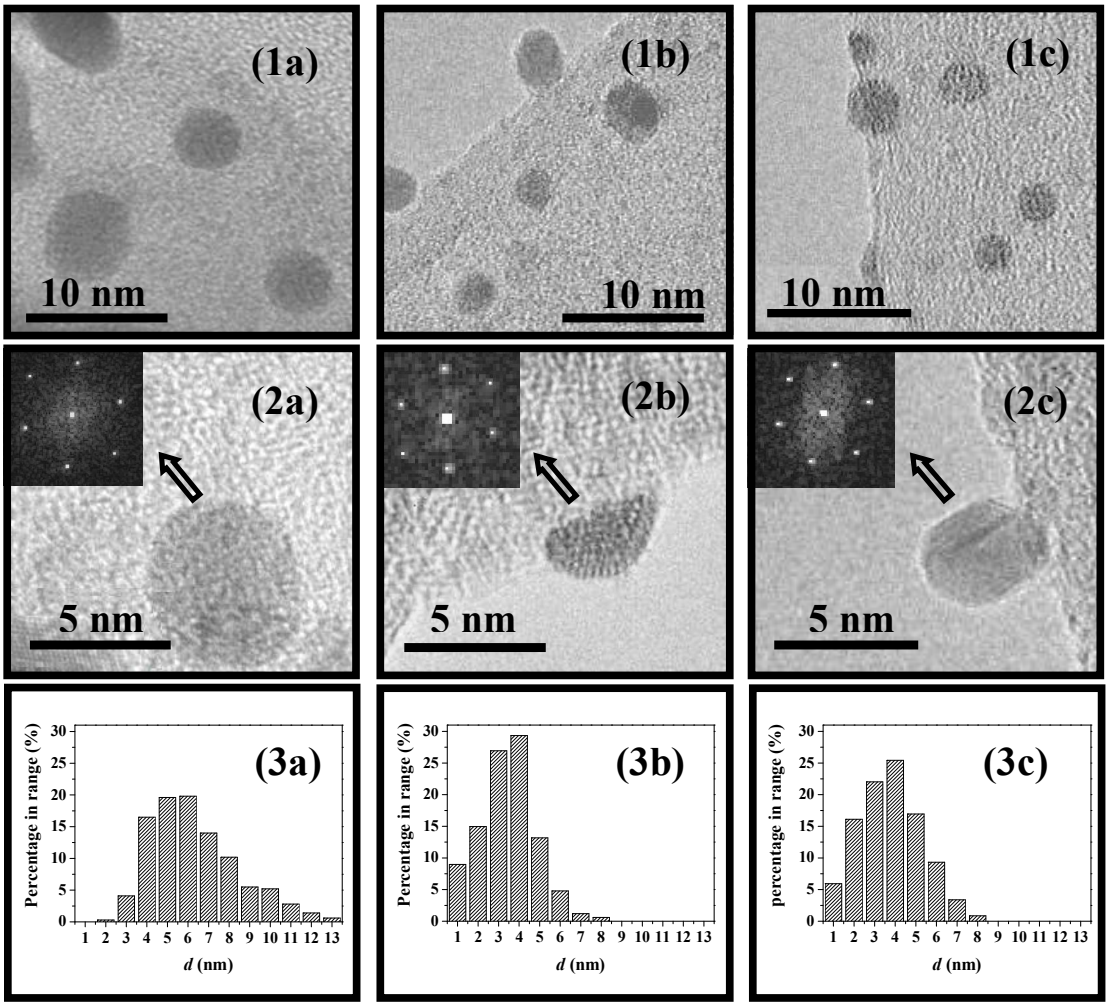

Figure 3.9: Representative (1) medium and (2) high magnification TEM images and (3) Au particle size distribution associated with (a) Au/β-Mo_2N, (b) Au/γ-Mo_2N-a and (c) Au/γ-Mo_2N-b. Note: Insets in high magnification TEM images show diffractogram patterns for single Au particles.

The diffractogram patterns for isolated Au particles are included (as insets) in the high magnification images **(2)** where the *d*-spacings (0.20/0.23) are consistent with the (111) and (200) planes of metallic gold. For the three catalysts, the Au particles (number average mean of 4-7 nm) are predominantly within the size range (≤ 10 nm) that has been deemed critical for hydrogenation activity [3.87]. The smaller mean Au size associated with γ-Mo_2N (see **Table 3.2**) can be ascribed to the prolonged deposition time where pH < pH_{PZC} (see **Figure 3.8**), resulting in stronger interactions with the support that minimise particle agglomeration.

3.3.2.2 Catalytic Results

The chemoselective hydrogenation of nitro-compounds over oxide supported Au is now established [3.59,3.60]. It has been shown that Au catalysts preferentially promote N=O reduction over other reactive functional groups, such as C≡N [3.88],C=O [3.89],C=C [3.60], Br [3.73] and Cl [3.90]. Activity and selectivity are dependent on Au particle size [3.91] and the nature of the support [3.59]. In the gas phase hydrogenation of *p*-CNB, we have demonstrated exclusive nitro-group reduction over Au supported on non-reducible (SiO_2, Al_2O_3) [3.92] and reducible (CeO_2, TiO_2, Fe_2O_3) [3.90] carriers. The results of this study demonstrate that this chemoselective response extends to Au supported on β-Mo_2N and γ-Mo_2N where reaction exclusivity to *p*-CAN was maintained. Moreover, incorporation of Au enhanced hydrogenation performance, as shown in **Figure 3.7**, where the specific rate delivered by Au/β-Mo_2N exceeded that obtained with both Au/γ-Mo_2N (**Table 3.3**). Increased activity due to Au inclusion can be linked to an increase in reactive hydrogen as established by TPD analysis.

3.4 Conclusion

Temperature programmed treatment of MoO_3 in flowing N_2+H_2 was used to synthesise tetragonal β-Mo_2N (7 m^2 g^{-1}) and cubic γ-Mo_2N (36 and 66 m^2 g^{-1}). The γ-form exhibits a platelet (*ca.* 15 μm×25 μm) morphology whereas β-Mo_2N takes the form of aggregates of small (< 5 μm) crystallites. Passivation of the synthesised samples provided a protective oxide layer that prevented bulk oxidation and facilitated *ex-situ* handling. In the synthesis of Au/Mo_2N, solution pH exceeded support pH_{PZC} (3.4 ± 1) resulting in a less favourable surface interaction with the anionic Au precursor. This was particularly pronounced in the case of β-Mo_2N and resulted in lower Au loading and the formation of larger Au particles (mean diameter = 7 nm for Au/β-Mo_2N *vs.* 4 nm for Au/γ-Mo_2N) after activation. Temperature programmed reduction to 673 K was necessary to remove the passivation layer where the inclusion of Au shifted the TPR profile to lower temperatures (by up to 60 K).

100% selectivity to the target *p*-CAN product in the hydrogenation of *p*-CNB was achieved over Mo_2N, regardless of the phase. Hydrogen TPD analysis has established H_2 uptake on each nitride during TPR where β-Mo_2N exhibited a higher specific (per unit area) H_2 content relative to γ-Mo_2N. This is associated with a greater

number of nitrogen deficient sites on β-Mo_2N (as established by XPS analysis), which translates into a higher specific selective hydrogenation rate. An equivalent specific rate was obtained for both γ-Mo_2N samples, indicative of invariance with respect to surface area. The addition of Au served to increase H_2 uptake capacity and elevated hydrogenation rate where *p*-CAN was again the sole product; Au/β-Mo_2N outperformed Au/γ-Mo_2N. The results demonstrate that the combination of Au with Mo_2N is a viable catalyst formulation for selective nitroarene hydrogenation.

3.5 References

[3.1] A. M. Alexander and J. S. J. Hargreaves, *Alternative catalytic materials: carbides, nitrides, phosphides and amorphous boron alloys*, Chem. Soc. Rev. 39 (2010) 4388-4401.

[3.2] E. Furimsky, *Metal carbides and nitrides as potential catalysts for hydroprocessing*, Appl. Catal. A: General 240 (2003) 1-28.

[3.3] M. Nagai, *Transition-metal nitrides for hydrotreating catalyst: Synthesis, surface properties and reactivities*, Appl. Catal. A: General 322 (2007) 178-190.

[3.4] Z. Wu, S. Yang, Q. Xin and C. Li, *In situ IR spectroscopic studies on molybdenum nitride catalysts: active sites and surface reactions*, Catal. Survey. Asia 7 (2003) 103-119.

[3.5] Z. X. Hao, Z. B. Wei, L. J. Wang, X. H. Li, C. Li, E. Z. Min and Q. Xin, *Selective hydrogenation of ethyne on gamma-Mo_2N*, Appl. Catal. A: General 192 (2000) 81-84.

[3.6] A. Guerrero-Ruiz, Y. Zhang, B. Bachiller-Baeza and I. Rodríguez-Ramos, *Hydrogenation of crotonaldehyde over carbon- supported molybdenum nitrides*, Catal. Lett. 55 (1998) 165-168.

[3.7] Y. Li, Y. Fan, J. He, B. Xu, H. Yang, J. Miao and Y. Chen, *Selective liquid hydrogenation of long chain linear alkadienes on molybdenum nitride and carbide modified by oxygen*, Chem. Eng. J. 99 (2004) 213-218.

[3.8] F. Cárdenas-Lizana, S. Gómez-Quero, N. Perret, L. Kiwi-Minsker and M. A. Keane, *β-Molybdenum nitride: Synthesis mechanism and catalytic response in the gas phase hydrogenation of p-chloronitrobenzene*, Catal. Sci. Tech. 1 (2011) 794–801.

[3.9] M. K. Neylon, S. Choi, H. Kwon, K. E. Curry and L.T. Thompson, *Catalytic properties of early transition metal nitrides and carbides: n-butane*

hydrogenolysis, dehydrogenation and isomerization, Appl. Catal. A: General 183 (1999) 253-263.

[3.10] M. E. Eberhart and J. M. MacLaren, *The chemistry of transition metal carbides and nitrides in The chemistry of transition metal carbides and nitrides*, S. T. Oyama (Ed.), Blackie academic & professional, Glasgow, 1996, pp 107-119.

[3.11] A. Boehncke, J. Kielhorn, G. Könnecker, C. Pohlenz-Michel and I. Mangelsdorf, *4-chloroaniline, Concise International Chemical Assessment Document 48*, World Health Organization, Stuttgart, 2003, pp. 7-9.

[3.12] S. Li, W. B. Kim and J. S. Lee, *Effect of the reactive gas on the solid-state transformation of molybdenum trioxide to carbides and nitrides*, Chem. Mater. 10 (1998) 1853-1862.

[3.13] M. Nagai, Y. Goto, O. Uchino and S. Omi, *TPD and XRD studies of molybdenum nitride and its activity for hydrodenitrogenation of carbazole*, Catal. Today 43 (1998) 249-259.

[3.14] E. J. Markel, S. E. Burdick, M. E. Leaphart and K L. Roberts, *Synthesis, characterization, and thiophene desulfurization activity of unsupported gamma-Mo_2N macrocrystalline catalysts*, J. Catal. 182 (1999) 136-147.

[3.15] Z. B. Z. Wei, P. Grange and B. Delmon, *XPS and XRD studies of fresh and sulfided Mo_2N*, Appl. Surf. Sci. 135 (1998) 107-114.

[3.16] D. McKay, J. S. J. Hargreaves, J. L. Rico, J. L. Rivera and X. L. Sun, *The influence of phase and morphology of molybdenum nitrides on ammonia synthesis activity and reduction characteristics*, J. Solid State Chem. 181 (2008) 325-333.

[3.17] S. Gong, H. Chen, W. Li and B. Li, *Synthesis of beta-$Mo_2N_{0.78}$ hydrodesulfurization catalyst in mixtures of nitrogen and hydrogen*, Appl. Catal. A: General 279 (2005) 257-261.

[3.18] A. G. Cairns, J. G. Gallagher, J. S. J. Hargreaves, D. McKay, E. Morrison, J. L. Rico and K. Wilson, *The influence of precursor source and thermal parameters upon the formation of beta-phase molybdenum nitride*, J. Alloys Compd. 479 (2009) 851-854.

[3.19] K. L. Roberts and E. J. Markel, *Generation of Mo_2N nanoparticles from topotactic Mo_2N crystallites*, J. Phys. Chem. 98 (1994) 4083-4086.

[3.20] R. S. Wise and E. J. Markel, *Synthesis of high surface area molybdenum nitride in mixtures of nitrogen and hydrogen*, J. Catal. 145 (1994) 344-355.

[3.21] R. Marchand, F. Tessier and F. J. DiSalvo, *New routes to transition metal nitrides: preparation and characterization of new phases*, J. Mater. Chem. 9 (1999) 297-304.

[3.22] J.-G. Choi, R. L. Curl and L. T. Thompson, *Molybdenum nitride catalysts I. Influence of the synthesis factors on structural properties*, J. Catal. 146 (1994) 218-227.

[3.23] C. H. Jaggers, J. N. Michaels and A. M. Stacy, *Preparation of high-surface-area transition-metal nitrides-Mo_2N and MoN*, Chem. Mater. 2 (1990) 150-157.

[3.24] R. C. V. McGee, S. K. Bej and L. T. Thompson, *Basic properties of molybdenum and tungsten nitride catalysts*, Appl. Catal. A: General 284 (2005) 139-146.

[3.25] L. Volpe and M. Boudart, *Compounds of molybdenum and tungsten with high specific surface-area. 1. Nitrides*, J. Solid State Chem. 59 (1985) 332-347.

[3.26] Z. B. Wei, Q. Xin, P. Grange and B. Delmon, *TPD and TPR studies of molybdenum nitride*, J. Catal. 168 (1997) 176-182.

[3.27] X. S. Li, Y. X. Chen, Y. J. Zhang, C. X. Ji and Q. Xin, *Temperature-programmed desorption and adsorption of hydrogen on Mo_2N*, React. Kinet. Catal. Lett. 58 (1996) 391-396.

[3.28] J. G. Choi, H. J. Lee and L. T. Thompson, *Temperature-programmed desorption of H_2 from molybdenum nitride thin-films*, Appl. Surf. Sci. 78 (1994) 299-307.

[3.29] C. W. Colling, J.-G. Choi and L. T. Thompson, *Molybdenum nitride catalysts II. H_2 temperature programmed reduction and NH_3 temperature programmed desorption*, J. Catal. 160 (1996) 35-42.

[3.30] W. Setthapun, S. K. Bej and L. T. Thompson, *Carbide and nitride supported methanol steam reforming catalysts: Parallel synthesis and high throughput screening*, Top. Catal. 49 (2008) 73-80.

[3.31] J. W. Logan, J. L. Heiser, K. R. McCrea, B. D. Gates and M. E. Bussell, *Thiophene hydrodesulfurization over bimetallic and promoted nitride catalysts*, Catal. Lett. 56 (1998) 165-171.

[3.32] G. H. Xie and Z. C. Jiang, *The first observation of Mo^{5+} in the passivation layer of Mo_2N*, Chin. Sci. Bull. 45 (2000) 1562-1564.

[3.33] J. A. Peck, C. D. Tait, B. I. Swanson and G. E. Brown, *Speciation of aqueous gold(III) chlorides from ultraviolet/visible absorption and Raman/resonance Raman spectroscopies*, Geochim. Cosmochim. Acta 55 (1991) 671-676.

[3.34] I. Dobrosz, K. Jiratova, V. Pitchon and J. M. Rynkowski, *Effect of the preparation of supported gold particles on the catalytic activity in CO oxidation reaction*, J. Mol. Catal. A: Chemical 234 (2005) 187-197.

[3.35] H. S. Oh, J. H. Yang, C. K. Costello, Y. M. Wang, S. R. Bare, H. H. Kung and M. C. Kung, *Selective catalytic oxidation of CO: Effect of chloride on supported Au catalysts*, J. Catal. 210 (2002) 375-386.

[3.36] R. Zanella and C. Louis, *Influence of the conditions of thermal treatments and of storage on the size of the gold particles in Au/TiO_2 samples*, Catal. Today 107 (2005) 768-777.

[3.37] S. W. Gong, H. K. Chen, W. Li and B. Q. Li, *Catalytic behaviors of beta-$Mo_2N_{0.78}$ as a hydrodesulfurization catalyst*, Energy Fuels 20 (2006) 1372-1376.

[3.38] M. Nagai, Y. Goto, A. Miyata, M. Kiyoshi, K. Hada, K. Oshikawa and S. Omi, *Temperature-programmed reduction and XRD studies of ammonia-treated molybdenum oxide and its activity for carbazole hydrodenitrogenation*, J. Catal. 182 (1999) 292-301.

[3.39] A. de Lucas Consuegra, P. M. Patterson and M. A. Keane, *Use of unsupported and silica supported molybdenum carbide to treat chloroarene gas streams*, Appl. Catal. B: Environmental 65 (2006) 227-239.

[3.40] J. Sĺoczyński and W. Bobiński, *Autocatalytic effect in the processes of metal-oxide reduction .2. Kinetics of molybdenum oxide reduction*, J. Solid State Chem. 92 (1991) 436-448.

[3.41] D. McKay, J. S. J. Hargreaves and R. F. Howe, *XPS evidence for molybdenum nitride formation in ZSM-5*, Catal. Lett. 112 (2006) 109-113.

[3.42] S. M. Aouadi, Y. Paudel, B. Luster, S. Stadler, P. Kohli, C. Muratore, C. Hager and A. A. Voevodin, *Adaptive Mo_2N/ MoS_2/ Ag tribological nanocomposite coatings for aerospace applications*, Tribol. Lett. 29 (2008) 95-103.

[3.43] P. J. Cai, Z. H. Yang, C. Y. Wang, Y. L. Gu and Y. T. Qian, *A simple approach to synthesize Mo_2N nanocrystals*, Chem. Lett. 34 (2005) 1360-1361.

[3.44] K. Inumaru, K. Baba and S. Yamanaka, *Synthesis and characterization of superconducting beta-Mo_2N crystalline phase on a Si substrate: An application*

of pulsed laser deposition to nitride chemistry, Chem. Mater. 17 (2005) 5935-5940.

[3.45] F. Cárdenas-Lizana, S. Gómez-Quero, N. Perret, L. Kiwi-Minsker and M. A. Keane, *Au/Mo_2N as a new catalyst formulation for the hydrogenation of p-Chloronitrobenzene in both liquid and gas phase*, Catal. Commun. 21 (2012) 46-51.

[3.46] S. W. Gong, H. K. Chen, W. Li and B. Q. Li, *Thiophene hydrodesulfurization over alumina-supported beta-$Mo_2N_{0.78}$ catalyst*, Catal. Commun. 5 (2004) 621-624.

[3.47] R. N. Panda and S. Kaskel, *Synthesis and characterization of high surface area molybdenum nitride*, J. Mater. Sci. 41 (2006) 2465-2470.

[3.48] G. W. Haddix, J. A. Reimer and A. T. Bell, *Characterization of H_2 adsorbed on gamma-Mo_2N by NMR-spectroscopy*, J. Catal. 108 (1987) 50-54.

[3.49] X. S. Li, K. J. Zhang, Q. Xin, C. X. Ji, Y. F. Miao and L. Wang, *Irreversible hydrogen uptake on Mo_2N catalyst*, React. Kinet. Catal. Lett. 57 (1996) 177-182.

[3.50] Y. Zhang, Q. Xin, I. Rodriguez-Ramos and A. Guerrero-Ruiz, *Temperature dependence of the pseudomorphic transformation of MoO_3 to gamma-Mo_2N*, Mater. Res. Bull. 34 (1999) 145-156.

[3.51] K. Dewangan, S. S. Patil, D. S. Joag, M. A. More and N. S. Gajbhiye, *Topotactical nitridation of alpha-MoO_3 fibers to gamma-Mo_2N fibers and its field emission properties*, J. Phys. Chem. C 114 (2010) 14710-14715.

[3.52] C. Shi, A. M. Zhu, X. F. Yang and C. T. Au, *NO reduction with hydrogen over cobalt molybdenum nitride and molybdenum nitride: a comparison study*, Catal. Lett. 97 (2004) 9-16.

[3.53] J.-G. Choi, D. Choi and L. T. Thompson, *Surface properties of high- surface-area powder and thin molybdenum nitrides treated in H_2 and H_2S*, Appl. Surf. Sci. 108 (1997) 103-111.

[3.54] J. Qi, L. H. Jiang, Q. A. Jiang, S. L. Wang and G. Q. Sun, *Theoretical and experimental studies on the relationship between the structures of molybdenum nitrides and their catalytic activities toward the oxygen reduction reaction*, J. Phys. Chem. C 114 (2010) 18159-18166.

[3.55] H. He, H. X. Dai, K. Y. Ngan and C. T. Au, *Molybdenum nitride for the direct decomposition of NO*, Catal. Lett. 71 (2001) 147-153.

[3.56] Y. H. Wang, W. Li, M. H. Zhang, N. J. Guan and K. Y. Tao, *Characterization and catalytic properties of supported nickel molybdenum nitrides for hydrodenitrogenation*, Appl. Catal. A: General 215 (2001) 39-45.

[3.57] X. S. Li, S. S. Sheng, H. R. Chen, C. X. Ji, Y. J. Zhang and Q. Xin, *Reduction effects of the passivated Mo_2N studied by XPS and H_2 chemisorption*, Acta Phys. Chim. Sin. 11 (1995) 678-680.

[3.58] M. Nagai and S. Omi, *Preparation, surface and catalytic properties of molybdenum nitrides*, Sekiyu Gakkaishi 38 (1995) 363-373.

[3.59] H.-U. Blaser, H. Steiner and M. Studer, *Selective catalytic hydrogenation of fonctionalized nitroarenes: an update*, ChemCatChem 1 (2009) 210-221.

[3.60] A. Corma, C. Gonzalez-Arellano, M. Iglesias and F. Sanchez, *Gold complexes as catalysts: Chemoselective hydrogenation of nitroarenes*, Appl. Catal. A: General 356 (2009) 99-102.

[3.61] X. D. Wang, M. H. Liang, J. L. Zhang and Y. Wang, *Selective hydrogenation of aromatic chloronitro compounds*, Curr. Org. Chem. 11 (2007) 299-314.

[3.62] S. R. Kanth, G. V. Reddy, V. V. V. N. S. R. Rao, D. Maitraie, B. Narsaiah and P. S. Rao, *A simple and convenient method for the reduction of nitroarenes*, Synth. Commun. 32 (2002) 2849-2853.

[3.63] S. U. Sonavane, M. B. Gawande, S. S. Deshpande, A. Venkataraman and R. V. Jayaram, *Chemoselective transfer hydrogenation reactions over nanosized gamma-Fe_2O_3 catalyst prepared by novel combustion route*, Catal. Commun. 8 (2007) 1803-1806.

[3.64] J. Xiong, J. X. Chen and J. Y. Zhang, *Liquid-phase hydrogenation of o-chloronitrobenzene over supported nickel catalysts*, Catal. Commun. 8 (2007) 345-350.

[3.65] F. Cárdenas-Lizana, S. Gómez-Quero, N. Perret and M. A. Keane, *Gold catalysis at the gas–solid interface: role of the support in determining activity and selectivity in the hydrogenation of m-dinitrobenzene*, Catal. Sci. Tech. 1 (2011) 652-661

[3.66] A. Corma, P. Serna, P. Concepcion and J. J. Calvino, *Transforming nonselective into chemoselective metal catalysts for the hydrogenation of substituted nitroaromatics*, J. Am. Chem. Soc. 130 (2008) 8748-8753.

[3.67] Y. Z. Chen and Y. C. Chen, *Hydrogenation of para-Chloronitrobenzene over nickel borides*, Appl. Catal. A: General 115 (1994) 45-57.

[3.68] B. Coq, A. Tijani and F. Figueras, *Particle-size effect on the kinetics of p-chloronitrobenzene hydrogenation over platinum alumina catalysts*, J. Mol. Catal. 68 (1991) 331-345.

[3.69] A. Tijani, B. Coq and F. Figueras, *Hydrogenation of para-chloronitrobenzene over supported ruthenium-based catalysts*, Appl. Catal. 76 (1991) 255-266.

[3.70] V. Vishwanathan, V. Jayasri, P. M. Basha, N. Mahata, L. Sikhwivhilu and N. J. Coville, *Gas phase hydrogenation of ortho-chloronitrobenzene (O-CNB) to ortho-chloroaniline (O-CAN) over unpromoted and alkali metal promoted-alumina supported palladium catalysts*, Catal. Commun. 9 (2008) 453-458.

[3.71] J. Ren, J. G. Wang, C. F. Huo, X. D. Wen, Z. Cao, S. P. Yuan, Y. W. Li and H. J. Jiao, *Adsorption of NO, NO_2, pyridine and pyrrole on alpha-Mo_2C(0001): A DFT study*, Surf. Sci. 601 (2007) 1599-1607.

[3.72] L. J. Deiner, D. H. Kang and C. A. Friend, *Low-temperature reduction of NO_2 on oxidized Mo(110)*, J. Phys. Chem. B 109 (2005) 12826-12831.

[3.73] F. Cárdenas-Lizana, S. Gómez-Quero and M. A. Keane, *Ultra-selective gas phase catalytic hydrogenation of aromatic nitro compounds over Au/Al_2O_3*, Catal. Commun. 9 (2008) 475-481.

[3.74] M. Kosmulski, *Chemical Properties of Material Surfaces* in Surfactant Science Series Vol. 102, M. Kosmulski (Ed.), Marcel Dekker, New York, 2001, pp.65-222.

[3.75] J. W. Geus and A. J. van Dillen, *Preparation of Supported Catalysts by Deposition-Precipitation* in Preparation of Solid Catalysts, Ertl G, Knözinger H, Weitkamp J (Eds), Wiley-VCH, Weinheim, 1999, pp. 460-486.

[3.76] F. Moreau and G. C. Bond, *Preparation and reactivation of Au/TiO_2 catalysts*, Catal. Today 122 (2007) 260-265.

[3.77] M. Kosmulski, *Compilation of PZC and IEP of sparingly soluble metal oxides and hydroxides from literature*, Adv. Colloid Interface Sci. 152 (2009) 14-25.

[3.78] F. Moreau, G. C. Bond and A. O. Taylor, *Gold on titania catalysts for the oxidation of carbon monoxide: control of pH during preparation with various gold contents*, J. Catal. 231 (2005) 105-114.

[3.79] F. Somodi, I. Borbath, M. Hegedus, A. Tompos, I. E. Sajo, A. Szegedi, S. Rojas, J. L. G. Fierro and J. L. Margitfalvi, *Modified preparation method for highly active Au/SiO_2 catalysts used in CO oxidation*, Appl. Catal. A: General 347 (2008) 216-222.

[3.80] G. Postole, A. Gervasini, C. Guimon, A. Auroux and B. Bonnetot, *Influence of the preparation method on the surface characteristics and activity of boron-nitride-supported noble metal catalysts*, J. Phys. Chem. B 110 (2006) 12572-12580.

[3.81] B. A. A. Silberova, G. Mul, M. Makkee and J. A. Moulijn, *DRIFTS study of the water-gas shift reaction over Au/Fe_2O_3*, J. Catal. 243 (2006) 171-182.

[3.82] S. E. Collins, J. M. Cíes, E. del Río, M. López-Haro, S. Trasobares, J. J. Calvino, J. M. Pintado and S. Bernal, *Hydrogen interaction with a ceria-zirconia supported gold catalyst. Influence of CO co-adsorption and pretreatment conditions*, J. Phys. Chem. C 111 (2007) 14371-14379.

[3.83] N. A. Hodge, C. J. Kiely, R. Whyman, M. R. H. Siddiqui, G. J. Hutchings, Q. A. Pankhurst, F. E. Wagner, R. R. Rajaram and S. E. Golunski, *Microstructural comparison of calcined and uncalcined gold/iron-oxide catalysts for low-temperature CO oxidation*, Catal. Today 72 (2002) 133-144.

[3.84] N. N. Greenwood and A. Earnshaw, *Chemistry of the Elements*, 2nd edn Butterworth-Heinemann, Oxford, 1997.

[3.85] L. McEwan, M. Julius, S. Roberts and J.C.Q. Fletcher, *A Review of the use of gold catalysts in selective hydrogenation reactions*, Gold Bull. 43 (2010) 298-306.

[3.86] P. Claus, H. Hofmeister and C. Mohr, *Identification of active sites and influence of real structure of gold catalysts in the selective hydrogenation of acrolein to allyl alcohol*, Gold Bull. 37 (2004) 181-186.

[3.87] G. Bond, C. Louis and D. T. Thompson, *Catalysis by Gold in Catalytic Science Series*, G. J. Hutchings (Ed.), Imperial College Press, London, 2006, pp. 150-153.

[3.88] A. Corma and P. Serna, *Preparation of substituted anilines from nitro compounds by using supported gold catalysts*, Nat. Protoc. 1 (2006) 2590-2595.

[3.89] A. Corma and P. Serna, *Chemoselective hydrogenation of nitro compounds with supported gold catalysts*, Science 313 (2006) 332-332.

[3.90] F. Cárdenas-Lizana, S. Gómez-Quero, N. Perret and M. A. Keane, *Support effects in the selective gas phase hydrogenation of p-chloronitrobenzene over gold*, Gold Bull. 42 (2009) 124-132.

[3.91] A. Corma and H. Garcia, *Supported gold nanoparticles as catalysts for organic reactions*, Chem. Soc. Rev. 37 (2008) 2096-2126.

[3.92] F. Cárdenas-Lizana, S. Gómez-Quero and M. A. Keane, *Exclusive production of chloroaniline from chloronitrobenzene over Au/TiO_2 and Au/Al_2O_3*, ChemSusChem 1 (2008) 215-221.

Chapter 4

Enhanced Selective Nitroarene Hydrogenation over Au Supported on β-Mo_2C and β-Mo_2C/Al_2O_3

In this Chapter, the application of Mo carbide for the reduction of -NO_2 is investigated. Au/β-Mo_2C and Au/β-Mo_2C/Al_2O_3 are synthesised and characterised in order to establish a promotional effect of Au with β-Mo_2C. The catalytic actions of the four systems (β-Mo_2C, β-Mo_2C/Al_2O_3, Au/β-Mo_2C, Au/β-Mo_2C/Al_2O_3) are considered in the gas phase hydrogenation of *p*-chloronitrobenzene and *m*-dinitrobenzene.

4.1 Introduction

It is known that molybdenum carbide exhibits catalytic properties that are similar to noble metals (*e.g.* Pd and Ru) [4.1]. Indeed, carbides have been shown to be promising catalysts in ammonia synthesis [4.2], thiophene [4.3] and dibenzothiophene [4.4] hydrodesulfurization, Fischer-Tropsch processing [4.5], the water gas shift reaction [4.6], alcohol steam reforming [4.7] and *n*-butane hydrogenolysis [4.8]. In comparison with noble metal catalysts, carbides are less expensive to produce and are tolerant to sulphur poisoning [4.7]. Moreover, in hydrogenation reactions [4.9], carbides exhibit selectivities that are quite distinct from Group VIII metal catalysts but this response has yet to be fully exploited.

Molybdenum carbide can adopt a face-centred cubic (*fcc*, α-MoC_{1-x}), orthorhombic (α-Mo_2C) and hexagonal close packed (*hcp*, β-Mo_2C) crystal structure [4.9,4.10]. The particular crystalline phase, which is dependent on the method of synthesis, exhibits different catalytic behaviour [4.11]. Molybdenum carbides can be prepared by the reaction of graphite with vaporised Mo metal or MoO_3 but this method generates a low surface area material (1-2 m^2 g^{-1}) and delivers a low product yield [4.12]. The principal means of Mo carbide synthesis involves temperature programmed nitridation and carburisation or direct carburisation [4.9]. A reduction and nitridation of MoO_3 (with NH_3) generates *fcc* Mo nitride that, in a subsequent carburisation step (in *e.g.* CH_4/H_2), can be converted to *fcc* α-MoC_{1-x} [4.5]. Alternatively, a direct carburisation of MoO_3 (to 900-1000 K) yields *hcp* β-Mo_2C [4.13]. Both approaches can

produce a high surface area carbide (40-200 m^2 g^{-1}) at high yield where the variables that impact on surface area include heating rate [4.14], gas space velocity [4.15], carbon source (*e.g.* CH_4, C_2H_6 and C_3H_8) [4.16,4.17] and % v/v H_2 in the feed [4.18].

It is possible to deposit the Mo oxide precursor on a support (*e.g.* Al_2O_3), which with carburisation generates Mo_2C/Al_2O_3 [4.3,4.19]. The resultant dispersion on the carrier can result in enhanced catalytic performance relative to the bulk carbide [4.20,4.21]. Moreover, the incorporation of a transition metal (*e.g.* Ni [4.22] or Pt [4.7,4.23]) with Mo carbide has also been shown to influence catalytic activity [4.23] and selectivity [4.7]. In terms of hydrogenation, the focus of this study, Mo_2C has been used to promote the conversion of cyclohexene [4.24], naphthalene [4.21], benzene [4.20] and toluene [4.25]. However, a search through the literature did not unearth any reported study of the gas phase hydrogenation of aromatic nitro compounds over Mo carbide.

Gold catalysts deliver lower hydrogenation activity relative to conventional transition metal (Pd, Pt and Ni) catalysts as a result of a less effective activation/dissociation of H_2 [4.26]. In the hydrogenation of nitro compounds [4.27], ketones [4.28], aldehydes [4.29] and dienes [4.30], gold catalysts can exhibit enhanced selectivity to the target product. Activity and selectivity for hydrogenation reactions are dependent on Au particle size where significant catalytic activity requires a well dispersed Au phase (particles < 5 nm) [4.31]. Moreover, it has been shown that electron transfer from the support to nano-sized Au particles influences the catalytic response [4.32]. Of direct relevance to this study is the finding of Florez and co-workers [4.33] that charge transfer in Au-carbide systems is greater than that observed for oxide supports. Previous work conducted in this laboratory [4.32,4.34-36] demonstrated exclusivity (with respect to $-NO_2$ reduction) in the gas phase continuous hydrogenation of a range of polyfunctional nitroarenes over Au supported on Al_2O_3, TiO_2, Fe_2O_3 and CeO_2. The goal of this study is to combine the catalytic properties of Mo carbide and Au in order to achieve a synergy that elevates reaction rate while maintaining hydrogenation selectivity.

para-Chloroaniline (*p*-CAN) and *meta*-nitroaniline (*m*-NAN) are commercially important chemicals in the manufacture of polymers, dyes and agrochemicals [4.37]. Conventional synthesis routes exhibit serious drawbacks in terms of low selectivity to the target amine with the generation of appreciable toxic waste [4.38]. This Chapter

reports the first synthesis and use of Au/Mo_2C and $Au/Mo_2C/Al_2O_3$ to promote the hydrogenation of *para*-chloronitrobenzene (*p*-CNB) and *meta*-dinitrobenzene (*m*-DNB). The catalytic responses are compared with that obtained using Au/Al_2O_3 as a benchmark and the catalytic data are correlated with critical catalyst structural characteristics.

4.2 Experimental

4.2.1 Catalyst Preparation and Activation

Bulk *β*-Mo_2C was synthesised *via* the temperature programmed carburisation of ammonium heptamolybdate tetrahydrate ($(NH_4)_6Mo_7O_{24}\cdot 4H_2O$, Merck (99%)) in 80 cm^3 min^{-1} 20% v/v CH_4 (99.995%, Air Liquide) in H_2 (99.995 %, Air Liquide). The temperature was ramped at 1 K min^{-1} to 973 K, maintained for 1 h and cooled to room temperature under H_2 with sample passivation in 1% v/v O_2/Ar (30 cm^3 min^{-1}) for 1 h. The passivation step was necessary to circumvent autothermal oxidation upon contact with air [4.39]. In the preparation of *δ*-alumina (Degussa) supported *β*-Mo_2C with a nominal Mo_2C loading of 10% w/w, 5 g of support was mixed with 40 cm^3 solution containing 0.92 g $(NH_4)_6Mo_7O_{24}\cdot 4H_2O$ and stirred for 1 h at room temperature. Water was removed on a rotary evaporator at 353 K under vacuum for *ca.* 1 h and the solid was dried at 353 K for 12 h. The impregnated alumina was heated in 16 cm^3 min^{-1} Ar at 0.5 K min^{-1} and held at 673 K for 3 h. The sample was then contacted with 80 cm^3 min^{-1} 20% v/v CH_4/H_2 with temperature ramping from 673 to 873 K (1 K min^{-1}) and from 873 to 973 K (0.5 K min^{-1}); the final temperature was maintained for 1 h. The CH_4/H_2 flow was switched to H_2 and the sample was cooled to room temperature and passivated as above. The $(NH_4)_6Mo_7O_{24}\cdot 4H_2O$ impregnated alumina was also calcined in air at 673 K for 4 h to obtain MoO_3/Al_2O_3, which was subjected to XPS analysis for comparison purposes with the carburised sample.

Mo_2C and Mo_2C/Al_2O_3 supported Au (nominal loading = 1 % w/w Au) were prepared by deposition-precipitation with urea [4.40], where 78 cm^3 distilled water and 2 cm^3 $HAuCl_4$ solution (10 g dm^{-3}) were introduced into a double-walled glass reactor, with water circulation at 353 K that facilitated accurate temperature control with vigorous stirring. A suspension of 1 g Mo_2C (or Mo_2C/Al_2O_3) in 20 cm^3 distilled water was immersed in an ultrasound bath for 2 min to enhance dispersion and this was

introduced to the glass reactor with the immediate addition of 400 mg solid urea. The suspension was stirred at 353 K for 16 h in the absence of light, the solution pH was monitored continuously and the solid was separated by centrifugation and washed with 100 cm^3 distilled water. Washing was repeated four times and the solid was dried under vacuum in a desiccator in the dark for *ca.* 12 h. For comparison purposes, a 1% w/w Au/δ-Al_2O_3 was also prepared using the procedure described above. The catalyst precursors (*as prepared* samples) were sieved into a batch of 75 μm average particle diameter and stored at 277 K under He in the dark.

4.2.2 Catalyst Characterisation

The Au, Mo, Cl and Al content of the as prepared samples were measured by inductively coupled plasma atom emission spectroscopy (CNRS Centre of Chemical Analysis, Vernaison). Carbon content was determined using an Exeter CE-440 Elemental Analyser after sample combustion at *ca.* 1873 K. The pH values associated with the point of zero charge (pH_{PZC}) of the supports were determined using the potentiometric mass titration technique [4.41]. For each support, three different masses (0.025, 0.050 and 0.075 g) were immersed in 50 cm^3 0.1 M NaCl to which a known amount of NaOH (0.1 M) had been added to adjust the pH to *ca.* 11. After stabilisation of the pH (*ca.* 1 h), titration of the samples was performed under continuous agitation in a He atmosphere with HCl (0.1 M) as titrant. The pH was measured using a pH meter (Hanna Instruments) equipped with a crystal-body electrode coupled to a data logging and collection system (Pico Technology Ltd.); calibration was performed with standard buffer solutions.

Temperature programmed reduction (TPR) and BET surface area were determined using the commercial CHEM-BET 3000 (Quantachrome) unit. Samples of Mo_2C, Al_2O_3, Mo_2C/Al_2O_3, Au/Mo_2C, Au/Mo_2C/Al_2O_3 and Au/Al_2O_3 were loaded into a U-shaped quartz cell (10 cm×3.76 mm i.d.) and heated in 16 cm^3 min^{-1} (Brooks mass flow controlled) 5% v/v H_2/N_2 at 2 K min^{-1} to 573 ± 1 K. The effluent gas passed through a liquid N_2 trap and changes in H_2 consumption were monitored by TCD with data acquisition/manipulation using the TPR Win™ software. The activated samples were maintained at the final temperature in a constant flow of H_2/N_2 for 4 h, swept with 65 cm^3 min^{-1} N_2 for 1.5 h and cooled to room temperature. The passivation treatment of the carbides can be taken to result in a monolayer oxygen coverage. The H_2

consumption (mmol $g_{Mo_2C}^{-1}$) during TPR then represents the amount required to remove this passivating monolayer

$$O(s) + 3/2\ H_2\ (g) \rightarrow H\ (s) + H_2O\ (g) \quad (4.1)$$

where (s) indicates surface atoms and (g) the gas phase. Taking a stoichiometry of two oxygen atoms per Mo atom [4.42], the β-Mo_2C surface area (SA_{TPR}, $m^2\ g_{Mo_2C}^{-1}$) can be calculated from

$$SA_{TPR}\ (m^2\ g_{Mo_2C}^{-1}) = (2/3) \times n_{H_2} \times N_A/(2 \times N_{Mo}) \quad (4.2)$$

where n_{H_2} represents moles of H_2 consumed during TPR per gram Mo_2C (H_2 consumption, **Table 4.1**) and N_A is the Avogadro number. On the assumption that the surface of Mo_2C consists of an equal proportion of the main low index planes, an approximate Mo surface density (N_{Mo}) is given by 1×10^{19} Mo m^{-2} [4.42]. The BET surface area (SA_{BET}) was determined (after TPR) in 30% v/v N_2/He using pure N_2 (99.9%) as internal standard. At least three cycles of N_2 adsorption-desorption in the flow mode were employed to determine total surface area by the standard single point method; areas were reproducible to within ± 3% and the values quoted in this paper represent the mean. Post BET area measurement, the samples were passivated (as described above) for off-line analysis.

Powder X-ray diffractograms were recorded on a Bruker/Siemens D500 incident X-ray diffractometer using Cu Kα radiation. The samples were scanned at a rate of 0.02º $step^{-1}$ over the range $5º \leq 2\theta \leq 80º$. Diffractograms were identified using the JCPDS-ICDD reference standards, *i.e.* β-Mo_2C (Card No. 11-0680), δ-Al_2O_3 (16-394) and Au (04-784). The Au metal particle size (d_{hkl}) was estimated using the Scherrer equation

$$d_{hkl} = \frac{K \times \lambda}{\beta \times \cos\theta} \quad (4.3)$$

where $K = 0.9$, λ is the incident radiation wavelength (1.5056 Å), β is the peak width at half the maximum intensity and θ represents the diffraction angle corresponding to the (200) plane associated with metallic Au ($2\theta = 44.5°$). Transmission electron microscopy (TEM) combined with Energy-Dispersive X-ray spectroscopy (EDX) analysis was performed using a JEOL 2010 electron microscope operating at 200

kV. Samples for analysis were crushed and homogenously dispersed in ethanol by ultrasonication and a drop of the suspension was deposited on a carbon-coated copper grid and evaporated. The surface area weighted Au particle diameter was calculated from

$$d = \frac{\sum_i n_i d_i^3}{\sum_i n_i d_i^2} \tag{4.4}$$

where n_i is the number of particles of diameter d_i. XPS spectra were collected on a SPECS (Phoibos MCD 150) X-ray photoelectron spectrometer, using a Mg Kα (hv = 1253.6 eV) X-ray source. The samples were reduced by TPR and passivated before transfer in air to the XPS chamber. After collection, the binding energies were calibrated with respect to the C-C/C-H components of the C 1*s* peak (binding energy = 284.6 eV). All spectra processing was carried out using the Casa XPS software package.

4.2.3 Catalysis Procedure

Reactions were conducted under atmospheric pressure at 423-473 K in a fixed bed vertical glass reactor (l = 450 mm; i.d. = 15 mm). The samples were activated (in situ) in 60 cm^3 min^{-1} H_2 at 2 K min^{-1} to 573 K, maintaining the final temperature for 1 h. The catalytic reactor and operating conditions to ensure negligible heat/mass transport limitations have been fully described elsewhere [4.43] but some features, pertinent to this study, are given below. A layer of borosilicate glass beads served as preheating zone, ensuring that the organic reactants were vaporized and reached reaction temperature before contacting the catalyst. Isothermal conditions (± 1 K) were ensured by diluting the catalyst bed with ground glass (75 μm); the glass was mixed thoroughly with catalyst before insertion in the reactor. The reaction temperature was continuously monitored using a thermocouple inserted in a thermowell within the catalyst bed. The reactants, *p*-CNB and *m*-DNB, as solutions in ethanol, were delivered at a fixed calibrated flow rate to the reactor via a glass/teflon air-tight syringe and teflon line using a microprocessor controlled infusion pump (Model 100 kd Scientific). A co-current flow of *p*-CNB (or *m*-DNB) and ultra pure (> 99.99%, BOC) H_2 (< 1% v/v organic in H_2) was maintained at a GHSV = 2×10^4 h^{-1} with an inlet reactant molar flow (F) in the range 4-39$\times10^{-5}$ $mol_{p\text{-}CNB}$ h^{-1} (or 2-10$\times10^{-5}$ $mol_{m\text{-}DNB}$ h^{-1}). The H_2 content in the feed was up to 2400 times in excess of the stoichiometric requirement. Hydrogen flow rate was monitored

using a Humonics (Model 520) digital flowmeter. The ratio of mass of catalyst to inlet molar organic feed rate (*m/F*) spanned the range 76-1250 g h $mol_{p\text{-CNB}}^{-1}$ (or 3-2500 g h $mol_{m\text{-DNB}}^{-1}$). In a series of blank tests, passage of both reactants in a stream of H_2 through the empty reactor or over the Al_2O_3 support did not result in any detectable conversion. The reactor effluent was frozen in a liquid nitrogen trap for subsequent analysis, which was made using a Perkin-Elmer Auto System XL gas chromatograph equipped with a programmed split/splitless injector and a flame ionization detector, employing a DB-1 (50 m×0.33 mm, 0.20 μm film thickness) capillary column (J&W Scientific). *p*-CNB (Sigma-Aldrich, purity ≥ 99%), *m*-DNB (Fluka, ≥ 98%) and ethanol (Sigma Aldrich, ≥ 99%) were used as supplied without further purification. Taking the hydrogenation of *p*-CNB as representative, activity is quantified in terms of fractional conversion ($X_{p\text{-CNB}}$)

$$X_{p\text{-CNB}} = \frac{[p-CNB]_{in} - [p-CNB]_{out}}{[p-CNB]_{in}} \tag{4.5}$$

where selectivity with respect to *p*-chloroaniline (*p*-CAN) is given by

$$S_{p\text{-CAN}}(\%) = \frac{[p-CAN]_{out}}{[p-CNB]_{in} - [p-CNB]_{out}} \times 100 \tag{4.6}$$

and the subscripts in and out refer to the inlet and outlet streams. Repeated reactions with samples from the same batch of catalyst delivered conversion/selectivity values that were reproducible to within ± 3%.

4.3 Results and Discussion

4.3.1 Catalyst Characterisation

Elemental analysis (see **Table 4.1**) indicates that the deposition-precipitation procedure was efficient in preparing Au loaded on Al_2O_3, Mo_2C and Mo_2C/Al_2O_3 with a gold content of ca. 1 % w/w. The pH associated with the point of zero charge (pH_{PZC}) is a critical property of the support that determines the solution pH requirements to ensure precursor-support interactions during catalyst preparation by deposition-precipitation [4.40,4.44,4.45].

Table 4.1: Au and Mo_2C content (% w/w), Mo/C ratio, BET surface area (SA_{BET}), H_2 consumption during TPR and specific Mo_2C surface area calculated from TPR measurements (SA_{TPR}), Au particle size range, surface area weighted mean Au diameter (d) and dispersion (D).

Catalyst	Au (% w/w)	Mo_2C (% w/w)	Mo/C	SA_{BET} ($m^2\ g^{-1}$)	H_2 consumption (mmol $g_{Mo_2C}^{-1}$)	SA_{TPR} ($m^2\ g_{Mo_2C}^{-1}$)	Au size range[a]/d (nm)	D
Mo_2C	-	100	1.8	39	1.6	34	-	-
Mo_2C/Al_2O_3	-	12.1	1.5	82	5.2	110	-	-
Au/Mo_2C	0.94	99.1	1.7	47	1.7	36	4-20/13.4	0.09
$Au/Mo_2C/Al_2O_3$	1.03	5.6	1.5	89	5.5	116	6-12/8.3	0.15
Au/Al_2O_3	0.95	-	-	91	0.1[b]	-	1-3/2.3	0.54

[a]from TEM analysis
[b]mmol H_2 consumed g^{-1} during TPR

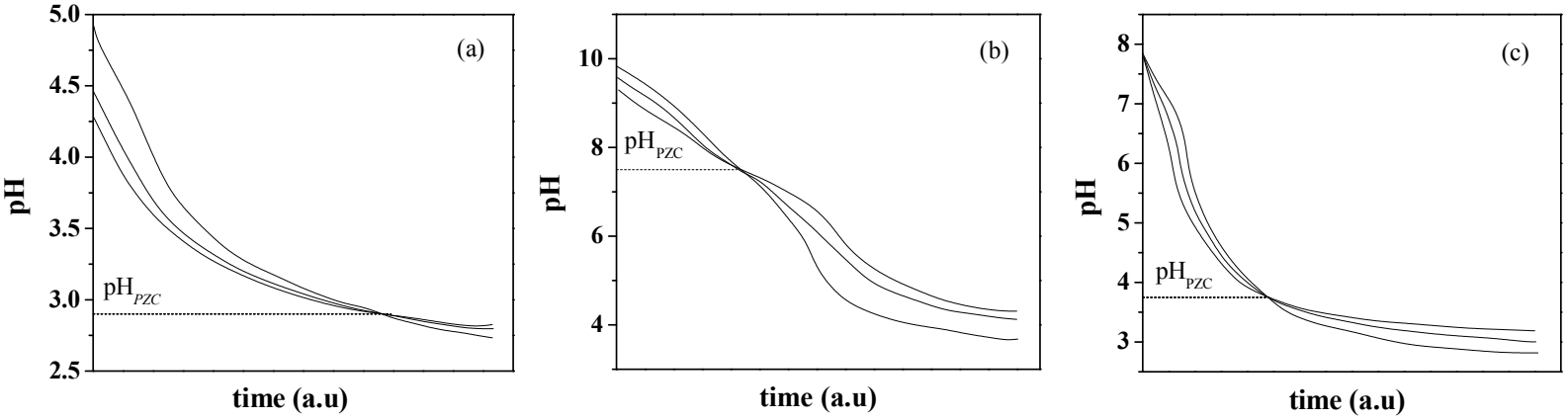

Figure 4.1: pH profiles associated with the pH of point of zero charge (pH_{PZC}) measurement for (a) Mo_2C, (b) Al_2O_3 and (c) Mo_2C/Al_2O_3.

The associated titration curves for the supports (**Figure 4.1**) show that the pH_{PZC} for Mo_2C (2.9) and Mo_2C/Al_2O_3 (3.7) are much lower than that measured for Al_2O_3 (7.5). The gold loadings achieved in this study are significant given that the pH_{PZC} values for Mo_2C and Mo_2C/Al_2O_3 are lower than *ca.* 5, the pH which has been identified as a prerequisite for effective deposition of the gold precursor on metal oxide and carbon supports [4.45]. When the solution pH < pH_{PZC}, the support surface bears a positive charge (due to protonation), favouring interaction with anionic species in solution and a pH in excess of pH_{PZC} results in a surface affinity for cationic species [4.46]. It is known that, in aqueous solution, $AuCl_4^-$ undergoes a sequential substitution of Cl^- with OH^- at pH = 4, 4.6, 6.5 and 9, at which point $Au(OH)_4^-$ predominates [4.45,4.47].

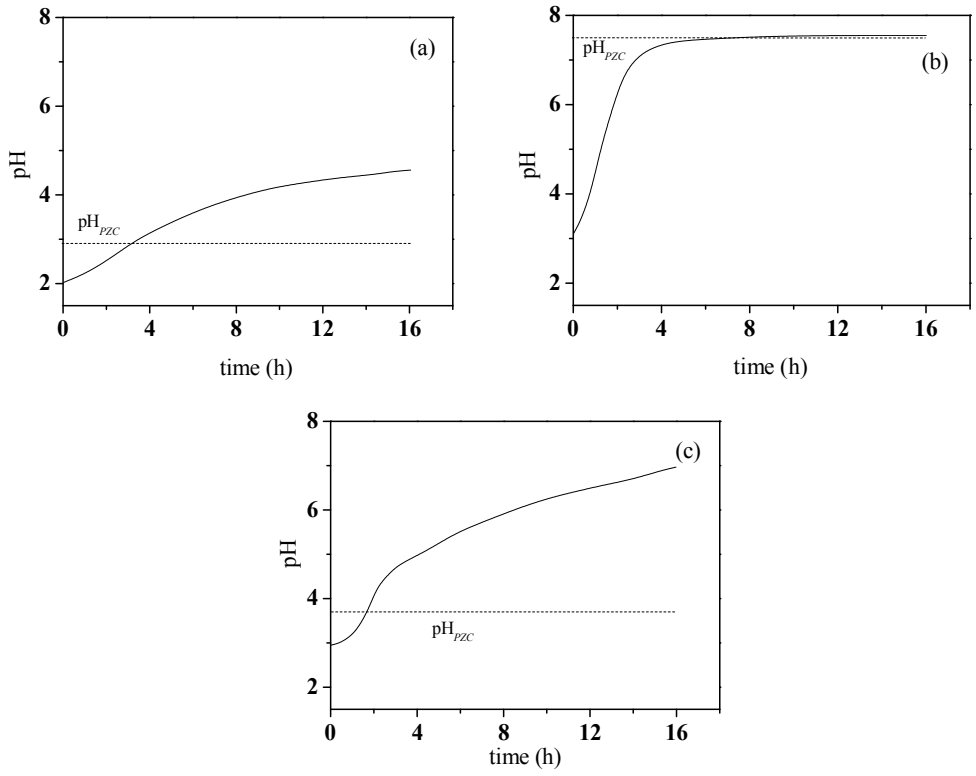

Figure 4.2: Temporal pH variations in the preparation of (a) Au/Mo_2C, (b) Au/Al_2O_3 and (c) $Au/Mo_2C/Al_2O_3$. Note: dashed lines identify pH_{PZC} of the supports.

The temporal pH variations in the preparation of Au/Mo_2C, Au/Al_2O_3 and $Au/Mo_2C/Al_2O_3$ are given in **Figure 4.2** where the pH_{PZC} of each support is identified as a dashed line. The observed temporal increase in pH corresponds to a progressive neutralisation of the acidity of the $HAuCl_4$ solution by OH^- generated via the decomposition of urea. In the case of Al_2O_3 (**Figure 4.2(b)**), the initial solution pH (3.1)

was far below the pH_{PZC} and the subsequent pH increase ultimately converged with the pH_{PZC}. Under these synthesis conditions, pH < pH_{PZC} over the first 2-3 hours of deposition-precipitation and Au precursor interactions with the (positively) charged Al_2O_3 were facilitated. However, solution pH in the preparation of Au/Mo_2C (**Figure 4.2(a)**) and Au/Mo_2C/Al_2O_3 (**Figure 4.2(c)**) exceeded the associated support pH_{PZC}. As a consequence, interactions of anionic Au precursor species with the negatively charged support were not favoured and deposition occurred principally via physical (as opposed to electrostatic) adsorption effects.

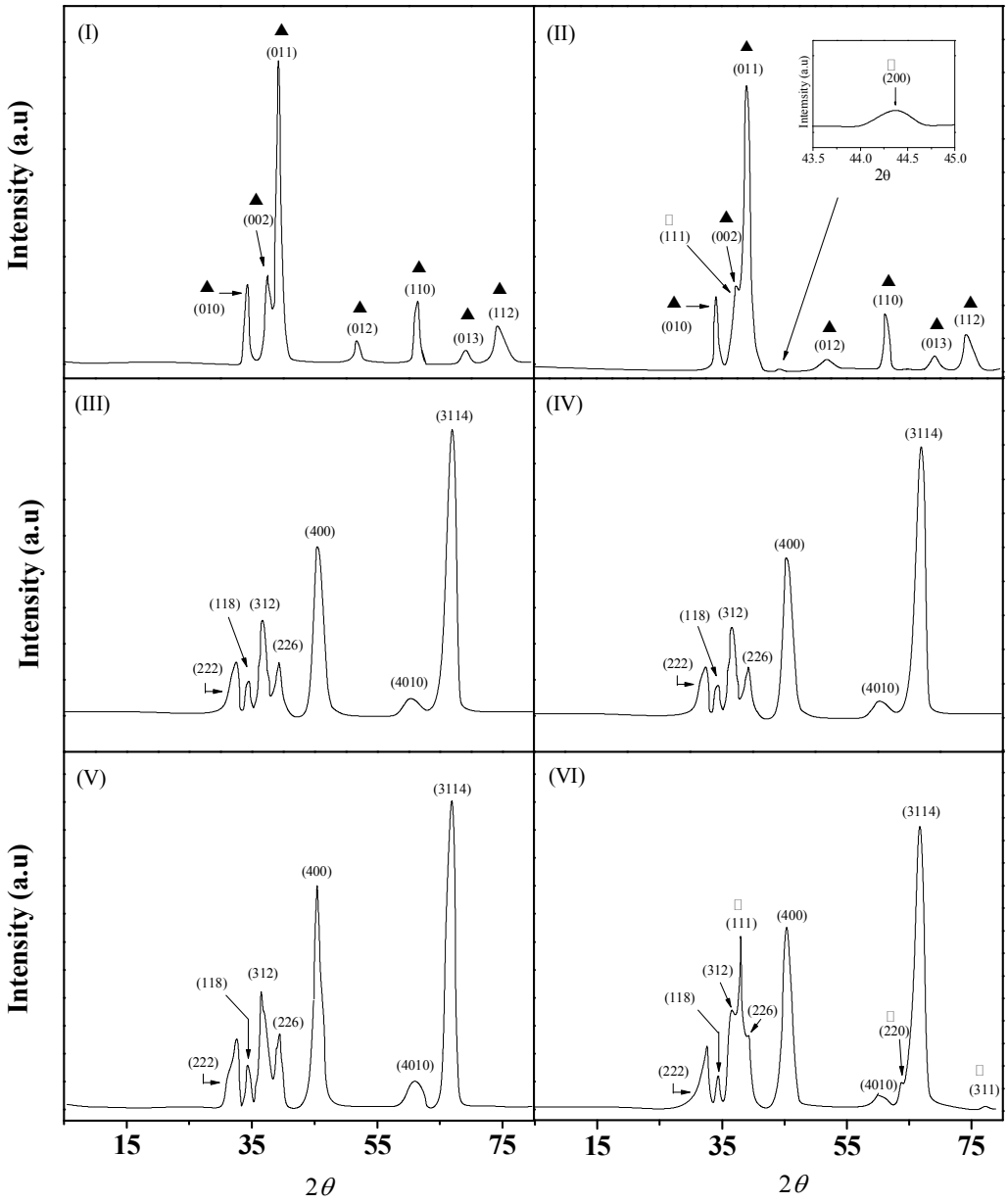

Figure 4.3: XRD patterns for Mo_2C (I), Au/Mo_2C (II), Al_2O_3 (III), Au/Al_2O_3 (IV), Mo_2C/Al_2O_3 (V) and Au/Mo_2C/Al_2O_3 (VI). Note: XRD peak assignments are based on JCPDS-ICDD reference standards: (▲) β-Mo_2C (Card No. 11-0680); (■) δ-Al_2O_3 (16-394); (●) Au (04-784).

XRD patterns of Mo_2C (I), Au/Mo_2C (II), Al_2O_3 (III), Au/Al_2O_3 (IV), Mo_2C/Al_2O_3 (V) and Au/Mo_2C/Al_2O_3 (VI) are presented in **Figure 4.3**. The XRD profile (**I**) of Mo_2C presents peaks that are characteristics of hexagonal *β*-Mo_2C. There was no evidence of any bulk oxide (MoO_3 or MoO_2) present in the carburised sample, *i.e.* the oxide precursor had been completely converted to the carbide and the passivation procedure resulted in a superficial (as opposed to bulk) oxidation. The TPR profile for Mo_2C is presented in **Figure 4.4(I)** and the H_2 consumption required to remove the passivation layer is given in **Table 4.1**. The TPR profile is characterised by a maximum H_2 consumption at 493 K with a lower temperature shoulder to the main peak. The amount of H_2 consumed was used to calculate the specific Mo_2C surface area (SA_{TPR}, see eqn. (4.2)) and the result (34 m^2 g^{-1}) is in good agreement with the value obtained by standard BET analysis (39 m^2 g^{-1}). The introduction of Au resulted in a shift in the reduction temperature to a lower value (by ca. 40 K, see **Figure 4.4(II)**) for Au/Mo_2C. A similar effect has been noted for Au supported on reducible carriers, *e.g.* Fe_2O_3 [4.48] and CeO_2 [4.30] with a decrease in the temperature required for a partial reduction of the support (by up to 400 K).

The XRD pattern for Au/Mo_2C *post*-activation (**Figure 4.3(II)**) exhibits the principal planes for *β*-Mo_2C with evidence of a signal due to the (111) plane of metallic Au ($2\theta = 38.1°$) that overlaps with the (002) peak for the support ($2\theta = 37.9°$). A peak at 44.4° related to Au (200) is also detectable as shown in the inset to **Figure 4.3(II)**. XRD analysis (pattern not shown) of the as prepared Au/Mo_2C also exhibited signals due to metallic Au, indicating that the gold precursor was reduced during preparation. The formation of metallic Au during catalyst synthesis has already been reported elsewhere, notably in the preparation of iron oxide supported Au by co-precipitation [4.49]. It should be noted that synthesis conditions were chosen in this study to avoid gold reduction, *i.e.* preparation and storage in the dark with room temperature drying in an inert atmosphere. The standard redox potential of ionic Mo (*e.g.* E^0 for $H_2Mo^{VI}O_4/Mo^{IV}O_2$ = +0.646 V) is significantly lower than that for ionic Au (E^0 for $Au^{III}(OH)_3/Au^0$ = +1.32 V, E^0 for $Au^{III}Cl_4^-/Au^0$ = +1.002 V) [4.50]. Surface oxidised Mo species (*post*-passivation), with a lower electrochemical potential, can act to reduce the Au precursor, resulting in a reductive deposition of Au.

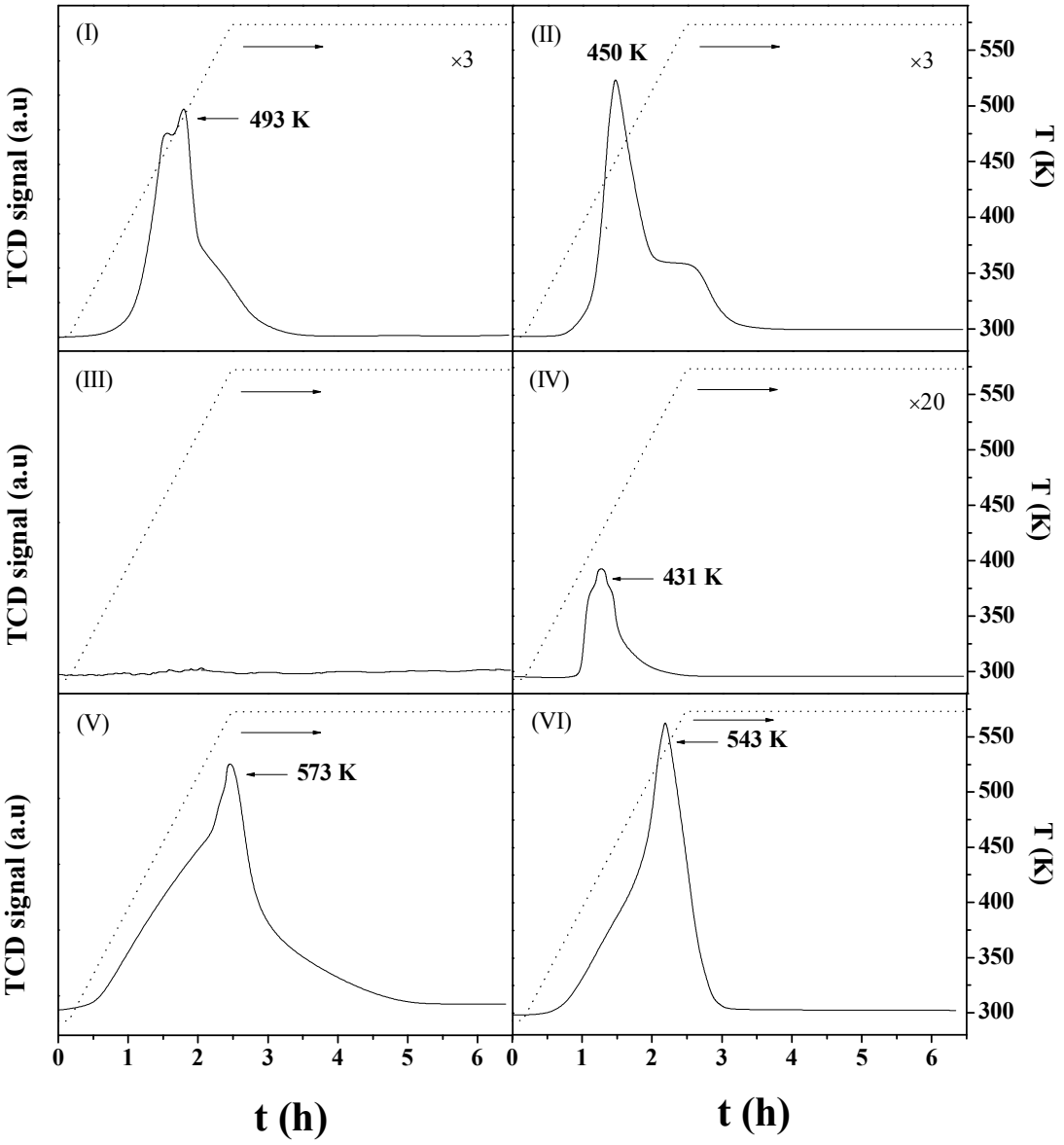

Figure 4.4: TPR profiles for Mo_2C (I), Au/Mo_2C (II), Al_2O_3 (III), Au/Al_2O_3 (IV), Mo_2C/Al_2O_3 (V) and Au/Mo_2C/Al_2O_3 (VI).

TEM-EDX analysis revealed a degree of heterogeneity associated with Au/Mo_2C and an apparent bimodal distribution of large (*ca.* 20 nm, **Figure 4.5(A-1)**) and small (4-6 nm, **Figure 4.5(A-2)**) Au particles; a representative EDX spectrum is included with image (A-2). A Cl content > 300 ppm has been shown to induce the formation of large Au particles (> 20 nm) [4.51] and poison catalyst activity [4.52]. However, in this study, the Cl content of all the catalysts was below detection limits (< 200 ppm), *i.e.* sample washing (see Experimental section) was effective in removing residual Cl. The mean Au diameter obtained from TEM analysis (13.4 nm, see **Table**

4.1) is in good agreement with the value (16 nm) from XRD peak line broadening analysis, *i.e.* application of eqn. (4.3). EDX surface mapping revealed areas of the Mo_2C support with a low (Au/Mo = 0.0012 in **Figure 4.5(A-1)**) or undetectable Au content. The formation of larger gold particles has also been observed for Au on oxide carriers characterized by low pH_{PZC}, notably SiO_2, which delivered poor Au dispersion after deposition-precipitation with urea [4.40], as a direct consequence of weaker interaction with the support.

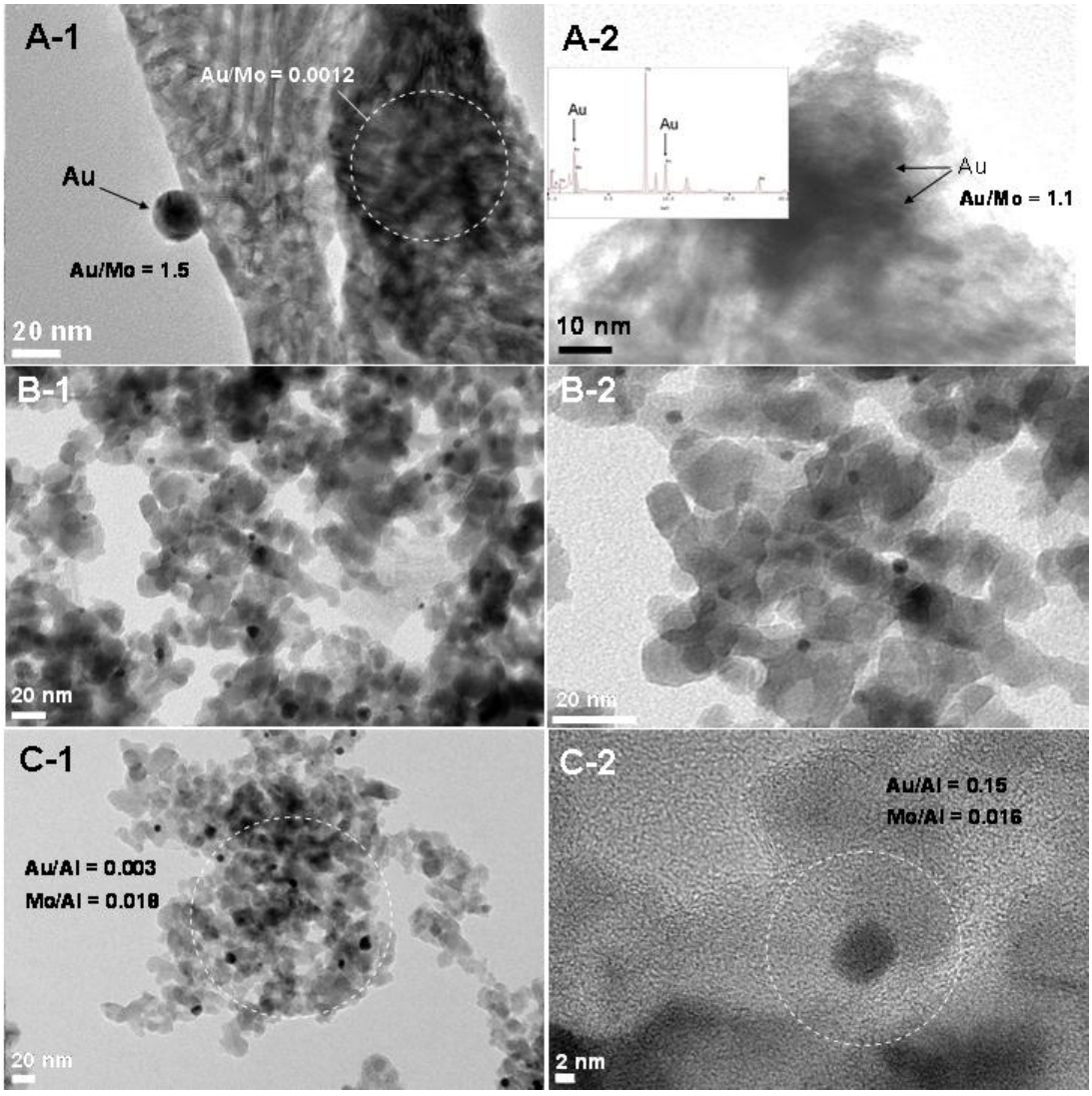

Figure 4.5: Representative TEM images with EDX measurements over selected areas for Au/Mo_2C (A, with representative EDX spectrum in A-2), Au/Al_2O_3 (B) and Au/Mo_2C/Al_2O_3 (C).

The TPR profile of δ-Al_2O_3 is featureless with no evidence of H_2 uptake (**Figure 4.4(III)**), which was expected and is in agreement with the literature [4.53]. The TPR response exhibited by as prepared Au/Al_2O_3 is presented in **Figure 4.4(IV)** and shows a single peak at 431 K. Hydrogen consumption during TPR matched that required for the reduction of the precursor to the metallic form, *i.e.* $Au^{3+} \rightarrow Au^0$. An equivalent response in terms of Au reduction has been reported elsewhere with T_{max} at 434 K [4.35] and 436 K [4.54]. The BET surface area of Au/Al_2O_3 (91 m^2 g^{-1}, **Table 4.1**) was lower than that of the starting Al_2O_3 support (101 m^2 g^{-1}), which can be attributed to a partial pore filling by the metal component [4.55]. The XRD profiles for δ-Al_2O_3 (**Figure 4.3(III)**) and Au/Al_2O_3 (**Figure 4.3(IV)**) exhibit the seven main characteristic XRD peaks for δ-Al_2O_3. There was no observable XRD response due to Au, indicative of the formation of a well dispersed metallic phase. Indeed, Au particles with an average size of 2.3 nm were detected by TEM (**Table 4.1**), which is consistent with stronger metal/support interactions that limit particle agglomeration. This response finds agreement with previous reports of Au/Al_2O_3 prepared by deposition-precipitation with urea [4.40]. Representative low (B-1) and higher (B-2) magnification TEM images are presented in **Figure 4.5**, where well dispersed pseudo-spherical particles (in the 1-3 nm range) are in evidence.

With regard to $Au/Mo_2C/Al_2O_3$, the Mo_2C loading was decreased by over a factor of 2 after Au deposition on the parent Mo_2C/Al_2O_3 (see **Table 4.1**). This loss of supported Mo_2C into solution can be attributed to a leaching of surface oxidised Mo, formed during the passivation step, into solution as H_2MoO_4 [4.56]. There were no detectable peaks due to Mo_2C in the XRD of Mo_2C/Al_2O_3 (**Figure 4.3(V)**), which can be attributed to strong interaction between MoO_3 and Al_2O_3, resulting in finely dispersed Mo_2C [4.57]. Moreover, the four principal Mo_2C XRD peaks (at 2θ = 34.4°, 37.9°, 39.4° and 61.6° associated with the (010), (002), (011) and (110) planes) overlap with the characteristic peaks (at 2θ = 34.5°, 36.5°, 39.5° and 61.1°) for δ-Al_2O_3. It should be noted that the formation of Mo_2C supported on γ-Al_2O_3 has been reported previously using the same approach, *i.e.* impregnation with $(NH_4)_6Mo_7O_{24}{\cdot}4H_2O$ and subsequent temperature programmed carburisation [4.3,4.58]. Carbon contents were measured and the resultant Mo/C ratios (< 2, see **Table 4.1**) suggest full carburisation of all the samples, where the occurrence of excess C can be due to the presence of free surface carbon [4.42].

The temperature requirement for surface reduction, *i.e.* to remove the passivated layer, was significantly higher (by 80 K) for the alumina supported Mo_2C (**Figure 4.4(V)**) relative to bulk Mo_2C (**Figure 4.4(I)**). This has been noted elsewhere and attributed to interaction between the carbide and the alumina carrier [4.20,4.56]. Hydrogen consumption (per gram Mo_2C) during TPR was appreciably greater for Mo_2C/Al_2O_3 (5.2 mmol $g_{Mo_2C}^{-1}$, **Table 4.1**) relative to Mo_2C (1.6 mmol $g_{Mo_2C}^{-1}$), suggesting a dispersion effect. Indeed, the specific carbide surface area (SA_{TPR}) showed a significant increase on the alumina support, which was unaffected by the incorporation of Au. An invariance in surface area after Au deposition is consistent with the BET measurements (**Table 4.1**). As in the case of Au/Mo_2C, the presence of Au on Mo_2C/Al_2O_3 resulted in a shift in the TPR profile to a lower temperature (see **Figure 4.4(VI)**). The XRD pattern (**Figure 4.3(VI)**) for $Au/Mo_2C/Al_2O_3$ shows three peaks at 38.1°, 64.5° and 77.5°, that are characteristic of Au metal.

TEM-EDX has demonstrated the presence of Au particles in the 6-12 nm size range with a mean particle size of 8.3 nm (**Table 4.1**), which is in good agreement with the Au particle size based on XRD line broadening (9 nm). A representative low magnification TEM image is presented in **Figure 4.5(C-1)** where EDX analysis of a large sample area (see dotted line circle) reveals the presence of both Au and Mo with Au/Mo ratio (0.16) close to the nominal value (0.1) in terms of bulk content. Further EDX mapping (not shown) of areas with Mo/Al in the range = 0.015-0.019) showed no detectable Au.

XPS spectra over the Mo 3*d*, C 1*s* and Au 4*f* binding energy (BE) regions are presented in **Figures 4.6** and **4.7**. The Mo 3*d* profiles for Mo_2C (**Figure 4.6(I)**) and Au/Mo_2C (**Figure 4.6(II)**) are very similar and present, after deconvolution, a principal Mo $3d_{5/2}$ contribution at BE = 228.3 ± 0.2 eV, corresponding to carbidic Mo [4.24]. Signals at higher BE (and lower intensity) can be related to the presence of Mo in an oxidised state due to passivation *i.e.* Mo(IV) (229.2 ± 0.2 eV) [4.7], Mo(V) (231.2 ± 0.2 eV) [4.59] and Mo(VI) (232.5 ± 0.2 eV) [4.60]. The presence of higher oxidation state Mo species is also consistent with our proposed Mo promoted oxido-reduction of the anionic Au precursor during deposition-precipitation. The Mo 3*d* profile for Mo_2C/Al_2O_3 (**Figure 4.6(III)**) coincides with that recorded for $Au/Mo_2C/Al_2O_3$ (**Figure 4.6(IV)**), where a carbidic Mo contribution is visible although the molybdenum phase is predominantly in the form of Mo oxides, *i.e.* Mo(IV), Mo(V) and Mo(VI), respectively,

at BE = 229.4, 231.3 and 232.7 eV. Comparison with the spectrum generated for the calcined supported precursor (MoO_3/Al_2O_3, **Figure 4.6(V)**) demonstrates that the carburisation procedure led to the formation of low oxidation state molybdenum species, *i.e.* carbidic Mo, Mo(IV) and Mo(V). Moreover, the presence of Mo_2C can be attested by the deconvoluted C 1*s* spectra shown in **Figure 4.7(I)-(IV)**, where a contribution due to carbidic carbon, at BE = 283.4 eV [4.61], is observed for all the catalysts. In addition, contributions assigned to graphitic carbon (BE = 284.6 eV) [4.62], C-O (BE = 286.3 eV) [4.7] and C=O (BE = 288.6 eV) [4.22] are also evident. XPS analysis of Mo_2C supported on zeolites [4.21] and Al_2O_3 [4.19,4.22] has generated similar spectra. Our XPS results reveal carbidic character for the alumina supported Mo_2C, *pre*- and *post*-Au incorporation that may be more consistent with a supported oxycarbide phase. Indeed, we should flag an IR-study by Wu *et al.* [4.63] that established the presence of $Mo^{\delta+}$ ($0 < \delta < 2$) in as prepared Mo_2C/Al_2O_3 where subsequent passivation resulted in superficial oxycarbide formation ($2 \leq \delta < 4$) with carbide regeneration by reduction in H_2.

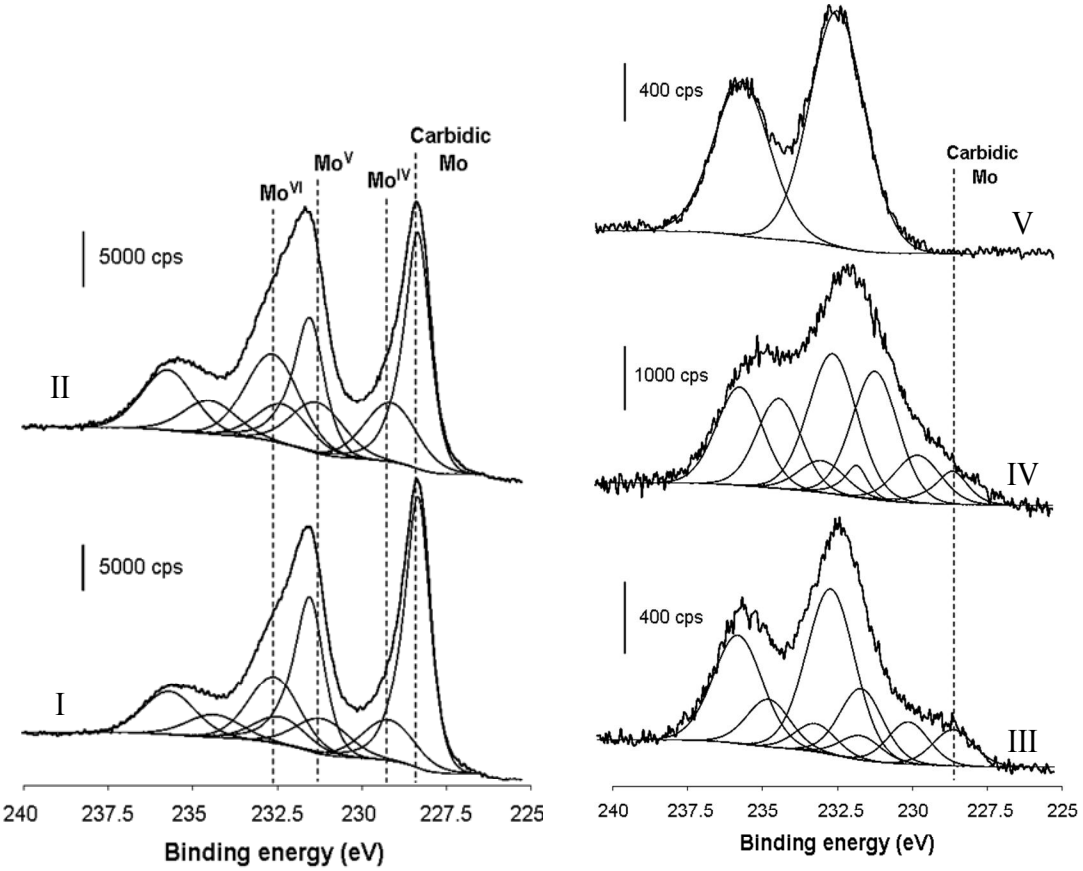

Figure 4.6: XPS spectra over the Mo 3*d* region for Mo_2C (I), Au/Mo_2C (II), Mo_2C/Al_2O_3 (III), $Au/Mo_2C/Al_2O_3$ (IV) and MoO_3/Al_2O_3 (V).

The Au $4f_{7/2}$ (BE = 84.0 ± 0.2 eV) and Au $4f_{5/2}$ (BE = 87.6 ± 0.2 eV) peaks for Au/Mo_2C (**Figure 4.7(V)**) are characteristic of Au in the metallic state [4.64]. The Au $4f_{7/2}$ peaks for Au/Al_2O_3 (**Figure 4.7(VII)**) and $Au/Mo_2C/Al_2O_3$ (**Figure 4.7(VI)**) are both centered at 83.5 ± 0.2 eV. Similar values have been reported in the literature for Au/Al_2O_3 [4.65] and attributed to electron transfer from the support. The equivalence of the Au BE values in this study suggests that there is no detectable specific interaction between Au and Mo in $Au/Mo_2C/Al_2O_3$.

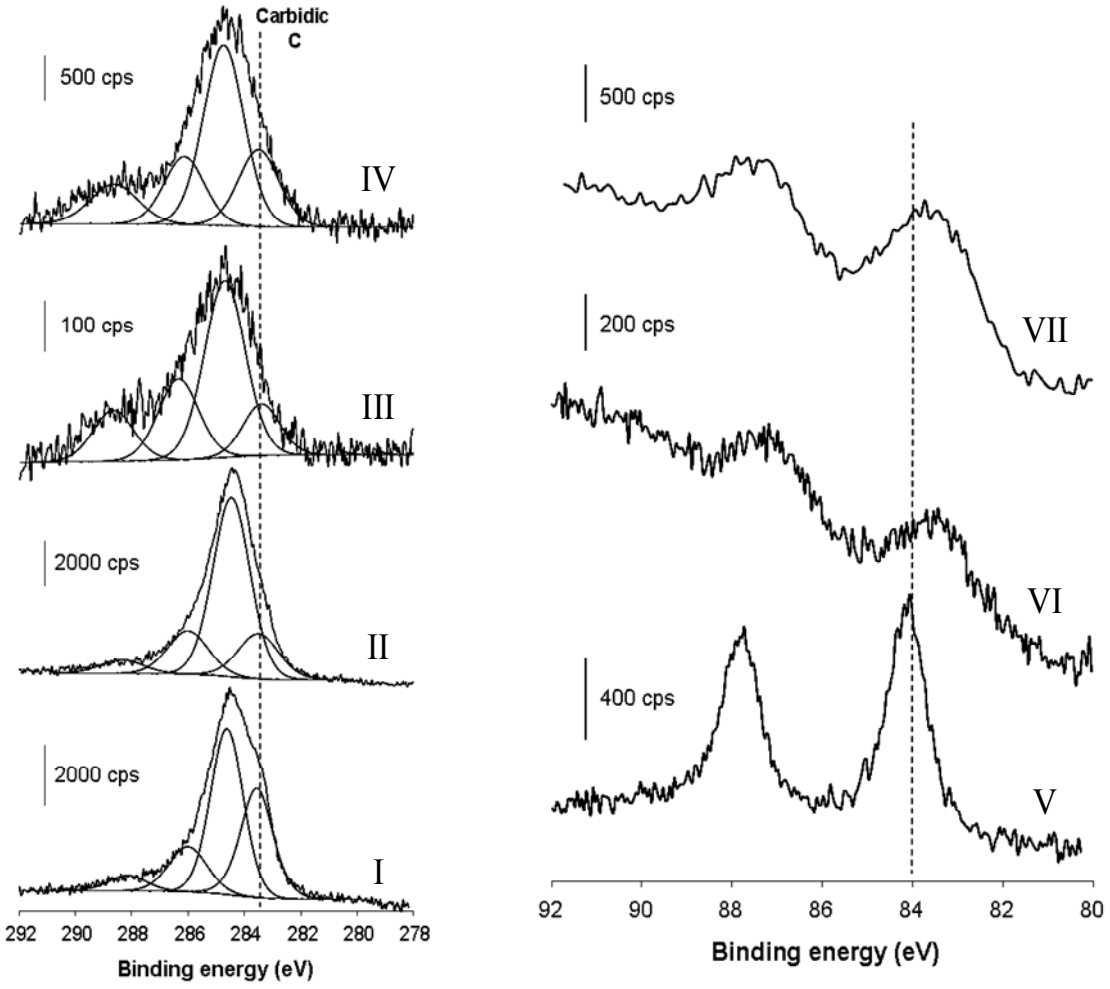

Figure 4.7: XPS spectra over the C 1*s* region for Mo_2C (I), Au/Mo_2C (II), Mo_2C/Al_2O_3 (III), $Au/Mo_2C/Al_2O_3$ (IV) and Au 4*f* region for Au/Mo_2C (V), $Au/Mo_2C/Al_2O_3$ (VI) and Au/Al_2O_3 (VII).

4.3.2 Catalytic Activity/Selectivity

Reaction selectivity is critical in para-chloronitrobenzene (*p*-CNB) and meta-dinitrobenzene (*m*-DNB) hydrogenation where a number of intermediates and by-products are possible, as identified in **Figure 4.8**.

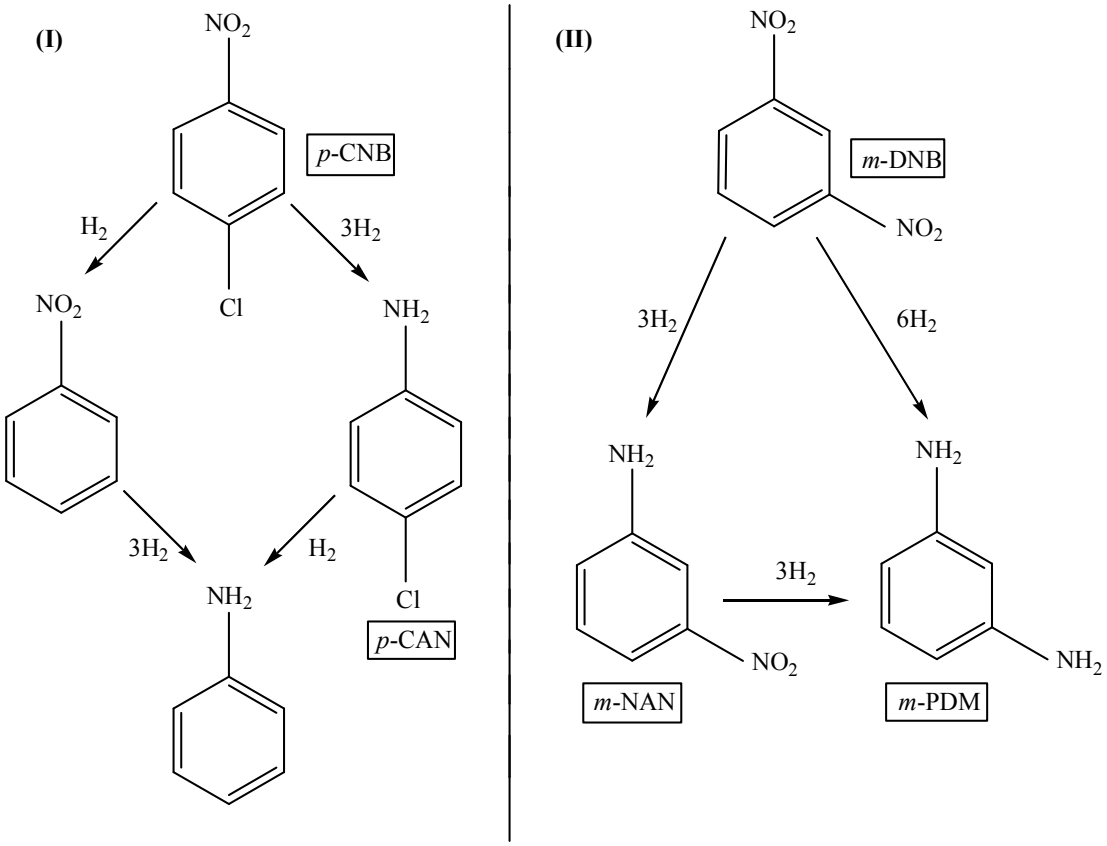

Figure 4.8: Reaction pathways in the hydrogenation of *p*-CNB (I) and *m*-DNB (II).

Previous studies in this laboratory have shown that the gas phase hydrogenation of *p*-CNB over Pd/Al_2O_3 generated nitrobenzene (hydrodechlorination) and aniline (hydrodechlorination/hydrogenation) as products [4.34] whereas supported Au exclusively produced *p*-chloroaniline (*p*-CAN) [4.32,4.34,4.35]. The hydrogenation of *m*-DNB (**Figure 4.8(II)**) involves even greater selectivity demands in terms of partial $-NO_2$ hydrogenation. We have chosen *m*-DNB as a model reactant because the partially hydrogenated *m*-nitroaniline (*m*-NAN) product is commercially important in the manufacture of polymers and dyes [4.37]. Earlier work has established that complete reduction to *m*-phenylenediamine (*m*-PDM) is achieved over supported Ni while the *m*-DNB → *m*-NAN step is selectively promoted over supported Au at low levels of

conversion [4.36]. The existing literature on the hydrogenation of nitroarenes has focused on batch liquid systems operated at elevated pressures [4.66] that have delivered low selectivities to the target amine [4.67]. A move from batch liquid to gas phase continuous operation serves to lower the associated energy demands while economies of scale favour continuous processes for large throughput. This is the first reported application of Mo carbide (as both catalyst and Au support) in gas phase nitroarene hydrogenation.

4.3.2.1 Hydrogenation of p-chloronitrobenzene (p-CNB)

The temporal response of *p*-CNB conversion ($X_{p\text{-CNB}}$) over the five catalyst systems is shown in **Figure 4.9(I)**, where a decline in activity with time on-stream is in evidence. The temporal variation of conversion has been fitted to a first order exponential decay in order to extract a value for the initial conversion (X_0). The applicability of a pseudo-first order kinetic treatment has been established previously [4.68]

$$\ln(1 - X_0)^{-1} = k\left(\frac{n}{F}\right) \tag{4.7}$$

where n represents either moles of Mo_2C (n_{Mo_2C}) or gold (n_{Au}) and the ratio n/F has the physical significance of contact time. The specific rates obtained from the linear relationships shown **Figure 4.9(II)** are given in **Table 4.2**. All the catalysts were 100 % selective in terms of *p*-CNB hydrogenation to the target *p*-CAN product with no evidence of hydrodechlorination or ring hydrogenation.

The rate constant, normalised with respect to Mo_2C surface area (k ($\mu mol_{p\text{-CNB}}$ $m_{Mo_2C}^{-2}$ h^{-1}), **Table 4.2**) generated for Mo_2C/Al_2O_3 was significantly lower than that recorded for Mo_2C, *i.e.* supporting the carbide on the alumina carrier inhibited hydrogenation. We can link this to the observed (by XPS, see **Figure 4.6(III)**) lesser carbidic (or rather oxycarbide) character for the alumina supported system. Moreover, the presence of free carbon (Mo/C = 1.5, **Table 4.1**) on the surface can block Mo active sites and limit activity [4.42]. It has been reported elsewhere [4.69] that strong interaction between the carbide phase and Al_2O_3 support can render the carbide sites less active in the catalytic decomposition of hydrazine. However, Brungs and co-workers [4.70], have shown that Mo_2C/Al_2O_3 was more stable in methane reforming

than bulk Mo_2C where coke deposition was limited on the supported carbide. Indeed, reaction over Mo_2C/Al_2O_3 was characterised by a significantly higher ratio of the conversion achieved after 3 h to the initial value (X_{3h}/X_0) relative to Mo_2C (**Table 4.2**). Loss of activity in gas phase hydrogenation of *p*-CNB has been attributed to metal leaching [4.71], metal sintering [4.72], deposition of polymeric products formed by condensation [4.73], occlusion of active sites by surface carbonate species [4.74] and poisoning by the water generated during reaction [4.75].

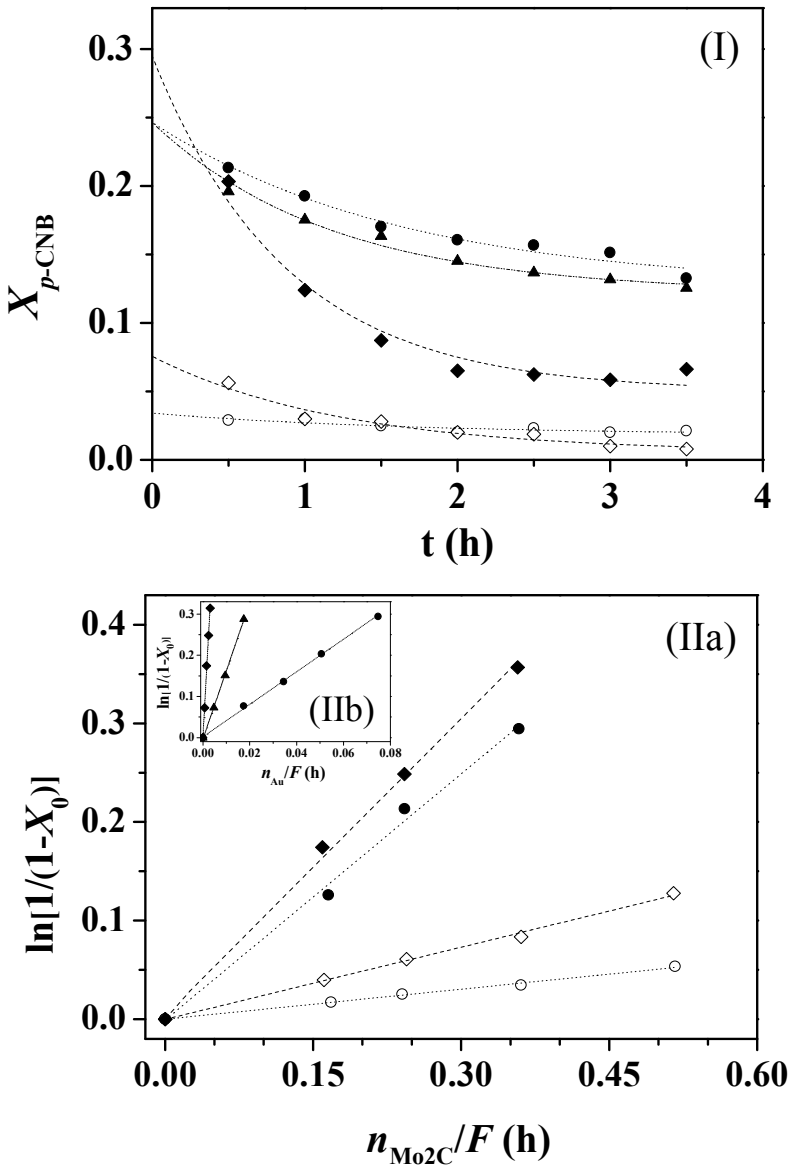

Figure 4.9: (I) Variation of *p*-CNB fractional conversion ($X_{p\text{-CNB}}$) with time on-stream. (II) pseudo-first order kinetic plots with respect to (a) Mo_2C and (b) Au: (◇) Mo_2C, (◆) Au/Mo_2C, (▲) Au/Al_2O_3, (○) Mo_2C/Al_2O_3 and (●) $Au/Mo_2C/Al_2O_3$.

The introduction of Au (on both Mo_2C and Mo_2C/Al_2O_3) resulted in an appreciable increase in hydrogenation rate, which can be attributed to the catalytic action of both carbide and the supported Au phase. Gold dispersion (**Table 4.1**) was obtained from *d* values [4.76] and used to determine turnover frequency (*TOF* (h^{-1}), **Table 4.2**). We apply *TOF* as a quantitative measure of catalyst performance in terms of the Au component but recognise the contribution of both support (Mo_2C) and metal to the overall hydrogenation rate. Activity in hydrogenation reactions over supported Au has been deemed to be dependent on Au particle size [4.77]. Previous work conducted in this laboratory [4.32] demonstrated an increase (forty-fold) in *p*-CNB hydrogenation rate over oxide supported Au with decreasing particle size (from 9 to 3 nm). As Au/Mo_2C is characterised by a larger mean Au size compared with Au/Al_2O_3, we should expect a lower resultant specific activity. A major finding in this Chapter is the appreciably higher *TOF* delivered by Au/Mo_2C relative to Au/Al_2O_3. This is taken as a demonstration of a surface synergism between Au and Mo_2C that results in enhanced catalytic efficiency. Given that the activation of H_2 is rate limiting in hydrogenation reactions over Au, H_2 dissociation on Mo_2C must contribute to the observed elevation of hydrogenation rate, possibly by supplying reactive atomic hydrogen to Au in a "reverse" spillover step.

Table 4.2: Specific rate constant (*k*, with respect to Mo_2C surface area), turnover frequency (*TOF*, with respect to Au dispersion) and ratio of fractional conversion after 3 h to the initial value (X_{3h}/X_0) for the hydrogenation of *p*-CNB.

Catalyst	k ($\mu mol_{p\text{-CNB}}\ m_{Mo_2C}^{-2}\ h^{-1}$)	*TOF* (h^{-1})	X_{3h}/X_0 $X_0 \approx 0.15$
Mo_2C	36	-	0.12
Mo_2C/Al_2O_3	4	-	0.70
Au/Mo_2C	139	1098	0.12
$Au/Mo_2C/Al_2O_3$	33	27	0.60
Au/Al_2O_3	-	26	0.50

4.3.2.2 Hydrogenation of m-dinitrobenzene (m-DNB)

The hydrogenation of *m*-DNB also exhibited a time on-stream decline that was more severe than observed for *p*-CNB, as can be assessed from the X_{3h}/X_0 entries in **Table 4.3**. Alumina supported Mo_2C delivered a comparable specific hydrogenation rate relative to the bulk carbide and retained a higher degree of the initial conversion with time on-stream. Incorporation of Au enhanced hydrogenation performance with an increase in rate (per Mo_2C surface area) by a factor of 3-4. As in the case of *p*-CNB hydrogenation, the *TOF* generated by Au/Mo_2C was significantly greater than that recorded for Au/Al_2O_3. The hydrogenation of *m*-DNB presents a particular challenge in terms of selectivity where *m*-NAN, as the target product, can serve as a reactive intermediate in the formation of *m*-PDM (**Figure 4.8(II)**). Any meaningful comparison of hydrogenation selectivity is only feasible at a common fractional *m*-DNB conversion ($X_{m\text{-DNB}}$): selectivity values are given in **Table 4.3** where $X_{m\text{-DNB}} \approx 0.05$ and 0.15. The variation of *m*-NAN and *m*-PDM selectivity (S) as a function of $X_{m\text{-DNB}}$ is presented **Figure 4.10** for reaction over Au/Mo_2C and Au/Al_2O_3. At low fractional conversions ($X_{m\text{-DNB}} < 0.06$), Mo_2C exhibited 100 % selectivity to *m*-NAN, with decreasing selectivity at higher conversions; *m*-PDM was the principal product where $X_{m\text{-DNB}} > 0.15$. Au/Mo_2C also exhibited reaction exclusivity in terms of *m*-NAN production at low $X_{m\text{-DNB}}$ (**Figure 4.10**, $X_{m\text{-DNB}} < 0.07$) with a switch to preferential *m*-PDM formation at higher conversions ($X_{m\text{-DNB}} > 0.20$); see also entries in **Table 4.3**. The net effect is a significantly higher rate of *m*-NAN production over Au/Mo_2C (0.18 $g_{m\text{-NAN}}\ g_{catalyst}^{-1}\ h^{-1}$, where $X_{m\text{-DNB}} < 0.20$) compared with Mo_2C (0.05 $g_{m\text{-NAN}}\ g_{catalyst}^{-1}\ h^{-1}$, where $X_{m\text{-DNB}} < 0.12$). In complete contrast, Au/Al_2O_3 (**Figure 4.10**) generated *m*-PDM as the principal product (S > 80%), regardless of $X_{m\text{-DNB}}$.

The hydrogenation of nitroarenes has been proposed to proceed *via* a nucleophilic mechanism, where a weak nucleophilic agent (hydrogen) attacks the activated $-NO_2$ group(s) [4.78]. Differences in reaction selectivity can be associated with differences in the mode of reactant adsorption on the catalyst surface where *m*-NAN formation requires an intermediate resonance structure with a single delocalized positive charge on the ring, *i.e.* only one $-NO_2$ group is activated for nucleophilic attack. *m*-PDM results from the formation of a resonance structure with two positive localized charges on the ring where both $-NO_2$ groups are activated.

Table 4.3: Specific rate constant (*k*, with respect to Mo_2C surface area), turnover frequency (*TOF*, with respect to Au dispersion) selectivity to *m*-NAN ($S_{m\text{-NAN}}$ at $X_{m\text{-DNB}} \approx 0.05$ and $X_{m\text{-DNB}} \approx 0.15$) and ratio of fractional conversion after 3 h to the initial value (X_{3h}/X_0) for the hydrogenation of *m*-DNB.

Catalyst	k ($\times 10^6$) ($\mu mol_{m\text{-DNB}}\ m_{Mo_2C}^{-2}\ h^{-1}$)	TOF (h^{-1})	X_{3h}/X_0	$S_{m\text{-NAN}}$ (%) at $X_{m\text{-DNB}} \approx 0.05$	$S_{m\text{-NAN}}$ (%) at $X_{m\text{-DNB}} \approx 0.15$
Mo_2C	13	-	0.10	100	37
Mo_2C/Al_2O_3	15	-	0.15	100	45
Au/Mo_2C	38	229	0.10	100	56
$Au/Mo_2C/Al_2O_3$	60	50	0.30	85	38
Au/Al_2O_3	-	34	0.10	0[a]	21

[a]100 % selectivity with respect to *m*-PDM

Differences in *m*-DNB hydrogenation selectivity can be attributed to the electronic character of the Au sites where adsorption on $Au^{\delta-}$ results in repulsion between the π-delocalized electrons and the partially (negatively) charged gold resulting in the formation of a resonance structure with two positive localized charges on the ring and both $–NO_2$ groups are activated. The latter effect predominates in the case of Au/Al_2O_3 and is consistent with the XPS response that shows electron transfer from Al_2O_3 to Au.

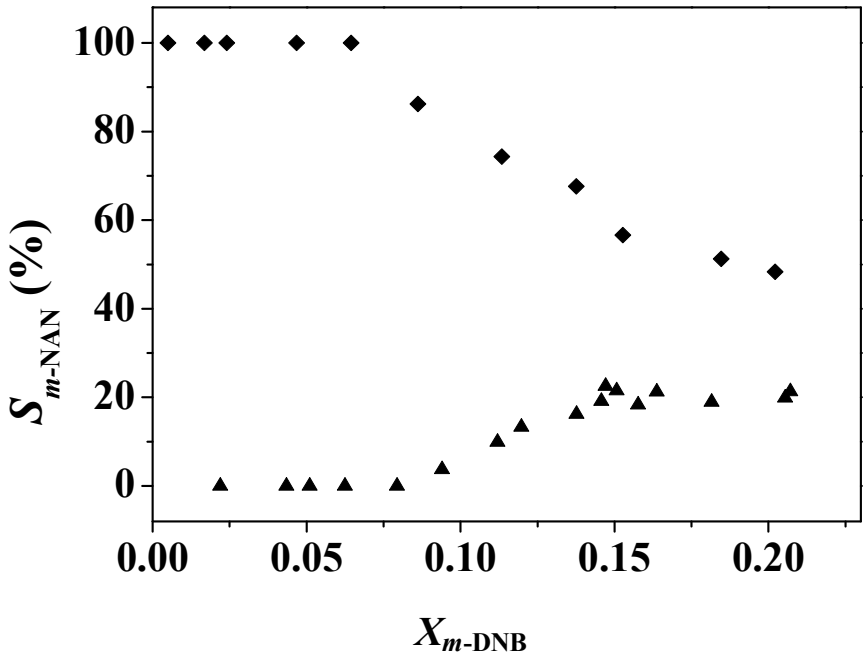

Fig. 4.10: Variation of *m*-NAN selectivity ($S_{m\text{-NAN}}$) as a function of *m*-DNB fractional conversion ($X_{m\text{-DNB}}$) for reaction over (◆) Au/Mo_2C and (▲) Au/Al_2O_3.

We can associate the selectivity of Au/Mo_2C towards *m*-NAN, in part, to interactions with Au sites that (based on XPS measurements) do not bear a partial negative charge and which favour the formation of a resonance form with a single delocalized positive charge on the ring where only one of the $–NO_2$ groups is activated [4.79]. We can not discount possible *m*-DNB activation *via* interactions with Mo_2C and/or at the Au/carbide interface which, from a consideration of the catalytic response, favour *m*-NAN formation. The results in this Chapter demonstrate that the use of Mo_2C as support serves to both enhance hydrogenation rate and influence selectivity.

4.4 Conclusion

The first synthesis of gold catalysts supported on molybdenum carbide (Mo_2C and Mo_2C/Al_2O_3) is reported in this Chapter; gold was deposited by deposition-precipitation of $HAuCl_4$ (as precursor) with urea. The (*β*-phase) Mo_2C support was prepared by a temperature programmed carburisation and confirmed by XRD analysis. Mo_2C was characterised by a lower pH_{PZC} (2.9) when compared with Mo_2C/Al_2O_3 (3.7) and Al_2O_3 (7.5). In the synthesis of Au/Mo_2C and $Au/Mo_2C/Al_2O_3$, solution pH exceeded support pH_{PZC} resulting in a less favourable interaction with the anionic Au precursor. The latter effect led to a poorer dispersion of Au relative to Au/Al_2O_3. The formation of metallic Au was observed during Au/Mo_2C preparation and can be attributed to the lower electrochemical potential of the passivated carbide support with a consequent reductive deposition of Au. Preparation of $Au/Mo_2C/Al_2O_3$ was accompanied by a significant Mo leaching into solution and the supported Mo_2C phase exhibited lesser carbidic character than bulk Mo_2C.

This Chapter is the first reported application of Au/Mo carbide combinations as catalytic materials. The results for the gas phase hydrogenation of substituted nitroarenes have established a synergism where the combined catalytic action of Au with Mo_2C resulted in higher hydrogenation efficiency for the conversion of *p*-CNB and *m*-DNB, exceeding the performance of Au/Al_2O_3. In the hydrogenation of *m*-DNB, exclusive formation of the partially reduced *m*-NAN was enhanced over Au/Mo_2C relative to Mo_2C under conditions where Au/Al_2O_3 was non-selective.

4.5 References

[4.1] A. M. Alexander and J. S. J. Hargreaves, *Alternative catalytic materials: carbides, nitrides, phosphides and amorphous boron alloys*, Chem. Soc. Rev. 39 (2010) 4388-4401.

[4.2] R. Kojima and K. Aika, *Molybdenum nitride and carbide catalysts for ammonia synthesis*, Appl. Catal. A: General 219 (2001) 141-147.

[4.3] P. A. Aegerter, W. W. C. Quigley, G. J. Simpson, D. D. Ziegler, J. W. Logan, K. R. McCrea, S. Glazier and M. E. Bussell, *Thiophene hydrodesulfurization over alumina-supported molybdenum carbide and nitride catalysts: Adsorption sites,*

catalytic activities, and nature of the active surface, J. Catal. 164 (1996) 109-121.

[4.4] A. Szymańska-Kolasa, M. Lewandowski, C. Sayag and G. Djéga-Mariadassou, *Comparison of molybdenum carbide and tungsten carbide for the hydrodesulfurization of dibenzothiophene*, Catal. Today 119 (2007) 7-12.

[4.5] P. M. Patterson, T. K. Das and B. H. Davis, *Carbon monoxide hydrogenation over molybdenum and tungsten carbides*, Appl. Catal. A: General 251 (2003) 449-455.

[4.6] N. M. Schweitzer, J. A. Schaidle, O. K. Ezekoye, X. Pan, S. Linic and L. T. Thompson, *High activity carbide supported catalysts for water gas shift*, J. Am. Chem. Soc. 133 (2011) 2378-2381.

[4.7] A. C. Lausche, J. A. Schaidle and L. T. Thompson, *Understanding the effects of sulfur on Mo_2C and Pt/Mo_2C catalysts: Methanol steam reforming*, Appl. Catal. A: General 401 (2011) 29-36.

[4.8] J. S. Lee, S. Locatelli, T. Oyama and M. Boudart, *Molybdenum carbide catalysts*, J. Catal. 125 (1990) 157-170.

[4.9] S. T. Oyama, *Preparation and catalytic properties of transition metal carbides and nitrides*, Catal. Today 15 (1992) 179-200.

[4.10] H. Liu, J. Zhu, Z. Lai, R. Zhao and D. He, *A first-principles study on structural and electronic properties of Mo_2C*, Scr. Mater. 60 (2009) 949-952.

[4.11] J. G. Chen, *Carbide and nitride overlayers on early transition metal surfaces: Preparation, characterization, and reactivities*, Chem. Rev. 96 (1996) 1477-1498.

[4.12] E. K. Storms, *The Refractory Carbides in Refractory Materials*, J. L. Margrave (Ed.), Academic Press, New York and London, 1967, pp.122-125.

[4.13] K. Y. Park, W. K. Seo and J. S. Lee, *Selective synthesis of light olefins from sungas over potassium-promoted molybdenum carbide catalysts*, Catal. Lett. 11 (1991) 349-356.

[4.14] J.-G. Choi, J. R. Brenner and L. T. Thompson, *Pyridine hydrodenitrogenation over molybdenum carbide catalysts*, J. Catal. 154 (1995) 33-40.

[4.15] L. Volpe and M. Boudart, *Compounds of molybdenum and tungsten with high specific surface-area. 1. Nitrides*, J. Solid State Chem. 59 (1985) 332-347.

[4.16] K. T. Jung, W. B. Kim, C. H. Rhee and J. S. Lee, *Effects of transition metal addition on the solid-state transformation of molybdenum trioxide to molybdenum carbides*, Chem. Mater. 16 (2004) 307-314.

[4.17] X.-H. Wang, H.-L. Hao, M.-H. Zhang, W. Li and K.-Y. Tao, *Synthesis and characterization of molybdenum carbides using propane as carbon source*, J. Solid State Chem. 179 (2006) 538-543.

[4.18] G. Ertl, H. Knözinger and J. Weitkamp, *Preparation of solid catalysts*, Wiley-VCH, Weinheim, 1999, pp. 147-149.

[4.19] D. J. Sajkowski and S. T. Oyama, *Catalytic hydrotreating by molybdenum carbide and nitride: unsupported Mo_2N and Mo_2C/Al_2O_3*, Appl. Catal. A: General 134 (1996) 339-349.

[4.20] J. S. Lee, M. H. Yeom, K. Y. Park, I.-S. Nam, J. S. Chung, Y. G. Kim and S. H. Moon, *Preparation and benzene hydrogenation activity of supported molybdenum carbide catalysts*, J. Catal. 128 (1991) 126-136.

[4.21] S. J. Ardakani, X. Liu and K. J. Smith, *Hydrogenation and ring opening of naphthalene on bulk and supported Mo_2C catalysts*, Appl. Catal. A: General 324 (2007) 9-19.

[4.22] Q. L. Zhu, B. Zhang, J. Yang, J. X. Wang, J. Zhao, S. F. Ji and H. Q. Wang, *The promotion of nickel to Mo_2C/Al_2O_3 catalyst for the partial oxidation of methane to syngas*, New J. Chem. 27 (2003) 1633-1638.

[4.23] M. Lewandowski, A. Szymańska-Kolasa, P. Da Costa and C. Sayag, *Catalytic performances of platinum doped molybdenum carbide for simultaneous hydrodenitrogenation and hydrodesulfurization*, Catal. Today 119 (2007) 31-34.

[4.24] Espinoza-Monjardín, J. Cruz-Reyes, M. Del Valle-Granados, E. Flores-Aquino, M. Avalos-Borja and S. Fuentes-Moyado, *Synthesis, characterization and catalytic activity in the hydrogenation of cyclohexene with molybdenum carbide*, Catal. Lett. 120 (2008) 137-142.

[4.25] M.-L. Frauwallner, F. López-Linares, J. Lara-Romero, C. E. Scott, V. Ali, E. Hernández and P. Pereira-Almao, *Toluene hydrogenation at low temperature using a molybdenum carbide catalyst*, Appl. Catal. A: General 394 (2011) 62-70.

[4.26] B. Hammer and J. K. Norskov, *Why Gold Is the Noblest of All the Metals*, Nature 376 (1995) 238-240.

[4.27] A. Corma and P. Serna, *Chemoselective hydrogenation of nitro compounds with supported gold catalysts*, Science 313 (2006) 332-332.

[4.28] C. Milone, R. Ingoglia, A. Pistone, G. Neri, F. Frusteri and S. Galvagno, *Selective hydrogenation of α, β-unsaturated ketones to α, β-unsaturated alcohols on gold-supported catalysts*, J. Catal. 222 (2004) 348-356.

[4.29] J. E. Bailie and G. J. Hutchings, *Promotion by sulfur of gold catalysts for crotyl alcohol formation from crotonaldehyde hydrogenation*, Chem. Commun. (1999) 2151-2152.

[4.30] A. Hugon, L. Delannoy and C. Louis, *Supported gold catalysts for selective hydrogenation of 1,3-butadiene in the presence of an excess of alkenes*, Gold Bull. 41 (2008) 127-139.

[4.31] S. A. Nikolaev and V.V. Smirnov, *Selective hydrogenation of phenylacetylene on gold nanoparticles*, Gold Bull. 42 (2009) 182-189.

[4.32] F. Cárdenas-Lizana, S. Gómez-Quero, N. Perret and M. A. Keane, *Support effects in the selective gas phase hydrogenation of p-chloronitrobenzene over gold*, Gold Bull. 42 (2009) 124-132.

[4.33] E. Florez, F. Viñes, J. A. Rodriguez and F. Illas, *Adsorption and diffusion of Au atoms on the (001) surface of Ti, Zr, Hf, V, Nb, Ta, and Mo carbides*, J. Chem. Phys. 130 (2009) 244706.

[4.34] F. Cárdenas-Lizana, S. Gómez-Quero and M. A. Keane, *Ultra-selective gas phase catalytic hydrogenation of aromatic nitro compounds over Au/Al_2O_3*, Catal. Commun. 9 (2008) 475-481.

[4.35] F. Cárdenas-Lizana, S. Gómez-Quero and M. A. Keane, *Exclusive production of chloroaniline from chloronitrobenzene over Au/TiO_2 and Au/Al_2O_3*, ChemSusChem 1 (2008) 215-221.

[4.36] F. Cárdenas-Lizana, S. Gómez-Quero, N. Perret and M. A. Keane, *Gold catalysis at the gas–solid interface: role of the support in determining activity and selectivity in the hydrogenation of m-dinitrobenzene*, Catal. Sci. Tech. 1 (2011) 652-661

[4.37] V. L. Khilnani and S. B. Chandalia, *Selective hydrogenation. II. m-dinitrobenzene to m-nitroaniline using palladium on carbon as catalyst*, Org. Proc. Res. Dev. 5 (2001) 263-266.

[4.38] J. Xiong, J. X. Chen and J. Y. Zhang, *Liquid-phase hydrogenation of o-chloronitrobenzene over supported nickel catalysts*, Catal. Commun. 8 (2007) 345-350.

[4.39] Y. S. Kwon, A. A. Gromov, A. P. Ilyin, A. A. Ditts, J. S. Kim, S. H. Park and M. H. Hong, *Features of passivation, oxidation and combustion of tungsten nanopowders by air*, Int. J. Refract. Met. Hard Mater 22 (2004) 235-241.

[4.40] A. Hugon, N. El Kolli and C. Louis, *Advances in the preparation of supported gold catalysts: Mechanism of deposition, simplification of the procedures and relevance of the elimination of chlorine*, J. Catal. 274 (2010) 239-250.

[4.41] J. Vakros, C. Kordulis and A. Lycourghiotis, *Potentiometric mass titrations: a quick scan for determining the point of zero charge*, Chem. Commun. 17 (2002) 1980-1981.

[4.42] J. S. Choi, G. Bugli and G. Djéga-Mariadassou, *Influence of the degree of carburization on the density of sites and hydrogenating activity of molybdenum carbides*, J. Catal. 193 (2000) 238-247.

[4.43] M.A. Keane, *Gas phase hydrogenation/hydrogenolysis of benzaldehyde and o-tolualdehyde over Ni/SiO_2*, J. Mol. Catal. A: Chemical 118 (1997) 261-269.

[4.44] F. Moreau and G. C. Bond, *Influence of the surface area of the support on the activity of gold catalysts for CO oxidation*, Catal. Today 122 (2007) 215-221.

[4.45] R. Zanella and C. Louis, *Influence of the conditions of thermal treatments and of storage on the size of the gold particles in Au/TiO_2 samples*, Catal. Today 107 (2005) 768-777.

[4.46] S. Gomez-Quero, F. Cardenas-Lizana and M. A. Keane, *Effect of metal dispersion on the liquid-phase hydrodechlorination of 2,4-dichlorophenol over Pd/Al_2O_3*, Ind. Eng. Chem. Res. 47 (2008) 6841-6853.

[4.47] F. Moreau, G. C. Bond and A. O. Taylor, *Gold on titania catalysts for the oxidation of carbon monoxide: control of pH during preparation with various gold contents*, J. Catal. 231 (2005) 105-114.

[4.48] B. A. A. Silberova, G. Mul, M. Makkee and J. A. Moulijn, *DRIFTS study of the water-gas shift reaction over Au/Fe_2O_3*, J. Catal. 243 (2006) 171-182.

[4.49] N. A. Hodge, C. J. Kiely, R. Whyman, M. R. H. Siddiqui, G. J. Hutchings, Q. A. Pankhurst, F. E. Wagner, R. R. Rajaram and S. E. Golunski, *Microstructural comparison of calcined and uncalcined gold/iron-oxide catalysts for low-temperature CO oxidation*, Catal. Today 72 (2002) 133-144.

[4.50] N. N. Greenwood and A. Earnshaw, *Chemistry of the Elements*, 2nd edn Butterworth-Heinemann, Oxford, 1997.

[4.51] I. Dobrosz, K. Jiratova, V. Pitchon and J. M. Rynkowski, *Effect of the preparation of supported gold particles on the catalytic activity in CO oxidation reaction*, J. Mol. Catal. A: Chemical 234 (2005) 187-197.

[4.52] H. S. Oh, J. H. Yang, C. K. Costello, Y. M. Wang, S. R. Bare, H. H. Kung and M. C. Kung, *Selective catalytic oxidation of CO: Effect of chloride on supported Au catalysts*, J. Catal. 210 (2002) 375-386.

[4.53] M. Trueba and S. P. Trasatti, *Gamma-alumina as a support for catalysts: A review of fundamental aspects*, Eur. J. Inorg. Chem. 17 (2005) 3393-3403.

[4.54] A.C. Gluhoi, X. Tang, P. Marginean and B.E. Nieuwenhuys, *Characterization and catalytic activity of unpromoted and alkali (earth)-promoted Au/Al_2O_3 catalysts for low-temperature CO oxidation*, Top. Catal. 39 (2006) 101-110.

[4.55] A. Saadi, Z. Rassoul and M.M. Bettahar, *Gas phase hydrogenation of benzaldehyde over supported copper catalysts*, J. Mol. Catal. A: Chemical 164 (2000) 205-216.

[4.56] J. R. Regalbuto and J.-W. Ha, *A corrected procedure and consistent interpretation for temperature programmed reduction of supported MoO_3* Catal. Lett. 29 (1994) 189-207.

[4.57] A. R. S. Darujati and W. J. Thomson, *Stability of supported and promoted-molybdenum carbide catalysts in dry-methane reforming*, Appl. Catal. A: General 296 (2005) 139-147.

[4.58] B. Diaz, S. J. Sawhill, D. H. Bale, R. Main, D. C. Phillips, S. Korlann, R. Self and M. E. Bussell, *Hydrodesulfurization over supported monometallic, bimetallic and promoted carbide and nitride catalysts*, Catal. Today 86 (2003) 191-209.

[4.59] M. Shimoda, T. Hirata, K. Yagisawa, M. Okochi and A. Yoshikawa, *Deconvolution of Mo 3d X-ray photoemission spectra gamma-Mo_4O_{11}-agreement with prediction from bond length bond strength relationships*, J. Mater. Sci. Lett. 8 (1989) 1089-1091.

[4.60] Z. B. Z. Wei, P. Grange and B. Delmon, *XPS and XRD studies of fresh and sulfided Mo_2N*, Appl. Surf. Sci. 135 (1998) 107-114.

[4.61] T. P. St Clair, S. T. Oyama, D. F. Cox, S. Otani, Y. Ishizawa, R. L. Lo, K. Fukui and Y. Iwasawa, *Surface characterization of alpha-Mo_2C (0001)*, Surf. Sci. 426 (1999) 187-198.

[4.62] S. D. Gardner, C. S. K. Singamsetty, G. L. Booth, G. R. He and C. U. Pittman, *Surface characterization of carbon-fibers using angle-resolved XPS and ISS*, Carbon 33 (1995) 587-595.

[4.63] W. C. Wu, Z. L. Wu, C. H. Liang, P. L. Ying, Z. C. Feng and C. Li, *An IR study on the surface passivation of Mo_2C/Al_2O_3 catalyst with O_2, H_2O and CO_2*, Phys. Chem. Chem. Phys. 6 (2004) 5603-5608.

[4.64] A. V. Naumkin, A. Y. Vasil'kov, I. O. Volkov, V. V. Smirnov and S. A. Nikolaev, *X-ray photoelectron spectra and structure of composites prepared via deposition of Au, Ni, and Au plus Ni nanoparticles on SiO_2 from colloidal solutions in triethylamine*, Inorg. Mater. 43 (2007) 381-385.

[4.65] Y. F. Han, Z. Y. Zhong, K. Ramesh, F. X. Chen, L. W. Chen, T. White, Q. L. Tay, S. N. Yaakub and Z. Wang, *Au promotional effects on the synthesis of H_2O_2 directly from H_2 and O_2 on supported Pd-Au alloy catalysts*, J. Phys. Chem. C 111 (2007) 8410-8413.

[4.66] A. Corma and P. Serna, *Preparation of substituted anilines from nitro compounds by using supported gold catalysts*, Nat. Protoc. 1 (2006) 2590-2595.

[4.67] K. Koprivova and L. Červený, *Hydrogenation of nitrobenzonitriles using Raney nickel catalyst*, Res. Chem. Intermed. 34 (2008) 93-101.

[4.68] F. Cárdenas-Lizana, S. Gómez-Quero and M.A. Keane, *Clean production of chloroanilines by selective gas phase hydrogenation over supported Ni catalysts*, Appl. Catal. A: General 334 (2008) 199-206.

[4.69] J. Sun, M. Zheng, X. Wang, A. Wang, R. Cheng, T. Li and T. Zhang, *Catalytic performance of activated carbon supported tungsten carbide for hydrazine decomposition*, Catal. Lett. 123 (2008) 150-155.

[4.70] A. J. Brungs, A. P. E. York, J. B. Claridge, C. Márquez-Alvarez and M. L. H. Green, *Dry reforming of methane to synthesis gas over supported molybdenum carbide catalysts*, Catal. Lett. 70 (2000) 117-122.

[4.71] Y. Y. Chen, C. A. Wang, H. Y. Liu, J. S. Qiu and X. H. Bao, *Ag/SiO_2: A novel catalyst with high activity and selectivity for hydrogenation of chloronitrobenzenes*, Chem. Commun. (2005) 5298-5300.

[4.72] J. Chen, N. Yao, R. Wang and J. Zhang, *Hydrogenation of chloronitrobenzene to chloroaniline over Ni/TiO_2 catalysts prepared by sol-gel method*, Chem. Eng. J. 148 (2009) 164-172.

[4.73] V. Kratky, M. Kralik, M. Mecarova, M. Stolcova, L. Zalibera and M. Hronec, *Effect of catalyst and substituents on the hydrogenation of chloronitrobenzenes*, J. Mol. Catal. A: Chemical 235 (2002) 225-231.

[4.74] Y. Hao, R. Liu, X. Meng, H. Cheng and F. Zhao, *Deactivation of Au/TiO_2 catalyst in the hydrogenation of o-chloronitrobenzene in the presence of CO_2*, J. Mol. Catal. A: Chemical 335 (2011) 183-188.

[4.75] P. Sangeetha, P. Seetharamulu, K. Shanthi, S. Narayanan and K. S. Rama Rao, *Studies on Mg-Al oxide hydrotalcite supported Pd catalysts for vapor phase hydrogenation of nitrobenzene*, J. Mol. Catal. A: Chemical 273 (2007) 244-249.

[4.76] J. J. F. Scholten, A. P. Pijpers and A. M. L. Hustings, *Surface characterization of supported and nonsupported hydrogenation catalysts*, Catal. Rev. Sci. Eng. 27 (1985) 151-206.

[4.77] A. Corma, P. Serna, P. Concepcion and J. J. Calvino, *Transforming nonselective into chemoselective metal catalysts for the hydrogenation of substituted nitroaromatics*, J. Am. Chem. Soc. 130 (2008) 8748-8753.

[4.78] F. Cárdenas-Lizana, Z. M. de Pedro, S. Gómez-Quero and M. A. Keane, *Gas phase hydrogenation of nitroarenes: A comparison of the catalytic action of titania supported gold and silver*, J. Mol. Catal. A: Chemical 326 (2010) 48-54.

[4.79] F. Cárdenas-Lizana, S. Gómez-Quero, N. Perret, L. Kiwi-Minsker and M. A. Keane, *β-Molybdenum nitride: Synthesis mechanism and catalytic response in the gas phase hydrogenation of p-chloronitrobenzene*, Catal. Sci. Tech. 1 (2011) 794–801.

Chapter 5

Characterisation and Hydrogenation Performance of Ternary Nitride Catalysts

In this Chapter, the effect of the inclusion of a second metal on the catalytic response of Mo based systems is investigated. Co_3Mo_3N and Fe_3Mo_3N are synthesised, characterised and their catalytic response considered in the gas phase hydrogenation of *p*-chloronitrobenzene.

5.1 Introduction

Research has shown that nitrides of early transition metals (Groups IV-VI) exhibit catalytic properties [5.1-4]. This has been attributed to a hybridisation of the nitrogen *p*-orbitals with the metal *d*-orbitals, resulting in an electronic structure with a Fermi energy close to that of Group VIII metals [5.1]. The majority of the studies to date have focused on binary nitrides such as W_2N [5.5], TiN [5.6], VN [5.7] and Mo_2N [5.4]. Ternary nitride systems are divided into two groups, *i.e.* metallic and covalent/ionic. The former represents catalytically active systems in which metal-metal interactions are dominant and N atoms are interstitial within the metal array. Ternary Mo nitrides have been investigated to a lesser extent, largely due to the challenge of synthesising a pure phase that circumvents the concomitant formation of Mo_2N and the second metal [5.8,5.9]. As Co_3Mo_3N has been identified as effective in hydrotreating, the synthesis and catalytic properties of intermetallic ternary Mo-nitride systems is now receiving renewed attention [5.10-12].

The catalytic action of ternary Mo nitrides, notably Co-Mo, Fe-Mo and Ni-Mo, has been studied in ammonia synthesis [5.11,5.13-16], pyridine [5.17,5.18] and quinoline [5.19] hydrodenitrogenation (HDN), thiophene [5.9,5.20-22] and dibenzothiophene [5.19,5.23] hydrodesulfurisation (HDS) and NO reduction [5.12,5.24]. The incorporation of a second metal has resulted in higher activity relative to the binary system (*i.e.* Mo_2N) [5.9,5.10,5.15,5.17,5.20,5.22,5.24-26]. In ammonia synthesis [5.15,5.25,5.26], the increase in activity has been correlated with the energetics of N_2 adsorption/activation, which is a function of the second metal and

follows the order Co_3Mo_3N > Fe_3Mo_3N > Ni_2Mo_3N > Mo_2N. In the case of pyridine HDN, Chu and co-workers [5.17] proposed that H_2 is activated on the second metal and migrates to Mo sites, leading to a different HDN activity/selectivity response from the binary nitride.

Both Co_3Mo_3N and Fe_3Mo_3N are characterised by a face centred cubic (*fcc*) arrangement of the metal (Co and Mo or Fe and Mo) atoms with the lattice nitrogen occupying octahedral interstitial sites [5.13,5.27,5.28]. These nitrides are typically synthesised *via* temperature programmed nitridation of a bimetallic oxide precursor [5.29,5.30], obtained from a combination of metal nitrate (or metal chloride) with ammonium heptamolybdate (or sodium molybdate) [5.8,5.9,5.13,5.14,5.16,5.24, 5.27,5.28]. The precursors (*e.g.* $CoMoO_4{\cdot}nH_2O$ and $FeMoO_4$) can be nitrided in a flow of NH_3 with a temperature ramp to 873-1073 K [5.8,5.28,5.31]. The effects of precursor [5.15,5.32,5.33], nitridation (gas composition and final temperature) [5.34] and activation conditions [5.14,5.32] on nitride structure have been the subject of studies directed at optimising synthesis.

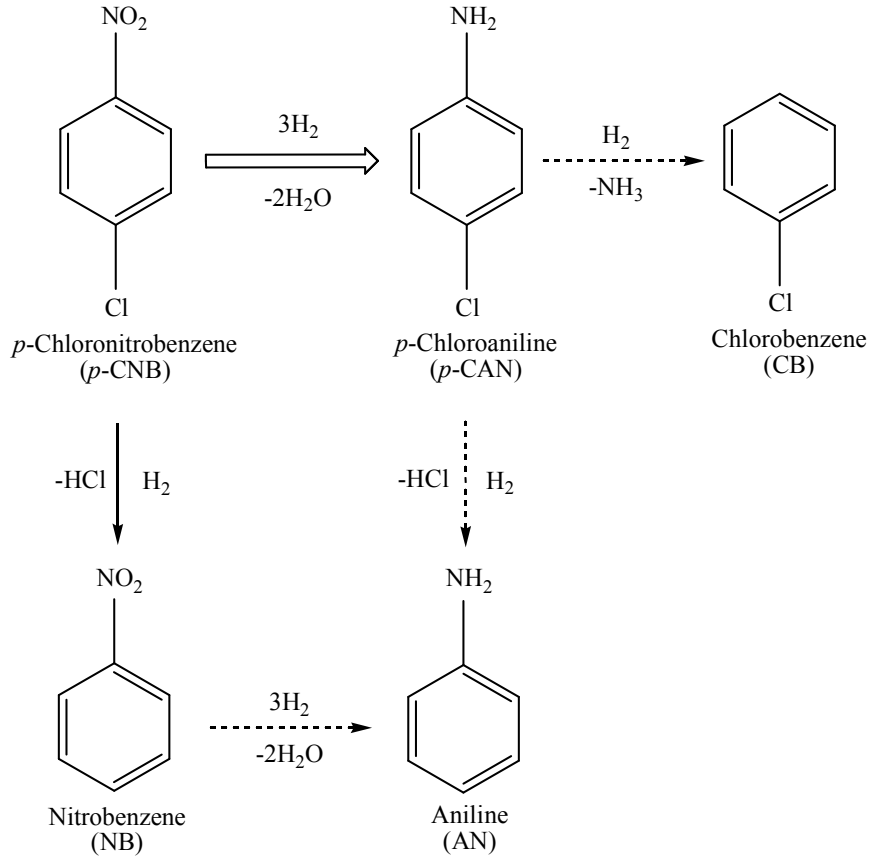

Figure 5.1: Reaction pathways for the hydrogenation of *p*-chloronitrobenzene to the target *p*-chloroaniline (⇨), the observed by-product (nitrobenzene (NB),→) and reaction products (chlorobenzene (CB) and aniline (AN), ⇢) reported in the literature.

While ternary Mo nitride systems have shown activity for hydrogen mediated reactions (HDN, NO reduction and ammonia synthesis) [5.12,5.24], there has been no reported application in hydrogenation. However it is worth flagging studies that have established hydrogenation activity for Mo_2N in the conversion of crotonaldehyde [5.35], ethyne [5.36] and nitroarenes [5.37,5.38]. Taking the latter, selective hydrogenation of *p*-chloronitrobenzene to *p*-chloroaniline is commercially important in the manufacture of polymers, dyes and agrochemicals [5.39]. Reaction over traditional metal (*e.g.* Pt [5.40] and Pd [5.41]) catalysts generates by-products resulting from hydrodechlorination (nitrobenzene) with subsequent hydrogenation (aniline), as shown in **Figure 5.1**. The formation of chlorobenzene has also been reported [5.40]. The literature to date has focused on batch liquid phase operation [5.42,5.43] but results Chapter 2 demonstrated that reaction over Mo_2N in continuous gas phase delivers *p*-chloroaniline as the sole product. Surface adsorption/activation of the reactant is critical where the rate is influenced by surface composition (*e.g.* nitrogen deficient Mo nitride site density and degree of nitridation) [5.44,5.45], Mo oxidation state [5.46] and crystallographic phase (β- vs. γ- Mo_2N) [5.47]. The goal of this chapter is to probe the catalytic hydrogenation properties of bimetallic nitrides, taking Co_3Mo_3N and Fe_3Mo_3N as *iso*-structural stable ternary nitrides and employing *p*-chloronitrobenzene → *p*-chloroaniline as a model reaction.

5.2 Experimental

5.2.1 Catalyst Preparation

In the synthesis of Co_3Mo_3N, the molybdate precursor was prepared by combining aqueous solutions of cobalt nitrate ($Co(NO_3)_2 \cdot 6H_2O$, Sigma Aldrich, 98+%) and ammonium heptamolybdate ($(NH_4)_6Mo_7O_{24} \cdot 4.H_2O$, Sigma Aldrich, 81-83% as MoO_3) and heating to 353 K for 3 h. In the case of Fe_3Mo_3N, the molybdate precursor was synthesised by drop-wise addition of 400 cm^3 0.25 M $FeCl_2 \cdot 4H_2O$ (Sigma-Aldrich > 99%) to 0.66 M $Na_2MoO_4 \cdot 2H_2O$ (Sigma-Aldrich, > 99%). After vacuum filtration, the precipitate obtained was washed twice with distilled water, once with ethanol and dried overnight at 393 K. The powders were calcined in air (Co-Mo) or N_2 (Fe-Mo) for 5 h at 773 K. The $CoMoO_4 \cdot nH_2O$ or $FeMoO_4$ obtained was loaded into a vertical quartz reactor (i.d. 10.5 mm) for nitridation by ammonolysis. A 94 cm^3 min^{-1} flow of NH_3

(BOC, 99.98%) was introduced to the reactor with temperature ramping over three stages, *i.e.* from ambient to 630 K (at 5.6 K min^{-1}), then to 720 K (at 0.5 K min^{-1}) and finally to 1058 K (at 2.1 K min^{-1}), which was maintained for 5 h. The nitrided sample was cooled to ambient temperature in flowing NH_3, followed by a purge in N_2 to remove any residual NH_3. In order to prevent pyrolysis on exposure to air, the material was passivated in a 100 cm^3 min^{-1} flow of O_2/N_2 (v/v O_2 < 0.1%) overnight. Samples were subsequently activated in a 60 cm^3 min^{-1} flow of 3:1 H_2/N_2 (BOC, H_2 99.998%, N_2 99.995%) at 973 K for 2 h and were exposed to air at ambient temperature.

5.2.2 Catalyst Characterisation

The nitrogen content of Co_3Mo_3N and Fe_3Mo_3N was determined using an Exeter CE-440 Elemental Analyser after sample combustion at *ca.* 1873 K. Temperature programmed reduction (TPR), H_2 chemisorption and temperature programmed desorption (TPD) measurements were performed using the commercial CHEM-BET 3000 (Quantachrome) unit. The samples, as prepared, were loaded into a U-shaped Quartz cell (10 cm×3.76 mm i.d.) and heated in 17 cm^3 min^{-1} (Brooks mass flow controlled) 5% v/v H_2/N_2 at 2 K min^{-1} to 823 K. The effluent gas passed through a liquid N_2 trap and changes in H_2 consumption were monitored by TCD with data acquisition/manipulation using the TPR Win™ software. The final temperature was maintained (in a constant flow of H_2/N_2) until return of the signal to baseline, samples swept with 65 cm^3 min^{-1} N_2 for 1.5 h and cooled to room temperature. The nitrides were then subjected to H_2 chemisorption using a pulse (10 μl) titration procedure, followed by H_2-TPD in N_2 (65 cm^3 min^{-1}) at 50 K min^{-1} to 973 K with an isothermal hold until the signal returned to the baseline. Nitrogen adsorption-desorption isotherms were obtained at 77 K using a commercial automated system (Micromeritics Gemini 2390). The specific surface areas were calculated from the isotherms using the standard BET method. Average pore size and cumulative pore volume was obtained from BJH analysis of the desorption isotherms; samples were outgassed at 423 K under N_2 for 1 h prior to analysis.

Powder X-ray diffractograms were recorded on a Bruker/Siemens D500 incident X-ray diffractometer using Cu Kα radiation. The samples were scanned at a rate of 0.02º $step^{-1}$ over the range $15º \leq 2\theta \leq 85º$. Diffractograms were identified using the JCPDS-ICDD reference standards for Co_3Mo_3N (89-7953) and Fe_3Mo_3N (89-7952).

Crystal particle size (d_{hkl}) was estimated using the Scherrer equation assuming negligible contribution of strain and instrumental broadening to reflection widths:

$$d_{hkl} = \frac{K \times \lambda}{\beta \times \cos\theta} \tag{5.1}$$

where K = 0.9 radians, λ is the incident radiation wavelength (1.5056 Å), β is the peak width at half the maximum intensity and θ represents the diffraction angle corresponding to the main plane associated with Co_3Mo_3N (2θ = 42.6°) and Fe_3Mo_3N (2θ = 42.3°). Lattice parameters were determined using TOPAS (version 3) software.

Samples for XPS analysis were pressed into self supporting disks, mounted on nickel sample stubs with double sided tape and evacuated at 10^{-8} mbar for 12 h before insertion into the analysis chamber of a VG ESCALAB II spectrometer (base vacuum 10^{-9} mbar). Spectra were obtained with an Al Kα X-ray source (10 kV, 20 mA, 14 eV) where correction for sample charging was made by setting the C 1*s* binding energy to 285.0 eV. Spectral curve fitting was performed using Gaussian line shape functions, constrained by the intensity ratios and peak splitting required for Mo 3*d* or 3*p* spin-orbit doublets: intensity ratio 3:2 and splitting of 3.2 eV for Mo 3*d*; intensity ratio 2:1 and splitting of 17.2 eV for Mo 3*p*; intensity ratio 2:1 and splitting of 15.4 eV for Co 2*p*; intensity ratio of 2:1 and splitting of 13.2 eV for Fe 2*p*). Binding energies were reproducible to within 0.2 eV. Atomic ratios were estimated by normalising peak areas using the appropriate atomic sensitivity factors. Analysis by scanning electron microscopy (SEM) was conducted with an ISAAC Quanta 200F field emission environmental unit equipped with an EDAX Genesis System for data acquisition/manipulation. Prior to analysis, samples were prepared by dry dispersion onto carbon stubs.

5.2.3 Catalysis Procedure

Co_3Mo_3N and Fe_3Mo_3N were pre-treated *in situ* in a flow (60 cm^3 min^{-1}) of H_2 at 2 K min^{-1} to 823 K, which was maintained for 1 h. Reactions were carried out at T = 493 K (and 1 atm) in a fixed bed vertical glass reactor (l = 600 mm; i.d. = 15 mm). The catalytic reactor and operating conditions to ensure negligible heat/mass transport limitations have been fully described elsewhere [5.48] but some features, pertinent to this study, are given below. A layer of borosilicate glass beads served as preheating zone, ensuring that the organic reactant (*p*-chloronitrobenzene, chlorobenzene or

nitrobenzene) was vaporised and reached reaction temperature before contacting the catalyst. Isothermal conditions (± 1 K) were ensured by diluting the catalyst bed with ground glass (75 μm); the ground glass was mixed thoroughly with catalyst before insertion into the reactor. The reaction temperature was continuously monitored using a thermocouple inserted in a thermowell within the catalyst bed.

The aromatic reactant (as a solution in ethanol) was delivered at a fixed calibrated flow rate to the reactor *via* a glass/teflon air-tight syringe and teflon line using a microprocessor controlled infusion pump (Model 100 kd Scientific). A co-current flow of *p*-chloronitrobenzene (or chlorobenzene or nitrobenzene) and ultra pure H_2 (< 1% v/v organic in H_2) was maintained at a GHSV = 2.0×10^4 h^{-1} with an inlet reactant molar flow (F) = 2.1-4.6×10^{-5} mol h^{-1}. The H_2 content was maintained far in excess of stoichiometric requirements where the mass of catalyst to inlet molar feed rate (m/F) ratio spanned the range 328-2315 g h mol^{-1}. In a series of blank tests, passage of each reactant in a stream of H_2 through the empty reactor did not result in any detectable conversion. The reactor effluent was frozen in a liquid nitrogen trap for subsequent analysis, which was made using a Perkin-Elmer Auto System XL gas chromatograph equipped with a programmed split/splitless injector and a flame ionization detector, employing a DB-1 50 m×0.20 mm i.d., 0.33 μm film thickness capillary column (J&W Scientific). *p*-Chloronitrobenzene (Sigma-Aldrich, purity ≥ 99.0%), nitrobenzene (Fluka, purity ≥ 99.0%), chlorobenzene (Sigma-Aldrich, purity ≥ 99.9%) and ethanol (Sigma Aldrich, ≥ 99% v/v) were used without further purification. Repeated reactions with samples from the same batch of catalyst delivered conversion (X) and selectivity (S) values that were reproducible to better than ± 5%.

5.3 Results and Discussion

5.3.1 Catalyst Characterisation: Pre-reaction

5.3.1.1 XRD

The synthesis of both nitrides drew on prior literature that reported the formation of a pure ternary nitride phase [5.9,5.28,5.32]. The occurrence of Mo_2N and Co or Fe has been reported elsewhere to lower catalytic activity [5.21,5.49] and the synthesis of pure ternary nitrides has been identified as critical in catalytic applications. The XRD pattern for Co_3Mo_3N is presented **Figure 5.2(A)** where the 14 peaks in the 2θ range at

22-79° are characteristic of the ternary Co-Mo nitride; the associated planes are identified in the figure. XRD analysis of Fe_3Mo_3N (see **Figure 5.2(B)**) presents 14 peaks in the same range that match the JCPDS-ICDD standard. In both cases, there were no detectable signals due to Mo_2N, Co or Fe or oxide formation, confirming that the samples had not undergone bulk oxidation upon storage in air. The lattice parameter obtained for Co_3Mo_3N (a = 11.016Å, **Table 5.1**) is close (within 0.1%) to that reported in the JCPDS reference database and falls within the range (11.004-11.032) of experimental values reported in the literature [5.13,5.28,5.50]. As Co_3Mo_3N and Fe_3Mo_3N possess a η-structure and belong to the *Fd-3m* space group, the lattice parameter for both is close and the value for Fe_3Mo_3N (11.067Å, **Table 5.1**) is also in good agreement with the JCPDS standard.

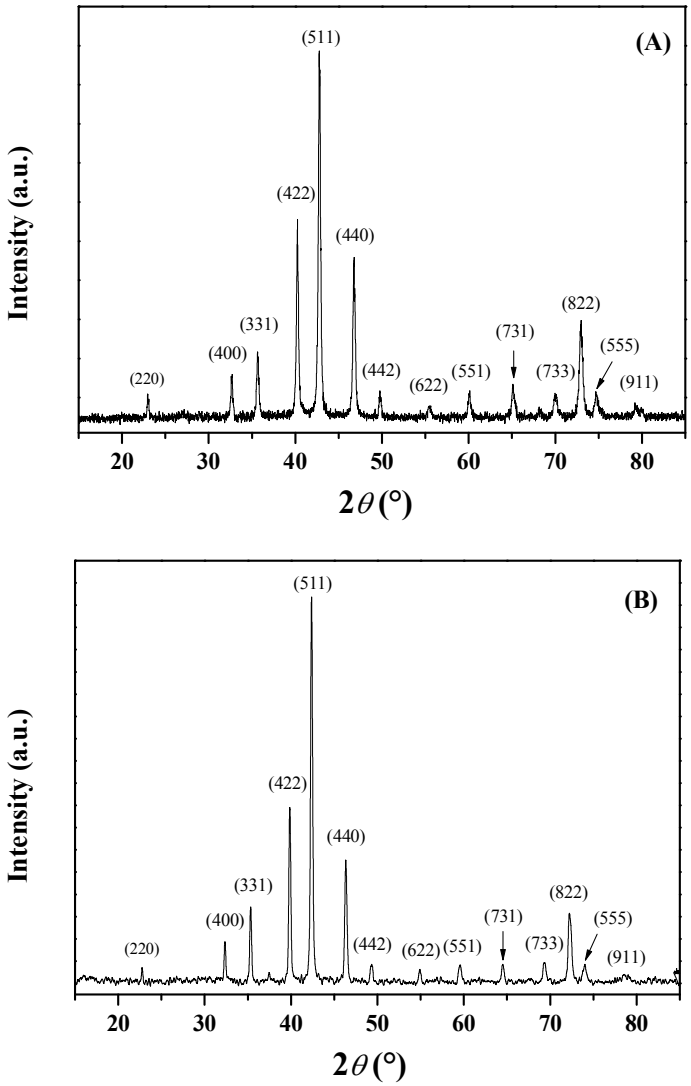

Figure 5.2: XRD patterns for (A) Co_3Mo_3N and (B) Fe_3Mo_3N with the associated planes from the JCPDS-ICDD references (Co_3Mo_3N: card No. 89-7953 and Fe_3Mo_3N: card No. 89-7952).

Table 5.1: Ternary nitride crystal size (d_{hkl}), lattice parameter (a), N content, BET surface area, total pore volume and average pore radius, temperature related maximum (T_{max}) and H_2 consumed/desorbed during TPR and TPD.

		Co_3Mo_3N	Fe_3Mo_3N
d_{hkl} (nm)		29	29
Lattice parameter: a (Å)[a]		11.016 (11.027[b])	11.067 (11.086[c])
N (wt%)	*Pre*-TPR	2.7	3.1
	Post-TPR	2.7	2.8
	After 5 h on-stream[d]	2.7	2.6
BET (m^2 g^{-1})		9	4
Total pore volume (cm^3 g^{-1})		0.028	0.005
Average pore radius (Å)		52	82
TPR	T_{max} (K)	773	795
	H_2 consumed (μmol m^{-2})	295	316
H_2 chemisorption (10^3 μmol m^{-2})		44	67
TPD	T_{max} (K)	973	973
	H_2 released (μmol m^{-2})	15	32

[a]obtained from XRD
[b]from JCPDS-ICDD Co_3Mo_3N reference (89-7953)
[c]from JCPDS-ICDD Fe_3Mo_3N reference (89-7952)
[d]hydrogenation of *p*-chloronitrobenzene

5.3.1.2 Textural properties: BET, pore volume and SEM

There have been few reports demonstrating the synthesis of pure ternary nitrides [5.20,5.28,5.32,5.51] and the available literature dealing with nitride characterisation is limited. Critical textural characteristics for the synthesised Co_3Mo_3N and Fe_3Mo_3N are presented in **Table 5.1**. The BET surface area recorded for Co_3Mo_3N (9 m^2 g^{-1}) falls below the range (12-52 m^2 g^{-1}) given in the literature [5.14,5.20,5.21] but is measurably higher than that of Fe_3Mo_3N (4 m^2 g^{-1}). Previous studies of Fe_3Mo_3N recorded BET values < 18 m^2 g^{-1} [5.14,5.15,5.52]. Both ternary nitrides exhibited the same apparent crystallite size (29 nm, see eqn. (5.1)) that is consistent with recorded [5.16,5.53,5.54] values (21-52 nm).

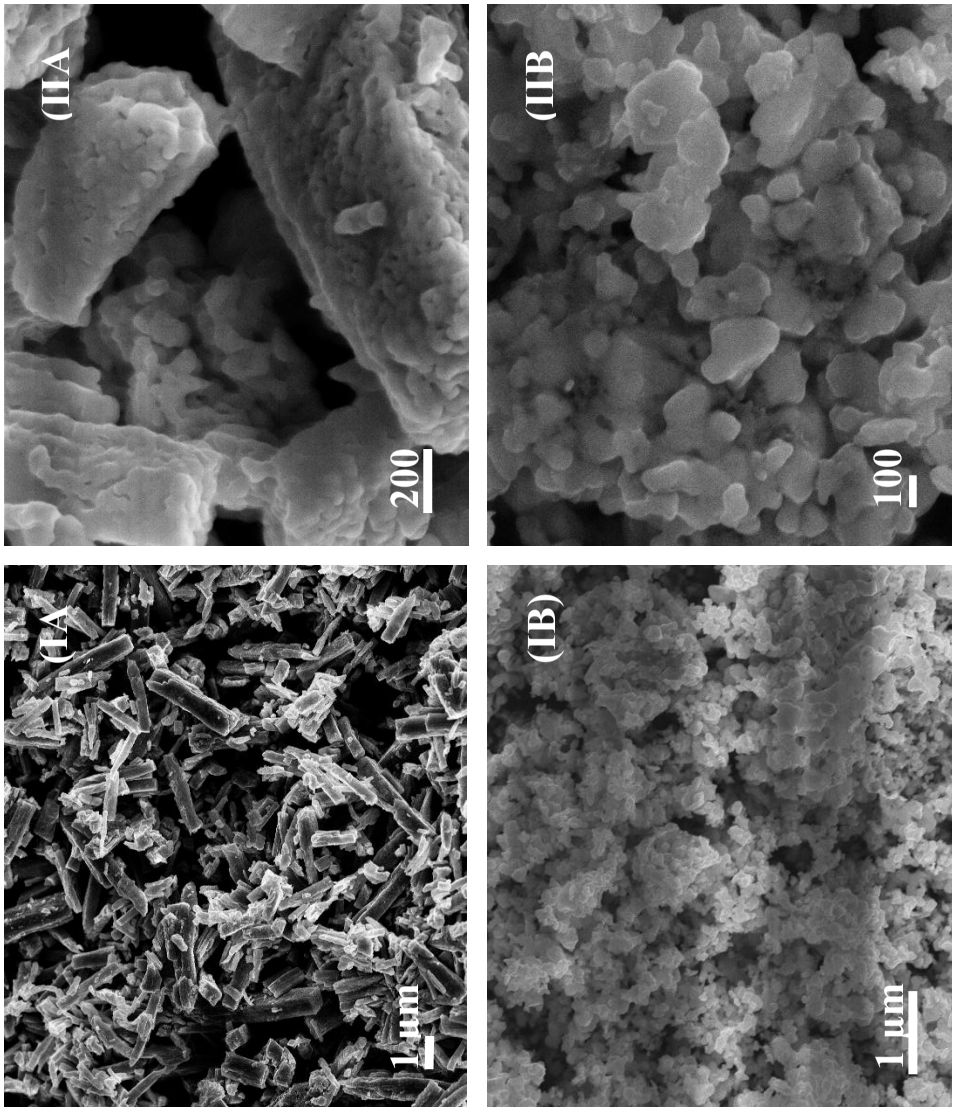

Figure 5.3: Representative (I) low and (II) higher magnification SEM images for (A) Co_3Mo_3N and (B) Fe_3Mo_3N.

The total pore volume (0.028 cm^3 g^{-1}) and average pore radius (52 Å) measured for Co_3Mo_3N agrees with the analysis of Hada and co-workers [5.21] who reported mesopores in the 40-50 Å size interval without any detectable micropore component. By comparison, Fe_3Mo_3N exhibited a lower total pore volume and larger mean pore radius (82 Å); a search through the literature did not reveal any published pore size analysis for an equivalent system.

The morphology of the ternary nitrides depends mainly on the precursor, where the treatment of aqueous solutions of metal chlorides ($FeCl_2$ and $CoCl_2$) results in a non-pseudomorphic transformation with variations in microstructure morphology, from elongated prisms to rounded particles [5.28]. By contrast, the use of a metal (Co and Ni) nitrate consistently results in the formation of rod-like particles [5.31,5.54,5.55]. Representative scanning electron microscopy (SEM) images are presented in **Figure 5.3** where it can be seen that Co_3Mo_3N **(IA)** is comprised of acicular crystallites. This reflects the morphology of the cobalt molybdate precursor (image not shown) and establishes the pseudomorphic nature of ammonolysis [5.25]. At higher magnification (**Figure** 5.**3(IIA)**), it is evident that these acicular crystallites are multidomainic. The morphology exhibited by Fe_3Mo_3N (**Figure 5.3(B)**) is very different and the crystallites show an irregular morphology with a wide size distribution, in agreement with the literature [5.28]. SEM-EDS analysis revealed the presence of surface Na in the case of Fe_3Mo_3N, which must result from sample preparation where sodium molybdate served as precursor. There was no detectable Na associated with Co_3Mo_3N prepared from ammonium heptamolybdate.

5.3.1.3 XPS

The surface composition of the catalysts before and after reaction was determined by XPS analysis. The results are given in **Table 5.2** where a significant Na content is associated with Fe_3Mo_3N, confirming the SEM-EDS observations. It should be noted that the N/Mo ratios are approximate due to the overlap of the N 1*s* signal with Mo 3*p*. Nevertheless, the values for both nitrides demonstrate a surface N enrichment relative to bulk values where N/Mo ≈ 0.3. Surface stoichiometry differing from the bulk has been noted elsewhere for Mo nitride [5.56]. In the case of binary systems, it has

been proposed [5.57] that nitrogen can be accommodated at near surface interstitial sites and defects, such as grain boundaries that leads to higher N/Mo.

Table 5.2: Surface atomic ratios obtained from XPS analysis of Co_3Mo_3N and Fe_3Mo_3N *pre-* and *post-* reaction (hydrogenation of *p*-chloronitrobenzene).

	Co_3Mo_3N		Fe_3Mo_3N	
	pre- reaction	*post-* reaction[a]	*pre-* reaction	*post-* reaction[a]
N/Mo	0.6	0.7	0.9	0.7
Co (Fe)/Mo	1.0	1.0	0.9	1.9
Na/Mo	[b]	[b]	0.4	0.3
Cl/Mo	[b]	0.2	[b]	0.2

[a]after 5 h on-stream
[b]below detection limits

The XPS spectra of the passivated ternary nitrides are presented **Figures** 5.**4**. The Mo 3*d* profiles (**Figure 5.4(I)**) are dominated by a spin-orbit doublet (peaks C and D) at 232.6 ± 0.2 eV and 235.8 ± 0.2 eV due to the presence of oxidised species (Mo $3d_{5/2}$ for Mo(V) = 231.6 eV and Mo(VI) = 233.0 eV), which result from the passivation step as already observed for binary [5.58] and ternary [5.24] Mo nitrides. The profile for Co_3Mo_3N (**IA**) presents a second doublet (peaks A and B) at lower binding energy (228.5 ± 0.2 eV and 231.8 ± 0.2 eV) close to that attributed to Mo^{2+} (Mo $3d_{5/2}$ = 228.2 eV) [5.59], which has been reported for Co_3Mo_3N [5.21]. The Mo $3d_{5/2}$ signal for Fe_3Mo_3N (**IB**) occurs at a higher binding energy (229.0 ± 0.2 eV) that approaches the value for Mo^{3+} (229.2 eV) [5.21], suggesting a higher oxidation state relative to Co_3Mo_3N. Such differences in XPS response may, however, only reflect differences in the extent of passivation prior analysis.

The Co 2*p* spectrum for Co_3Mo_3N (**Figure 5.4(IIA)**) is dominated by a spin-orbit doublet (peaks C and D; 782.2 ± 0.2 eV and 797.6 ± 0.2 eV) where each is accompanied by a higher binding energy satellite (peaks E and F; 787.3 ± 0.2 eV and 803.4 ± 0.2 eV). A second doublet (peaks A and B) is also in evidence at lower binding energy (778.6 ± 0.2 eV and 794.1 ± 0.2 eV). The stronger signal (peak A) is close to that reported for Co_4N supported on alumina (782.5 eV) [5.60] with a binding energy attributed to Co^{3+} (781.6 eV) [5.21] while peak B falls within the range (777.6-779.9 eV) reported for Co and Co^{2+} [5.21]. The Fe 2*p* spectrum for Fe_3Mo_3N is likewise

dominated by a spin-orbit doublet (peak A and B, **Figure 5.4(IIB))**. The Fe 2*p* binding energy (711.8 ± 0.2 eV and 725.8 ± 0.2 eV) is close to that for Fe^{3+} in Fe_2O_3 (711.6 eV) [5.61] and Fe_3Mo_3N (710.9 eV) [5.53]. The presence of a satellite peak (C) at *ca.* 719 eV supports the identification of Fe^{3+}, which has been reported at 718.7-718.8 eV for Fe_2O_3 [5.62]. The Fe 2*p* spectrum shows no evidence of Fe at lower oxidation states; zero valent iron in Fe_3N is reported to exhibit an Fe $2p_{3/2}$ binding energy = 706.7 eV [5.63].

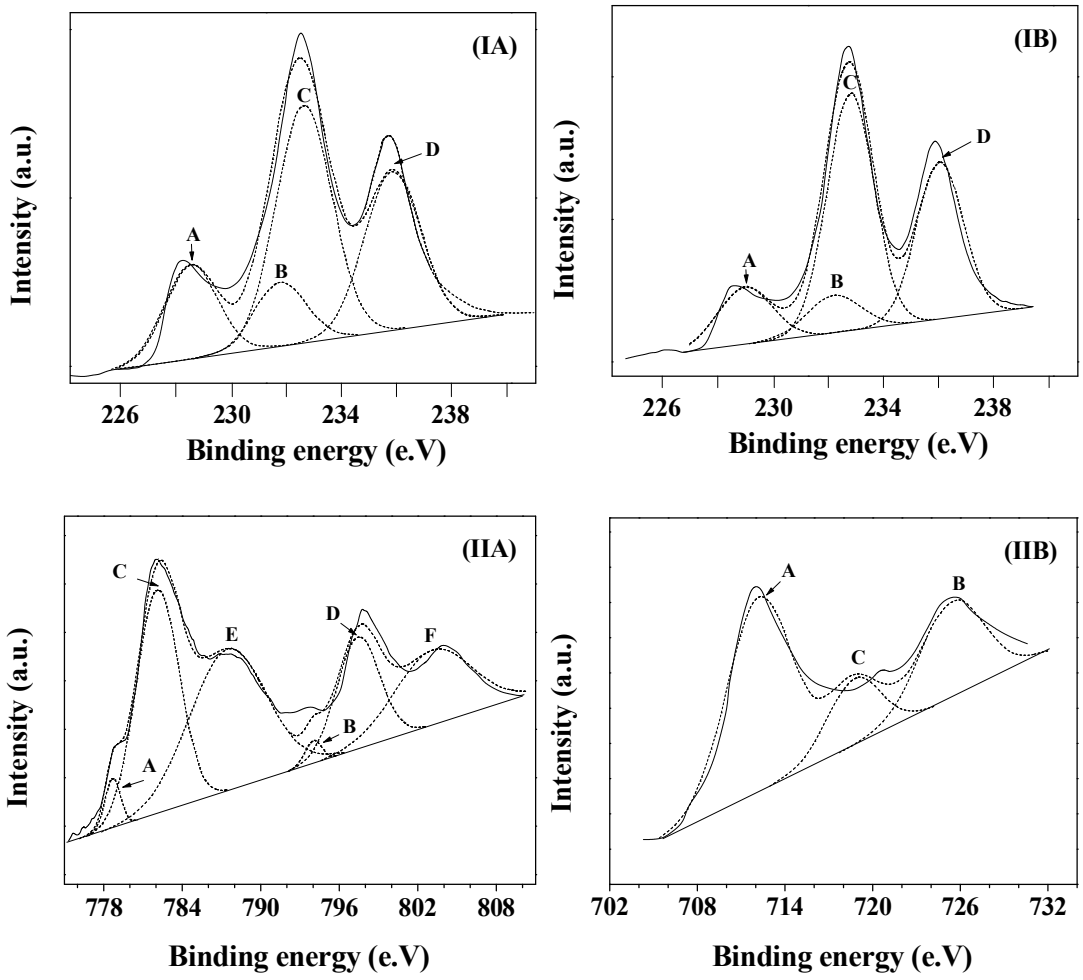

Figure 5.4: XPS spectra over the (I) Mo 3*d*, (II) Co 2*p* and Fe 2*p* regions for (A) Co_3Mo_3N and (B) Fe_3Mo_3N *pre*-reaction; dotted lines represent the fits.

5.3.1.4 TPR, Elemental analysis, H_2 chemisorption and TPD

A temperature programmed reduction (TPR) step is necessary to remove the surface oxidation layer prior to catalysis. The TPR profiles for Co_3Mo_3N **(A)** and Fe_3Mo_3N **(B)** are presented in **Figure 5.5 (I)**.

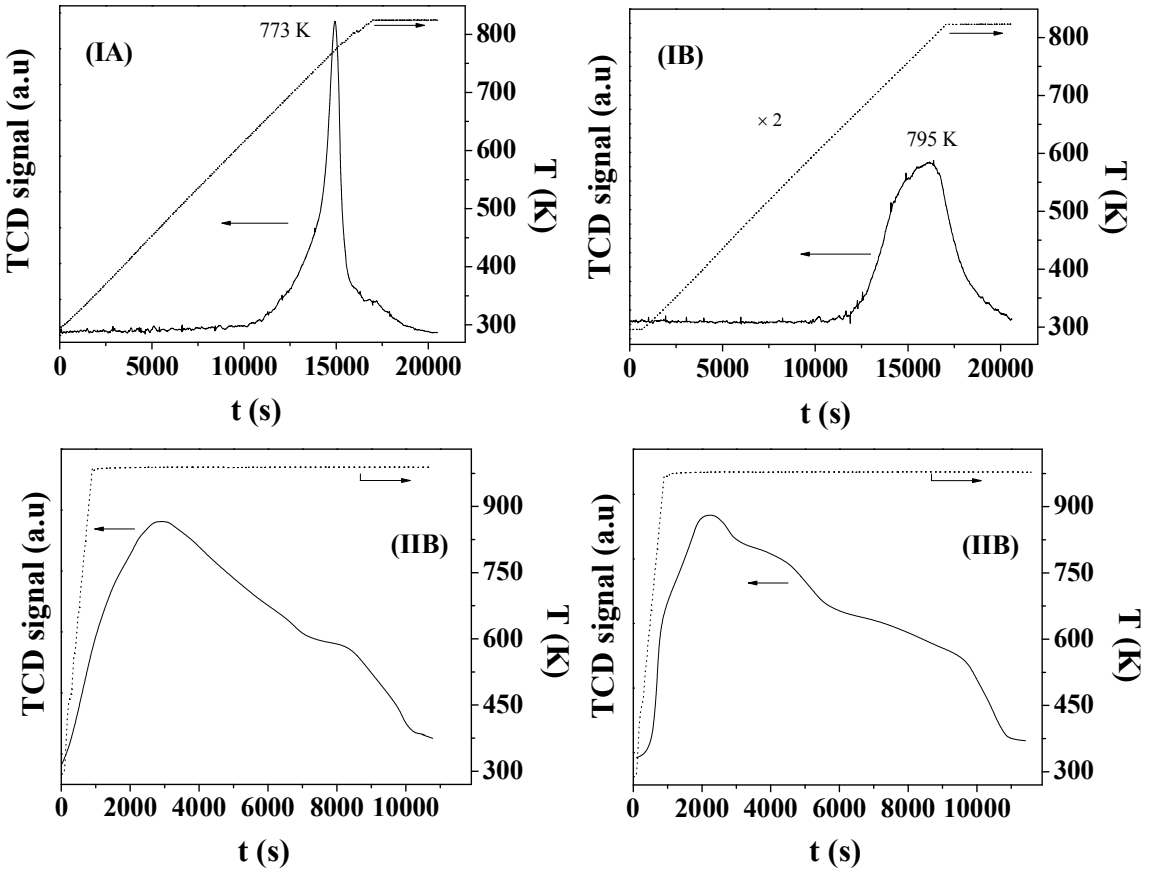

Figure 5.5: H_2 (I) Temperature programmed reduction (TPR) and (II) temperature programmed desorption (TPD) profiles with associated temperature ramp (dotted line) for Co_3Mo_3N (A) and Fe_3Mo_3N (B).

Both show a positive peak associated with H_2 consumption (T_{max} at 773 K for Co_3Mo_3N and 795 K for Fe_3Mo_3N). Maxima in hydrogen consumption in the range 590-780 K have been recorded for Ni_xMoN and Mo_2N and attributed to the removal of the passivation layer [5.17,5.64,5.65], while thermal treatment in the range 673-973 K [5.22,5.25,5.66,5.67] has been employed for Co_3Mo_3N and Fe_3Mo_3N. It is commonly assumed that the passivation layer corresponds to a monolayer of oxygen atoms [5.68]. The specific H_2 consumption (μmol m^{-2}) presented in **Table 5.1** is essentially equivalent for both ternary nitrides. As the TPR signal returned to baseline for both samples, a final temperature of 823 K was deemed sufficient for nitride activation. The BET surface

areas measured *post*-TPR were unchanged. Kojima and co-workers [5.14,5.49] have studied the effect of the pretreatment gas composition to remove the passivation layer from Co_3Mo_3N and observed partial sample decomposition (to Co and Mo_2N) for treatment in pure H_2 or N_2, an effect that was circumvented when using 25% v/v N_2/H_2. In this study, TPR activation in 5% v/v H_2/N_2 and pure H_2 with subsequent passivation did not result in any detectable differences in terms of the XRD response relative to the as synthesised samples. However, Fe_3Mo_3N exhibited lower nitrogen content after TPR (see **Table 5.1**), which was not feature of the thermal treatment of Co_3Mo_3N. This nitrogen loss can be due to excess nitrogen (*pre*-TPR), relative to the stoichiometry (2.9% N), that was labile and consumed with the passivation layer during the reductive treatment.

This Chapter reports the first H_2 chemisorption (by pulse titration) and TPD analysis for Co_3Mo_3N (**Figure 5.5 (IIA)**) and Fe_3Mo_3N (**Figure 5.5 (IIB)**) conducted following TPR. The ambient temperature H_2 uptake values are given in **Table 5.1** where the nature of the second metal (Fe or Co) appears to play a critical role with measurably greater uptake on Fe_3Mo_3N. Indeed, it has been proposed that H_2 adsorbs predominantly on the second metal (in ternary nitrides) with dissociation and subsequent migration to Mo sites [5.17]. Hydrogen TPD from Mo_2N has been reported to generate peaks in the range 370-900 K with total H_2 desorption < 4 μmol m^{-2} [5.64,5.69-71]. The ternary nitrides exhibit desorption over a broad temperature range (T_{max} = 973 K) with a specific H_2 release (**Table 5.1**) that is 4-8 times higher than that reported for the binary system. As the quantity of H_2 desorbed is appreciably greater than that consumed during the chemisorption step, H_2 uptake must be an activated process that is facilitated during TPR. In the case of Mo_2N, H_2 adsorbed can migrate to sub-layers where it is more strongly bound with a resultant high temperature requirement for desorption [5.72]; this may also apply to ternary nitrides. The results indicate a higher uptake/release (per m^2) from Fe_3Mo_3N relative to Co_3Mo_3N. There is evidence in the literature [5.73,5.74] that H_2 adsorption on Mo nitride occurs at nitrogen deficient sites. The loss of nitrogen from Fe_3Mo_3N during TPR may generate defect sites that contribute to increased H_2 uptake. Moreover, Li *et al.* have linked structural changes, as observed during the synthesis of Fe_3Mo_3N (see section 5.3.1.2.), to the generation of boundary and grain sites [5.18] that are known to enhance hydrogen interaction [5.75-77].

5.3.2 Catalytic Results

Nitroarene hydrogenation was conducted under atmospheric pressure in continuous gas phase operation. This represents a significant departure from traditional batch liquid phase operation at elevated pressures [5.43], facilitating higher throughput and minimising separation operations, in line with the principles of sustainable chemical processing [5.78]. Existing batch operations deliver low selectivities to the target amine [5.79] where enhanced selectivity has required additives/promoters (*e.g.* NaHS and KOH) [5.80,5.81] and operation under reflux conditions. The hydrogenation of nitrobenzene was taken as a benchmark to test the activity of the nitride systems for -NO_2 reduction. Indeed, nitrobenzene hydrogenation has been extensively studied [5.82,5.83] where aniline as product is commercially important as an intermediate in the production of dyes [5.84]. Exclusive -NO_2 reduction over binary nitride were established in Chapter 2 and Chapter 3.

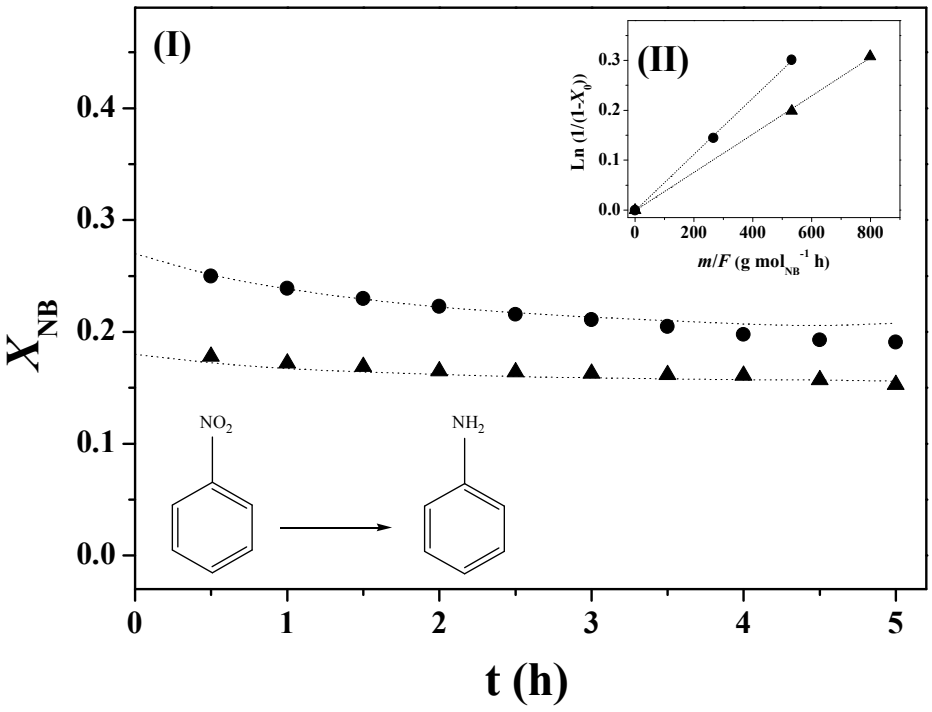

Figure 5.6: (I) Time on-stream fractional nitrobenzene conversion (X_{NB}) to aniline and (II) pseudo-first order kinetic plots for reaction over Co_3Mo_3N (▲) and Fe_3Mo_3N (●).

The hydrogenation of nitrobenzene generated aniline as the sole product over both ternary nitrides. The slight temporal decline in conversion (**Figure 5.6(I)**) can be expressed in terms of the empirical relationship [5.41]

$$\frac{(X_{\mathrm{NB}} - X_0)}{(X_{5\mathrm{h}} - X_0)} = \frac{\mathrm{t}}{(\beta + \mathrm{t})} \tag{5.2}$$

from which a value for the initial conversion (X_0) can be obtained, where $X_{5\mathrm{h}}$ represents fractional conversion after 5 h on-stream and β is a time scale fitting parameter. The applicability of pseudo-first order kinetics for nitroarene hydrogenation over Mo_2N has been established Chapter 2 and 3 where

$$\ln(1 - X_0)^{-1} = k\left(\frac{m}{F}\right) \tag{5.3}$$

and the m/F parameter has the physical significance of contact time. The rate constants obtained from the linear relationships shown in **Figure 5.6(II)** are given **Table 5.3**. Fe_3Mo_3N exhibited a higher hydrogenation rate constant (normalised with respect to catalyst mass (k) or surface area (k')) relative to Co_3Mo_3N, which can be correlated to the greater levels of hydrogen uptake/release recorded in **Table 5.1**. The results suggest that hydrogen availability for reaction is the limiting factor.

Table 5.3: Rate constants (k, normalised per unit catalyst mass and k', normalised per unit surface area) and selectivities (at $X_0 \approx 0.50$) with respect to *p*-chloroaniline ($S_{p\text{-}CAN}$) and nitrobenzene (S_{NB}) in the reaction of nitrobenzene (NB), *p*-chloronitrobenzene (*p*-CNB) and chlorobenzene (CB) over Fe_3Mo_3N and Co_3Mo_3N.

Catalysts	Reactant	k μmol g^{-1} h^{-1}	k' μmol m^{-2} h^{-1}	$S_{p\text{-CAN}}$	S_{NB}
Fe_3Mo_3N	NB	561	94	-	-
	p-CNB	296	49	1	0
	CB	[a]	[a]	-	-
Co_3Mo_3N	NB	381	42	-	-
	p-CNB	633	70	0.35	0.65
	CB	157	17	-	-

[a]below detection limits

Selectivity in the hydrogenation of *p*-chloronitrobenzene (*p*-CNB) is critical with a targeted reduction of the nitro group to generate *p*-chloroaniline (*p*-CAN, **Figure 5.1**), avoiding hydrodechlorination (to nitrobenzene or aniline) or hydrodenitrogenation to generate chlorobenzene. The temporal response for *p*-CNB conversion ($X_{p\text{-CNB}}$) over Co_3Mo_3N **(A)** and Fe_3Mo_3N **(B)** is shown in **Figure 5.7**, where a significant decline in activity with time on-stream is in evidence. Application of a pseudo-first order kinetic treatment (**Figure 5.7(C)**) generated specific rate constants (**Table 5.3**) that exceeded those (20-40 μmol m^{-2} h^{-1}) recorded for Mo_2N under similar reaction conditions [5.47]. It should be noted that the incorporation of the second metal has also resulted in increased activity in ammonia synthesis [5.15,5.25,5.26], NO reduction [5.24], HDN [5.10,5.17] and HDS [5.9,5.10,5.20,5.22].

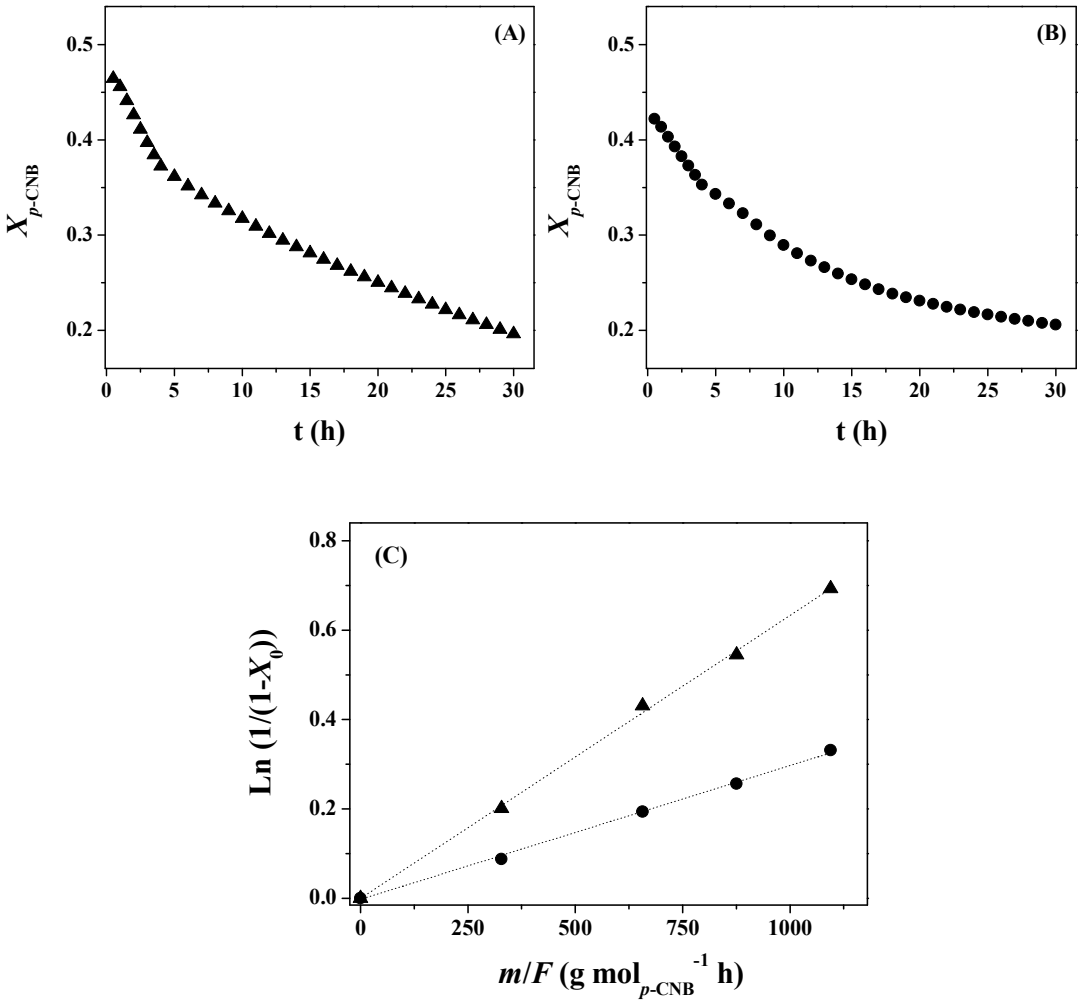

Figure 5.7: Time on-stream fractional *p*-chloronitrobenzene conversion ($X_{p\text{-CNB}}$) for reaction over (A) Co_3Mo_3N (▲) and (B) Fe_3Mo_3N (●) with (C) pseudo-first order kinetic plots.

Reaction over Fe_3Mo_3N promoted the sole formation of *p*-CAN (**Table 5.3**). IR analyses [5.85,5.86] have established nitro group interaction with Mo (110), Mo_2N and $CoMoN_x$. Selective activation of the $-NO_2$ group can proceed on Mo where the incorporation of Fe increases the available hydrogen. The reaction rate was lower than that recorded for nitrobenzene, indicating a deactivating effect due to the *p*-substituted Cl. Indeed, surface interaction through the Cl substituent can result in a decrease in N=O bond polarity that inhibits nitro group activation with an accompanying lower activity. In contrast, Co_3Mo_3N generated nitrobenzene as the principal product, in addition to *p*-CAN. This is in agreement with literature that has established hydrodechlorination of mono- [5.87-89], and di-chlorobenzene [5.87] over Mo and Co systems. Given that Co_3Mo_3N exhibited a lower associated hydrogen content but delivered higher specific activity (**Table 5.3**), activation of the ring substituents in *p*-CNB must be the limiting factor.

Deviation in selectivity for different ternary Mo-nitrides has been noted previously for HDN applications [5.10,5.17] but this feature was not developed in those studies. The different activity/selectivity response exhibited by the two ternary nitrides was probed further by examining the conversion of chlorobenzene as reactant. Reaction of chlorobenzene over Co_3Mo_3N produced benzene with 100% selectivity and a loss of activity with time on-stream (**Figure 5.8(I)**); the associated pseudo-first order plot is given in **Figure 5.8(II)** and specific rate constants are recorded in **Table 5.3**. Under the same reaction conditions, there was no detectable conversion of chlorobenzene over Fe_3Mo_3N, which is consistent with the observed exclusive *p*-CNB → *p*-CAN. These tests establish catalytic hydrodechlorination properties for Co_3Mo_3N that are not a feature of Fe_3Mo_3N. Dechlorination of chloroarenes is known to proceed with the formation of a surface σ-complex [5.87,5.90]. There is evidence in the literature [5.46,5.91,5.92] that interaction between organic reactants and Mo species is stronger when the latter are at low oxidation states. The XPS results suggest that the Co_3Mo_3N surface exhibits a lower oxidation state (with Co^{n+} ($0 \leq n \leq 3$) and Mo^{2+}) relative to Fe_3Mo_3N (with Fe^{3+} and Mo^{3+}). The nature of the second metal (Co *vs.* Fe) and differences in oxidation must impact on *p*-CNB adsorption. Given the product distribution, interaction of *p*-CNB (and chlorobenzene) with Co_3Mo_3N activates C-Cl for hydrogen scission.

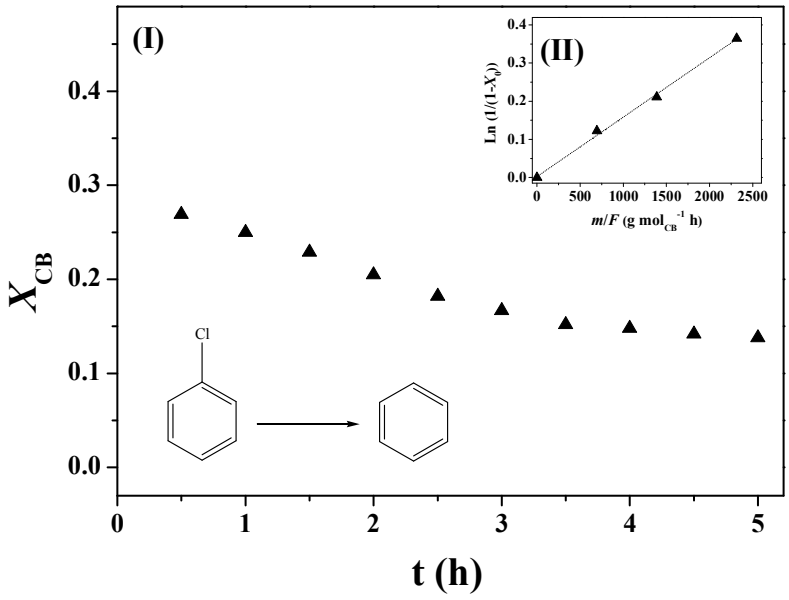

Figure 5.8: (I) Time on-stream fractional chlorobenzene conversion (X_{CB}) to benzene and (II) pseudo-first order kinetic plot for reaction over Co_3Mo_3N.

5.3.3 Catalyst Characterisation: Post-reaction

Loss of activity in gas phase hydrogenation of *p*-CNB over supported transition metals (*e.g.* Ni, Au, Pd and Cu) has been attributed to metal leaching and sintering [5.93], coke formation [5.94] and poisoning by the water [5.95] or chloride [5.96] generated during reaction. Work on the application of ternary nitrides in catalysis is at too early a stage to draw any conclusions from the available literature regarding possible deactivation effects. Kojima and co-workers [5.49] have attributed the deactivation of a Co-Mo nitride system in ammonia synthesis to a change in structure with partial decomposition to Co and Mo_2N.

In the case of Co_3Mo_3N, we have recorded a temporal loss of activity in the conversion of *p*-CNB (**Figure 5.7(A)**) and chlorobenzene (**Figure 5.8(I)**) but essentially an invariance in the conversion of nitrobenzene with time on-stream (**Figure 5.6(I)**). This suggests that deactivation is associated with dechlorination, possibly due to Cl poisoning. Indeed, XPS analysis provides evidence for surface residual Cl *post*-reaction; see Cl/Mo ratios given in **Table 5.2**. Variation in selectivity in the conversion of *p*-CNB is shown in **Figure 5.9(A)** where the temporal decline in conversion (see **Figure 5.7(A)**) is accompanied by a switch in selectivity from nitrobenzene as the predominant product to *p*-CAN, which was the sole product at extended reaction times (≥ 12 h). This

suggests a preferential poisoning of the active sites responsible for dechlorination. The XRD response, in terms of peak position, d_{hkl} and relative intensity was unchanged after reaction with no evidence of ternary nitride decomposition to Mo_2N or Co. Moreover, the bulk N content was the same *pre-* and *post*-reaction (**Table 5.1**). The Co 2*p* XPS profile of the samples *post*-reaction (not shown) did not present any major change relative to the spectrum (**Figure 5.4(IIA)**) generated for the unused catalyst. The Mo $3d_{5/2}$ signal was shifted to a higher binding energy (by 0.3 eV), which may result from a partial oxidation of the Mo component during reaction.

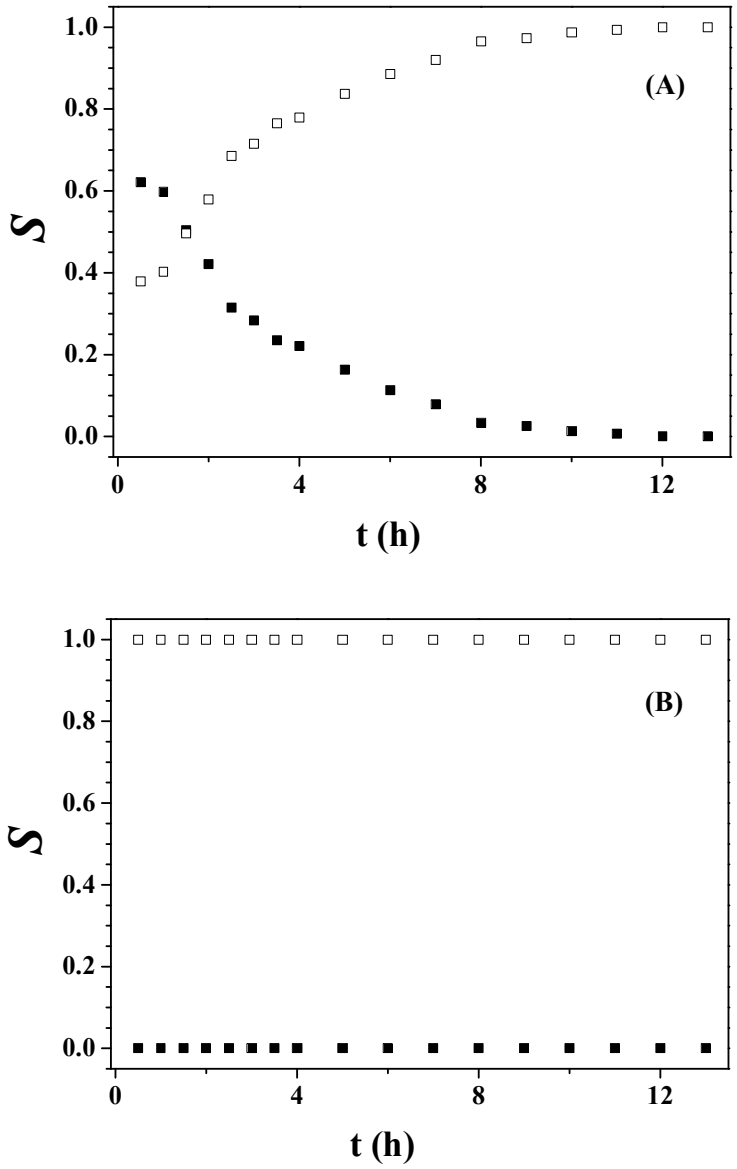

Figure 5.9: Variation of selectivity (*S*) to *p*-chloroaniline (□) and nitrobenzene (■) with time on-stream for the hydrogenation of *p*-chloronitrobenzene over Co_3Mo_3N (A) and Fe_3Mo_3N (B).

The exclusive hydrogenation of *p*-chloronitrobenzene to *p*-chloroaniline over Fe_3Mo_3N was maintained for prolonged reaction times (**Figure 5.9**(**B**)) and the temporal decline in conversion (**Figure 5.7**(**B**)) did not impact on product selectivity. The XRD pattern after reaction coincided with that presented in **Figure 5.2**(**B**). However, the bulk N content was lowered following reaction (**Table 5.1**), implying some structural change that accompanies deactivation. Indeed, the XPS results given in **Table 5.2** reveal a dramatic enhancement of Fe/Mo ratio following reaction. A decline in activity with a decrease in the relative surface Mo content suggests that $-NO_2$ activation occurs principally on Mo sites over Fe_3Mo_3N. While the XPS Fe 2*p* profile and associated binding energy was essentially unchanged after use, a shift of Mo $3p_{5/2}$ by 0.3 eV to a higher value may again be indicative of a change in oxidation state. XPS analysis has revealed the presence of Cl in the used sample (**Table 5.2**), which can not be associated with dechlorination. This residual Cl may, however, be attributed to the use of $FeCl_2 \cdot 2H_2O$ as precursor, which may move from the bulk to the surface during reaction and possibly poison the catalyst.

5.4 Conclusion

Two pure ternary nitrides (Co_3Mo_3N and Fe_3Mo_3N) have been synthesised and confirmed by XRD and elemental analysis. Both present a similar lattice parameter and crystal size. SEM analysis has revealed structural differences, where Co_3Mo_3N takes the form of acicular crystallites and Fe_3Mo_3N presents a wide size range of aggregates. The bulk N content in Fe_3Mo_3N exceeded the stoichiometry, where temperature programmed reduction (TPR) served to remove the superficial passivation oxide layer from both nitrides and excess nitrogen from Fe_3Mo_3N. XPS analysis has revealed a surface N/Mo ratio greater than the bulk value, indicating surface N enrichment for both nitrides. The XPS results indicate similar Co/Mo and Fe/Mo ratios with evidence of possible differences in oxidation states for the two systems. Hydrogen TPD analysis has demonstrated significant H_2 release from both ternary nitrides (15-32 μmol m^{-2}), exceeding that measured previously for Mo_2N (< 4 μmol m^{-2}). Fe_3Mo_3N exhibited higher H_2 uptake/release than Co_3Mo_3N that resulted in an increased rate of nitrobenzene hydrogenation (to aniline).

Hydrogenation of *p*-chloronitrobenzene over Fe_3Mo_3N generated *p*-chloronitroaniline as the sole product, whereas Co_3Mo_3N promoted a composite

hydrodechlorination and hydrogenation to give *p*-chloronitroaniline and nitrobenzene. The hydrodechlorination character of the Co nitride was established in the conversion of chlorobenzene to benzene under conditions where Fe_3Mo_3N was inactive. Both ternary nitrides exhibited time on-stream deactivation that can be linked, in the case of Co_3Mo_3N, to Cl poisoning that accompanying the formation of nitrobenzene. Loss of activity over Fe_3Mo_3N is associated with a significant increase in surface Fe/Mo ratio and displacement of bulk Cl (from the $FeCl_2 \cdot 2H_2O$ synthesis precursor) to the surface.

5.5 References

[5.1] S. T. Oyama, *The chemistry of transition metal carbides and nitrides*, Blackie Academic, Glasgow, 1996, pp. 14-15.

[5.2] A. M. Alexander and J. S. J. Hargreaves, *Alternative catalytic materials: carbides, nitrides, phosphides and amorphous boron alloys*, Chem. Soc. Rev. 39 (2010) 4388-4401.

[5.3] J. G. Chen, *Carbide and nitride overlayers on early transition metal surfaces: Preparation, characterization, and reactivities*, Chem. Rev. 96 (1996) 1477-1498.

[5.4] E. Furimsky, *Metal carbides and nitrides as potential catalysts for hydroprocessing*, Appl. Catal. A: General 240 (2003) 1-28.

[5.5] R. C. V. McGee, S. K. Bej and L. T. Thompson, *Basic properties of molybdenum and tungsten nitride catalysts*, Appl. Catal. A: General 284 (2005) 139-146.

[5.6] S. Kaskel, K. Schlichte and T. Kratzke, *Catalytic properties of high surface area titanium nitride materials*, J. Mol. Catal. A: Chemical 208 (2004) 291-298.

[5.7] H. Kwon, S. Choi and L. T. Thompson, *Vanadium nitride catalysts: Synthesis and evaluation for n-butane dehydrogenation*, J. Catal. 184 (1999) 236-246.

[5.8] D. S. Bem, C. P. Gibson and H. C. Z. Loye, *Synthesis of intermetallic nitrides by solid-state precursor reduction*, Chem. Mater. 5 (1993) 397-399.

[5.9] B. Diaz, S. J. Sawhill, D. H. Bale, R. Main, D. C. Phillips, S. Korlann, R. Self and M. E. Bussell, *Hydrodesulfurization over supported monometallic, bimetallic and promoted carbide and nitride catalysts*, Catal. Today 86 (2003) 191-209.

[5.10] S. Chouzier, M. Vrinat, T. Cseri, M. Roy-Auberger and P. Afanasiev, *HDS and HDN activity of (Ni,Co)Mo binary and ternary nitrides prepared by*

decomposition of hexamethylenetetramine complexes, Appl. Catal. A: General 400 (2011) 82-90.

[5.11] D. Moszynski, R. Jedrzejewski, J. Ziebro and W. Arabczyk, *Surface and catalytic properties of potassium-modified cobalt molybdenum catalysts for ammonia synthesis*, Appl. Surf. Sci. 256 (2010) 5581-5584.

[5.12] Z. Yao, A. Zhu, C. T. Au and C. Shi, *Redox Properties of Cobalt Nitrides for NO Dissociation and Reduction*, Catal. Lett. 130 (2009) 63-71.

[5.13] D. McKay, D. H. Gregory, J. S. J. Hargreaves, S. M. Hunter and X. Sun, *Towards nitrogen transfer catalysis: reactive lattice nitrogen in cobalt molybdenum nitride*, Chem. Commun. (2007) 3051-3053.

[5.14] R. Kojima and K. Aika, *Cobalt molybdenum bimetallic nitride catalysts for ammonia synthesis - Part 1. Preparation and characterization*, Appl. Catal. A: General 215 (2001) 149-160.

[5.15] C. J. H. Jacobsen, *Novel class of ammonia synthesis catalysts*, Chem. Commun. (2000) 1057-1058.

[5.16] A. Boisen, S. Dahl and C. J. H. Jacobsen, *Promotion of binary nitride catalysts: Isothermal N_2 adsorption, microkinetic model, and catalytic ammonia synthesis activity*, J. Catal. 208 (2002) 180-186.

[5.17] Y. J. Chu, Z. B. Wei, S. W. Yang, C. Li, Q. Xin and E. Z. Min, *$NiMoN_x$/gamma-Al_2O_3 catalyst for HDN of pyridine*, Appl. Catal. A: General 176 (1999) 17-26.

[5.18] Y. Li, Y. Zhang, R. Raval, C. Li, R. Zhai and Q. Xin, *The modification of molybdenum nitrides: the effect of the second metal component*, Catal. Lett. 48 (1997) 239-245.

[5.19] S. Ramanathan, C. C. Yu and S. T. Oyama, *New catalysts for hydroprocessing: Bimetallic oxynitrides II. Reactivity studies*, J. Catal. 173 (1998) 10-16.

[5.20] D. W. Kim, D. K. Lee and S. K. Ihm, *CoMo bimetallic nitride catalysts for thiophene HDS*, Catal. Lett. 43 (1997) 91-95.

[5.21] K. Hada, M. Nagai and S. Omi, *Characterization and HDS activity of cobalt molybdenum nitrides*, J. Phys. Chem. B 105 (2001) 4084-4093.

[5.22] J. W. Logan, J. L. Heiser, K. R. McCrea, B. D. Gates and M. E. Bussell, *Thiophene hydrodesulfurization over bimetallic and promoted nitride catalysts*, Catal. Lett. 56 (1998) 165-171.

[5.23] Y. Q. Liu, C. G. Liu and G. H. Que, *Hydrodesulfurization of dibenzothiophene over cobalt-molybdenum nitride catalysts*, Energy Fuels 16 (2002) 531-535.

[5.24] C. Shi, A. M. Zhu, X. F. Yang and C. T. Au, *NO reduction with hydrogen over cobalt molybdenum nitride and molybdenum nitride: a comparison study*, Catal. Lett. 97 (2004) 9-16.

[5.25] D. McKay, J. S. J. Hargreaves, J. L. Rico, J. L. Rivera and X. L. Sun, *The influence of phase and morphology of molybdenum nitrides on ammonia synthesis activity and reduction characteristics*, J. Solid State Chem. 181 (2008) 325-333.

[5.26] R. Kojima and K. Aika, *Cobalt molybdenum bimetallic nitride catalysts for ammonia synthesis Part 2. Kinetic study*, Appl. Catal. A: General 218 (2001) 121-128.

[5.27] S. K. Jackson, R. C. Layland and H. C. zur Loye, *The simultaneous powder X-ray and neutron diffraction refinement of two eta-carbide type nitrides, Fe_3Mo_3N and Co_3Mo_3N, prepared by ammonolysis and by plasma nitridation of oxide precursors*, J. Alloys Compd. 291 (1999) 94-101.

[5.28] S. Alconchel, F. Sapina, D. Beltran and A. Beltran, *Chemistry of interstitial molybdenum ternary nitrides M_nMo_3N (M = Fe, Co, n = 3; M = Ni, n = 2)*, J. Mater. Chem. 8 (1998) 1901-1909.

[5.29] R. Niewa and F. J. DiSalvo, *Recent developments in nitride chemistry*, Chem. Mater. 10 (1998) 2733-2752.

[5.30] C. C. Yu, S. Ramanathan and S. T. Oyama, *New catalysts for hydroprocessing: Bimetallic oxynitrides M_I-M_{II}-O-N (M_I, M_{II} = Mo, W, V, Nb, Cr, Mn, and Co) Part I. Synthesis and characterization*, J. Catal. 173 (1998) 1-9.

[5.31] K. Hada, J. Tanabe, S. Omi and M. Nagai, *Characterization of cobalt molybdenum nitrides for thiophene HDS by XRD, TEM, and XPS*, J. Catal. 207 (2002) 10-22.

[5.32] S. M. Hunter, D. McKay, R. J. Smith, J. S. J. Hargreaves and D. H. Gregory, *Topotactic Nitrogen Transfer: Structural Transformation in Cobalt Molybdenum Nitrides*, Chem. Mater. 22 (2010) 2898-2907.

[5.33] R. Kojima and K. Aika, *Cobalt molybdenum bimetallic nitride catalysts for ammonia synthesis*, Chem. Lett. (2000) 514-515.

[5.34] J. S. J. Hargreaves and D. McKay, *A comparison of the reactivity of lattice nitrogen in Co_3Mo_3N and Ni_2Mo_3N catalysts*, J. Mol. Catal. A: Chemical 305 (2009) 125-129.

[5.35] A. Guerrero-Ruiz, Y. Zhang, B. Bachiller-Baeza and I. Rodríguez-Ramos, *Hydrogenation of crotonaldehyde over carbon- supported molybdenum nitrides*, Catal. Lett. 55 (1998) 165-168.

[5.36] Z. X. Hao, Z. B. Wei, L. J. Wang, X. H. Li, C. Li, E. Z. Min and Q. Xin, *Selective hydrogenation of ethyne on gamma-Mo_2N*, Appl. Catal. A: General 192 (2000) 81-84.

[5.37] F. Cárdenas-Lizana, S. Gómez-Quero, N. Perret, L. Kiwi-Minsker and M. A. Keane, *Au/Mo_2N as a new catalyst formulation for the hydrogenation of p-Chloronitrobenzene in both liquid and gas phase*, Catal. Commun. 21 (2012) 46-51.

[5.38] F. Cárdenas-Lizana, D. Lamey, S. Gómez-Quero, N. Perret, L. Kiwi-Minsker and M. A. Keane, *selective three-phase hydrogenation of aromatic nitro-compounds over beta-Mo_2N*, Catal. Today 173 (2011) 53-61.

[5.39] A. Boehncke, J. Kielhorn, G. Könnecker, C. Pohlenz-Michel and I. Mangelsdorf, *4-chloroaniline, Concise International Chemical Assessment Document 48*, World Health Organization, Stuttgart, 2003, pp. 7-9.

[5.40] B. Coq, A. Tijani and F. Figueras, *Particle-size effect on the kinetics of p-chloronitrobenzene hydrogenation over platinum alumina catalysts*, J. Mol. Catal. 68 (1991) 331-345.

[5.41] F. Cárdenas-Lizana, S. Gómez-Quero and M. A. Keane, *Ultra-selective gas phase catalytic hydrogenation of aromatic nitro compounds over Au/Al_2O_3*, Catal. Commun. 9 (2008) 475-481.

[5.42] H. Bonnemann, W. Wittholt, J. D. Jentsch and A. S. Tilling, *Supported Pt-colloid catalysts for the selective hydrogenation of 3,4-dichloronitrobenzene*, New J. Chem. 22 (1998) 713-717.

[5.43] A. Corma and P. Serna, *Preparation of substituted anilines from nitro compounds by using supported gold catalysts*, Nat. Protoc. 1 (2006) 2590-2595.

[5.44] J. G. Choi, *Influence of surface composition on HDN activities of molybdenum nitrides*, J. Ind. Eng. Chem. 8 (2002) 1-11.

[5.45] C. W. Colling and L. T. Thompson, *The structure and function of supported molybdenum nitride hydrodenitrogenation catalysts*, J. Catal. 146 (1994) 193-203.

[5.46] Y. Z. Li, G. F. Luo, Y. N. Fan and Y. Chen, *A novel route to the synthesis of nanosized metallic molybdenum at moderate temperature and its catalytic properties*, Mater. Res. Bull. 39 (2004) 195-203.

[5.47] N. Perret, F. Cárdenas-Lizana, D. Lamey, V. Laporte, L. Kiwi-Minsker and M. A. Keane, *Effect of Crystallographic Phase (β vs. γ) and Surface Area on Gas Phase Nitroarene Hydrogenation over Mo_2N and Au/Mo_2N*, Top. Catal., Manuscript Accepted (2012)

[5.48] M. A. Keane, *Gas phase reaction of hydrogen with carboxyl and carbonyl functions in aromatic systems over Ni/SiO_2*, J. Mol. Catal. A: Chemical 138 (1999) 197-209.

[5.49] R. Kojima and K. Aika, *Cobalt molybdenum bimetallic nitride catalysts for ammonia synthesis Part 3. Reactant gas treatment*, Appl. Catal. A: General 219 (2001) 157-170.

[5.50] Y. Chen, J. Shen and N.-X. Chen, *The effect of Mo atoms in ternary nitrides with eta-type structure*, Solid State Commun. 149 (2009) 121-125.

[5.51] S. Korlann, B. Diaz and M. E. Bussell, *Synthesis of bulk and alumina-supported bimetallic carbide and nitride catalysts*, Chem. Mater. 14 (2002) 4049-4058.

[5.52] R. N. Panda and N. S. Gajbhiye, *Electronic and magnetic properties of Fe_3Mo_3N*, J. Alloys Compd. 256 (1997) 102-107.

[5.53] R. N. Panda, G. Balaji, P. K. Pandey and N. S. Gajbhiye, *Magnetic, Mossbauer and X-ray photoelectron spectroscopic investigations on nanocrystalline Fe_3Mo_3N, $FeMoN_2$ and Ni_3Mo_3N nitrides*, Hyperfine Interact. 184 (2008) 245-250.

[5.54] H. M. Wang, W. Li and M. H. Zhang, *New approach to the synthesis of bulk and supported bimetallic molybdenum nitrides*, Chem. Mater. 17 (2005) 3262-3267.

[5.55] S. Chouzier, P. Afanasiev, M. Vrinat, T. Cseri and M. Roy-Auberger, *One-step synthesis of dispersed bimetallic carbides and nitrides from transition metals hexamethylenetetramine complexes*, J. Solid State Chem. 179 (2006) 3314-3323.

[5.56] B. G. Demczyk, J. G. Choi and L. T. Thompson, *Surface-structure and composition of high-surface-area molybdenum nitrides*, Appl. Surf. Sci. 78 (1994) 63-69.

[5.57] I. T. Ghampson, C. Sepúlveda, R. Garcia, B. G. Frederick, M. C. Wheeler, N. Escalona and W. J. DeSisto, *Guaiacol transformation over unsupported molybdenum-based nitride catalysts*, Appl. Catal. A: General 413-414 (2012) 78-84.

[5.58] G. H. Xie and Z. C. Jiang, *The first observation of Mo^{5+} in the passivation layer of Mo_2N*, Chin. Sci. Bull. 45 (2000) 1562-1564.

[5.59] K. Hada, M. Nagai and S. Omi, *XPS and TPR studies of nitrided molybdena-alumina*, J. Phys. Chem. B 104 (2000) 2090-2098.

[5.60] Z. Yao, X. Zhang, F. Peng, H. Yu, H. Wang and J. Yang, *Novel highly efficient alumina-supported cobalt nitride catalyst for preferential CO oxidation at high temperatures*, Int. J. Hydrogen Energy 36 (2011) 1955-1959.

[5.61] P. Mills and J. L. Sullivan, *A study of the core level electrons in iron and its 3 oxides by means of X-Ray photoelectron-spectroscopy*, J. Phys. D: Appl. Phys. 16 (1983) 723-732.

[5.62] T. Yamashita and P. Hayes, *Analysis of XPS spectra of Fe^{2+} and Fe^{3+} ions in oxide materials*, Appl. Surf. Sci. 254 (2008) 2441-2449.

[5.63] W. Huang, J. Wu, W. Guo, R. Li and L. Cui, *Preparation and magnetic properties of nanoscale epsilon-Fe_3N particles*, J. Alloys Compd. 443 (2007) 48-52.

[5.64] Z. B. Wei, Q. Xin, P. Grange and B. Delmon, *TPD and TPR studies of molybdenum nitride*, J. Catal. 168 (1997) 176-182.

[5.65] C. W. Colling, J.-G. Choi and L. T. Thompson, *Molybdenum nitride catalysts II. H_2 temperature programmed reduction and NH_3 temperature programmed desorption*, J. Catal. 160 (1996) 35-42.

[5.66] X.-H. Wang, M.-H. Zhang, W. Li and K.-Y. Tao, *A simple synthesis route and characterisation of Co_3Mo_3C*, Dalton Trans. (2007) 5165-5170.

[5.67] D. H. Gregory, J. S. J. Hargreaves and S. M. Hunter, *On the Regeneration of Co_3Mo_3N from Co_6Mo_6N with N_2*, Catal. Lett. 141 (2011) 22-26.

[5.68] J. S. Choi, G. Bugli and G. Djéga-Mariadassou, *Influence of the degree of carburization on the density of sites and hydrogenating activity of molybdenum carbides*, J. Catal. 193 (2000) 238-247.

[5.69] J. G. Choi, H. J. Lee and L. T. Thompson, *Temperature-programmed desorption of H_2 from molybdenum nitride thin-films*, Appl. Surf. Sci. 78 (1994) 299-307.

[5.70] M. Nagai, Y. Goto, O. Uchino and S. Omi, *TPD and XRD studies of molybdenum nitride and its activity for hydrodenitrogenation of carbazole*, Catal. Today 43 (1998) 249-259.

[5.71] S. Li, W. B. Kim and J. S. Lee, *Effect of the reactive gas on the solid-state transformation of molybdenum trioxide to carbides and nitrides*, Chem. Mater. 10 (1998) 1853-1862.

[5.72] X. S. Li, Y. X. Chen, Y. J. Zhang, C. X. Ji and Q. Xin, *Temperature-programmed desorption and adsorption of hydrogen on Mo_2N*, React. Kinet. Catal. Lett. 58 (1996) 391-396.

[5.73] G. W. Haddix, J. A. Reimer and A. T. Bell, *Characterization of H_2 adsorbed on gamma-Mo_2N by NMR-spectroscopy*, J. Catal. 108 (1987) 50-54.

[5.74] Z. Wu, S. Yang, Q. Xin and C. Li, *In situ IR spectroscopic studies on molybdenum nitride catalysts: active sites and surface reactions*, Catal. Survey. Asia 7 (2003) 103-119.

[5.75] A. Ramasubramaniam, M. Itakura, M. Ortiz and E. A. Carter, *Effect of atomic scale plasticity on hydrogen diffusion in iron: Quantum mechanically informed and on-the-fly kinetic Monte Carlo simulations*, J. Mater. Res. 23 (2008) 2757-2773.

[5.76] R. Matsumoto, M. Riku, S Taketomi and N. Miyazaki, *Hydrogen-Grain Boundary Interaction in Fe, Fe-C, and Fe-N Systems*, J. Nucl. Sci. Technol. 2 (2011) 9-15.

[5.77] K. J. Bryden and J. Y. Ying, *Nanostructured palladium-iron membranes for hydrogen separation and membrane hydrogenation reactions*, J. Membr. Sci. 203 (2002) 29-42.

[5.78] P. T. Anastas, M. M. Kirchhoff and T. C. Williamson, *Catalysis as a foundational pillar of green chemistry*, Appl. Catal. A: General 221 (2001) 3-13.

[5.79] K. Koprivova and L. Červený, *Hydrogenation of nitrobenzonitriles using Raney nickel catalyst*, Res. Chem. Intermed. 34 (2008) 93-101.

[5.80] S. R. Kanth, G. V. Reddy, V. V. V. N. S. R. Rao, D. Maitraie, B. Narsaiah and P. S. Rao, *A simple and convenient method for the reduction of nitroarenes*, Synth. Commun. 32 (2002) 2849-2853.

[5.81] S. U. Sonavane, M. B. Gawande, S. S. Deshpande, A. Venkataraman and R. V. Jayaram, *Chemoselective transfer hydrogenation reactions over nanosized gamma-Fe_2O_3 catalyst prepared by novel combustion route*, Catal. Commun. 8 (2007) 1803-1806.

[5.82] S. Meijers and V. Ponec, *Infrared spectroscopic study of the adsorption of nitro-compounds and amines on cobalt oxide*, J. Catal. 149 (1994) 307-316.

[5.83] E. A. Gelder, *The hydrogenation of nitrobenzene over metal catalysts* in PhD thesis, University of Glasgow, UK, 2004.

[5.84] M. T. Nguyen, *The chemistry of anilines* in Patai Series: The chemistry of Functional Groups, Z. Rappoport (Ed.), Wiley, 2007, Chichester, pp.79-80.

[5.85] L. J. Deiner, D. H. Kang and C. A. Friend, *Low-temperature reduction of NO_2 on oxidized Mo(110)*, J. Phys. Chem. B 109 (2005) 12826-12831.

[5.86] S. W. Yang, Y. X. Li, J. Xu, C. Li, Q. Xin, I. Rodriguez-Ramos and A. Guerrero-Ruiz, *FTIR study of CO and NO adsorbed on nitrided $CoMo/Al_2O_3$ catalysts*, Phys. Chem. Chem. Phys. 2 (2000) 3313-3317.

[5.87] A. de Lucas Consuegra, P. M. Patterson and M. A. Keane, *Use of unsupported and silica supported molybdenum carbide to treat chloroarene gas streams*, Appl. Catal. B: Environmental 65 (2006) 227-239.

[5.88] S. T. Srinivas, L. J. Lakshmi, N. Lingaiah, P. S. S. Prasad and P. K. Rao, *Selective vapour-phase hydrodechlorination of chlorobenzene over alumina supported platinum bimetallic catalysts*, Appl. Catal. A: General 135 (1996) L201-L207.

[5.89] H. Q. Li, S. J. Liao, Y. Xu and D. R. Yu, *Highly active polymer-supported palladium-cobalt catalysts for the hydrodechlorination of organic chlorides*, Synth. Commun. 27 (1997) 829-836.

[5.90] Y. A. Serguchev and Y. V. Belokopytov, *Kinetics and mechanism of the heterogeneous catalytic hydrogenolysis of chlorobenzenes and chlorocydohexanes*, Kinet. Catal. 42 (2001) 174-181.

[5.91] Z. L. Wu, C. Li, P. L. Ying, Z. B. Wei and Q. Xin, *Low-temperature isomerization of 1-butene on Mo_2N/gamma-Al_2O_3 catalyst studied by in situ FT-IR spectroscopy*, J. Phys. Chem. B 105 (2001) 9183-9190.

[5.92] M. Yamada, J. Yasumaru, M. Houalla and D. M. Hercules, *Distribution of molybdenum oxidation-states in reduced Mo/Al_2O_3 catalysts. Correlation with benzene hydrogenation activity*, J. Phys. Chem. 95 (1991) 7037-7042.

[5.93] J. Chen, N. Yao, R. Wang and J. Zhang, *Hydrogenation of chloronitrobenzene to chloroaniline over Ni/TiO_2 catalysts prepared by sol-gel method*, Chem. Eng. J. 148 (2009) 164-172.

[5.94] Y. Hao, R. Liu, X. Meng, H. Cheng and F. Zhao, *Deactivation of Au/TiO_2 catalyst in the hydrogenation of o-chloronitrobenzene in the presence of CO_2*, J. Mol. Catal. A: Chemical 335 (2011) 183-188.

[5.95] P. Sangeetha, P. Seetharamulu, K. Shanthi, S. Narayanan and K. S. Rama Rao, *Studies on Mg-Al oxide hydrotalcite supported Pd catalysts for vapor phase hydrogenation of nitrobenzene*, J. Mol. Catal. A: Chemical 273 (2007) 244-249.

[5.96] M. V. Twigg and M. S. Spencer, *Deactivation of supported copper metal catalysts for hydrogenation reactions*, Appl. Catal. A: General 212 (2001) 161-174.

Chapter 6

New Insights into the Effect of Nitrogen Incorporation in Mo: Significance in Catalytic Hydrogenation

In Chapter 2 and Chapter 3, β-Mo_2N was shown to exhibit catalytic activity in hydrogenation of nitro-compounds. In this Chapter, the catalytic activity of Mo metal and the role of nitrogen in Mo nitride for -NO_2 and C=O reduction are assessed.

6.1 Introduction

The application of Mo nitrides in catalytic hydrotreatment is now established [6.1-3] with higher activity relative to commercial Ni-Mo/Al_2O_3 in hydrodesulfurisation [6.1] and hydrodenitrogenation [6.2]. Enhanced hydrogenation selectivity has also been reported with respect to conventional supported metal (*e.g.* Pd or Pt) catalysts [6.4,6.5]. The two allotropic forms (cubic γ-Mo_2N and tetragonal β-Mo_2N) have shown different catalytic properties where β-Mo_2N has delivered higher specific (*i.e.* surface area normalised) hydrogenation rates [6.6-9]. While the catalytic application of γ-Mo_2N has been the subject of appreciable research [6.10-13], the use of β-Mo_2N has not been considered to the same extent. Nevertheless, β-Mo_2N has been employed to promote hydrodenitrogenation of carbazole [6.14], hydrodesulfurisation of thiophene [6.15] and dibenzothiophene [6.16] and in ammonia synthesis [6.6]. Moreover, the results presented in Chapter 2 and Chapter 3 demonstrated activity and selectivity for β-Mo_2N in the hydrogenation of nitro-compounds.

An explicit identification of the catalytically active site remains challenging. It is generally accepted that the adsorption and catalytic properties of transition metal nitrides in hydrogen mediated reactions are governed by bulk structure and surface composition where Mo oxidation state, degree of nitridation, Mo (and nitrogen deficient Mo nitride) site density are critical parameters [6.17]. In the hydrogenation of alkadiene, Mo species at lower oxidation states ($Mo^{\delta+}$ where $0 \leq \delta < 4$) were proposed to exhibit higher activity, which was attributed to a more effective alkadiene activation [6.18]. Change in bulk structure can influence the distribution of exposed planes, which impacts on surface interactions. An observed [6.2,6.17] dependence of pyridine

hydrodenitrogenation on surface Mo/N serves to illustrate the importance of the degree of nitridation in the catalytic response. On the one hand, an increased in activity was recorded at low ratios as a result of enhanced pyridine activation [6.17]. On the other hand, H_2 adsorption was proposed to take place in nitrogen deficient sites (*i.e.* more abundant in nitrides with high Mo/N ratios) [6.2]. Metallic Mo edge and nitrogen deficient sites have been proposed as the source of appreciable hydrogenation and hydrogenolysis activity [6.7,6.12,6.19-21] but the specific contribution of each in terms of hydrogen and/or organic reactant activation remains unresolved. Indeed, while there is some evidence that H_2 adsorbs on Mo_2N at nitrogen deficient sites [6.12,6.19], it has also been suggested that the activity response in the hydrogenation of carbazole (to perhydrocarbazole) [6.7,6.20], indole (to indoline) [6.21] and butadiene (to butane) [6.12] is related to the action of metallic Mo. Moreover, carbazole and perhydrocarbazole C-N hydrogenolysis is thought to proceed on N deficient sites [6.7,6.20] whereas hydrogenolysis of the indoline C-N bond occurs on Mo sites [6.21].

β-Mo_2N can be synthesised *via* temperature programmed reduction/nitridation of MoO_3 in N_2/H_2 [6.6,6.15,6.22]. Nitride formation follows a non-topotactic route, *i.e.* disruption of reactant morphology, with a stepwise reduction ($MoO_3 \rightarrow MoO_2 \rightarrow Mo$) and subsequent nitridation [6.23,6.24]. The oxide precursor (MoO_3) can be reduced to Mo in a flow of H_2 at temperatures in excess of 933 K [6.15,6.24,6.25]. Metallic Mo has exhibited catalytic activity in a range of hydrogen mediated reactions, including hydrogenation of benzene [6.25], 1-hexene [6.26,6.27], alkadiene [6.18] and hydrogenolysis of propanol [6.28]. A search through the literature revealed only one study that considered the catalytic action of β-Mo_2N in relation to Mo where the former delivered higher carbazole hydrodenitrogenation but lower hydrogenation rates [6.7]. This was attributed to different active site requirements for hydrogen scission (N deficient Mo nitride) and addition (Mo) steps.

In this Chapter, the catalytic consequence of N incorporating in Mo is examined. The Mo/N content can be effectively controlled by varying the duration or temperature of the nitridation step [6.15,6.29]. Drawing on Chapter 2 and 3 that have established nitro-group hydrogenation activity and selectivity for β-Mo_2N, nitrobenzene and *p*-chloronitrobenzene are employed as model reactants. The catalytic testing is extended to evaluate carbonyl group reduction, taking benzaldehyde as reactant.

6.2 Experimental

6.2.1 Catalyst Preparation

Bulk Mo (metal) preparation was conducted in a horizontally mounted quartz reactor (1 cm i.d.) *via* the temperature programmed reduction of MoO_3 (*ca.* 4 g, 99.9995%, Alfa Aesar) in pure H_2 (30 cm^3 min^{-1}, GHSV = 460 h^{-1}) at 5 K min^{-1} to 933 K, maintaining the final temperature for 75 h then switching to an Ar flow (30 cm^3 min^{-1}) for 30 min and cooling to ambient temperature. Samples for off-line analysis were passivated at 298 K in 1% v/v O_2/He; no increase in temperature was detected during passivation. The latter step was introduced to avoid uncontrolled sample oxidation upon exposure to air [6.30].

The Mo powder obtained was subjected to temperature programmed nitridation in H_2/N_2, using a commercial CHEM-BET 3000 (Quantachrome) unit. The Mo precursor was loaded in a quartz cell (3.76 mm i.d.) and contacted with 15 cm^3 min^{-1} (GHSV = 1500 h^{-1}) 15% v/v H_2/N_2, maintained at 293 K for 1 h and then heated at 5 K min^{-1} to 933 K. The effluent gas passed through a liquid N_2 trap and changes in N_2 and H_2 consumption were monitored by a thermal conductivity detector (TCD) with data acquisition/manipulation using the TPR Win^{TM} software. The TCD response is presented in **Figure 6.1**.

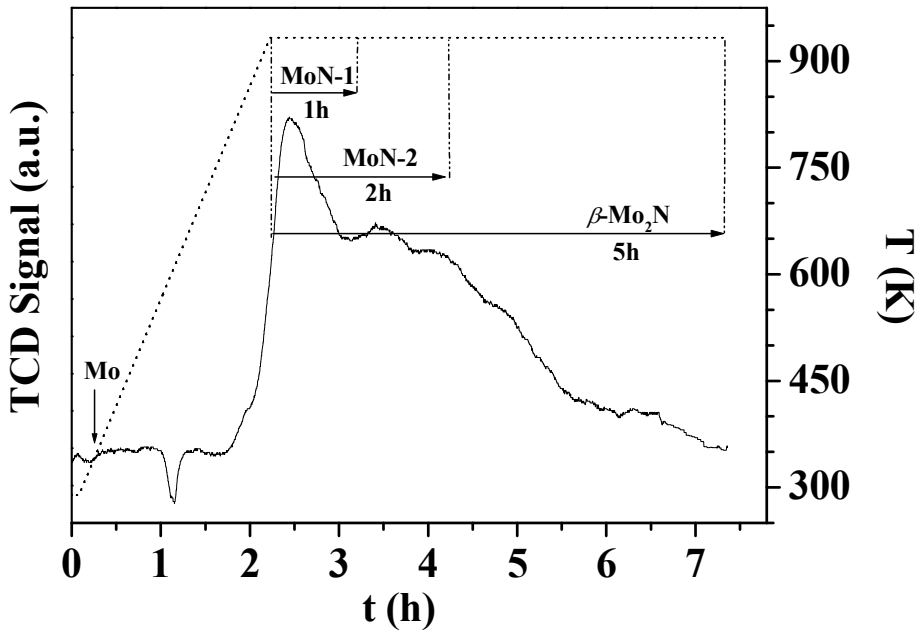

Figure 6.1: TCD response resulting from the temperature programmed treatment of Mo at 5 K min^{-1} to 933 K in 15% v/v N_2/H_2. The final isothermal hold was maintained for 1 h, 2 h and 5 h (see solid arrow) for the formation of MoN-1, MoN-2 and β-Mo_2N, respectively.

The final temperature (933 K) was maintained for 5 h at which point the signal returned to baseline, *i.e.* nitridation was complete. It is known [6.29] that altering the duration of the final isothermal hold can affect the degree of nitridation. Two partially nitrided samples, denoted as MoN-1 and MoN-2, were accordingly generated by maintaining the final temperature for 1 h and 2 h, respectively (see **Figure 6.1**). The reaction was then quenched by switching to an Ar flow (65 cm^3 min^{-1}) and the samples cooled to ambient temperature, followed by passivation as described above.

6.2.2 Characterisation

Temperature programmed reduction (TPR) of the passivated samples, BET surface area, H_2 chemisorption and temperature programmed desorption (TPD) were determined using the CHEM-BET 3000 unit. Passivated samples (Mo, MoN-1, MoN-2 and β-Mo_2N) were loaded in a quartz cell and heated in 17 cm^3 min^{-1} 5% v/v H_2/N_2 at 5 K min^{-1} to 673 K. The activated samples were maintained at the final temperature in a constant flow of H_2/N_2 until return of the signal to baseline, swept with 65 cm^3 min^{-1} N_2 for 1.5 h and cooled to ambient temperature. The samples were then subjected to H_2 chemisorption (at 298 K) using a pulse (10 µl) titration procedure, followed by temperature programmed desorption (TPD) in N_2 (65 cm^3 min^{-1}) at 45 K min^{-1} to 933 K. BET areas were determined in 30% v/v N_2/He using N_2 as internal standard. At least 3 cycles of N_2 adsorption-desorption in the flow mode were employed to determine the total area using the standard single point method. The measurements were reproducible to within ± 6% and the values quoted represent the mean.

Powder X-ray diffractograms were recorded on a Bruker/Siemens D500 incident X-ray diffractometer using Cu Kα radiation. The samples were scanned at a rate of 0.02º $step^{-1}$ over the range $5º \leq 2\theta \leq 85º$. Diffractograms were identified using the JCPDS-ICDD reference standards, *i.e.* Mo (42-1120) and β-Mo_2N (25-1368). Crystal particle size (d_{hkl}) was estimated using the Scherrer equation:

$$d_{hkl} = \frac{K \times \lambda}{\beta \times \cos\theta} \qquad \textbf{(6.1)}$$

where $K = 0.9$, λ is the incident radiation wavelength (1.5056 Å), β is the peak width at half the maximum intensity and θ represents the diffraction angle corresponding to the main plane associated with Mo ($2\theta = 40.5°$) and β-Mo_2N ($2\theta = 37.7°$). Elemental (bulk

nitrogen) analyses were conducted using an Exeter CE-440 Elemental Analyser after sample combustion at *ca.* 1873 K.

Analysis by scanning electron microscopy (SEM) was carried out with a Philips FEI XL30-FEG equipped with an Everhart-Thornley secondary-electron (SE) detector, operated at an accelerating voltage of 10-15 kV and using NORAN System SIX (version 1.6) for data acquisition/manipulation. Before analysis, the samples were subjected to hydrocarbon decontamination using a plasma-cleaner (EVACTRON). X-ray photoelectron spectroscopy (XPS) measurements were conducted using an Axis Ultra instrument (Kratos) with a monochromatic Al Kα X-ray source (1486.6 eV). Prior to analysis, the samples were adhered to a conducting carbon tape, mounted in the sample holder and subjected to ultra-high vacuum conditions (< 10^{-8} Torr). The source power was maintained at 150 W and the emitted photoelectrons were sampled from a square area of 750×350 μm^2; the photoelectron take-off angle was 90°. The analyser pass energy was 80 eV for survey spectra (0–1000 eV) and 40 eV for high resolution spectra (over the Mo $3d_{3/2}$ and Mo $3d_{5/2}$ binding energy (BE) range, 226-238 eV). The adventitious C 1*s* peak was calibrated at 284.5 eV and used as internal standard to compensate for any charging effects. The instrument work function was calibrated to give a BE of 84.00 eV for the Au $4f_{7/2}$ line for metallic gold (Metalor) and the spectrometer dispersion was adjusted to give a BE of 932.70 eV for the Cu $2p_{3/2}$ line for metallic copper (Metalor). Spectral curve quantification employed the CasaXPS software, using relative sensitivity factors provided by Kratos.

6.2.3 Catalysis Procedure

The catalytic conversion of nitrobenzene, *p*-chloronitrobenzene and benzaldehyde was carried out under atmospheric pressure at T = 493-523 K, *in situ* immediately after activation, in a fixed bed vertical glass tubular reactor (i.d. = 15 mm). The reactions were conducted under operating conditions where heat/mass transport limitations were negligible. A layer of borosilicate glass beads served as preheating zone, ensuring that the organic reactant was vaporised and reached reaction temperature before contacting the catalyst. The reaction temperature was continuously monitored using a thermocouple inserted in a thermowell within the catalyst bed.

Each reactant (as a solution in ethanol) was delivered at a fixed calibrated flow rate (1.2 $cm^3\ h^{-1}$) *via* a glass/Teflon air-tight syringe and Teflon line using a microprocessor controlled infusion pump (Model 100 kd Scientific). A *co*-current flow of the reactant and ultra pure H_2 (< 1% v/v organic in H_2) was maintained at a GHSV = $2\times10^4\ h^{-1}$ with an inlet reactant molar flow (F) of 9-46 μmol h^{-1}. The H_2 content was well in excess of the stoichiometric requirement (for the observed products) and the flow rate was monitored using a Humonics (Model 520) digital flowmeter. The mass of catalyst to inlet reactant molar feed rate (m/F) spanned the range 131-5281 g h mol^{-1}. The catalytic hydrogen treatment of benzyl alcohol was carried out over Mo and β-Mo_2N under similar reaction conditions to those used for benzaldehyde (T = 523 K, m/F = 1250-2083 g h mol^{-1}) in order to investigate the carbonyl reduction pathway. In a series of blank tests, passage of each reactant in a stream of H_2 through the empty reactor did not result in any detectable conversion. The reactor effluent was frozen in a liquid nitrogen trap for subsequent analysis, which was made using a Perkin-Elmer Auto System XL gas chromatograph equipped with a programmed split/splitless injector and a flame ionization detector, employing a DB-1 50 m×0.33 mm i.d., 0.20 μm film thickness capillary column (J&W Scientific). Nitrobenzene (Fluka, purity ≥ 99%), *p*-chloronitrobenzene (Sigma-Aldrich, ≥ 99%), benzaldehyde (Fluka, ≥ 98%), benzyl alcohol (Riedel-de Haën, ≥ 99%) and ethanol (Sigma Aldrich, ≥ 99%) were used as supplied without further purification. All the gases (H_2, N_2, Ar, O_2 and He) employed were of ultra high purity (> 99.99%, BOC). Reactant fractional conversion ($X_{p\text{-CNB}}$), taking *p*-chloronitrobenzene (*p*-CNB) as representative, was obtained from

$$X_{p-CNB} = \frac{[p-\text{CNB}]_{in} - [p-\text{CNB}]_{out}}{[p-\text{CNB}]_{in}} \qquad \textbf{(6.2)}$$

and selectivity with respect to *p*-chloroaniline (*p*-CAN), as the target product, is given by

$$S_{p-CAN}(\%) = \frac{[p-\text{CAN}]_{out}}{[p-\text{CNB}]_{in} - [p-\text{CNB}]_{out}} \times 100 \qquad \textbf{(6.3)}$$

Repeated reactions with different samples from the same batch of catalyst delivered conversion/selectivity values that were reproducibility to within ± 4%.

6.3 Results and Discussion

6.3.1 Mo Nitride Synthesis and Characterisation

Treatment of MoO_3 in H_2 to 933 K generated solely Mo, as confirmed by XRD analysis (**Figure 6.2(a)**) where the peaks at 40.5°, 58.6° and 73.7° match the JCPDS-ICDD reference standard (42-1120) in terms of both position and relative peak intensities. There were no detectable peaks associated with the main planes of MoO_3 or MoO_2 based on JCPDS-ICDD cards (35-0609) and (32-0671), respectively.

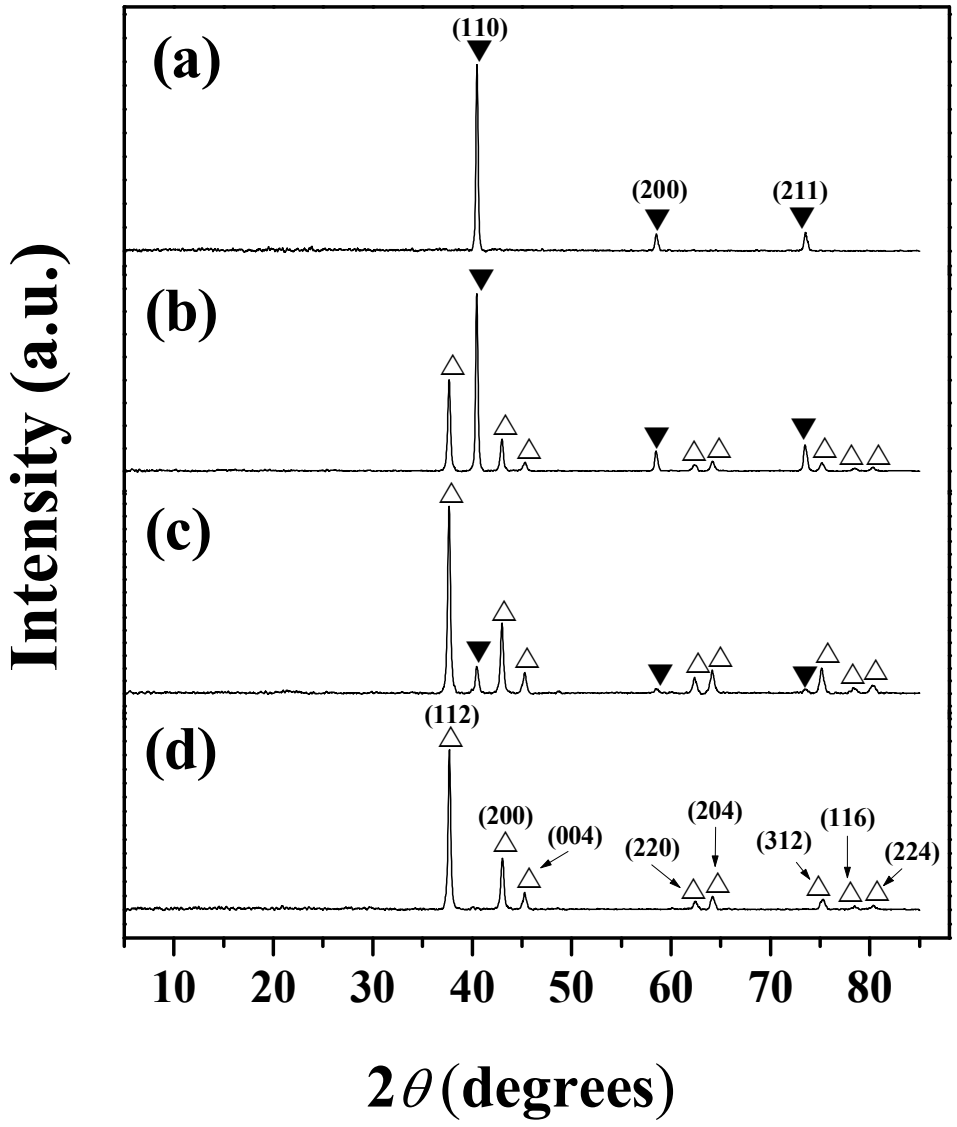

Figure 6.2: XRD patterns with crystallographic plane characteristic of each peak associated with (a) Mo, (b) MoN-1, (c) MoN-2 and (d) *β*-Mo_2N. XRD peak assignments are based on JCPDS-ICDD reference data: (▼) Mo (42-1120) and (△) *β*-Mo_2N (25-1368).

The Scherrer expression (eqn. (6.1)) was used to calculate Mo crystal size (d_{hkl} = 36 nm, **Table 6.1**), which falls within the range (10-100 nm) of values quoted in the literature [6.31]. SEM analysis was conducted to evaluate morphological features and a representative micrograph of Mo is shown in **Figure 6.3(a)**, which reveals irregularly shaped aggregates (< 5 μm). The associated BET area is low (*ca*. 4 m^2 g^{-1}, **Table 6.1**) but comparable to that recorded for both commercial and laboratory synthesised Mo samples (1-13 m^2 g^{-1}) [6.31].

Table 6.1: Bulk β-Mo_2N:Mo ratios from XRD analysis, BET surface area, bulk (from N_2 consumption during nitridation and elemental analysis) and surface (from XPS analysis) Mo/N with XPS binding energies (BE) for Mo $3d_{3/2}$ and Mo $3d_{5/2}$.

Catalysts	Mo	MoN-1	MoN-2	β-Mo_2N
β-Mo_2N:Mo[a]	-[b]	0.34:0.66	0.88:0.12	-[c]
BET (m^2 g^{-1})	3.9	4.5	4.1	4.4
Bulk Mo/N	-	5.1[d]/4.9[e]	2.8[d]/2.8[e]	2.5[d]/2.6[e]
Surface Mo/N	-	2.2	1.1	0.9
Mo 3*d* BE (eV)	231.3 228.0	231.7 228.4	231.8 228.6	231.8 228.5

[a]from XRD analysis
[b]d_{hkl} = 36 nm using (110) plane associated with Mo at $2\theta = 40.5^{\circ}$ (see eqn. (6.1))
[c]d_{hkl} = 27 nm using (112) plane associated with β-Mo_2N at $2\theta = 37.7^{\circ}$ (see eqn. (6.1))
[d]from N_2 consumption during nitridation
[e]from elemental analysis

The TCD response generated during the nitridation of Mo is shown in **Figure 6.1**. The negative peak, observed during the temperature ramp can be attributed to H_2 consumption due to the removal of the passivation layer (see experimental section) before incorporation of nitrogen. Nitrogen consumption generated a broad positive signal with a return to baseline after the isothermal hold for 5 h, indicating complete nitridation of the sample. The bulk Mo/N ratio for β-Mo_2N obtained from N_2 consumed during nitridation matches that obtained from elemental analyses (**Table 6.1**) and is in good agreement with the literature (2.5-2.8) [6.6,6.7,6.22]. XRD analysis (**Figure 6.2(d)**) confirms full nitridation with no additional peak(s) due to residual Mo in

evidence. The 8 peaks identified are consistent with the main reflections of β-Mo_2N (JCPDS-ICDD reference 25-1368). A particle size (d_{hkl}, **Table 6.1**) of 27 nm is in the upper range of values (3-30 nm) reported previously [6.7,6.9,6.32]. The BET surface area is similar to that of the starting Mo (*ca.* 4 m^2 g^{-1}) and comparable with values (2-17 m^2 g^{-1}) [6.6,6.15,6.24] recorded for β-Mo_2N synthesised *via* temperature programmed reaction in N_2+H_2.

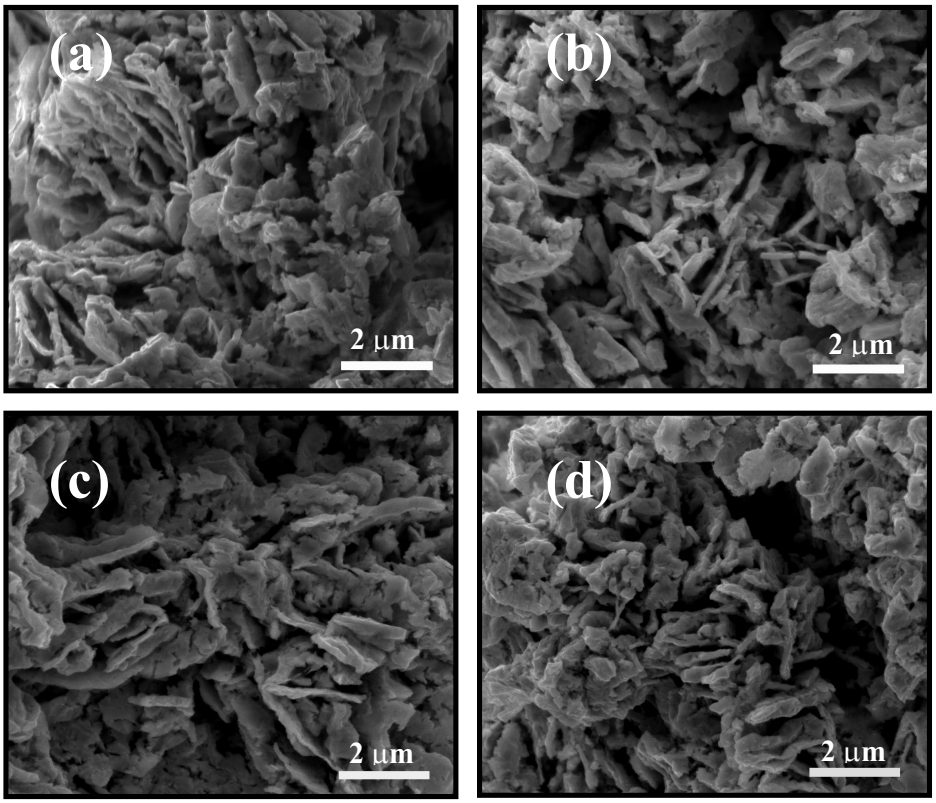

Figure 6.3: Representative SEM micrographs for (a) Mo, (b) MoN-1, (c) MoN-2 and (d) β-Mo_2N.

In order to probe the catalytic effect due to nitrogen incorporation, two additional samples (MoN-1 and MoN-2) were generated by modifying the duration of the nitridation step (1-2 h, **Figure 6.1**). The XRD diffractograms shown in **Figure 6.2** for **(b)** MoN-1 and **(c)** MoN-2 exhibit only peaks due to Mo or β-Mo_2N. The intensity ratio of the principal plane for β-Mo_2N (at 37.7º) relative to that of Mo (40.5º) was used to estimate the β-Mo_2N:Mo ratios presented in **Table 6.1** where a higher Mo_2N content is established for the composite sample (MoN-2) that was subjected to nitridation for 2 h.

The bulk Mo/N measured from N_2 consumption and elemental analysis of the solid samples are again in good agreement where the ratios follow the order MoN-1 > MoN-2

> β-Mo_2N. Representative micrographs for **(b)** MoN-1, **(c)** MoN-2 and **(d)** β-Mo_2N shown **Figure 6.3** reveal an equivalent overall morphology to that exhibited by the starting Mo, as noted previously [6.23,6.24]. In previous work [6.24], we proposed that a disruption of the crystal structure occurs during the $MoO_3 \rightarrow MoO_2$ reduction step and the resultant structure is retained in the subsequent steps $MoO_2 \rightarrow Mo \rightarrow \beta$-$Mo_2N$. This is in agreement with the results presented here where the switch from a body-centred cubic to tetragonal structure with nitrogen incorporation was not accompanied by any distinguishable variation in morphology or surface area (**Table 6.1**).

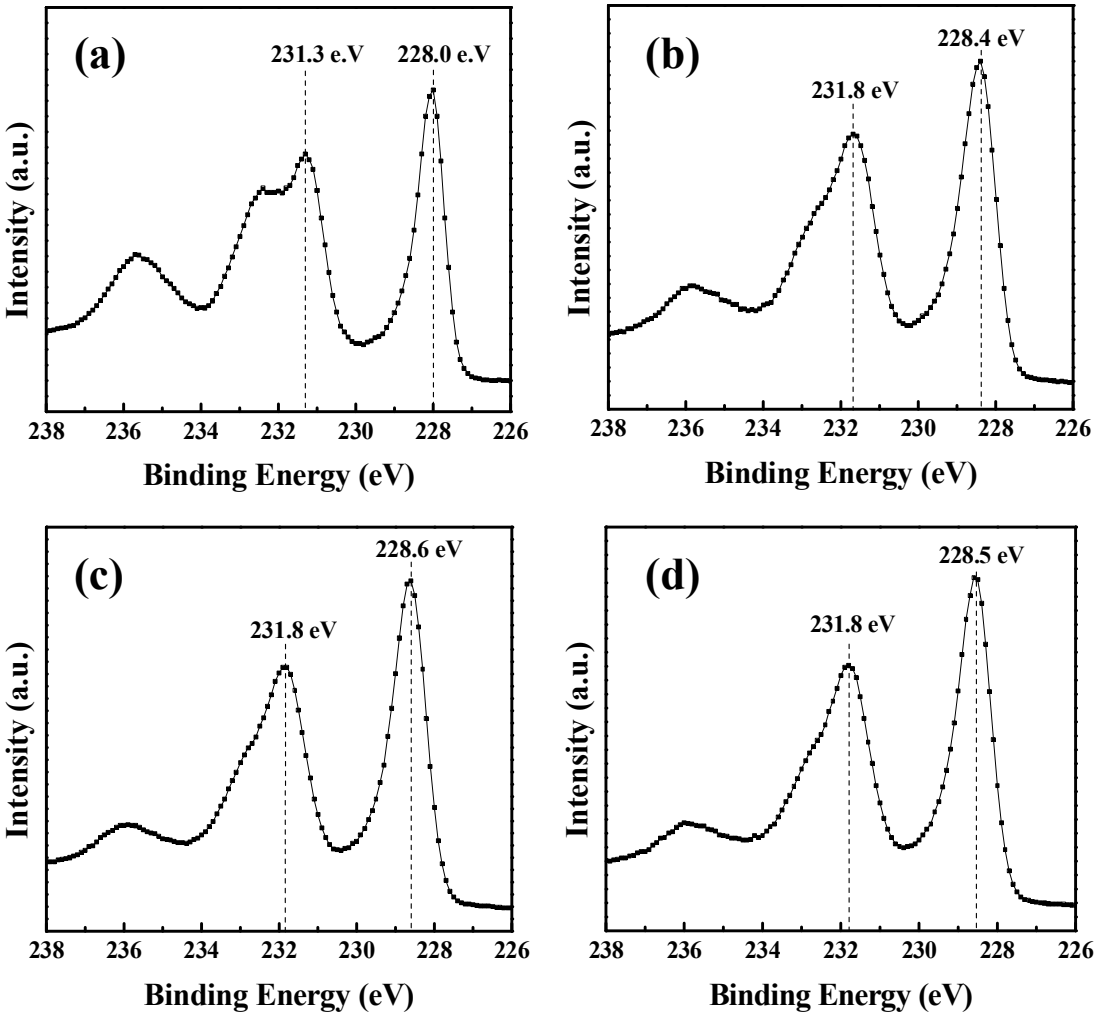

Figure 6.4: XPS spectra in the Mo 3*d* region for (a) Mo, (b) MoN-1, (c) MoN-2 and (d) β-Mo_2N.

XRD and elemental analyses provide information on bulk properties but these can differ significantly from surface characteristics [6.33]. As the catalytic step proceeds on the surface actives sites, complementary characterisation of surface composition is essential. The XPS profile measured for Mo **(Figure 6.4(a))** is dominated by a peak with a binding energy (BE) = 228.0 eV, which can be attributed to $Mo^{\delta+}$ ($0 \leq \delta < 2$) for passivated Mo. While metallic Mo is characterized by a Mo $3d_{5/2}$ spin component at 227.8 ± 0.1 eV [6.26,6.27,6.34], the formation of a passivating oxide layer is known to shift the peak to higher BE [6.18,6.27]. The XPS profile for β-Mo_2N **(Figure 6.4(d))** exhibits a main peak at higher BE (= 228.5 eV) that is characteristic of $Mo^{\delta+}$ ($2 \leq \delta < 4$) for passivated β-Mo_2N [6.32,6.35,6.36]. The second spin component for both Mo and β-Mo_2N (BE include **Table 6.1**), can be ascribed to contributions from Mo^{4+} (229.9 eV [6.25]) and Mo^{5+} (231.6 eV, [6.30,6.37]) species. The Mo $3d_{5/2}$ signal for β-Mo_2N is shifted to a significantly higher BE (by 0.5 eV) relative to Mo, suggesting differences in oxidation state for both samples. The XPS response for MoN-1 **(b)** and MoN-2 **(c)** largely converges with the profile for β-Mo_2N, with a main peak at 228.5 ± 0.1 eV. The results suggest there is no significant influence due to the degree of nitridation on the distribution of Mo valence state, in agreement with previous literature [6.29]. The signal at higher BE (235.7-236.0 eV) for the four samples can be related to the occurrence of Mo^{6+} resulting from the passivation step [6.6,6.37]. Surface Mo/N obtained from XPS (**Table 6.1**) demonstrate decreasing Mo/N with increasing nitridation and a surface enrichment by nitrogen relative to bulk values. Demczyk and co-workers [6.33] also observed a higher surface nitrogen content and attributed this to a stoichiometry (possibly $Mo_2N_{3-x}O_x$) that differs from the bulk. Moreover, Ghampson *et al.* [6.9] proposed that nitrogen can be accommodated on the near surface at interstitial sites and defects, such as grain boundaries leading to lower Mo/N.

6.3.2 Hydrogen Uptake and Release

Removal of the protective passivation layer prior to catalysis was achieved by temperature programmed reduction (TPR). The profile for passivated Mo is presented in **Figure 6.5(aI)** and shows a single positive peak at 673 K. Li *et al.* [6.18] also applied a reductive treatment (in H_2 at 723 K) to remove the passivation layer from Mo but did not provide any detailed TPR analysis. TPR of β-Mo_2N **Figure 6.5(aII)** also exhibited a similar H_2 consumption with a T_{max} that is within the 590-780 K range reported for passivated Mo_2N [6.13,6.38]. The TPR profiles for MoN-1 and MoN-2 (not shown)

generated an equivalent response in terms of peak intensity and temperature. The passivation treatment can be taken to result in a monolayer oxygen coverage and H_2 consumed during TPR should be proportional to surface area. Equivalency in H_2 consumption for the four samples (**Table 6.2**) is consistent with the similar total (BET) area (*ca.* 4 m^2 g^{-1}).

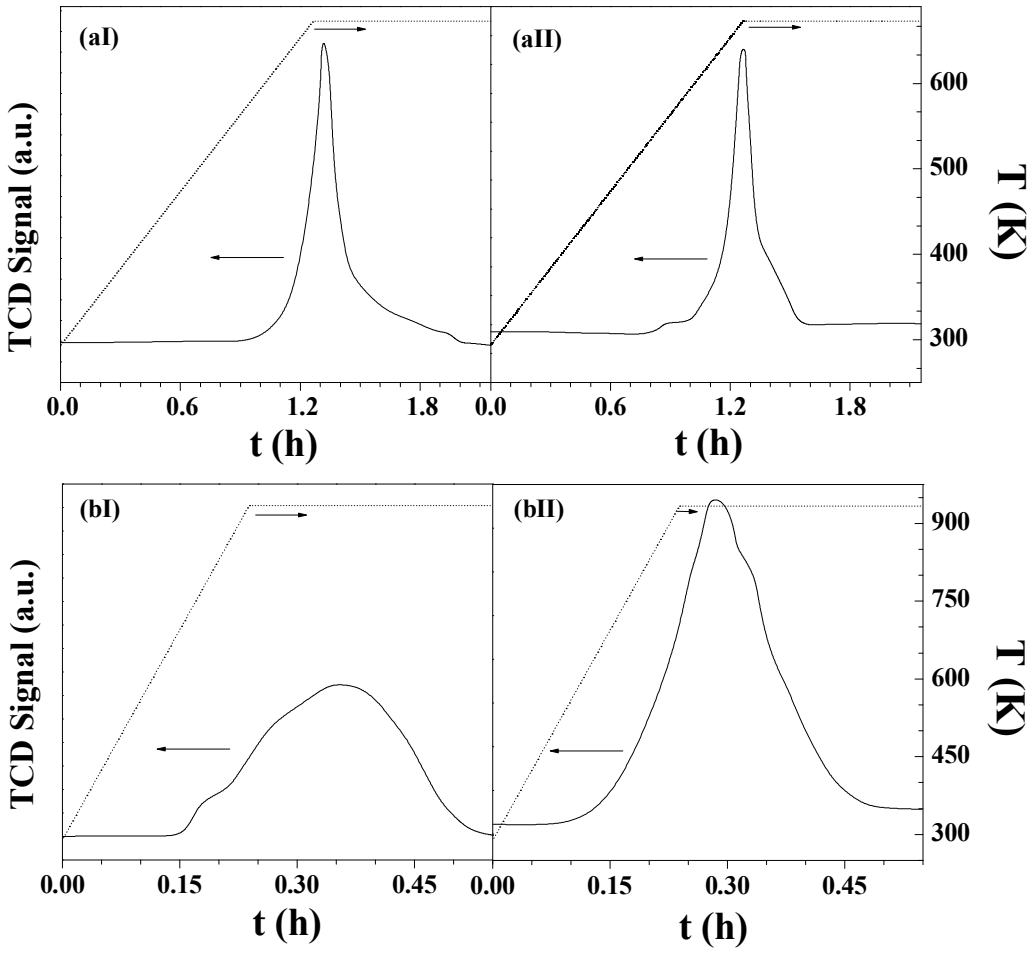

Figure 6.5: H_2 (a) TPR and (b) TPD profiles (solid lines) with temperature ramp (dotted lines) generated for passivated (I) Mo and (II) β-Mo_2N.

There is evidence in the literature [6.12,6.39-41] that the incorporation of N in Mo creates supplementary sites that can modify reactant (H_2 and organic) adsorption and alter the catalytic response. Hydrogen interaction with metallic Mo can lead to homolytic dissociation [6.42] while heterolytic dissociation on Mo-N pairs results in Mo-H and N-H formation [6.43,6.44]. Both dissociation mechanisms are possible for Mo nitride but heterolytic interaction is favoured on coordinatively unsaturated Mo sites

[6.44]. Hydrogen uptake and release (by temperature programmed desorption (TPD)) were measured and the results are given in **Table 6.2**. The available literature on the dynamics of H_2 interaction with Mo is limited [6.45-47]. ARPES [6.46] and LEED [6.47] analyses have shown that H_2 can adsorb on the (110) plane of Mo but quantitative measurements were not provided in these studies. We recorded a total H_2 uptake of 0.23 μmol g^{-1} on Mo during pulse chemisorption measurements at ambient temperature but could not find any value to compare this with in the open literature. A measurably higher H_2 uptake was observed for β-Mo_2N (0.35 μmol g^{-1}, **Table 6.2**). Adsorption on MoN-1 and MoN-2 delivered intermediate values where uptake increased with increasing degree of nitridation.

Table 6.2: Hydrogen consumed during TPR with H_2 uptake in subsequent chemisorption and release during TPD.

Catalysts	Mo	MoN-1	MoN-2	β-Mo_2N
TPR H_2 consumption (μmol g^{-1})	141	143	151	174
H_2 chemisorption (μmol g^{-1})	0.23	0.26	0.33	0.35
H_2 TPD (μmol g^{-1})	5.5	5.6	7.1	7.9

Hydrogen TPD generated the profiles for **(I)** Mo and **(II)** β-Mo_2N shown in **Figure 6.5(b)**, which are characterised by H_2 release over a broad temperature interval with T_{max} in the final isothermal hold (933 K). Desorption at temperatures > 500 K have been associated with loss of H_2 from bulk (as opposed to surface) β-Mo_2N [6.48]. Hydrogen released during TPD (**Table 6.2**) was up to 30 times greater than that chemisorbed, suggesting that the majority of hydrogen uptake was generated during TPR. A migration of hydrogen to nitride sub-layers has been proposed, which results in strong interactions [6.43,6.44,6.48] and the requirement of elevated temperatures for release. The increase in H_2 chemisorption (and total release) in this study can be linked to lower surface (and bulk) Mo/N ratios, where the incorporation of nitrogen serves to facilitate H_2 uptake.

6.3.3 Catalytic Response: Nitro Group Reduction

The catalytic activity of Mo nitrides in nitro group reduction has been demonstrated [6.49,6.50]. We set out, in this work, to study the effect of N incorporation in Mo on nitroarene hydrogenation, taking Mo and β-Mo_2N as the two boundary systems. Hydrogenation of nitrobenzene generates aniline (**Figure 6.6(a)**), an important aromatic amine used as an intermediate in commercial dye, fine chemical (*e.g.* polyurethane) and pharmaceutical (*e.g.* antifebrin) manufacture [6.51]. This reaction has been extensively studied [6.52-54] and nitrobenzene is commonly used as a model reactant to test the catalytic potential of new systems for -NO_2 reduction. Nitrobenzene adsorption can proceed *via* the aromatic ring or the nitro group, where the latter has been shown to generate aniline [6.54,6.55]. Strong interaction through the aromatic ring can result in the formation of cyclohexylamine (over Ni film [6.56]) or nitrocyclohexane (over Rh complex [6.57]).

The four systems (Mo, MoN-1, MoN-2 and β-Mo_2N) considered in this study produced aniline as the sole product. While no published report of the application of Mo in the hydrogenation of nitro-compounds were found, IR analysis [6.58] has shown that NO_2 can adsorb on Mo (110). Previous work conducted in this laboratory established nitrobenzene hydrogenation to aniline over β-Mo_2N in liquid phase batch operation [6.49]. The data presented here confirm that this extends to continuous gas phase reaction where exclusivity to aniline as product suggests nitrobenzene activation on Mo and β-Mo_2N *via* the -NO_2 function. This is consistent with literature that has demonstrated weak interaction of the aromatic ring with MoO_3 [6.59], Mo nitride [6.49] and carbide [6.59,6.60].

Representative time on-stream nitrobenzene conversion (X_{NB}) profiles are presented in **Figure 6.7(a)**. In each case, there is a temporal decline in conversion that can be expressed in terms of the empirical relationship [6.55]

$$\frac{(X_{NB} - X_0)}{(X_{4h} - X_0)} = \frac{t}{(\beta + t)} \qquad \textbf{(6.4)}$$

where X_{4h} represents fractional conversion after 4 h on-stream and β is a time scale fitting parameter.

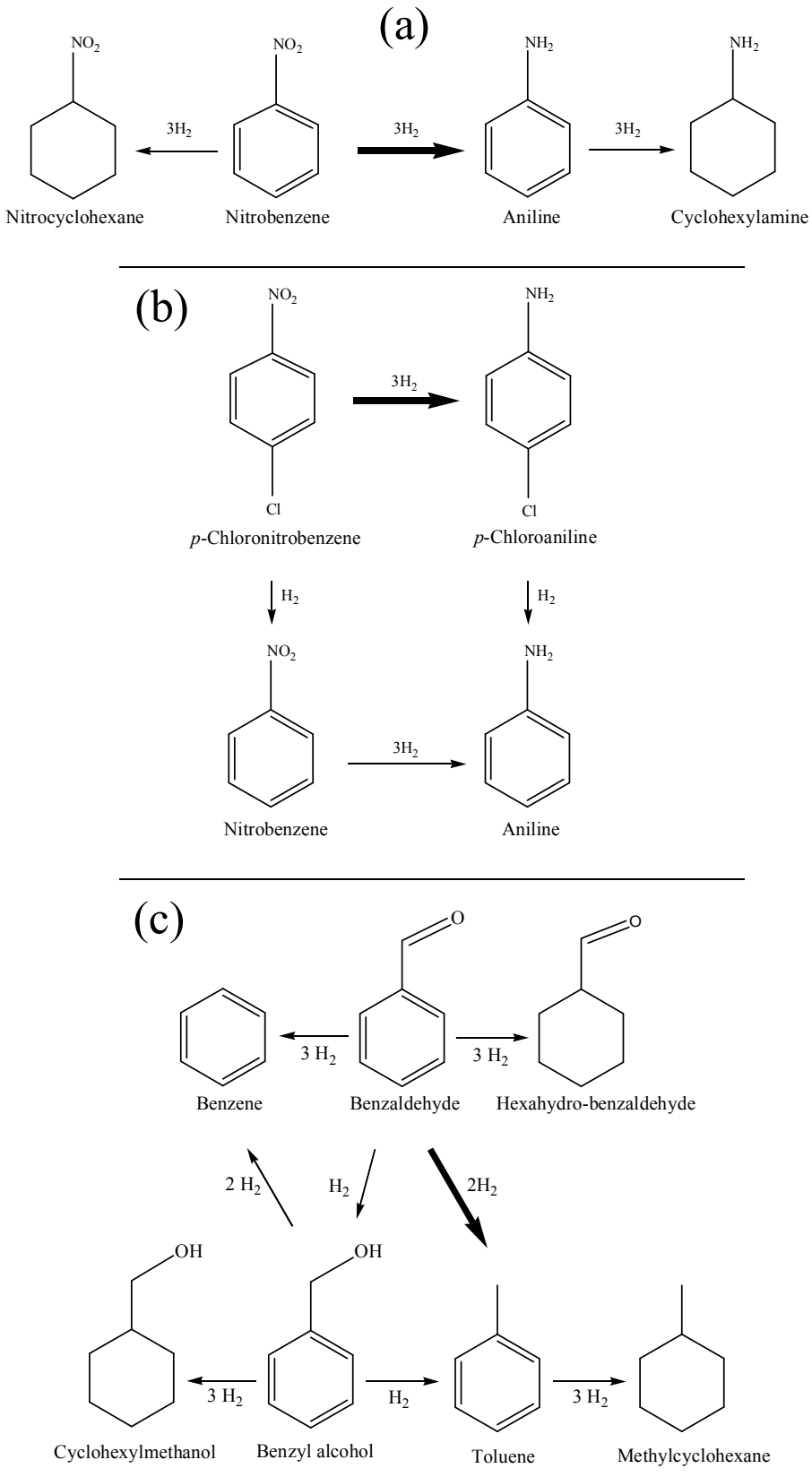

Figure 6.6: Reaction pathways reported for the hydrogenation of (a) nitrobenzene, (b) *p*-chloronitrobenzene and (c) benzaldehyde; solid arrows identify the steps observed in this study.

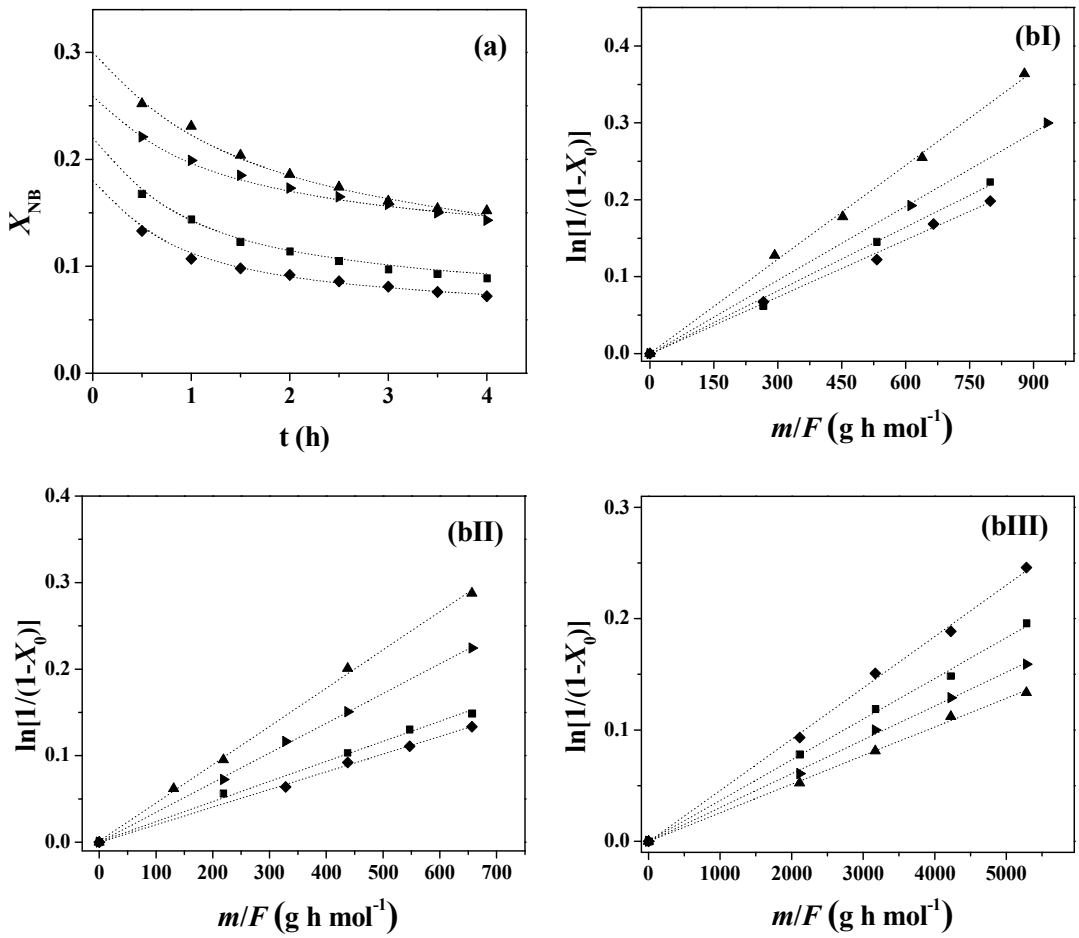

Figure 6.7: (a) Variation of nitrobenzene fractional conversion (X_{NB}) with time on-stream ($m/F \approx$ 800-900 g h mol^{-1}); (b) pseudo first order plots for hydrogenation of (I) nitrobenzene, (II) *p*-chloronitrobenzene and (III) benzaldehyde; Mo (♦), MoN-1 (■), MoN-2 (▶) and β-Mo_2N (▲).

Deactivation of Mo nitride in hydrotreating and hydrogenation reactions has been examined by IR [6.61] and XPS [6.62] and attributed to nitrogen loss and carbon deposition during reaction. Moreover, the water generated during -NO_2 reduction has been proposed to have a detrimental effect on activity [6.63]. Values for initial conversion (X_0) were obtained from the fit to Eqn (6.4), as shown in **Figure 6.7(a)**). The applicability of pseudo-first order kinetics has previously been established [6.8,6.24]

$$\ln(1-X_0)^{-1} = k\left(\frac{m}{F}\right) \qquad \textbf{(6.5)}$$

where m/F is the ratio of mass of catalyst to inlet nitrobenzene molar feed rate. The pseudo-first order kinetic plots are given in **Figure 6.7(bI)** where the linear fit (passing

through the origin) confirms adherence to the model. The extracted rate constants (k_1, μmol g^{-1} h^{-1}), given in **Table 6.3**, exhibit an increase in the order: Mo < MoN-1 < MoN-2 < β-Mo_2N. This matches the observed order of increasing H_2 chemisorption and release, as recorded in **Table 6.2**, which can, in turn, be correlated with increasing N content (decreasing Mo/N ratio, see **Table 6.1**). Nitrobenzene hydrogenation proceeds *via* a nucleophilic mechanism [6.54] where the polarised N=O function undergoes a nucleophilic hydrogen attack with the formation of a negatively charged intermediate. The higher rate observed due to N inclusion in Mo can be due to enhanced polarisation of the -NO_2 group. Indeed, HREELS analysis [6.41] has identified NO interaction with both Mo and N sites and -NO_2 activation may be sensitive to surface Mo/N, which influences hydrogenation rate. The characterisation results reported in this study point to the generation of reactive hydrogen as rate limiting where the availability of hydrogen is favoured by increased nitridation.

Table 6.3: Rate constants (μmol g^{-1} h^{-1}) for the conversion of nitrobenzene (k_1), *p*-chloronitrobenzene (k_2) and benzaldehyde (k_3).

Catalysts	Mo	MoN-1	MoN-2	β-Mo_2N
k_1	249	271	319	407
k_2	204	233	343	444
k_3	46	37	30	26

Nitro group reduction selectivity was further probed by examining the catalytic conversion of *p*-chloronitrobenzene. The hydrogenation of the -NO_2 function in *p*-chloronitrobenzene (**Figure 6.6(b)**) generates *p*-chloroaniline, which can undergo hydrodechlorination (C-Cl hydrogen scission) to form aniline. Alternatively, aniline can result from the hydrodechlorination of *p*-chloronitrobenzene (to nitrobenzene) with subsequent hydrogenation. Reaction over conventional transition metal (*e.g.* Pd [6.55]) catalysts is non-selective, delivering nitrobenzene and aniline as by-products. The results Chapter 2 and Chapter 3 reported selective *p*-chloroaniline formation over β-Mo_2N in gas phase [6.24,6.50] and, from the results generated here, this also applies to Mo, MoN-1 and MoN-2. Kinetic analysis of *p*-chloronitrobenzene hydrogenation (see

Figure 6.7(bII) and **Table 6.3**) resulted in the same activity trend as that observed for nitrobenzene where rate was again elevated with decreasing Mo/N and increasing H_2 availability.

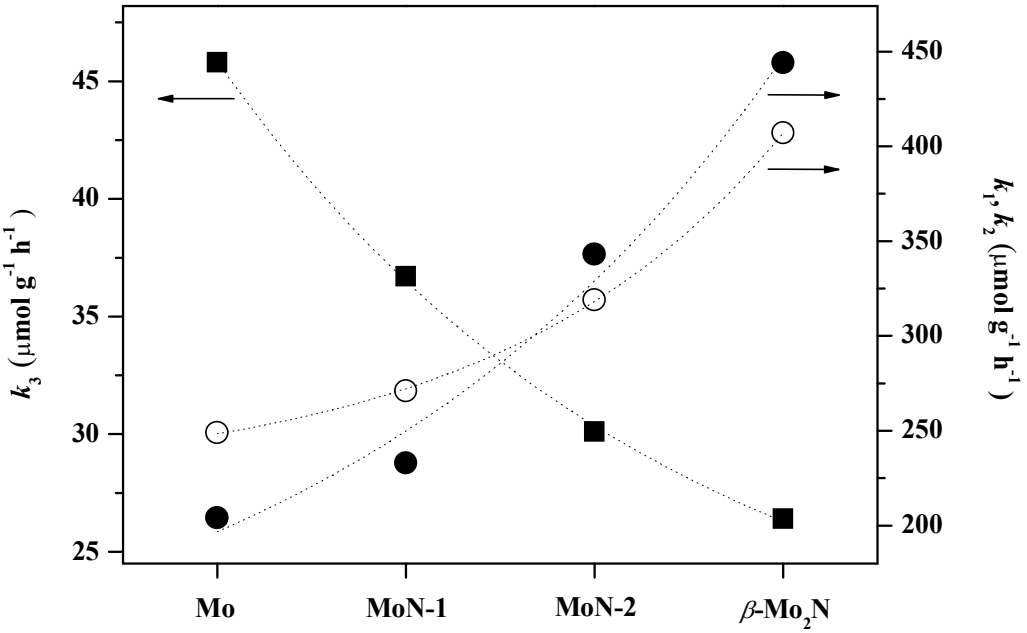

Figure 6.8: Rate constants associated with the hydrogenation of nitrobenzene (k_1,○), *p*-chloronitrobenzene (k_2,●) and benzaldehyde (k_3, ■) over Mo, MoN-1, MoN-2 and *β*-Mo_2N.

The catalytic response in the hydrogenation of nitrobenzene (k_1) and *p*-chloronitrobenzene (k_2) for the four systems is illustrated in **Figure 6.8**. Inductive and conjugative effects due to the electronegative *para*-substituted Cl result in electron transfer to -NO_2 [6.64]. Consequently, the anionic intermediate is stabilised, which should favour nucleophilic reduction. The rate constant in the hydrogenation of *p*-chloronitrobenzene is accordingly higher than that of nitrobenzene for reaction over *β*-Mo_2N and MoN-2. However, this does not apply to MoN-1 or Mo where the Cl substituent had an inhibiting effect with a higher rate of nitrobenzene hydrogenation relative to *p*-chloronitrobenzene. It is known that Cl can interact with Mo [6.65] and hydrodechlorination of mono- [6.59,6.66] and di-chlorobenzene [6.59] has been reported for MoO_3 and Mo. While we did not observe any dechlorination in the conversion of *p*-CNB, surface interaction through the Cl substituent facilitated at higher Mo site density can result in a decrease in N=O bond polarity, which destabilises the activated nitroarene intermediate with a resultant decrease in rate relative to nitrobenzene.

6.3.4 Catalytic Response: Carbonyl Group Reduction

The catalytic hydrogenation of benzaldehyde has been promoted using transition metals (Pt, Pd, Ru, Au and Ni) supported on oxides (Al_2O_3, ZrO_2, CeO_2, TiO_2 and SiO_2) in both liquid [6.67-70] and gas [6.71-74] phase operation. The reaction pathway is shown in **Figure 6.6(c)** where benzyl alcohol and toluene have been the principal reported products. The conversion of benzaldehyde to benzyl alcohol follows a nucleophilic mechanism [6.71] where C=O polarisation renders the oxygen susceptible to attack with proton transfer [6.75]. Toluene can result from hydrogenolysis of benzaldehyde, which is favoured by a strong surface interaction with the carbonyl oxygen that undergoes hydrogenolytic cleavage [6.76]. Conversion of benzyl alcohol to toluene over oxide supported metals has been proposed to involve adsorption/activation of the alcohol on the support and reaction with hydrogen dissociated at the metal site [6.75]. When benzaldehyde is strongly held on the surface, *e.g.* in the presence of strong basic sites, benzene is formed directly from hydrogenolysis [6.77]. Methylcyclohexane can result from the further reduction of toluene, *e.g.* over Ni/Al_2O_3 [6.72]. In liquid phase operation over Ru/C, hydrogenation of the aromatic ring generated hexahydro-benzaldehyde [6.78] and cyclohexylmethanol [6.70] from benzaldehyde and benzyl alcohol, respectively.

Reaction over the four catalytic systems in this study generated toluene as the sole product, consistent with hydrogenolytic character. β-Mo_2N has exhibited catalytic activity in C-N [6.14] and C-S [6.15,6.16] hydrogenolysis. We should note the work of Ghampson *et al.* [6.9] who reported C-O hydrogenolysis in the conversion of 2-methoxyphenol to phenol over γ-Mo_2N. In addition, Guerrero-Riuz and co-workers [6.5] observed γ-Mo_2N/C promoted C=O (crotonaldehyde) hydrogenolysis. A pseudo first order kinetic treatment was also applicable to the benzaldehyde reaction data, as demonstrated in **Figure 6.7(bIII)**; the associated rate constants are given in **Table 6.3**. In order to establish if toluene is generated by direct conversion of benzaldehyde or successive benzaldehyde → benzyl alcohol → toluene steps, the reaction of benzyl alcohol under the same conditions was examined over Mo and β-Mo_2N. Benzyl alcohol was converted with 100% selectivity to benzene where the rate constant over Mo (124 μmol g^{-1} h^{-1}) and β-Mo_2N (49 μmol g^{-1} h^{-1}) was significantly higher than that observed for benzaldehyde as reactant (**Table 6.3**). These results indicate that toluene must be formed by direct hydrogenolysis of the carbonyl bond.

In marked contrast to nitro group reduction, the activity sequence for the benzaldehyde reaction follows the order β-Mo_2N < MoN-2 < MoN-1 < Mo, as depicted in **Figure 6.8**. The catalytic response in this case is not governed by reactive hydrogen but by benzaldehyde adsorption/activation. The higher rate exhibited by Mo relative to β-Mo_2N points to enhanced activation of the carbonyl oxygen that facilitates hydrogen scission. There are no reported studies of aldehyde adsorption on Mo_2N. However, IR analysis of acetaldehyde uptake on Mo_2C [6.79] has revealed a chemisorptive interaction of the carbonyl oxygen with Mo atoms, which preceded C-O bond scission. It can be noted that Mo exhibits greater activity for CO adsorption than Mo_2N [6.80] where a repulsive interaction occurs between the negatively charged nitrogen atom and the oxygen lone pair [6.81]. Moreover, a stronger interaction of organic reactants (*e.g.* alkadiene [6.18], benzene [6.25], 1-butene [6.40]) has been reported for Mo species at low oxidation states. The shift in the XPS response to higher BE (higher Mo oxidation state) after incorporation of nitrogen may then result in a weaker interaction of benzaldehyde with the surface of Mo-nitride relative to Mo. Mo atoms are proposed as active sites for the activation of C=O where a decrease in Mo/N ratio lowers the number of available active sites. The results suggest that C=O activation for hydrogenolysis is favoured on Mo and inhibited by the progressive incorporation of N. The -NO_2 function is more reactive than C=O due to inductive effects [6.82], leading to higher rates for nitrobenzene and *p*-chloronitrobenzene relative to benzaldehyde (**Figure 6.8**).

6.4 Conclusion

Nitro (nitrobenzene and *p*-chloronitrobenzene) and carbonyl (benzaldehyde) group reduction show a contrasting dependence on Mo/N ratio. Variation in Mo/N is possible by altering the duration of Mo nitridation (in N_2/H_2) where β-Mo_2N was the product of complete nitridation. Surface area (*ca.* 4 m^2 g^{-1}) and bulk morphology (aggregates < 5μm) was unchanged as a result of nitridation. XPS measurements have revealed a surface enrichment by nitrogen (lower Mo/N) relative to the bulk where the passivated nitrided samples exhibit higher oxidation states than passivated Mo. Ambient temperature H_2 uptake and release during TPD increased with increasing nitridation. Selective -NO_2 reduction (to -NH_2) was observed for the gas phase conversion of nitrobenzene and *p*-chloronitrobenzene over the four catalyst systems. Increasing rates can be correlated with decreasing Mo/N ratio and associated increased availability of reactive hydrogen. The electronegative Cl substituent served to activate -NO_2 for

reaction over β-Mo_2N while surface interaction with Mo lowered activity. Reaction of benzaldehyde resulted in toluene formation with increasing rate from β-Mo_2N to Mo that was not limited by surface hydrogen but by C=O activation for hydrogenolytic attack.

6.5 References

[6.1] D. J. Sajkowski and S. T. Oyama, *Catalytic hydrotreating by molybdenum carbide and nitride: unsupported Mo_2N and Mo_2C/Al_2O_3*, Appl. Catal. A: General 134 (1996) 339-349.

[6.2] C. W. Colling and L. T. Thompson, *The structure and function of supported molybdenum nitride hydrodenitrogenation catalysts*, J. Catal. 146 (1994) 193-203.

[6.3] J. C. Schlatter, S. T. Oyama, J. E. Metcalfe and J. M. Lambert, *Catalytic behavior of selected transition-metal carbides, nitrides, and borides in the hydrodenitrogenation of quinoline*, Ind. Eng. Chem. Res. 27 (1988) 1648-1653.

[6.4] Z. X. Hao, Z. B. Wei, L. J. Wang, X. H. Li, C. Li, E. Z. Min and Q. Xin, *Selective hydrogenation of ethyne on gamma-Mo_2N*, Appl. Catal. A: General 192 (2000) 81-84.

[6.5] A. Guerrero-Ruiz, Y. Zhang, B. Bachiller-Baeza and I. Rodríguez-Ramos, *Hydrogenation of crotonaldehyde over carbon- supported molybdenum nitrides*, Catal. Lett. 55 (1998) 165-168.

[6.6] D. McKay, J. S. J. Hargreaves, J. L. Rico, J. L. Rivera and X. L. Sun, *The influence of phase and morphology of molybdenum nitrides on ammonia synthesis activity and reduction characteristics*, J. Solid State Chem. 181 (2008) 325-333.

[6.7] M. Nagai, Y. Goto, A. Miyata, M. Kiyoshi, K. Hada, K. Oshikawa and S. Omi, *Temperature-programmed reduction and XRD studies of ammonia-treated molybdenum oxide and its activity for carbazole hydrodenitrogenation*, J. Catal. 182 (1999) 292-301.

[6.8] N. Perret, F. Cárdenas-Lizana, D. Lamey, V. Laporte, L. Kiwi-Minsker and M. A. Keane, *Effect of Crystallographic Phase (β vs. γ) and Surface Area on Gas Phase Nitroarene Hydrogenation over Mo_2N and Au/Mo_2N*, Top. Catal., Manuscript Accepted (2012)

[6.9] I. T. Ghampson, C. Sepúlveda, R. Garcia, B. G. Frederick, M. C. Wheeler, N. Escalona and W. J. DeSisto, *Guaiacol transformation over unsupported molybdenum-based nitride catalysts*, Appl. Catal. A: General 413-414 (2012) 78-84.

[6.10] M. Nagai and S. Omi, *Preparation, surface and catalytic properties of molybdenum nitrides*, Sekiyu Gakkaishi 38 (1995) 363-373.

[6.11] D. W. Kim, D. K. Lee and S. K. Ihm, *Preparation of Mo nitride catalysts and their applications to the hydrotreating of indole and benzothiophene*, Korean J. Chem. Eng. 19 (2002) 587-592.

[6.12] Z. Wu, S. Yang, Q. Xin and C. Li, *In situ IR spectroscopic studies on molybdenum nitride catalysts: active sites and surface reactions*, Catal. Survey. Asia 7 (2003) 103-119.

[6.13] Z. B. Wei, Q. Xin, P. Grange and B. Delmon, *TPD and TPR studies of molybdenum nitride*, J. Catal. 168 (1997) 176-182.

[6.14] M. Nagai, Y. Goto, O. Uchino and S. Omi, *TPD and XRD studies of molybdenum nitride and its activity for hydrodenitrogenation of carbazole*, Catal. Today 43 (1998) 249-259.

[6.15] S. Gong, H. Chen, W. Li and B. Li, *Synthesis of beta-$Mo_2N_{0.78}$ hydrodesulfurization catalyst in mixtures of nitrogen and hydrogen*, Appl. Catal. A: General 279 (2005) 257-261.

[6.16] S. W. Gong, H. K. Chen, W. Li, B. Q. Li and T. D. Hu, *Dibenzothiophene hydrodesulfurization over alumina-supported beta-$Mo_2N_{0.78}$ catalyst*, J. Mol. Catal. A: Chemical 225 (2005) 213-216.

[6.17] J. G. Choi, *Influence of surface composition on HDN activities of molybdenum nitrides*, J. Ind. Eng. Chem. 8 (2002) 1-11.

[6.18] Y. Z. Li, G. F. Luo, Y. N. Fan and Y. Chen, *A novel route to the synthesis of nanosized metallic molybdenum at moderate temperature and its catalytic properties*, Mater. Res. Bull. 39 (2004) 195-203.

[6.19] G. W. Haddix, J. A. Reimer and A. T. Bell, *Characterization of H_2 adsorbed on gamma-Mo_2N by NMR-spectroscopy*, J. Catal. 108 (1987) 50-54.

[6.20] H. Ishii, M. Kiyoshi and M. Nagai, *Surface Properties and Active Sites of Nitrided Mo/Al_2O_3 Catalysts for the Hydrodenitrogenation of Carbazole*, Top. Catal. 52 (2009) 1525-1534.

[6.21] K. Miga, K. Stanczyk, C. Sayag, D. Brodzki and G. Djega-Mariadassou, *Bifunctional behavior of bulk MoO_xN_y and nitrided supported NiMo catalyst in hydrodenitrogenation of indole*, J. Catal. 183 (1999) 63-68.

[6.22] A. G. Cairns, J. G. Gallagher, J. S. J. Hargreaves, D. McKay, E. Morrison, J. L. Rico and K. Wilson, *The influence of precursor source and thermal parameters upon the formation of beta-phase molybdenum nitride*, J. Alloys Compd. 479 (2009) 851-854.

[6.23] S. Li, W. B. Kim and J. S. Lee, *Effect of the reactive gas on the solid-state transformation of molybdenum trioxide to carbides and nitrides*, Chem. Mater. 10 (1998) 1853-1862.

[6.24] F. Cárdenas-Lizana, S. Gómez-Quero, N. Perret, L. Kiwi-Minsker and M. A. Keane, *β-Molybdenum nitride: Synthesis mechanism and catalytic response in the gas phase hydrogenation of p-chloronitrobenzene*, Catal. Sci. Tech. 1 (2011) 794–801.

[6.25] M. Yamada, J. Yasumaru, M. Houalla and D. M. Hercules, *Distribution of molybdenum oxidation-states in reduced Mo/Al_2O_3 catalysts. Correlation with benzene hydrogenation activity*, J. Phys. Chem. 95 (1991) 7037-7042.

[6.26] H. Al-Kandari, F. Al-Kharafi and A. Katrib, *Catalytic activity-surface structure correlation of molybdenum-based catalysts*, J. Mol. Catal. A: Chemical 287 (2008) 128-134.

[6.27] F. Al-Kharafi, H. Al-Kandari and A. Katrib, *Different catalytic reactions of n-hexane and 1-hexene on molybdenum based catalysts*, Catal. Lett. 123 (2008) 269-275.

[6.28] P. Uvdal, B. C. Wiegand, J. G. Serafin and C. M. Friend, *Isotopic labeling as a tool to establish intramolecular vibrational coupling: The reaction of 2-propanol on Mo(110)*, J. Chem. Phys. 97 (1992) 8727-8735.

[6.29] Z. B. Z. Wei, P. Grange and B. Delmon, *XPS and XRD studies of fresh and sulfided Mo_2N*, Appl. Surf. Sci. 135 (1998) 107-114.

[6.30] G. H. Xie and Z. C. Jiang, *The first observation of Mo^{5+} in the passivation layer of Mo_2N*, Chin. Sci. Bull. 45 (2000) 1562-1564.

[6.31] R. Yuvakkumar, V. Elango, V. Rajendran and N. Kannan, *A New Approach to Preparing Crystalline Nano Molybdenum Particles*, Synth. React. Inorg. Met.-Org. Nano-Met. Chem. 41 (2011) 309-314.

[6.32] S. M. Aouadi, Y. Paudel, B. Luster, S. Stadler, P. Kohli, C. Muratore, C. Hager and A. A. Voevodin, *Adaptive Mo_2N/ MoS_2/ Ag tribological nanocomposite coatings for aerospace applications*, Tribol. Lett. 29 (2008) 95-103.

[6.33] B. G. Demczyk, J. G. Choi and L. T. Thompson, *Surface-structure and composition of high-surface-area molybdenum nitrides*, Appl. Surf. Sci. 78 (1994) 63-69.

[6.34] P. A. Spevack and N. S. McIntyre, *A Raman and XPS investigation of supported molybdenum oxide thin-films .2. Reactions with hydrogen-sulfide*, J. Phys. Chem. 97 (1993) 11031-11036.

[6.35] P. J. Cai, Z. H. Yang, C. Y. Wang, Y. L. Gu and Y. T. Qian, *A simple approach to synthesize Mo_2N nanocrystals*, Chem. Lett. 34 (2005) 1360-1361.

[6.36] K. Inumaru, K. Baba and S. Yamanaka, *Synthesis and characterization of superconducting beta-Mo_2N crystalline phase on a Si substrate: An application of pulsed laser deposition to nitride chemistry*, Chem. Mater. 17 (2005) 5935-5940.

[6.37] H. K. Park, J. K. Lee, J. K. Yoo, E. S. Ko, D. S. Kim and K. L. Kim, *Surface properties and reactivity of supported and unsupported molybdenum nitride catalysts*, Appl. Catal. A: General 150 (1997) 21-35.

[6.38] C. W. Colling, J.-G. Choi and L. T. Thompson, *Molybdenum nitride catalysts II. H_2 temperature programmed reduction and NH_3 temperature programmed desorption*, J. Catal. 160 (1996) 35-42.

[6.39] S. W. Yang, C. Li, J. Xu and Q. Xin, *Surface sites of alumina-supported molybdenum nitride characterized by FTIR, TPD-MS, and volumetric chemisorption*, J. Phys. Chem. B 102 (1998) 6986-6993.

[6.40] Z. L. Wu, C. Li, P. L. Ying, Z. B. Wei and Q. Xin, *Low-temperature isomerization of 1-butene on Mo_2N/gamma-Al_2O_3 catalyst studied by in situ FT-IR spectroscopy*, J. Phys. Chem. B 105 (2001) 9183-9190.

[6.41] J. F. Zhu, J. C. Guo, R. S. Zhai, X. Bao, X. Y. Zhang and S. Zhuang, *Preparation and adsorption properties of Mo_2N model catalyst*, Appl. Surf. Sci. 161 (2000) 86-93.

[6.42] E. Furimsky, *Metal carbides and nitrides as potential catalysts for hydroprocessing*, Appl. Catal. A: General 240 (2003) 1-28.

[6.43] X. S. Li, K. J. Zhang, Q. Xin, C. X. Ji, Y. F. Miao and L. Wang, *Irreversible hydrogen uptake on Mo_2N catalyst*, React. Kinet. Catal. Lett. 57 (1996) 177-182.

[6.44] X. S. Li, Y. X. Chen, Y. J. Zhang, C. X. Ji and Q. Xin, *Temperature-programmed desorption and adsorption of hydrogen on Mo_2N*, React. Kinet. Catal. Lett. 58 (1996) 391-396.

[6.45] M. W. Roberts and L. Whalley, *Chemisorption and displacement reactions on tungsten, molybdenum and tantalum films* Trans. Faraday Soc. 65 (1969) 1377-1385.

[6.46] K. Jeong, R. H. Gaylord and S. D. Kevan, *Symmetry effects of hydrogen chemisorption electronic-structure*, J. Vac. Sci. Technol. 7 (1989) 2199-2202.

[6.47] M. Arnold, S. Sologub, W. Frie, L. Hammer and K. Heinz, *Hydrogen-induced buckling of Mo(110) at submonolayer coverage*, J. Phys. Condens. Matter 9 (1997) 6481-6491.

[6.48] J. G. Choi, H. J. Lee and L. T. Thompson, *Temperature-programmed desorption of H_2 from molybdenum nitride thin-films*, Appl. Surf. Sci. 78 (1994) 299-307.

[6.49] F. Cárdenas-Lizana, D. Lamey, S. Gómez-Quero, N. Perret, L. Kiwi-Minsker and M. A. Keane, *selective three-phase hydrogenation of aromatic nitro-compounds over beta-Mo_2N*, Catal. Today 173 (2011) 53-61.

[6.50] F. Cárdenas-Lizana, S. Gómez-Quero, N. Perret, L. Kiwi-Minsker and M. A. Keane, *Au/Mo_2N as a new catalyst formulation for the hydrogenation of p-Chloronitrobenzene in both liquid and gas phase*, Catal. Commun. 21 (2012) 46-51.

[6.51] M. T. Nguyen, *The chemistry of anilines* in Patai Series: The chemistry of Functional Groups, Z. Rappoport (Ed.), Wiley, 2007, Chichester, pp.79-80.

[6.52] S. Meijers and V. Ponec, *Infrared spectroscopic study of the adsorption of nitro-compounds and amines on cobalt oxide*, J. Catal. 149 (1994) 307-316.

[6.53] E. A. Gelder, *The hydrogenation of nitrobenzene over metal catalysts* in PhD thesis, University of Glasgow, UK, 2004.

[6.54] F. Cárdenas-Lizana, Z. M. de Pedro, S. Gómez-Quero and M. A. Keane, *Gas phase hydrogenation of nitroarenes: A comparison of the catalytic action of titania supported gold and silver*, J. Mol. Catal. A: Chemical 326 (2010) 48-54.

[6.55] F. Cárdenas-Lizana, S. Gómez-Quero and M. A. Keane, *Ultra-selective gas phase catalytic hydrogenation of aromatic nitro compounds over Au/Al_2O_3*, Catal. Commun. 9 (2008) 475-481.

[6.56] S. X. Huang, D. A. Fischer and J. L. Gland, *Aniline hydrogenolysis on nickel: effects of the surface hydrogen and surface-structure*, Catal. Lett. 34 (1995) 365-374.

[6.57] I. Amer, T. Bravdo, J. Blum and K. P. C. Vollhardt, *Selective C-C bond hydrogenation in unsaturated nitro compounds in the presence of the $RhCl_3$-aliquat 336 catalyst system*, Tetrahedron Lett. 28 (1987) 1321-1322.

[6.58] L. J. Deiner, D. H. Kang and C. A. Friend, *Low-temperature reduction of NO_2 on oxidized Mo(110)*, J. Phys. Chem. B 109 (2005) 12826-12831.

[6.59] A. de Lucas Consuegra, P. M. Patterson and M. A. Keane, *Use of unsupported and silica supported molybdenum carbide to treat chloroarene gas streams*, Appl. Catal. B: Environmental 65 (2006) 227-239.

[6.60] N. Perret, X. Wang, L. Delannoy, C. Potvin, C. Louis and M. A. Keane, *Enhanced selective nitroarene hydrogenation over Au supported on beta-Mo_2C and beta-Mo_2C/Al_2O_3*, J. Catal. 286 (2012) 172-183.

[6.61] Z. Wu, Z. Hao, Z. Wei, C. Li and Q. Xin, *Selective hydrogenation of 1,3-butadiene on molybdenum nitride catalyst: Identification of the adsorbed hydrocarbonaceous species*, Stud. Surf. Sci. Catal. 138 (2001) 445.

[6.62] M. Nagai, *Transition-metal nitrides for hydrotreating catalyst: Synthesis, surface properties and reactivities*, Appl. Catal. A: General 322 (2007) 178-190.

[6.63] P. Sangeetha, P. Seetharamulu, K. Shanthi, S. Narayanan and K. S. Rama Rao, *Studies on Mg-Al oxide hydrotalcite supported Pd catalysts for vapor phase hydrogenation of nitrobenzene*, J. Mol. Catal. A: Chemical 273 (2007) 244-249.

[6.64] B. Zhao and Y.-W. Chen, *Hydrogenation of p-chloronitrobenzene on Mo, La, Fe, and W-modified NiCoB nanoalloy catalysts*, J. Non-Cryst. Solids 356 (2010) 839-847.

[6.65] M. Balooch, D. R. Olander, W. J. Siekhaus and D. E. Miller, *Reaction of Chlorine and Molybdenum by Modulated Molecular-Beam Mass-Spectrometry*, Surf. Sci. 249 (1991) 322-334.

[6.66] S. T. Srinivas, L. J. Lakshmi, N. Lingaiah, P. S. S. Prasad and P. K. Rao, *Selective vapour-phase hydrodechlorination of chlorobenzene over alumina supported platinum bimetallic catalysts*, Appl. Catal. A: General 135 (1996) L201-L207.

[6.67] D. Procházková, P. Zámostný, M. Bejblová, L. Červený and J. Čejka, *Hydrodeoxygenation of aldehydes catalyzed by supported palladium catalysts*, Appl. Catal. A: General 332 (2007) 56-64.

[6.68] D. Divakar, D. Manikandan, G. Kalidoss and T. Sivakumar, *Hydrogenation of benzaldehyde over palladium intercalated bentonite catalysts: Kinetic studies*, Catal. Lett. 125 (2008) 277-282.

[6.69] F. Pinna, F. Menegazzo, M. Signoretto, P. Canton, G. Fagherazzi and N. Pernicone, *Consecutive hydrogenation of benzaldehyde over Pd catalysts. Influence of supports and sulfur poisoning*, Appl. Catal. A: General 219 (2001) 195-200.

[6.70] P. Kluson and L. Červený, *Hydrogenation of substituted aromatic compounds over a ruthenium catalyst*, J. Mol. Catal. A: Chemical 108 (1996) 107-112.

[6.71] A. Saadi, Z. Rassoul and M.M. Bettahar, *Gas phase hydrogenation of benzaldehyde over supported copper catalysts*, J. Mol. Catal. A: Chemical 164 (2000) 205-216.

[6.72] A. Saadi, R. Merabti, Z. Rassoul and M.M. Bettahar, *Benzaldehyde hydrogenation over supported nickel catalysts*, J. Mol. Catal. A: Chemical 253 (2006) 79-85.

[6.73] M.A. Vannice and D. Poondi, *The effect of metal-support interactions on the hydrogenation of benzaldehyde and benzyl alcohol*, J. Catal. 169 (1997) 166-175.

[6.74] N. Perret, F. Cárdenas-Lizana and M. A. Keane, *Selective hydrogenation of benzaldehyde to benzyl alcohol over Au/Al_2O_3*, Catal. Commun. 16 (2011) 159–164.

[6.75] K. Lanasri, A. Saddi, K. Bachari, D. Halliche and O. Cherifi, *Gas phase hydrogenation of benzaldehyde over supported copper catalysts. Effect of copper loading*, Stud. Surf. Sci. Catal. 174 (2008) 1279-1282.

[6.76] R. Merabti, K. Bachari, D. Halliche, Z. Rassoul and A. Saadi, *Synthesis and characterization of activated carbon-supported copper or nickel and their catalytic behavior towards benzaldehyde hydrogenation*, React. Kinet., Mech. Catal. 101 (2010) 195-208.

[6.77] M.A. Peralta, T. Sooknoi, T. Danuthai and D.E. Resasco, *Deoxygenation of benzaldehyde over CsNaX zeolites*, J. Mol. Catal. A: Chem. 312 (2009) 78-86.

[6.78] L. Červený, Z. Bělohlav and M.N.H. Hamed, *Catalytic hydrogenation of aromatic aldehydes and ketones over ruthenium catalysts*, Res. Chem. Intermed. 22 (1996) 15-22.

[6.79] M. Siaj, C. Reed, S. T. Oyama, S. L. Scott and P. H. McBreen, *Dissociation of acetaldehyde on beta-Mo_2C to yield ethylidene and oxo surface groups: A possible pathway for active site formation in heterogeneous olefin metathesis*, J. Am. Chem. Soc. 126 (2004) 9514-9515.

[6.80] Z. L. Wu, A. Maroto-Valiente, A. Guerrero-Ruiz, I. Rodriguez-Ramos, C. Li and Q. Xin, *Microcalorimetric and IR spectroscopic studies of CO adsorption on molybdenum nitride catalysts*, Phys. Chem. Chem. Phys. 5 (2003) 1703-1707.

[6.81] G. Frapper, M. Pelissier and J. Hafner, *CO adsorption on molybdenum nitride's gamma-Mo_2N(100) surface: Formation of N=C=O species? A density functional study*, J. Phys. Chem. B 104 (2000) 11972-11976.

[6.82] A. K. Pahari and B. S. Chauhan, *Engineering Chemistry*, Laxmi Publications, New Delhi, 2006, pp. 95-97.

Chapter 7

Selective Hydrogenation of Benzaldehyde to Benzyl Alcohol over Au/Al_2O_3

This Chapter investigates the use of Au supported in hydrogenation of aldehyde as an alternative route in the production of commercially important alcohol. The catalytic behaviour of Au/Al_2O_3 in the continuous gas phase hydrogenation of benzaldehyde is examined and compared with Ni/Al_2O_3 and Pd/Al_2O_3.

7.1 Introduction

Benzyl alcohol is a commercially important chemical (with a projected production of 61 kt in 2012 [7.1]), employed as a solvent for inks, paints, lacquers and as precursor for the manufacture of a range of esters in the cosmetics and flavoring industries [7.2]. The standard industrial production route has involved the hydrolysis of benzyl chloride in alkaline media but the associated production of dibenzyl ether with chlorine release represent serious drawbacks that have now limited the applicability of this approach [7.3]. Two alternative catalytic routes, generally in liquid phase, are: (i) oxidation of toluene, typically over vanadia [7.4]; (ii) disproportionation of benzaldehyde (Cannizzaro reaction) over irreducible basic oxides such as MgO [7.5]. The oxidation route generates significant quantities of benzoic acid and benzaldehyde, requiring additional downstream separation/purification, while the use of additives (such as sodium bromide) to increase yield and/or avoid formation of by-products results in reactor corrosion [7.6]. The Cannizzaro reaction has not been studied to any significant extent and the low rates achieved (0.2 $mol_{alcohol}$ mol_{MgO} h^{-1}) have prevented commercial implementation.

The catalytic hydrogenation of benzaldehyde represents an alternative, which has now been promoted using transition metals (Pt, Pd, Ru and Ni) supported on oxides (Al_2O_3, ZrO_2, CeO_2, TiO_2 and SiO_2), largely in the liquid phase (T = 295-405 K; P = 1-60 atm) [7.7-10] but with limited gas phase [7.11-13] application. However, C=O hydrogenation selectivity is challenging and has not exceeded 80% over Group VIII metals due to a catalysed hydrogenolysis to generate toluene and benzene [7.7].

Moreover, catalyst deactivation from coke deposition has been a common feature of the catalysts tested to date [7.9]. In gas phase operation, activity has been related to the strength of reactant interaction while selectivity is governed by the competitive adsorption of benzaldehyde and benzyl alcohol [7.14]. Where benzaldehyde is strongly held on the surface, *e.g.* in the presence of strong basic sites, benzene formation is preferred [7.15]. The use of reducible oxides (TiO_2, ZrO_2 or CeO_2) favours interaction *via* the hydroxyl oxygen with the resultant generation of toluene, whereas benzyl alcohol interaction with irreducible supports is limited [7.11]. Moreover, a high surface capacity for hydrogen uptake (including spillover) is associated with increased activity and selectivity to toluene [7.12].

In this Chapter, the use of supported Au is considered, for the first time, to promote the selective hydrogenation of benzaldehyde to benzyl alcohol. Nevertheless, it should be noted that the reverse reaction (oxidation of benzyl alcohol) has been studied over Au (on TiO_2 and Al_2O_3) at elevated pressures (up to 147 atm) with a higher selectivity (close to 100%) to benzaldehyde than that obtained with Pt and Pd catalysts [7.16]. Catalysis by Au has attracted appreciable research activity as demonstrated in the review by Hutchings *et al.* [7.17] but the work to date has largely dealt with oxidation reactions involving CO, alcohol, aldehyde, and diol reactants [7.18]. By comparison, Au promoted hydrogenation has not been considered to the same extent, focusing largely on the conversion of ketones, aldehydes and nitroarenes [7.19]. Although supported Au delivers lower hydrogenation rates than conventional transition metal catalysts (*e.g.* Pd, Pt and Ni), enhanced performance in terms of selectivity and stability has been reported, notably in the hydrogenation of aldehydes to alcohols (*e.g.* crotonaldehyde, citral, acrolein) [7.20]. Moreover, there is some evidence [7.21] that edge sites on Au nanoparticles favour C=O adsorption/activation and hydrogenation. In this Chapter, critical Au/Al_2O_3 characterisation results are linked with benzaldehyde hydrogenation data in continuous flow gas phase operation and performance are compared with Ni/Al_2O_3 and Pd/Al_2O_3.

7.2 Experimental

7.2.1 Catalyst Preparation and Activation

Au/Al_2O_3 (1.1% w/w) was prepared by standard impregnation of Al_2O_3 (5 g, Puralox, Condea Vista Co.) with an aqueous $HAuCl_4$ solution (Aldrich, 7.3×10^{-3} M). The slurry was heated at 2 K min^{-1} to 353 K under vigorously stirring (*ca.* 600 rpm) and maintained in a He purge. The solid residue was dried in He at 2 K min^{-1} to 383 K for 3 h, sieved into a batch of 75 μm average particle diameter and stored under He at 278 K (in the dark). The Au loading was determined by inductively coupled plasma-optical emission spectrometry (ICP-OES, Vista-PRO, Varian Inc.). For comparative purposes, Pd/Al_2O_3 and Ni/Al_2O_3 prepared by impregnation with $Pd(NO_3)_2$ and $Ni(NO_3)_2$ [7.22], were employed as reference catalysts. Prior to use in catalysis, Au/Al_2O_3, Pd/Al_2O_3 and Ni/Al_2O_3 were activated in 60 cm^3 min^{-1} H_2 at 2 K min^{-1} to a final temperature in the range 473-723 K. The samples were passivated in 1% v/v O_2/He at room temperature for *ex situ* analysis.

7.2.2 Catalyst Characterisation

Temperature programmed reduction (TPR) and BET surface area analysis were conducted using the commercial CHEM-BET 3000 (Quantachrome) unit. The Au/Al_2O_3 sample was loaded into a U-shaped Quartz cell (10 cm×3.76 mm i.d.) and heated in 17 cm^3 min^{-1} (Brooks mass flow controlled) 5% v/v H_2/N_2 at 2 K min^{-1} to 473 ± 1 K. The effluent gas passed through a liquid N_2 trap and changes in H_2 consumption were monitored by TCD with data acquisition/manipulation using the TPR Win™ software. The reduced sample was maintained at the final temperature in a constant flow of H_2/N_2 until the TCD signal returned to baseline, swept with 65 cm^3 min^{-1} flow N_2 for 1.5 h and cooled to room temperature. The sample was then subjected to H_2 chemisorption using a pulse (10 μl) titration procedure. Hydrogen pulse introduction was repeated until the signal area was constant, indicating surface saturation. In a series of blank tests, chemisorption measurements on the alumina support did not result in any hydrogen uptake. BET area was recorded with a 30% v/v N_2/He flow using pure N_2 (99.9%) as internal standard. At least 3 cycles of N_2 adsorption-desorption in the flow mode were employed to determine total surface area using the standard single point method. BET

surface area and H_2 uptake values were reproducible to within ± 5%; the values quoted represent the mean.

UV-Vis spectra of the $HAuCl_4$ aqueous solution and Au/Al_2O_3 were obtained using, respectively, a Spectronic Unicam HEλIOS β UV-Vis Spectrophotometer and a Perkin-Elmer Lambda 35 UV-Vis Spectrometer (with $BaSO_4$ powder as reference). Powder X-ray diffractograms were recorded on a Bruker/Siemens D500 incident X-ray diffractometer with Cu Kα radiation. The sample was scanned at a rate of 0.02º $step^{-1}$ over the range $20º \leq 2\theta \leq 80º$. Diffractograms were identified using the JCPDS-ICDD reference standards, *i.e.* Al_2O_3 (10-0425) and Au (04-0784). Metal particle size (d_{hkl}) was estimated using the Scherrer equation:

$$d_{hkl} = \frac{K \times \lambda}{\beta \times \cos\theta} \tag{7.1}$$

where $K = 0.9$, λ is the incident radiation wavelength (1.5056 Å), β is the peak width at half the maximum intensity and θ represents the diffraction angle corresponding to the main plane associated with metallic Au ($2\theta = 38.1°$). Au particle morphology and size were also determined by transmission electron microscopy analysis; JEOL JEM 2011 HRTEM unit with a UTW energy dispersive X-ray detector (Oxford Instruments) operated at an accelerating voltage of 200 kV using Gatan DigitalMicrograph 3.4 for data acquisition/manipulation. The sample for analysis was prepared by dispersion in acetone and deposited on a holey carbon/Cu grid (300 Mesh). The mean Au particle size is given as a surface area-weighted mean (d) according to:

$$d = \frac{\sum_i n_i d_i^3}{\sum_i n_i d_i^2} \tag{7.2}$$

where n_i is the number of particles of diameter d_i and $\Sigma\ n_i = 650$. Characterisation details for the Pd/Al_2O_3 and Ni/Al_2O_3 catalysts have been published previously [7.22].

7.2.3 Catalysis Procedure

Reactions were carried out under atmospheric pressure at T = 393 K, *in situ* immediately after activation, in a fixed bed vertical glass tubular reactor (60 cm×15 mm i.d.). The catalytic reactor and operating conditions to ensure negligible heat/mass transport limitations, have been fully described elsewhere [7.23] but some features, pertinent to this study, are given below. A layer of borosilicate glass beads served as preheating zone, ensuring that the organic reactant was vaporized and reached reaction temperature before contacting the catalyst. Isothermal conditions (± 1 K) were ensured by diluting the catalyst bed with ground glass (75 μm). The reaction temperature was continuously monitored using a thermocouple inserted in a thermowell within the catalyst bed.

Benzaldehyde (or benzyl alcohol) as a solution in ethanol was delivered at a fixed calibrated flow rate to the reactor *via* a glass/teflon air-tight syringe and teflon line using a microprocessor controlled infusion pump (Model 100 kd Scientific). A co-current flow of benzaldehyde (or benzyl alcohol) and ultra pure H_2 (< 1% v/v organic in H_2) was maintained at a GHSV = 2×10^4 h^{-1} with an inlet reactant molar flow (F) = 4.8×10^{-5} mol h^{-1}. The H_2 content was up to 3000 times in excess of the stoichiometric requirement, the flow rate of which was monitored using a Humonics (Model 520) digital flowmeter. The molar metal to inlet molar organic feed rate (n/F) ratio spanned the range 5×10^{-3}-88×10^{-3} h. In a series of blank tests, passage of reactant in a stream of H_2 through the empty reactor or over the Al_2O_3 support did not result in any detectable conversion. A flow of benzaldehyde in a stream of He over Au/Al_2O_3 generated traces quantities of benzyl alcohol via disproportionation [7.5] where the amount produced was less than 3% of that formed by selective hydrogenation under the same reaction conditions. The reactor effluent was frozen in a liquid nitrogen trap for subsequent analysis, which was made using a Perkin-Elmer Auto System XL gas chromatograph equipped with a programmed split/splitless injector and a flame ionization detector, employing a DB-1 50 m×0.33 mm i.d., 0.20 μm film thickness capillary column (J&W Scientific). Benzaldehyde (Fluka, ≥ 98% w/w purity), benzyl alcohol (Riedel-de Haën, ≥ 99% w/w purity) and ethanol (Sigma Aldrich, ≥ 99% v/v) were used without further purification.

Fractional benzaldehyde conversion (x) is defined by

$$X = \frac{[\text{benzaldehyde}]_{in} - [\text{benzaldehyde}]_{out}}{[\text{benzaldehyde}]_{in}} \quad (7.3)$$

where the subscripts "out" and "in" refer to the outlet and inlet gas streams, respectively. Selectivity in terms of benzyl alcohol as the target product is given by

$$S_{\text{benzyl alcohol}}\% = \frac{[\text{benzylalcohol}]_{out}}{[\text{benzaldehyde}]_{in} - [\text{benzaldehyde}]_{out}} \times 100 \quad (7.4)$$

Repeated reactions with the same batch of catalyst delivered a product composition that was reproducibility to within ± 3%.

7.3 Results and Discussion

7.3.1 Catalyst Characterisation

The UV-Vis spectrum recorded for the Au precursor solution is presented in **Figure 7.1(A)** where the band at *ca.* 385 nm can be attributed to Au^{3+} [7.24]. The TPR of the Au/Al_2O_3 precursor generated the profile shown in **Figure 7.1(B)**, which is characterised by a single peak with T_{max} = 415 K. A single step reduction of cationic gold (Au^{3+}) to the zero valent state has been recorded elsewhere for Au/Al_2O_3 prepared by deposition-precipitation at 436 K [7.25] and 490 K [7.26]. Moreover, hydrogen consumption during TPR (**Table 7.1**) matched that required for the reduction of the precursor to the metallic form. It should be noted that both cationic (Au^{+} and Au^{3+}) [7.27] and metallic [7.28] gold have been proposed as the active species in hydrogenation reactions. The BET surface area for Au/Al_2O_3 (**Table 7.1**) was lower than that of the starting Al_2O_3 support (172 $m^2\ g^{-1}$), suggesting partial pore filling by the metal component [7.11].

The UV-Vis spectrum (**Figure 7.1(C**) of the activated catalyst exhibits an absorption band with maximum intensity (A_{max}) at *ca.* 545 nm characteristic of zero valent gold [7.25]. The wavelength corresponding to maximum band intensity is dependent on Au dispersion with a shift to lower wavelengths with decreasing Au particle size. The value quoted in this work is close that reported in the literature [7.25] for highly dispersed Au/Al_2O_3 (A_{max} = 540 nm; d = 4 nm) suggesting the presence of Au nano-particles. The UV response is consistent with a supported Au^0 phase *post*-TPR.

The XRD profile (**Figure 7.1(D)**) presents peaks at 2θ = 45.7° and 66.7° that correspond, respectively, to the (400) and (440) planes of cubic γ-Al_2O_3, where the broadness of the peaks is indicative of short range order. In addition, peaks at 2θ = 38.1°, 44.3°, 64.6° and 77.5° can be assigned to the (111), (200), (220) and (311) planes of metallic Au. Standard X-ray line broadening analysis based on the Scherrer formula (eqn. 7.1) yields a mean Au particle size of 8.5 nm (**Table 7.1**).

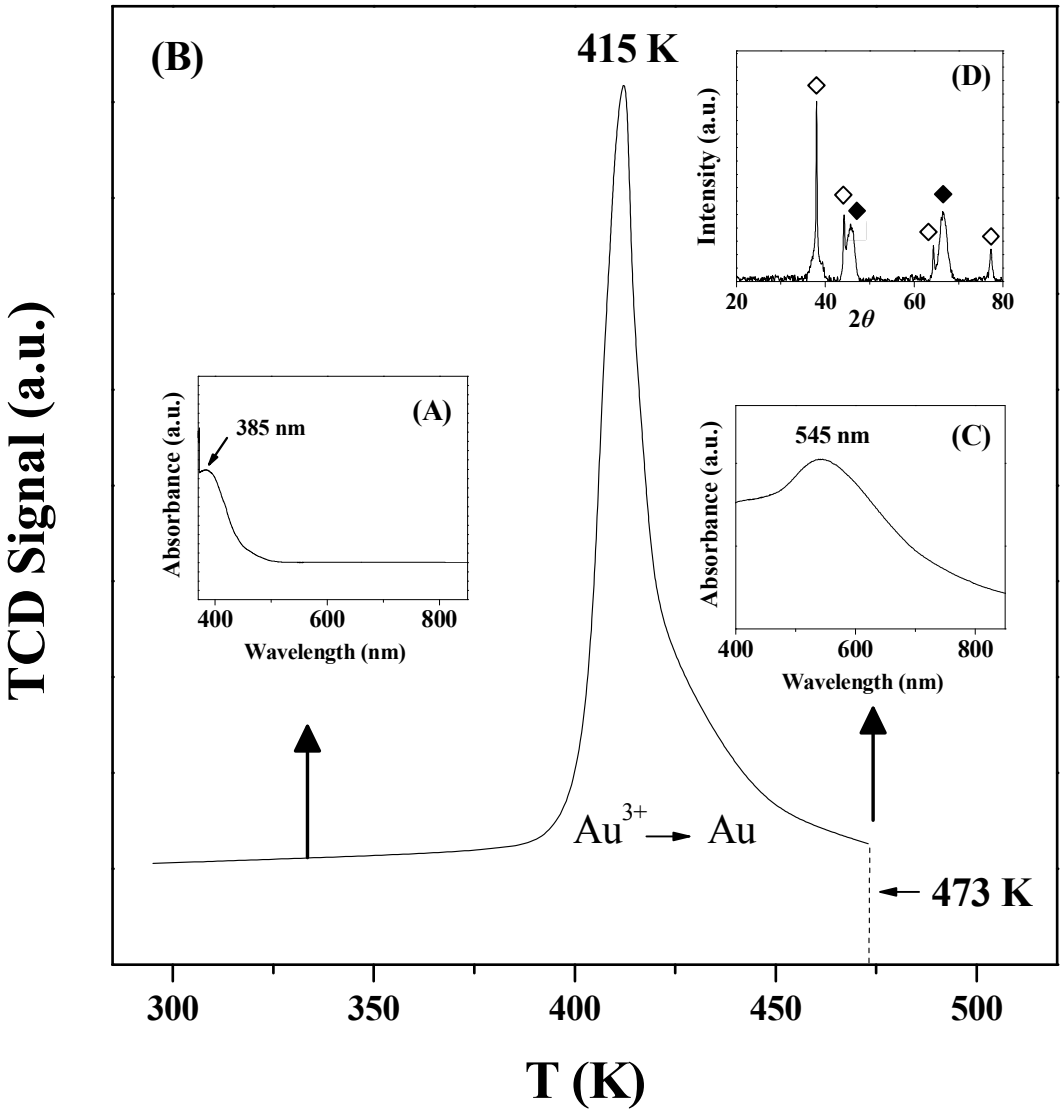

Figure 7.1: (A) UV-Vis spectrum of $HAuCl_4$ aqueous solution, (B) TPR profile, (C) UV-Vis spectrum and (D) XRD pattern for Au/Al_2O_3. Note: XRD peak assignments are based on JCPDS-ICDD reference data: (◆) γ-Al_2O_3 (10-0425); (◇) Au (04-0784).

Table 7.1: Characteristics of Au/Al_2O_3 catalyst.

Au loading (% w/w)	1.1
BET area ($m^2\ g^{-1}$)	161
TPR T_{max} (K)	415
TPR H_2 consumption ($\mu mol\ g^{-1}$)	78
UV-Vis A_{max} (nm)	545
d_{hkl} (nm)[a]	8.5
Au particle size range (nm)[b]	1-20
d (nm)[b]	7.9

[a]from XRD analysis: see eqn (7.1).
[b]from TEM analysis.

Representative (A) medium and (B) high magnification TEM images of Au/Al_2O_3 are given in **Figure 7.2**, which reveal discrete Au particles at the nano-scale that exhibit a quasi-spherical morphology. The diffractogram pattern for an isolated Au particle is included as an inset in **Figure 7.2(B)** where the associated *d*-spacings (0.20/0.23) are consistent with the (200) and (111) planes of metallic gold (0.204/0.235 nm). Although the nature of hydrogen/Au interactions has yet to be conclusively established, the consensus that emerges from the literature [7.29] suggests that chemisorption occurs predominantly at step, edge and corner sites, which are more prevalent on smaller particles. Moreover, a well dispersed Au phase at the nano-scale (< 10 nm) is required in order to optimise the catalytic response. A total count of 650 Au particles delivered a surface area-weighted metal diameter (*d*, **Table 7.1**) of 7.9 nm which is in good agreement with that obtained from XRD analysis.

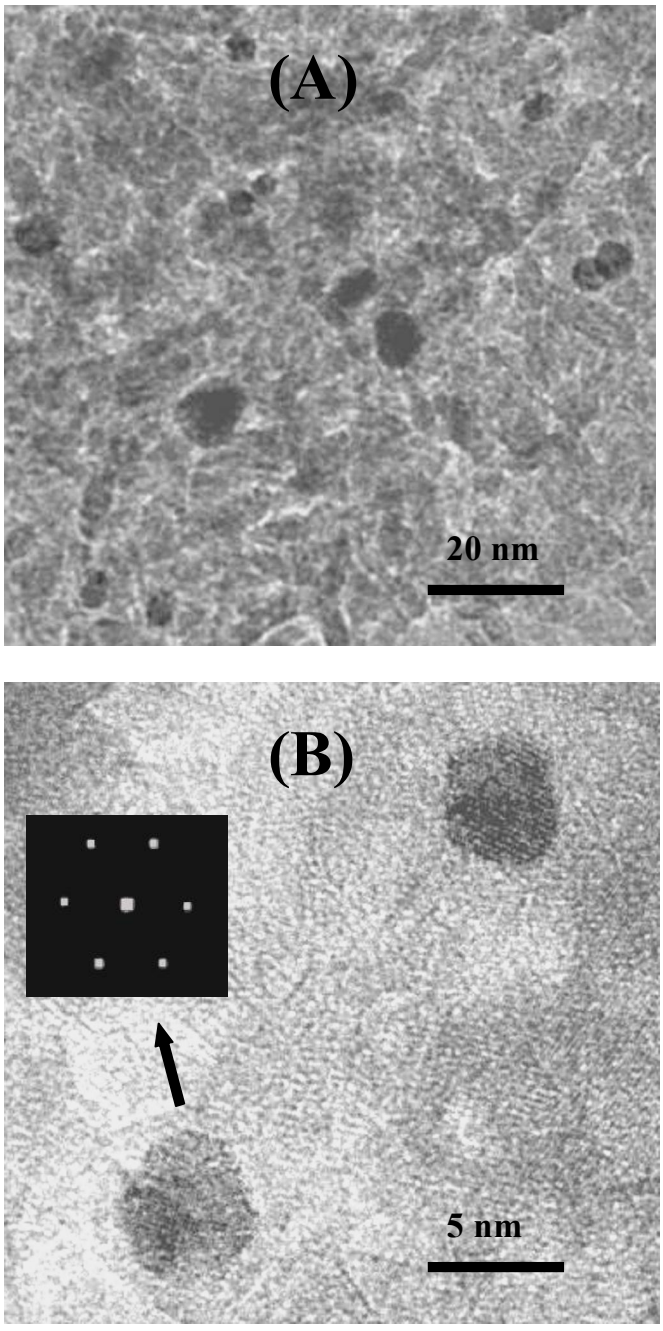

Figure 7.2: Representative (A) medium and (B) high magnification TEM images (with associated diffractogram pattern) of Au/Al_2O_3.

7.3.2 Catalytic Activity/Selectivity

The temporal dependence of benzaldehyde fractional hydrogenation (X) over Au/Al_2O_3 is shown in **Figure 7.3(A)** where a time invariant (for 6 h on-stream) conversion is in evidence.

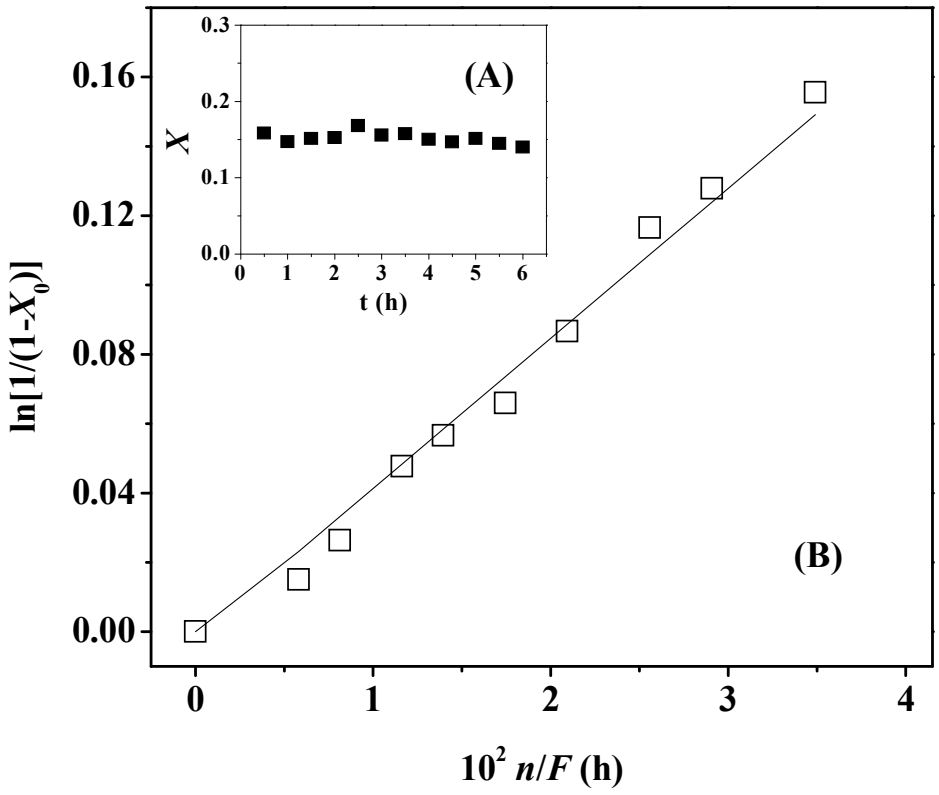

Figure 7.3: (A) Variation of benzaldehyde fractional conversion (X) with time-on-stream over Au/Al_2O_3 (n/F = 3.5×10^{-2} h); (B) Pseudo-first order kinetic plot for the hydrogenation of benzaldehyde to benzyl alcohol (P = 1 atm; T = 393 K).

Benzaldehyde hydrogenation over Au/Al_2O_3 generated benzyl alcohol as the sole product, *i.e.* 100% selective in promoting exclusive carbonyl group reduction to the alcohol. Reaction selectivity is challenging in benzaldehyde hydrogenation as a range of intermediates and by-products are possible as shown in **Figure 7.4**, which includes all the reaction pathways that have been proposed in the literature [7.5,7.7,7.10,7.12,7.13,7.30,7.31]; step I represents the target reduction of the carbonyl function. In both liquid and gas phase operation, catalytic hydrogenolysis with the formation of toluene and benzene is promoted [7.5,7.13].

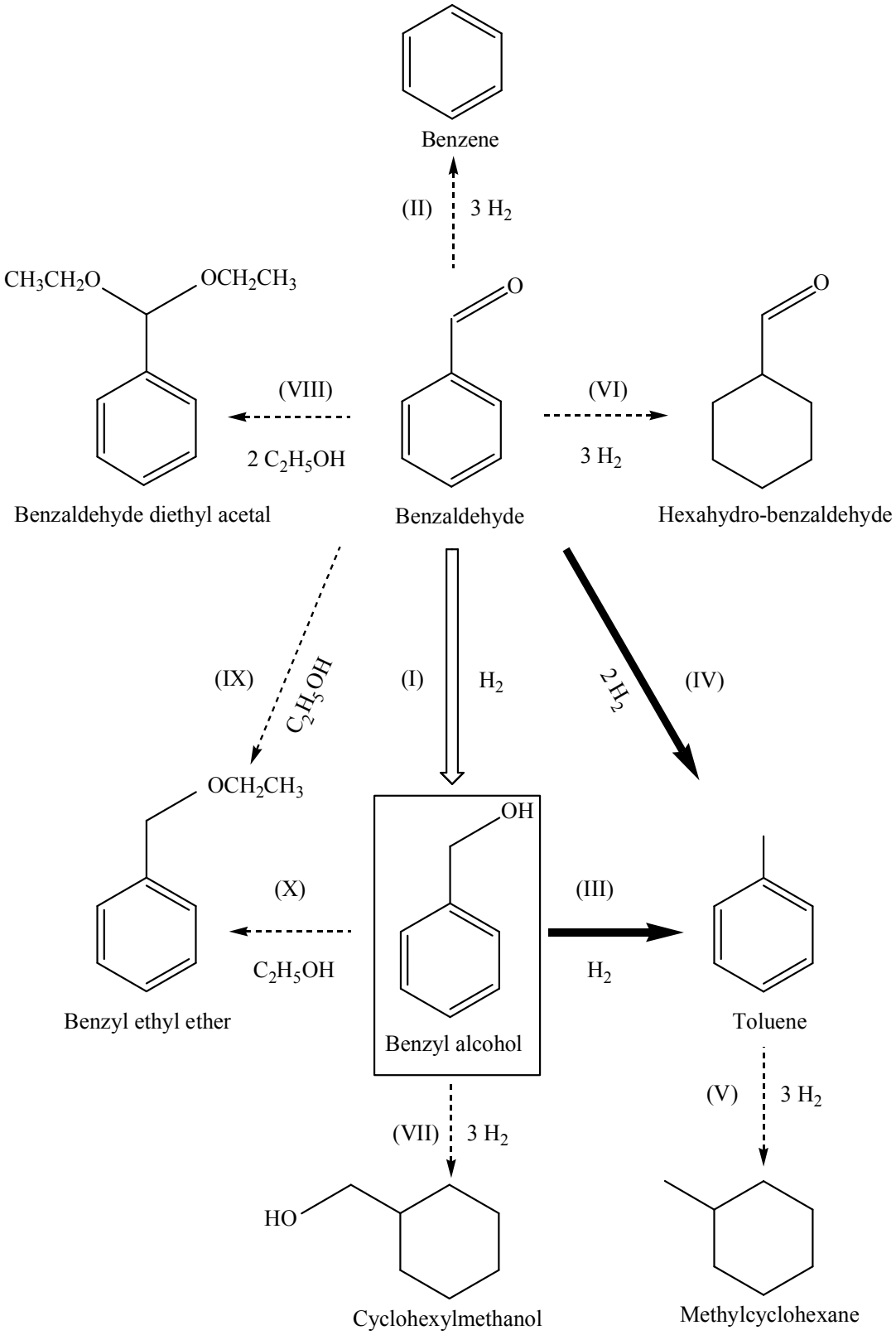

Figure 7.4: Possible reaction pathways associated with the hydrogenation of benzaldehyde to the target benzyl alcohol (⇨), isolated by-products (➔) and reaction products reported in the literature (⇢).

It has been proposed [7.5] that benzene is formed directly from benzaldehyde (step II) while toluene can result from the subsequent conversion of the alcohol (step III) and hydrogenolysis of benzaldehyde (step IV). Saadi and co-workers [7.12] isolated methylcyclohexane as a result of the further reduction of toluene (step V) during the gas phase hydrogenation of benzaldehyde over Ni/Al_2O_3. In liquid phase operation over Ru/C, hydrogenation of the aromatic ring (steps VI and VII) generated hexahydro-benzaldehyde [7.30] and cyclohexylmethanol [7.10] from benzaldehyde and benzyl alcohol, respectively. The nature of the solvent can influence both activity and selectivity [7.13] where the use of ethanol has resulted in benzaldehyde diethyl acetal formation by reaction with benzaldehyde (step VIII) and benzyl ethyl ether, formed from both benzaldehyde (step IX) and benzyl alcohol (step X) [7.7,7.31]. In our exclusive production of benzyl alcohol from benzaldehyde over Au/Al_2O_3, etherification of the reactant and/or product with the solvent (ethanol) did not occur and there was no detectable hydrogenolysis to generate toluene and/or benzene.

Benzaldehyde reaction kinetics have been reported for both liquid [7.8,7.9] and gas phase [7.11,7.12] operation. The applicability of a pseudo-first order kinetic treatment can be tested using the relationship [7.32]

$$\ln(1-X_0)^{-1} = k\left(\frac{n}{F}\right) \tag{7.5}$$

where X_0 represents the initial fractional conversion and n/F has the physical meaning of contact time. The linear relationship between $\ln(1\text{-}X_0)^{-1}$ and n/F, shown in **Figure 7.3(B)**, confirms adherence to pseudo-first order behaviour and the associated specific rate constant (k) is given in **Table 7.2**. In order to explore the potential of the Au/Al_2O_3 catalyst, Ni/Al_2O_3 and Pd/Al_2O_3 were employed as benchmark catalysts. The activities given in **Table 7.2** are in good agreement with values quoted in the literature [7.9,7.12,7.33] where both Pd and Ni catalysts delivered higher (by a factor up to 6) hydrogenation rates relative to Au. A lower hydrogenation activity for supported Au can be attributed to the higher energy barrier for H_2 dissociation [7.34]. Hydrogen uptake (at ambient temperature) on Au/Al_2O_3 was significantly lower than that measured for Pd/Al_2O_3 and Ni/Al_2O_3 (**Table 7.2**).

Table 7.2: Hydrogen chemisorption, pseudo-first order specific rate constants (k), initial reaction selectivities (S_0) and those obtained after 15 h on-stream (S_{15h}) for the conversion of benzaldehyde and benzyl alcohol over Au/Al_2O_3, Pd/Al_2O_3 and Ni/Al_2O_3.

		Benzaldehyde feed					Benzyl alcohol feed		
Catalyst	H_2 uptake (μmol g^{-1})	k (mmol m_{metal}^{-2} h^{-1})	S_0 (%) benzyl alcohol	S_0 (%) toluene	S_{15h} (%) benzyl alcohol	S_{15h} (%) toluene	k (mmol m_{metal}^{-2} h^{-1})	S_0 (%) toluene	S_0 (%) benzene
Au/Al_2O_3	< 1	0.5	100	0	100	0	< 0.01	0	100
Pd/Al_2O_3	24	2.6	10	90	95	5	1.7	100	0
Ni/Al_2O_3	4	3.1	0	100	-[a]	-[a]	1.4	100	0

[a]no detectable activity after 15h on-stream.

In terms of sustainable processing, the initial reaction rate is not the only consideration and catalyst lifetime must also be addressed. This feature was investigated for reaction over a prolonged period (15 h) and the results are presented in **Figure 7.5**, where temporal conversion is related to the initial value. While Au/Al_2O_3 largely retained the initial level of conversion (X_{15h}/X_0 = *ca.* 0.9), Ni/Al_2O_3 exhibited a drastic immediate decline in activity to deliver negligible conversion after 3 h on-stream while Pd/Al_2O_3 showed a continual decrease that was particularly marked at extended times (> 8 h on-stream). A temporal catalyst deactivation during benzaldehyde hydrogenation has been observed previously, attributed to coke deposition and associated with toluene formation [7.9].

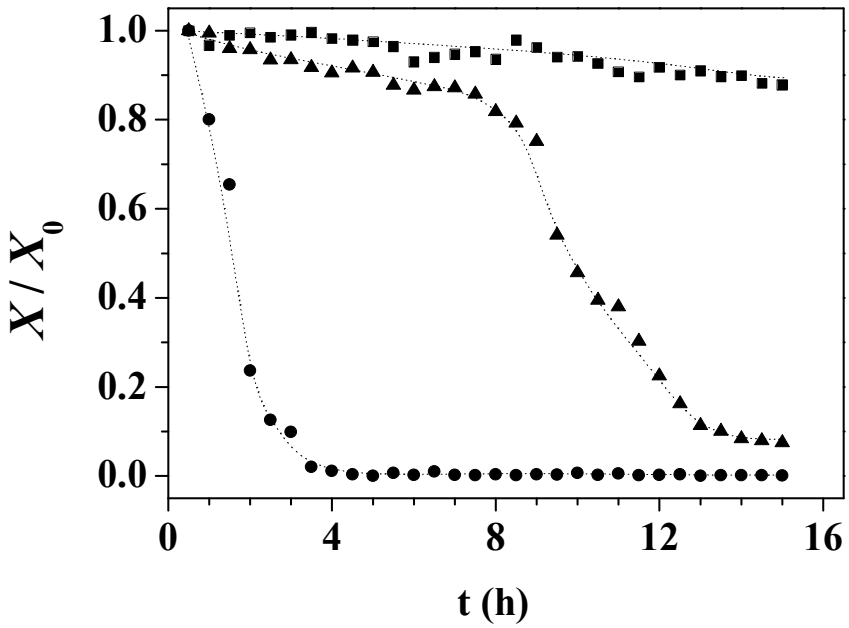

Figure 7.5: Ratio of benzaldehyde fractional conversion with time on-stream (X) to the initial value (X_0) for reaction over Au/Al_2O_3 (■), Pd/Al_2O_3 (▲) and Ni/Al_2O_3 (●) ($n/F = 3.5\times10^{-2}$ h; P = 1 atm; T = 393 K).

Initial reaction selectivities (S_0) are presented in **Table 7.2**. In common with Au/Al_2O_3, reaction over Pd/Al_2O_3 or Ni/Al_2O_3 did not result in any aromatic ring hydrogenation, hydrogenolysis to form benzene or reactant etherification/acetalisation. Reaction exclusivity to benzyl alcohol over Au/Al_2O_3 was maintained over extended time on-stream (see **Table 7.2**). The formation of benzyl alcohol (from benzaldehyde) has been proposed to occur *via* a nucleophilic mechanism where the carbonyl function is activated at the metal/support interface [7.11]. Adsorption of benzaldehyde where

both the aromatic ring and carbonyl group are co-planar to the surface facilitates C=O polarization, rendering the oxygen susceptible to nucleophilic attack with proton transfer to generate the alcohol [7.35]. The nature of the metal/support interface and the degree of metal dispersion are considered to be critical in determining benzyl alcohol formation [7.11]. Initially, toluene was the principal product resulting from reaction over Pd/Al_2O_3 with a low selectivity (10%) to benzyl alcohol while Ni/Al_2O_3 generated toluene as the only product. These selectivity trends find general agreement with the literature [7.7,7.9,7.12,7.23]. Initial selectivities to benzyl alcohol of 20-40% [7.9] and 10-20% [7.12] have been reported for Pd/Al_2O_3 (in liquid phase) and Ni/Al_2O_3 (in gas phase, T = 383-413 K), respectively. Toluene production from benzaldehyde is favoured by a strong interaction between the carbonyl oxygen and the surface with hydrogenolytic cleavage of C=O by dissociated hydrogen (**Figure 7.4**, step IV) [7.14].

In order to probe the possible reaction pathway, the conversion of benzyl alcohol under the same reaction conditions was considered and the results are included in **Table 7.2**. The rate constants generated for the alcohol feed were consistently lower than those obtained for the reaction of benzaldehyde and this can be attributed to the electrophilic character of C=O which renders this functionality more reactive relative to O-H [7.13]. Transformation of benzyl alcohol to toluene (**Figure 7.4**, step III) has been proposed to proceed *via* adsorption/activation on the support (formation of a benzoate on Al_2O_3) and reaction with hydrogen from the metal site [7.35]. The rate of toluene production over Ni/Al_2O_3 from benzaldehyde was significantly higher (by a factor of 2) than that obtained from benzyl alcohol and path IV (**Figure 7.4**) can be taken to be the predominant route to toluene. The rate of conversion of benzyl alcohol over Au/Al_2O_3 was two orders of magnitude lower than benzaldehyde hydrogenation; trace quantities of benzene were detected. The low reactivity of the alcohol on Au/Al_2O_3 must contribute to reaction exclusivity with respect to the benzaldehyde $\rightarrow$ benzyl alcohol step. In the case of Pd/Al_2O_3, benzyl alcohol conversion generated toluene as the sole product. The temporal decline in activity exhibited by Pd/Al_2O_3 during benzaldehyde conversion was accompanied by a switch in selectivity from toluene as the predominant product to benzyl alcohol. This response indicates a temporal inhibition of steps III and IV, limiting hydrogenolysis, while reaction *via* step I proceeds, resulting in the preferential production of benzyl alcohol. Ultimately, hydrogenation step (I) is limited with a residual conversion recorded after 15 h on-stream.

There was no detectable toluene formation in any reaction over Au/Al_2O_3, which represents a marked divergence in behaviour from both Pd/Al_2O_3 and Ni/Al_2O_3. We attribute this response to fundamental differences in surface reactive hydrogen and arene reactant activation at the metal/support interface.

7.4 Conclusion

This Chapter establishes the viability of benzaldehyde hydrogenation over Au/Al_2O_3 as a sustainable alternative route to benzyl alcohol. The reaction has been conducted under relatively mild reaction conditions (393 K, 1 atm) in continuous flow gas phase operation where 100% selectivity with respect to benzyl alcohol was achieved and maintained for 15 h on-stream. Temperature programmed reduction (TPR) of Au/Al_2O_3 to 473 K generated a supported Au metal phase, as confirmed by XRD and UV-Vis analyses, characterised by quasi-spherical particles with a surface weighted mean metal diameter = 7.9 nm. While Pd/Al_2O_3 and Ni/Al_2O_3 delivered higher activity (under the same reaction conditions), both exhibited severe deactivation with time-on-stream and promoted hydrogenolysis to toluene. The exclusive selectivity achieved with Au/Al_2O_3 is attributed to a polarization of the C=O bond which renders the oxygen susceptible to nucleophilic hydrogen attack to generate the alcohol, which does not undergo further reaction.

7.5 References

[7.1] *SIDS Initial Assessment report for 13th SIAM, OECD SIDS, Benzoates, CAS N° 65-85-0, 532-32-1, 582-25-2, 100-51-6*, UNEP publications, 2001, pp. 9-10.

[7.2] B. Nair, *Final report on the safety assessment of benzyl alcohol, benzoic acid, and sodium benzoate*, Int. J. Toxicol. 20 (2001) 23-50.

[7.3] V. van Brunt and J.S. Kanel, *Reactive Separation Processes*, S. Kulprathipanja (Ed.), Taylor & Francis, London, 2002, pp. 51-92.

[7.4] A. Bottino, G. Capannelli, A. Comite and R. di Felice, *Vapour phase oxidation of toluene in V/Al_2O_3–TiO_2 catalytic reactors*, Catal. Today 99 (2005) 171-177.

[7.5] D. Haffad, U. Kameswari, M.M. Bettahar, A. Chambellan and J.C. Lavalley, *Reduction of benzaldehyde on metal oxides*, J. Catal. 172 (1997) 85-92.

[7.6] C.-C. Guo, Q. Liu, X.-T. Wang and H.-Y. Hu, *Selective liquid phase oxidation of toluene with air*, Appl. Catal. A: General 282 (2005) 55-59.

[7.7] D. Procházková, P. Zámostný, M. Bejblová, L. Červený and J. Čejka, *Hydrodeoxygenation of aldehydes catalyzed by supported palladium catalysts*, Appl. Catal. A: General 332 (2007) 56-64.

[7.8] D. Divakar, D. Manikandan, G. Kalidoss and T. Sivakumar, *Hydrogenation of benzaldehyde over palladium intercalated bentonite catalysts: Kinetic studies*, Catal. Lett. 125 (2008) 277-282.

[7.9] F. Pinna, F. Menegazzo, M. Signoretto, P. Canton, G. Fagherazzi and N. Pernicone, *Consecutive hydrogenation of benzaldehyde over Pd catalysts. Influence of supports and sulfur poisoning*, Appl. Catal. A: General 219 (2001) 195-200.

[7.10] P. Kluson and L. Červený, *Hydrogenation of substituted aromatic compounds over a ruthenium catalyst*, J. Mol. Catal. A: Chemical 108 (1996) 107-112.

[7.11] A. Saadi, Z. Rassoul and M.M. Bettahar, *Gas phase hydrogenation of benzaldehyde over supported copper catalysts*, J. Mol. Catal. A: Chemical 164 (2000) 205-216.

[7.12] A. Saadi, R. Merabti, Z. Rassoul and M.M. Bettahar, *Benzaldehyde hydrogenation over supported nickel catalysts*, J. Mol. Catal. A: Chemical 253 (2006) 79-85.

[7.13] M.A. Vannice and D. Poondi, *The effect of metal-support interactions on the hydrogenation of benzaldehyde and benzyl alcohol*, J. Catal. 169 (1997) 166-175.

[7.14] R. Merabti, K. Bachari, D. Halliche, Z. Rassoul and A. Saadi, *Synthesis and characterization of activated carbon-supported copper or nickel and their catalytic*

behavior towards benzaldehyde hydrogenation, React. Kinet., Mech. Catal. 101 (2010) 195-208.

[7.15] M.A. Peralta, T. Sooknoi, T. Danuthai and D.E. Resasco, *Deoxygenation of benzaldehyde over CsNaX zeolites*, J. Mol. Catal. A: Chem. 312 (2009) 78-86.

[7.16] P. Haider, B. Kimmerle, F. Krumeich, W. Kleist, J.-D. Grunwaldt and A. Baiker, *Gold-catalyzed aerobic oxidation of benzyl alcohol: Effect of gold particle size on activity and selectivity in different solvents*, Catal. Lett. 125 (2008) 169-176.

[7.17] G. J. Hutchings, M. Brust and H. Schmidbaur, *Gold - an introductory perspective*, Chem. Soc. Rev. 37 (2008) 1759-1765.

[7.18] M. Besson and P. Gallezot, *Selective oxidation of alcohols and aldehydes on metal catalysts*, Catal. Today 57 (2000) 127-141.

[7.19] L. McEwan, M. Julius, S. Roberts and J.C.Q. Fletcher, *A Review of the use of gold catalysts in selective hydrogenation reactions*, Gold Bull. 43 (2010) 298-306.

[7.20] P. Claus, *Heterogeneously catalysed hydrogenation using gold catalysts*, Appl. Catal. A: General 291 (2005) 222-229.

[7.21] P. Claus, H. Hofmeister and C. Mohr, *Identification of active sites and influence of real structure of gold catalysts in the selective hydrogenation of acrolein to allyl alcohol*, Gold Bull. 37 (2004) 181-186.

[7.22] F. Cárdenas-Lizana, S. Gómez-Quero and M.A. Keane, *Clean production of chloroanilines by selective gas phase hydrogenation over supported Ni catalysts*, Appl. Catal. A: General 334 (2008) 199-206.

[7.23] M.A. Keane, *Gas phase hydrogenation/hydrogenolysis of benzaldehyde and o-tolualdehyde over Ni/SiO_2*, J. Mol. Catal. A: Chemical 118 (1997) 261-269.

[7.24] M. Harada and H. Einaga, *In situ XAFS studies of au particle formation by photoreduction in polymer solutions*, Langmuir 23 (2007) 6536-6543.

[7.25] A.C. Gluhoi, X. Tang, P. Marginean and B.E. Nieuwenhuys, *Characterization and catalytic activity of unpromoted and alkali (earth)-promoted Au/Al_2O_3 catalysts for low-temperature CO oxidation*, Top. Catal. 39 (2006) 101-110.

[7.26] C.K. Costello, J. Guzman, J.H. Yang, Y.M. Wang, M.C. Kung, B.C. Gates and H.H. Kung, *Activation of Au/gamma-Al_2O_3 catalysts for CO oxidation: Characterization by X-ray absorption near edge structure and temperature programmed reduction*, J. Phys. Chem. B 108 (2004) 12529-12536.

[7.27] X. Zhang, H. Shi and B.-Q. Xu, *Vital roles of hydroxyl groups and gold oxidation states in Au/ZrO_2 catalysts for 1,3-butadiene hydrogenation*, J. Catal. 279 (2011) 75-87.

[7.28] P. Claus, A. Brückner, C. Mohr and H. Hofmeister, *Supported gold nanoparticles from quantum dot to mesoscopic size scale: Effect of electronic and structural properties on catalytic hydrogenation of conjugated functional groups*, J. Am. Chem. Soc. 122 (2000) 11430-11439.

[7.29] G. Bond, C. Louis and D. T. Thompson, *Catalysis by Gold in Catalytic Science Series*, G. J. Hutchings (Ed.), Imperial College Press, London, 2006, pp. 150-153.

[7.30] L. Červený, Z. Bělohlav and M.N.H. Hamed, *Catalytic hydrogenation of aromatic aldehydes and ketones over ruthenium catalysts*, Res. Chem. Intermed. 22 (1996) 15-22.

[7.31] M. Arai, A. Obata and Y. Nishiyama, *The influence of reduction methods and conditions on the activity of alumina-supported platinum catalysts for the liquid phase hydrogenation of benzaldehyde in ethanol*, J. Catal. 166 (1997) 115-117.

[7.32] M.A. Keane, *Hydrodehalogenation of haloarenes over Silica supported Pd and Ni - A consideration of catalytic activity/selectivity and haloarene reactivity*, Appl. Catal. A: General 271 (2004) 109-118.

[7.33] T. Osaki, T. Hamada and Y. Tai, *Catalytic hydrogenation of C-60 on transition metals*, React. Kinet., Catal. Lett. 78 (2003) 217-223.

[7.34] B. Hammer and J.K. Nørskov, *Why gold is the noblest of all the metals*, Nature 376 (1995) 238-240.

[7.35] K. Lanasri, A. Saddi, K. Bachari, D. Halliche and O. Cherifi, *Gas phase hydrogenation of benzaldehyde over supported copper catalysts. Effect of copper loading*, Stud. Surf. Sci. Catal. 174 (2008) 1279-1282.

Chapter 8

Selectivity in the Gas Phase Hydrogenation of 4-Nitrobenzaldehyde over Supported Au Catalysts

In the previous Chapter, Au supported exhibited 100% selectivity in the hydrogenation of benzaldehyde to benzyl alcohol. The hydrogenation of 4-nitrobenzaldehyde represents a greater challenge as the reduction of both functional group (-NO_2 and C=O) can occur. In this Chapter, the roles of Au particle size, reaction temperature, support redox and acidity in determining selectivity for the hydrogenation of 4-nitrobenzaldehyde are examined.

8. 1 Introduction

Functionalised aromatic amines and alcohols are important intermediates in the production of a range of pharmaceuticals, agrochemicals, cosmetics, herbicides, dyes and polymers [8.1,8.2]. Amine and alcohol production can be achieved *via* the catalytic hydrogenation of nitro-compounds and aldehydes [8.3,8.4]. However, selectivity in terms of targeted -NO_2 or C=O reduction in the presence of other reactive functional groups (*e.g.* C≡N, C=C, COOH) remains challenging [8.5,8.6]. In this Chapter, the feasibility of controlling the selective hydrogenation of 4-nitrobenzaldehyde is examined. Reduction of -NO_2 is more facile than C=O and the amine should be the preferred product [8.7].

The possible pathways associated with the conversion of 4-nitrobenzaldehyde are presented in **Figure 8.1**, where 4-aminobenzaldehyde (step (I)) and 4-nitrobenzyl alcohol (step (II)) are commercially important compounds [8.8,8.9]. This reaction has been studied over soluble metal (Pd [8.10,8.11], Ru [8.8] and Co [8.12]) complexes and solid transition metal (supported Au, Ru, Ni, Pd and Pt [8.6,8.8,8.9,8.13-15] and PtO_2-H_2O [8.16]) catalysts in the liquid phase (P = 1-50 bar, T = 303-423 K). There has been only one reported gas phase application (for the hydrogenation of 3-nitrobenzaldehyde) over MgO [8.17].

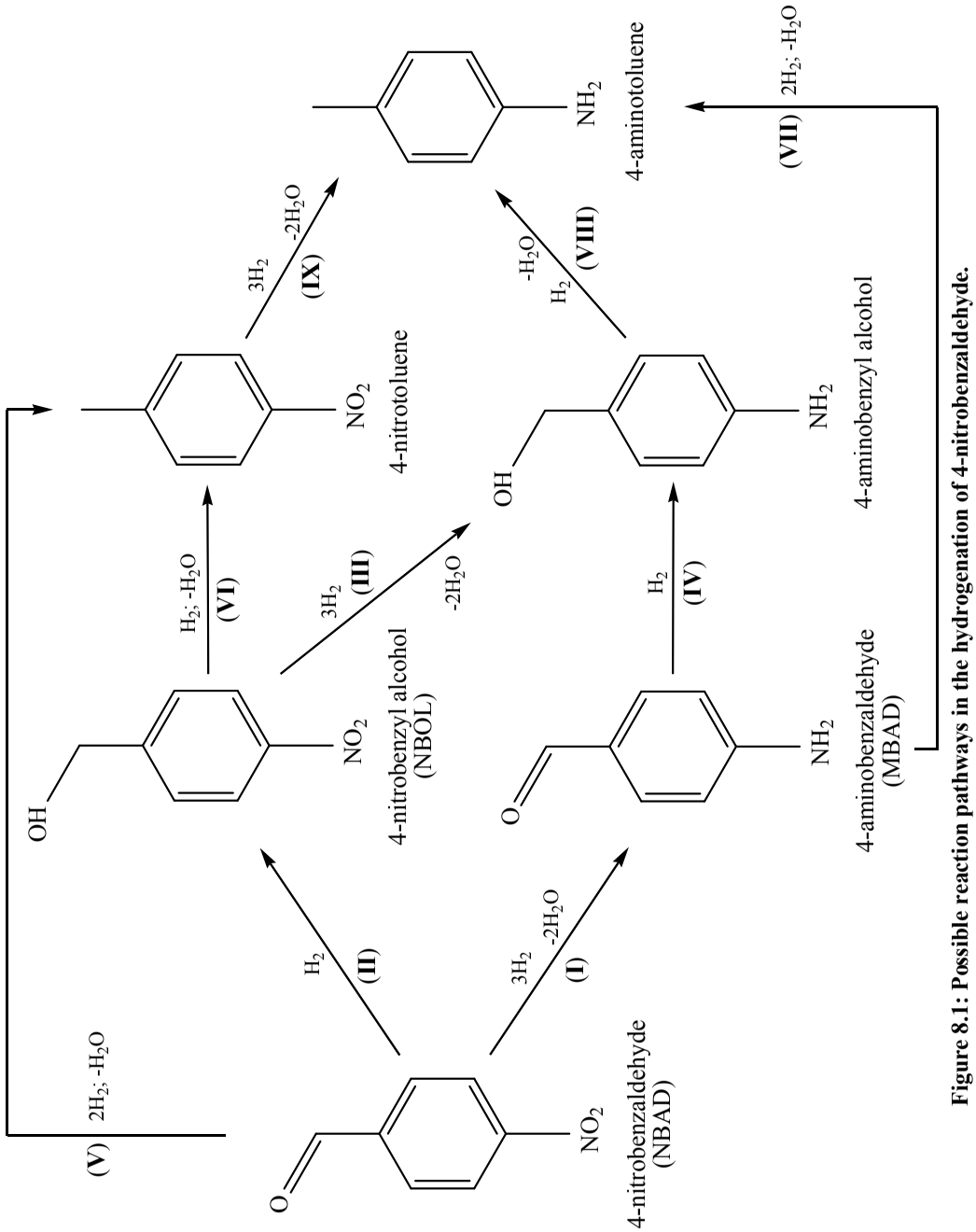

Figure 8.1: Possible reaction pathways in the hydrogenation of 4-nitrobenzaldehyde.

The reduction of both nitro and carbonyl functions generates 4-aminobenzyl alcohol (steps (III) and (IV)) as reported for reaction over PtO_2-H_2O [8.16], sol-gel entrapped Pd [8.18], MgO [8.17] and Ru/Al_2O_3 [8.8]. Moreover, formation of 4-nitrotoluene can result either from direct attack of C=O (step (V)) or further hydrogenation of 4-nitrobenzyl alcohol (step (VI)) and has been detected for reaction over Au/Fe_2O_3 and $Fe(OH)_x$ [8.13]. Generation of 4-aminotoluene can proceed *via* steps (VII), (VIII) and (IX). It is well established [8.6,8.9,8.11,8.16] that 4-aminobenzaldehyde and 4-aminobenzyl alcohol polymerise during hydrogenation with the formation of toxic azoxy compounds. The latter is favoured by the longer contact times that apply to conventional batch processes [8.11] and should be circumvented in continuous operation. Taking an overview of the literature, 4-aminobenzaldehyde has been the major product with selectivities up to 99% [8.6,8.9,8.10,8.12,8.13]. Preferential 4-nitrobenzyl alcohol formation has been demonstrated in reactions involving Ru complex [8.8] as catalysts but the precise source of this selectivity or the means of controlling product distribution remains unresolved.

Studies to date have focused on batch liquid phase processes where enhanced selectivity in homogenous catalysis required an alkali additive (KOH) [8.10,8.12] and operation under reflux conditions [8.12]. A switch to heterogeneous catalysis offers advantages in terms of product/catalyst separation while economies of scale favour continuous processes for high throughput. The use of Au catalysts has shown promise in the liquid phase conversion of 4-nitrobenzaldehyde to 4-aminobenzaldehyde although polymerisation was also observed [8.6,8.9,8.14]. Supported Au has exhibited chemoselectivity in $-NO_2$ reduction to $-NH_2$ in the presence of other reactive functionalities, *e.g.* C≡N [8.19], C=C [8.9], Br [8.20] and Cl [8.21]. Bailie and Hutchings [8.22] first demonstrated C=O activation on Au/ZrO_2, resulting in enhanced selectivity to crotyl alcohol. This work has led to a number of investigations on the selective hydrogenation of C=O to C-OH [8.23-33] over Au but none of these have considered the conversion of nitrobenzaldehyde. The catalytic response of Au/ZrO_2, as a starting point, is examined in the gas phase hydrogenation of 4-nitrobenzaldehyde. Previous work has established the importance of the support [8.26,8.34-36] and Au particle size [8.21,8.37-39] in determining hydrogenation performance. These effects are probed by investigating four catalysts that allow a decoupling of Au size, support redox and acidity effects; the role of reaction temperature is also assessed.

8.2 Experimental

8.2.1 Catalysts Preparation and Activation

The ZrO_2 support was prepared by precipitation of zirconium (IV) oxychloride octahydrate ($ZrOCl_2 \cdot 8H_2O$, ≥ 99.5%, Aldrich) with aqueous ammonia (35% w/w NH_3, Fisher). The $ZrOCl_2$ solution (0.1 M) was added dropwise with vigorous stirring to aqueous ammonia (2.5 M). Temporal pH changes were measured with a crystal-body electrode coupled to a data logging and collection system (Pico Technology), calibrated with standard buffer solutions (pH 7 and 10). The resultant hydrogel was washed with distilled water until the wash water was Cl-free ($AgNO_3$ test), dried at 373 K for 24 h and calcined in air (20 cm^3 min^{-1} g^{-1}) at 1 K min^{-1} to 673 K for 5 h.

Gold (*ca.* 1% w/w) supported on ZrO_2, TiO_2 (Degussa) and Al_2O_3 (Puralox) was prepared by deposition-precipitation (D-P) where a suspension (300 cm^3) of $HAuCl_4$ (99.999%, Aldrich), aqueous urea (100 cm^3) and support (5 g) was stirred (300 rpm) and heated (1 K min^{-1}) to 353 K for *ca.* 200 min. Synthesis was conducted in the dark to avoid formation of metallic colloids in solution by photoreduction of Au(III) [8.40]. As a high residual chloride content (> 300 ppm) results in the formation of larger (> 20 nm) Au particles [8.41] and can poison catalytic sites [8.42], the catalyst precursor was washed repeatedly. Gold on Al_2O_3 prepared by D-P is denoted by $AuAl_2O_3$-1. Alumina supported Au (*ca.* 1% w/w) was also prepared by standard impregnation of Al_2O_3 with an aqueous $HAuCl_4$ solution (Aldrich, 7.3×10^{-3} M, 39 cm^3) where the slurry was heated at 2 K min^{-1} to 353 K and agitated (600 rpm) in a He purge; this sample is denoted by $AuAl_2O_3$-2. The catalyst precursors were dried in He (10 cm^3 min^{-1} g^{-1}) at 383 K for 3 h and sieved into a batch of 75 μm average diameter. The samples were stored at 277 K under He in the dark in order to prevent Au agglomeration, which can occur when kept in air and in the light [8.43]. The precursors were activated in 60 cm^3 min^{-1} H_2 at 2 K min^{-1} to 473 K and passivated in 1% v/v O_2/He at ambient temperature for *ex situ* analysis.

8.2.2 Catalyst Characterisation

The pH associated with the point of zero charge (pH_{PZC}) of the supports was determined using the potentiometric mass titration [8.44]. In each case, three different masses (0.025, 0.050 and 0.075 g) were immersed in 50 cm^3 0.1 M NaCl to which a

known amount of NaOH (0.1 M) had been added to adjust the pH to 11. After stabilisation of the pH (*ca.* 1 h), titration with HCl (0.1 M) was performed under continuous agitation in He; temporal changes to pH were measured as described above. Temperature programmed reduction (TPR), BET surface area, total pore volume, H_2 chemisorption and temperature programmed desorption (TPD) were measured using the commercial CHEM-BET 3000 (Quantachrome) unit. Samples (0.2 g of Au/ZrO_2, Au/TiO_2, Au/Al_2O_3-1 and Au/Al_2O_3-2) were loaded into a U-shaped Quartz cell (10 cm×3.76 mm i.d.) and heated in 17 cm^3 min^{-1} (Brooks mass flow controlled) 5% v/v H_2/N_2 at 2 K min^{-1} to 473 ± 1 K. The effluent gas passed through a liquid N_2 trap and H_2 consumption was monitored by TCD with data acquisition/manipulation using the TPR Win™ software. The activated samples were maintained at 473 K in a constant flow of H_2/N_2 until the signal returned to baseline, swept with 65 cm^3 min^{-1} N_2 for 1.5 h and cooled to ambient temperature. The samples were subjected to H_2 chemisorption using a pulse (10 μl) titration procedure, followed by TPD in N_2 (65 cm^3 min^{-1}) at 45 K min^{-1} to 1173 K with an isothermal hold until the signal returned to baseline. Surface area and pore volume were determined, respectively, in 30% and 95% v/v N_2/He using undiluted N_2 as internal standard. At least 3 cycles of N_2 adsorption-desorption in the flow mode were employed using the standard single point method. The measurements were reproducible to within ± 8% and the values quoted represent the mean.

Surface acidity was determined by pyridine adsorption followed by infrared (IR) spectroscopy analysis. Samples were pressed (*ca.* 1×10^3 kg cm^{-2}) into thin wafers (*ca.* 10 mg cm^{-2}) and placed in the IR cell. Before pyridine adsorption/desorption, the samples were treated under static conditions at 473 K for 1 h in H_2 (666 mbar) and then outgas under secondary vacuum at 473 K for 1 h. The sample wafers were contacted at ambient temperature with gaseous pyridine (1.33 mbar) *via* a separate cell containing liquid pyridine. The spectra were recorded following desorption at 423 K with a Bruker Vector 22 spectrometer (resolution 2 cm^{-1}, 128 scans). The reported spectra were obtained after subtraction of the spectrum recorded prior to pyridine adsorption. The number of Lewis acid sites titrated by pyridine was obtained using a molar extinction coefficient value (ε = 2.22 cm μmol^{-1}) for the ν_{19b} vibration of coordinated pyridine (Py-L) at *ca.* 1455 cm^{-1} [8.45].

Gold content was measured by atomic absorption spectroscopy (AAS) using a Shimadzu AA-6650 spectrometer with an air-acetylene flame from the diluted extract in

aqua regia (25% v/v HNO_3/HCl). Powder X-ray diffractograms were recorded on a Bruker/Siemens D500 incident X-ray diffractometer using Cu Kα radiation. The samples were scanned over the range $10^o \leq 2\theta \leq 85^o$ (step: 0.02º; counting time: 0.5 s $step^{-1}$). Diffractograms were identified using the JCPDS-ICDD reference standards, *i.e.* tetragonal ZrO_2 (50-1089), monoclinic ZrO_2 (37-1487), anatase (21-1272), rutile (21-1276), Al_2O_3 (10-0425) and Au (04-0784). The fraction of monoclinic zirconia was calculated, based on the work of Toraya *et al*. [8.46], using the integrated intensities (I) of the (111) and (-111) monoclinic (m-ZrO_2) and (011) tetragonal (t-ZrO_2) planes,

$$X_m = \frac{I_m(\text{-}111)+I_m(111)}{I_m(\text{-}111)+I_m(111)+I_t(011)} \quad ; \quad V_m = \frac{1.31 \times X_m}{1+0.31 \times X_m} \tag{8.1}$$

where X_m represents the intensity ratio and V_m the fraction of monoclinic zirconia.

Gold particle morphology and size were determined by transmission electron microscopy analysis; JEOL JEM 2011 HRTEM unit with a UTW energy dispersive X-ray detector (Oxford Instruments) operated at an accelerating voltage of 200 kV using Gatan DigitalMicrograph 3.4 for data acquisition/manipulation. Samples for analysis were prepared by dispersion in acetone and deposited on a holey carbon/Cu grid (300 Mesh). Up to 420 individual Au particles were counted for each catalyst and the mean Au particle sizes are given as the surface area-weighted average (d) [8.34]. Gold dispersion (D) was calculated from d values [8.47] and used to determine turnover frequency (TOF (s^{-1})). XPS spectra were collected on a SPECS (Phoibos MCD 150) X-ray photoelectron spectrometer, using an Al Kα ($h\nu$ = 1486.6 eV) X-ray source. The binding energies were calibrated with respect to the C-C/C-H components of the C 1s peak (binding energy = 284.7 eV). All spectra processing was carried out using the Casa XPS software package.

8.2.3 Catalysis Procedure

Reactions were carried out under atmospheric pressure at 423-473 K, *in situ* after catalyst activation, in a fixed bed vertical glass tubular reactor (60 cm×15 mm i.d.). The catalytic reactor and operating conditions to ensure negligible heat/mass transport limitations have been described elsewhere [8.48] but some features, pertinent to this study, are given below. A layer of borosilicate glass beads served as preheating

zone, ensuring that the organic reactant was vaporised and reached reaction temperature before contacting the catalyst. Temperature was continuously monitored using a thermocouple inserted in a thermowell within the catalyst bed.

4-Nitrobenzaldehyde as a solution in ethanol was delivered at a fixed calibrated flow rate *via* a glass/teflon air-tight syringe and teflon line using a microprocessor controlled infusion pump (Model 100 kd Scientific). A co-current flow of 4-nitrobenzaldehyde and ultra pure H_2 (< 1% v/v 4-nitrobenzaldehyde in H_2) was maintained at GHSV = 2×10^4 h^{-1} with an inlet 4-nitrobenzaldehyde molar flow (F) = 6.0×10^{-5} mol h^{-1}. Hydrogen flow rate was monitored using a Humonics (Model 520) digital flowmeter where H_2 content was far in excess of the stoichiometric requirements. The mass of Au to inlet 4-nitrobenzaldehyde feed rate (m/F) ratio spanned the range 0.6-12 g_{Au} mol^{-1} h. The catalytic conversion of benzaldehyde and nitrobenzene over Au/ZrO_2 and Au/Al_2O_3-2 at 443 K was also examined. Passage of each reactant in a stream of H_2 through the empty reactor did not result in any detectable conversion. The reactor effluent was frozen in a liquid nitrogen trap for subsequent analysis, which was made using a Perkin-Elmer Auto System XL gas chromatograph equipped with a programmed split/splitless injector and a flame ionization detector, employing a DB-1 (50 m×0.33 mm i.d., 0.20 μm film thickness) capillary column (J&W Scientific). 4-Nitrobenzaldehyde (Aldrich, 98% w/w purity), benzaldehyde (Fluka, ≥ 98% w/w), nitrobenzene (Fluka, ≥ 99%) and ethanol (Sigma Aldrich, ≥ 99%) were used without further purification. Fractional 4-nitrobenzaldehyde conversion (X) is defined by

$$X = \frac{\left[4-nitrobenzaldehyde\right]_{in} - \left[4-nitrobenzaldehyde\right]_{out}}{\left[4-nitrobenzaldehyde\right]_{in}} \tag{8.2}$$

where the subscripts "out" and "in" refer to the outlet and inlet gas streams, respectively. Selectivity in terms of 4-aminobenzaldehyde (S_{MBAD}), as an example, is given by

$$S_{MBAD} = \frac{\left[4-aminobenzaldehyde\right]_{out}}{\left[4-nitrobenzaldehyde\right]_{in} - \left[4-nitrobenzaldehyde\right]_{out}} \tag{8.3}$$

where 4-aminobenzaldehyde (Y_{MBAD}) yield was obtained from

$$Y_{MBAD} = S_{MBAD} \times X \tag{8.4}$$

Repeated reactions with samples from the same batch of catalyst delivered a product composition that was reproducible to within ± 3%.

8.3 Results and discussion

8.3.1 Au/ZrO_2: Synthesis and Characterisation

The structural characteristics of ZrO_2 in terms of surface area and crystalline phase depend on a range of parameters, including the Zr salt precursor, pH and duration of precipitation and the *post*-treatment, notably washing and calcination stages [8.49-51]. Precipitation of hydrous zirconia was accompanied by a temporal pH decrease from 11.8 to 9.4, as presented in **Figure 8.2(a)**. The same pH response has been observed under equivalent synthesis conditions [8.52]. The XRD pattern of the calcined sample (**Figure 8.2(c)**) exhibits both tetragonal and monoclinic phases. Six of the nine XRD peaks can be ascribed to monoclinic ZrO_2 planes ((110), (-111), (111), (200), (022) and (310)) with three signals due to tetragonal ZrO_2 ((011), (112) and (121) planes); the fractional monoclinic phase content (V_m from eqn. (8.1)) = 0.65). Chuah *et al.* [8.52] have shown that zirconia phase composition is sensitive to precipitation temperature, pH and calcination. Synthesis at temperature in the range 303-353 K in basic medium and calcination at 773 K generated a mixed phase that was predominantly monoclinic (V_m = 0.50-0.78). The surface area (104 m^2 g^{-1}, **Table 8.1**) and total pore volume (0.14 cm^3 g^{-1}) are consistent with values (109 m^2 g^{-1} [8.53] and 0.16 cm^3 g^{-1} [8.54]) reported previously.

The pH associated with the point of zero charge (pH_{PZC}) is a critical support property that determines the solution pH requirements to ensure precursor-support interactions during catalyst preparation by deposition-precipitation [8.55]. A pH_{PZC} of 7.4 was determined experimentally for ZrO_2, which is in general agreement with the literature where pH_{PZC} in the 6.2-8.5 interval has been recorded [8.56,8.57]. The pH_{PZC} depends on oxide synthesis and composition where a lower value (6.2) is associated with the pure tetragonal form relative to the monoclinic phase (8.5) [8.56]. The temporal pH variation in the preparation of (0.8% w/w) Au/ZrO_2 is given in **Figure 8.2(b)** where the pH_{PZC} of ZrO_2 is identified by the horizontal dotted line. The increase in temperature (up to 353 K) resulted in a progressive decomposition of urea with an accompanying increase in solution pH. As the latter remained below the pH_{PZC} the support bears a positive charge (due to protonation), favouring interaction with anionic gold species in solution ($HAuCl_4$ and/or $Au(OH)Cl_3^-$) [8.43]. The surface sites act as nucleation centres for Au deposition [8.58].

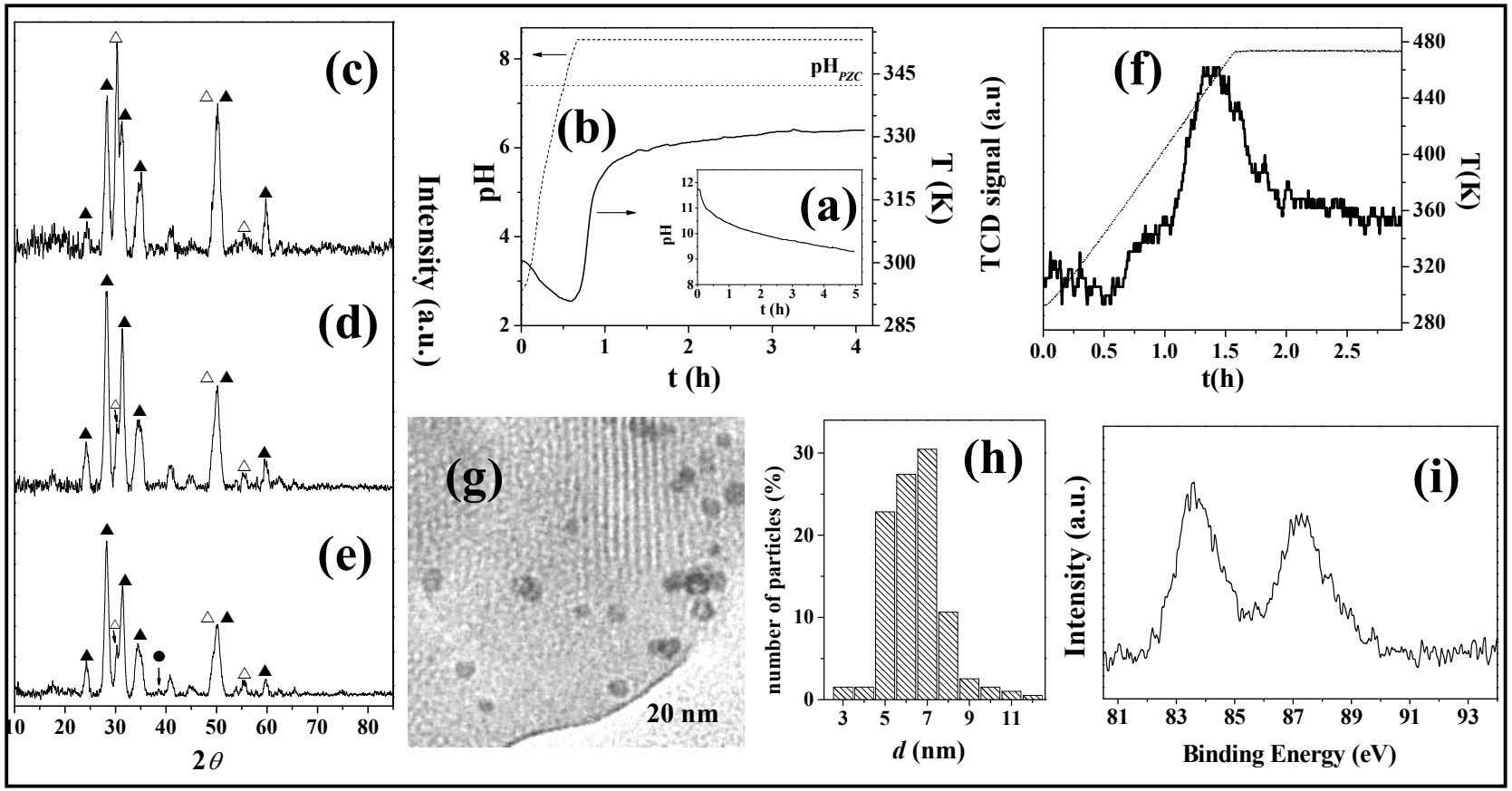

Figure 8.2: Temporal pH variations in the preparation of (a) ZrO_2 and (b) Au/ZrO_2 (pH_{PZC} of the support identified by the dotted line); XRD patterns for (c) ZrO_2 and Au/ZrO_2 (d) *pre-* and (e) *post*-TPR where (△) identifies tetragonal ZrO_2 (JCPDS card 50-1089), (▲) monoclinic ZrO_2 (37-1487) and (●) Au (04-0784); (f) TPR profile (solid line) with temperature ramp (dotted line) generated for Au/ZrO_2; (g) representative TEM image with (h) Au particle size distribution; (i) XPS spectrum of Au/ZrO_2 in the Au 4*f* region.

Table 8.1: Gold loading, BET surface area, total pore volume, temperature programmed reduction (TPR) T_{max} with associated H_2 consumption, H_2 chemisorbed/desorbed (TPD), surface area- weighted mean Au diameter (d), dispersion (D) and Au $4f_{7/2}$ binding energy (BE).

Catalyst		Au/ZrO_2	Au/TiO_2	Au/Al_2O_3-1	Au/Al_2O_3-2
Au loading (% w/w)		0.8	1.2	1.1	1.1
BET surface area ($m^2\ g^{-1}$)		93[a] (104[b])	48[a]	166[a]	161[a]
Total pore volume ($cm^3\ g^{-1}$)		0.13[a] (0.14[b])	0.12[a]	0.36[a]	0.36[a]
TPR	T_{max} (K)	452	364	457	415
	H_2 consumed (mmol g_{Au}^{-1})	7.0	10.5	7.9	7.1
H_2 chemisorption (μmol g_{Au}^{-1})		56	28	37	19
H_2 desorbed (mmol g_{Au}^{-1})		28	9	51	24
d (nm)		7.0	4.7	4.3	7.8
D		0.18	0.27	0.29	0.16
Au $4f_{7/2}$ BE (± 0.2 eV)		83.5	83.4	83.3	83.2

[a]activated catalyst
[b]support

The XRD pattern for Au/ZrO_2 as prepared (**Figure 8.2(d)**) only exhibits peaks due to monoclinic and tetragonal ZrO_2. Compared with the starting ZrO_2 (**Figure 8.2(c)**), the relative peak intensities differ and the fraction of monoclinic phase is higher (V_m = 0.85). This can be linked to the deposition step and the associated contact with aqueous Au salt solution, pH and temperature variations. Indeed, it should be noted that Xie *et al.* [8.59] observed a transformation of tetragonal ZrO_2 following immersion in water at 298 K (for 12 h), resulting in a 78% conversion to monoclinic ZrO_2 with no change to surface area, which they attributed to differences in surface free energy between the two phases after water adsorption.

Temperature programmed reduction (TPR) of Au/ZrO_2 generated the profile shown in **Figure 8.2(f)** where a positive peak (H_2 consumption) with T_{max} = 452 K is in evidence. There was no detectable H_2 consumption in the TPR (to 773 K) of the ZrO_2 support, which agrees with the literature [8.60,8.61] and the response recorded for Au/ZrO_2 can be attributed to the reduction of cationic gold. Positive TPR signals in the range 424 K-503 K range have been recorded elsewhere for Au/ZrO_2 [8.54,8.62]. In this study, the H_2 consumed (**Table 8.1**) corresponds to the amount required (to within 10%)

for the reduction of supported Au^{3+} to Au^0. The surface area (93 m^2 g^{-1}) and total pore volume (0.13 cm^3 g^{-1}) of the activated catalyst was lower than that recorded for the support alone (**Table 8.1**), which can be ascribed to partial pore blockage by the Au component. The relative intensity of the XRD signals coincide for Au/ZrO_2 *pre-* (**Figure 8.2(d)**) and *post-* (**Figure 8.2(e)**) TPR, indicating that the reduction step had no effect on support phase composition. A weak signal at 38.1° can be attributed to Au (111) but the peak intensity is too low to allow an accurate evaluation of Au particle size by standard line broadening analysis.

Gold particle morphology and size were probed by transmission electron microscopy (TEM) and a representative micrograph is given in **Figure 8.2(g)**, which reveals quasi-spherical particles at the nano-scale (3-12 nm). Particle size distribution is illustrated by the histogram presented in **Figure 8.2(h)**, which gives a surface area weighted mean Au diameter of 7 nm, matching that reported by Mohr *et al.* [8.38] for the synthesis of Au/ZrO_2 by deposition-precipitation. The majority of Au particles are < 10 nm, which has been established as critical for hydrogenation activity [8.63]. The electronic character of the supported Au phase can be critical in determining reactant adsorption/activation and consequent activity/selectivity [8.35,8.39] and is dependent on support interaction and dispersion [8.64]. XPS analysis was employed to probe Au electronic state where the profile (**Figure 8.2(i)**) over the Au 4*f* binding energy (BE) region generates signals at 83.5 ± 0.2 eV (**Table 8.1**) and 87.3 ± 0.2 eV, which are in line with Au $4f_{7/2}$ (83.7 eV [8.62], 83.8 eV [8.64]) and $4f_{5/2}$ (87.6 eV) values reported for Au/ZrO_2. This represents a shift to lower BE relative to the reference Au foil $4f_{7/2}$ (84.0 eV) and can be attributed to electron transfer from the support to the nano-scale Au [8.65].

Catalytic activity in hydrogen mediated reactions is dependent on the H_2 adsorption/dissociation capacity of the catalyst. Hydrogen chemisorption and release (H_2-TPD) results for Au/ZrO_2 are given in **Table 8.1**. The available literature on the dynamics of H_2 interaction with Au/ZrO_2 is limited but hydrogenation activity has been established [8.22,8.62,8.66,8.67]. Dissociative chemisorption of H_2 can occur at low coordination Au sites, *i.e.* at edges and corners [8.33,8.68] with the result that H_2 activation is enhanced with increased Au dispersion [8.32,8.63,8.69]. Zhang and co-workers [8.54] have proposed that H_2 activation requires the combined action of ZrO_2 hydroxyl groups and surface Au sites. Moreover, it is known that H_2 adsorbed on

supported metals can spillover onto the ZrO_2 support [8.70]. A search through the literature did not reveal any reported data with which to compare the ambient temperature H_2 chemisorption value (56 μmol g_{Au}^{-1}, **Table 8.1**). However, this level of uptake is appreciably lower than that recorded for other transition metal systems, such as Pt/ZrO_2 (up to 1440 μmol g_{Pt}^{-1}) [8.61,8.71]. Hydrogen released during TPD far exceeded H_2 chemisorbed, suggesting that uptake is an activated process with the possible contribution of spillover hydrogen during TPR to the total H_2 desorbed.

8.3.2 Au/ZrO_2: Catalytic Response

The hydrogenation of 4-nitrobenzaldehyde over Au/ZrO_2 generated 4-aminobenzaldehyde as the only product with no detectable hydrogenation or hydrogenolysis of the carbonyl group.

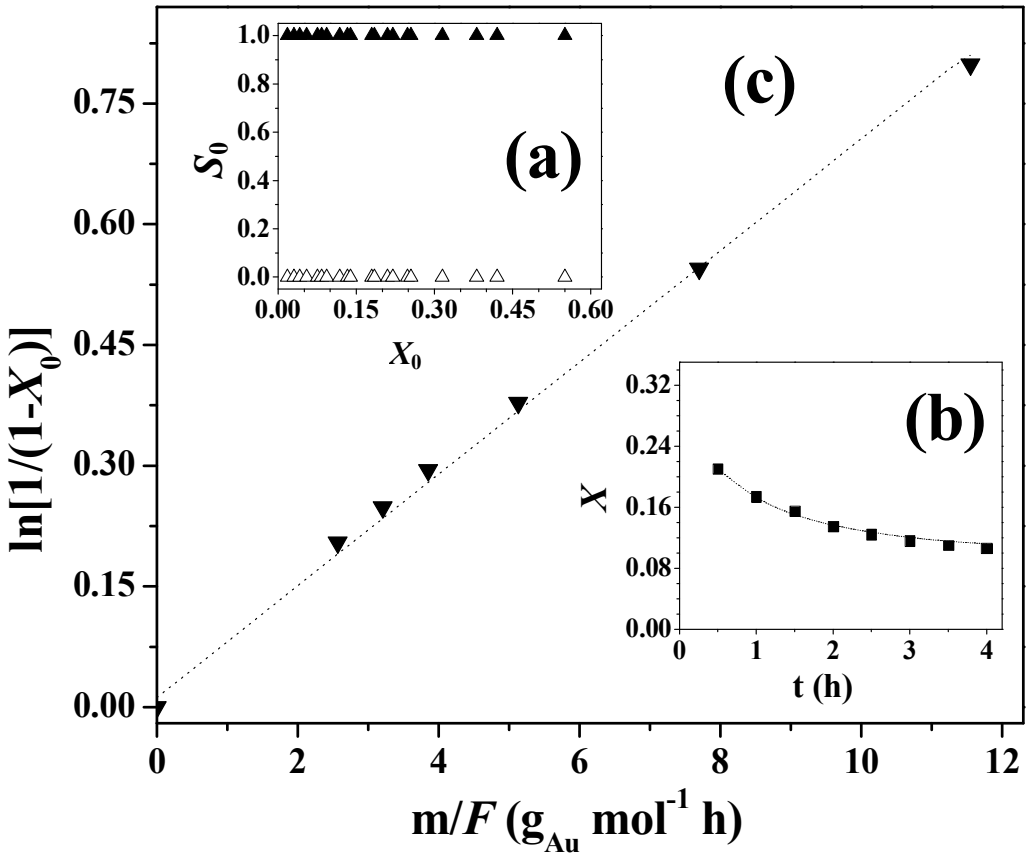

Figure 8.3: (a) Initial selectivity (S_0) to 4-aminobenzaldehyde (▲) and 4-nitrobenzyl alcohol (△) with fractional 4-nitrobenzaldehyde conversion (X_0) over Au/ZrO_2 at 443 K; (b) representative (m/F = 5 g_{Au} mol^{-1} h, T = 443 K) temporal 4-nitrobenzaldehyde fractional conversion profile with fit to eqn. (8.5); (c) pseudo-first order kinetic plot.

This is the first report of 100% selectivity to 4-aminobenzaldehyde over Au catalysts, where reaction exclusivity was maintained at high levels of 4-nitrobenzaldehyde conversion (**Figure 8.3(a)**). There was no evidence of any polymerisation or detectable azoxy formation, which may be attributed to the short contact time (180 ms) in the catalyst bed.

A representative time on-stream 4-nitrobenzaldehyde conversion (X) profile is presented in **Figure 8.3(b)** where a temporal decline is evident that can be expressed in terms of the empirical relationship [8.20]

$$\frac{(X - X_0)}{(X_{4h} - X_0)} = \frac{t}{(\beta + t)} \tag{8.5}$$

where X_{4h} represents fractional conversion after 4 h on-stream, β is a time scale fitting parameter and X_0 is the initial conversion (obtained from the fit to eqn. (8.5), shown in **Figure 8.3(b)**). Reaction exclusivity to 4-aminobenzaldehyde was maintained with time on-stream. Loss of activity during hydrogenation over Au catalysts has been attributed to coke deposition that occludes the active sites [8.72]. Moreover, water released as the by-product of nitro group reduction can have a deleterious effect on catalytic activity [8.54,8.73]. Previous work in this laboratory [8.20,8.31] have established the applicability of pseudo-first order kinetics for hydrogenation over supported Au,

$$\ln(1 - X_0)^{-1} = k\left(\frac{m}{F}\right) \tag{8.6}$$

where m/F is the ratio of mass of Au to inlet 4-nitrobenzaldehyde molar feed rate. The pseudo-first order plot is given in **Figure 8.3(c)** where the linear fit (passing through the origin) confirms adherence to the kinetic model; the associated rate constant (k) is given in **Table 8.2**.

Prior published work has demonstrated a dependence of activity and selectivity in the hydrogenation of nitro compounds and aldehydes on Au particle size [8.38,8.39] and the nature of the support [8.29,8.35,8.36] in term of reducibility and acid-base properties. The objective of this Chapter is to assess the feasibility of controlling product distribution in the hydrogenation of 4-nitrobenzaldehyde. The sole formation of 4-aminobenzaldehyde was obtained over 3-12 nm Au particles (mean = 7 nm) on a non-

reducible (ZrO_2) support. Metal-support interactions in the case of titania are known to influence the catalytic response [8.74]. Indeed, the use of Au/ZrO_2 and Au/TiO_2 in acrolein hydrogenation has revealed differences in activity/selectivity that were linked to variations in Au coordination and reactivity at the Au-support interface [8.38,8.39]. Therefore, the catalytic action of TiO_2 (with a comparable Au loading) was examined as an alternative Au support.

Table 8.2: Rate constant (k), turnover frequency (TOF) and initial selectivity to 4-aminobenzaldehyde (S_{MBAD}) and 4-nitrobenzyl alcohol (S_{NBOL}) at $X_0 \approx 0.2$ for the conversion of 4-nitrobenzaldehyde at 443 K.

	k (mmol g_{Au} h^{-1})	TOF (10^{-3} s^{-1})	S_{MBAD}	S_{NBOL}
Au/ZrO_2	71	22	1	0
Au/TiO_2	145	30	1	0
Au/Al_2O_3-1	176	33	0.82	0.18
Au/Al_2O_3-2	64	22	0	1

8.3.3 Au/TiO₂: Characterisation

Preparation of Au/TiO_2 by deposition-precipitation delivered a 1.2% w/w Au loading with a lower total (BET) surface area but comparable pore volume to Au/ZrO_2 (**Table 8.1**). TPR analysis (**Figure 8.4(a)**) generated a reduction peak 364 K that is close to the range (373-432 K) previously reported for Au/TiO_2 [8.34,8.75]. The associated H_2 consumption (**Table 8.1**) is higher than that required for the reduction of Au^{3+} to Au^0 (7.6 mmol g_{Au}^{-1}). The excess H_2 can contribute to a partial reduction of Ti^{4+} to Ti^{3+} at the Au-support interface [8.34,8.75].

The XRD measurement (**Figure 8.4(b)**) is consistent with a mixture of anatase and rutile forms of TiO_2 where anatase:rutile ≈ 5:1, which is characteristic of Degussa P25 [8.76] for thermal treatment up to 923 K [8.77]. The signal at 38.4° suggests the presence of Au metal but the peak overlaps with one due to anatase, which does not permit a calculation of Au size. The representative TEM image shown in **Figure 8.4(c)** reveals dispersed nano-scale Au particles. The TEM derived Au particle size histogram (**Figure 8.4(d)**) shows a narrower distribution of smaller Au particles relative to Au/ZrO_2 with a surface area weighted mean diameter = 4.7 nm. The Au $4f_{7/2}$ binding

energy measured by XPS (83.4 eV ± 0.2) (**Table 8.1,** spectrum not shown) is at the lower end of the range reported in the literature for Au/TiO_2 (83.3-84.2 eV) [8.64,8.65,8.78] and, despite the difference in Au size, essentially converges with the value recorded for Au/ZrO_2.

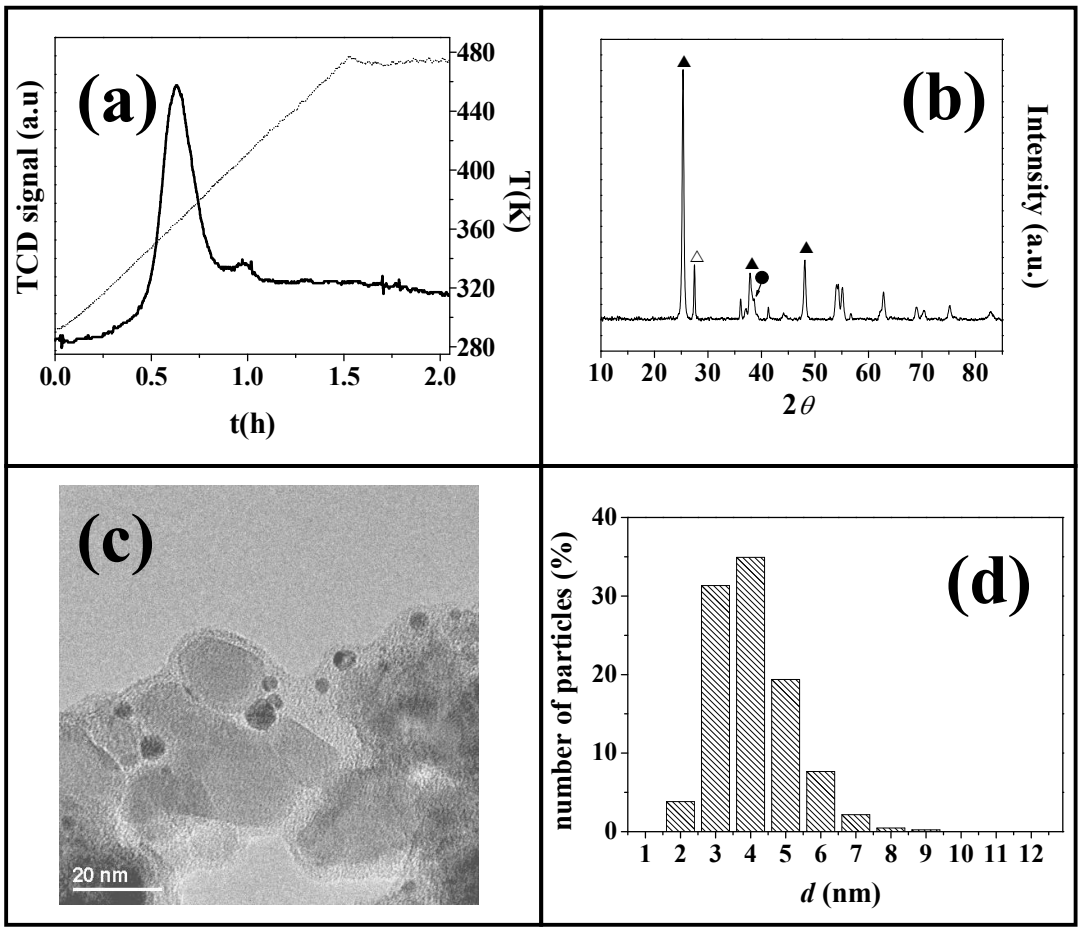

Figure 8.4: (a) TPR profile (solid line) with temperature ramp (dotted line) generated for Au/TiO_2; (b) XRD pattern *post*-TPR where (▲) identifies anatase (JCPDS Card 21-1272), (△) rutile (21-1276) and (●) Au (04-0784); (c) representative TEM image; (d) Au particle size distribution.

Dissociative hydrogen adsorption at ambient temperature has been established for Au/TiO_2 [8.79,8.80]. In this study, H_2 chemisorption and subsequent desorption was lower for Au/TiO_2 when compared with Au/ZrO_2 **(Table 8.1)**. It is known that TiO_x species, formed during activation, can migrate to the metal surface and occlude surface sites for H_2 adsorption [8.81]. The lower H_2-TPD can be attributed in part to the lower surface area that characterises Au/TiO_2, limiting the extent of hydrogen spillover during TPR.

8.3.4 Au/TiO_2: Catalytic Response

The hydrogenation of 4-nitrobenzaldehyde over Au/TiO_2 has been studied in batch liquid mode, where 4-aminobenzaldehyde selectivity up to 99% was obtained [8.6,8.9]. Batch operation required high H_2 pressure (10 bar) with laborious catalyst/product separation and purification stages. Gas phase continuous operation ensures higher throughput at a lower operating pressure (P_{H2} < 1 bar). As was observed for Au/ZrO_2, 4-nitrobenzaldehyde hydrogenation over Au/TiO_2 generated 4-aminobenzaldehyde as the only detectable product with time on-stream.

The reduction of nitro compounds requires effective polarisation of the N=O function with nucleophilic hydrogen attack and the formation of a negatively charged intermediate [8.82]. Boronat *et al.* [8.68] investigated the hydrogenation of nitrostyrene and observed a higher selectivity to aminostyrene for reaction over Au/TiO_2 (98%) relative to Au/SiO_2 (30%). Drawing on *in situ* IR analysis and quantum chemical calculations, they attributed this effect to -NO_2 activation at the Au-TiO_2 interface. In a recent application of the selective energy transfer (SET) model to hydrogenation kinetics for a range of functionalised nitroarenes over Au/TiO_2, activation of the O-N-O bending/stretching moiety at TiO_2 or Au-TiO_2 interface sites was proposed [8.83]. A similar surface dynamic can apply to selective -NO_2 reduction in the 4-nitrobenzaldehyde-Au/TiO_2 reaction system that also extends to Au/ZrO_2.

Au/TiO_2 delivered a higher turnover frequency (*TOF*) than Au/ZrO_2 (**Table 8.2**). However, Au/ZrO_2 exhibited higher H_2 uptake and release (**Table 8.1**), which should lead to greater hydrogenation efficiency. We therefore propose that -NO_2 activation/polarisation is the limiting factor. Corma *et al.* [8.84] have demonstrated that nitrobenzene can adsorb on both Au and TiO_2 where the interaction is weaker on the metal relative to the support but is significantly enhanced on highly uncoordinated Au atoms. The greater Au dispersion on TiO_2 will generate an increased proportion of edge and corner sites relative to Au/ZrO_2 and a greater number of interfacial low-coordinated Au sites [8.85] that contribute to enhanced *TOF*.

It is established that the Au support plays a crucial role in modifying organic reactant adsorption/activation in hydrogenation applications [8.26,8.35,8.68]. Reduction of both -NO_2 and C=C functions in nitrostyrene was recorded for Au supported on SiO_2 and C, in contrast to the selective action of Au on TiO_2 and Fe_2O_3 [8.68]. Moreover,

Au/FeOOH preferentially promoted the reduction of C=O relative to C=C in the hydrogenation of cinnamaldehyde, whereas both functional groups were reduced over Au/α-Fe_2O_3 [8.26]. In order to probe support effects further, we considered the catalytic consequences of using Al_2O_3 as an acidic carrier where two Au/Al_2O_3 samples with Au particle sizes that match Au/TiO_2 and Au/ZrO_2 were synthesised and tested.

8.3.5 Au/Al_2O_3: Characterisation

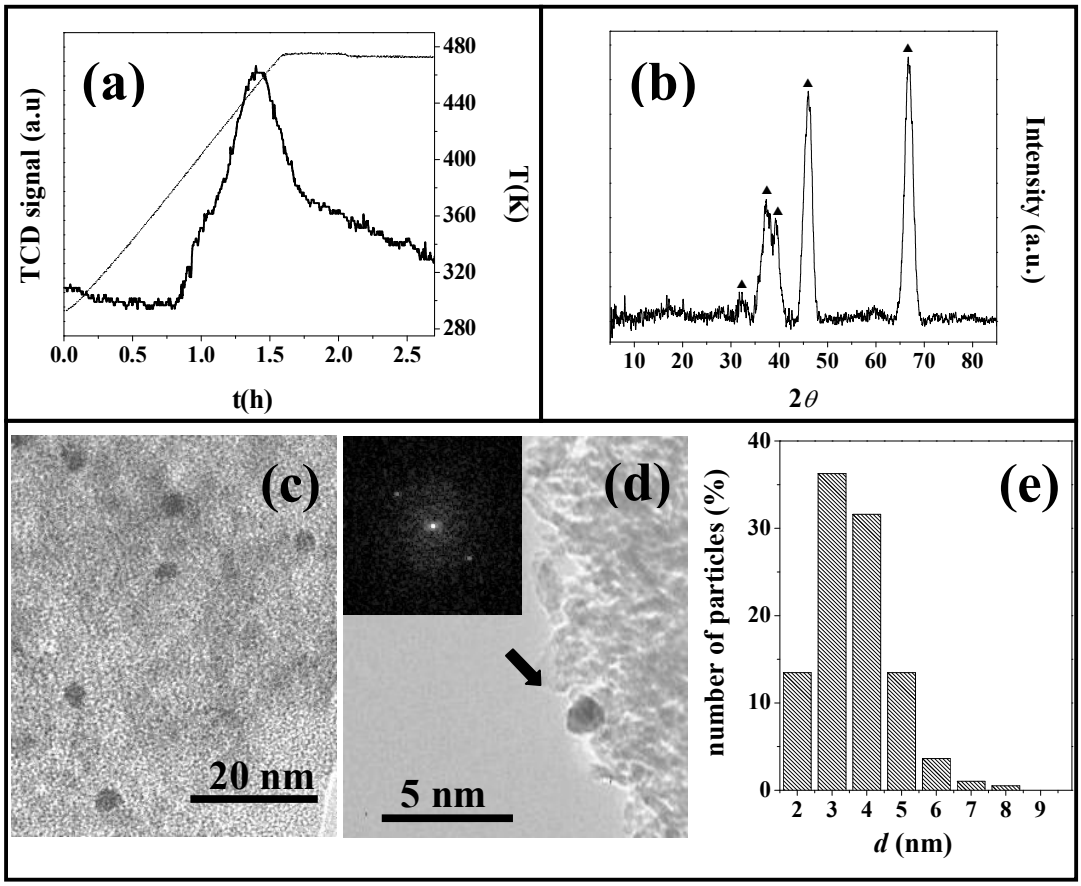

Figure 8.5: (a) TPR profile (solid line) with temperature ramp (dotted line) generated for Au/Al_2O_3-1; (b) XRD pattern post-TPR where (▲) identifies Al_2O_3 (JCPDS Card 10-0425); (c-d) representative TEM images with associated diffractogram pattern; (e) Au particle size distribution.

The BET areas and pore volumes recorded for both Au/Al_2O_3 samples (**Table 8.1**) are in good agreement with previous reports [8.20,8.86]. TPR of the catalyst prepared by deposition-precipitation (Au/Al_2O_3-1, see **Figure 8.5(a)**) generated a peak with T_{max} close to that recorded for Au/ZrO_2, where H_2 consumption matched the

requirement for precursor reduction to zero valent Au. Hydrogen chemisorption agrees with that reported previously (33-38 μmol g_{Au}^{-1} [8.87]) for equivalent Au/Al_2O_3 catalysts. Hydrogen desorption exceeded that measured for Au/ZrO_2 and Au/TiO_2 (**Table 8.1**), which can be attributed to the capability of Al_2O_3 to accommodate spillover hydrogen [8.88].

The five XRD signals at 2θ = 32-67° (**Figure 8.5(b)**) correspond to the (220), (311), (222), (400) and (440) planes of cubic γ-Al_2O_3, where the broadness of the peaks is indicative of short range order. The absence of a detectable XRD signal for Au suggests a well dispersed phase, which was confirmed by TEM analysis; a representative image is presented in **Figure 8.5(c)**. The diffractogram pattern for an isolated Au particle is included in the TEM image given in **Figure 8.5(d)** where the *d*-spacing (0.23) corresponds to the (111) plane of metallic gold. The Au particle size distribution (**Figure 8.5(e)**) delivers a mean diameter (= 4.3 nm), which is close to that for Au/TiO_2. Synthesis of alumina supported Au with the same loading by impregnation (Au/Al_2O_3-2) generated a larger mean Au size (7.8 nm, see **Table 8.1**); the associated catalyst characteristics are presented and discussed in detail elsewhere [8.31]. It is well established that catalyst synthesis by impregnation generates weak precursor/support interactions leading to larger Au particles [8.27,8.67]. XPS analysis has generated equivalent BE values for both samples (83.2-83.3 ± 0.2 eV, **Table 8.1**). A shift in the Au $4f_{7/2}$ signal to lower BE relative to the Au reference has already been reported for Au/Al_2O_3 and attributed to electron donation from the support [8.89,8.90].

8.3.6 Au/Al_2O_3: Catalytic Response

In contrast to Au/ZrO_2 and Au/TiO_2, reaction of 4-nitrobenzaldehyde over Au/Al_2O_3-1 generated 4-nitrobenzyl alcohol in addition to 4-aminobenzaldehyde as principal product (**Table 8.2**), *i.e.* reduction of both carbonyl and nitro functions (**Figure 8.1**). Liu and co-workers [8.13] reported that the C=O group of 4-nitrobenzaldehyde can be activated on Fe_2O_3 supported Au but this resulted in hydrogenolysis leading to the formation of 4-nitrotoluene and 4-aminotoluene. The only reported production of 4-nitrobenzyl alcohol involved the use of propyltriethylammonium ($CH_2CH_2CH_2Net_3^+$) functionalized MCM-41 supported $[H_3Ru_4(CO)_{12}]^-$ in liquid phase (P_{H2} = 50 bar) operation [8.8]. This is the first report of C=O group reduction with the formation of 4-nitrobenzyl alcohol over Au catalysts.

Initial product selectivity (S_0) was independent of 4-nitrobenzaldehyde conversion (X_0), as demonstrated in **Figure 8.6(a)**.

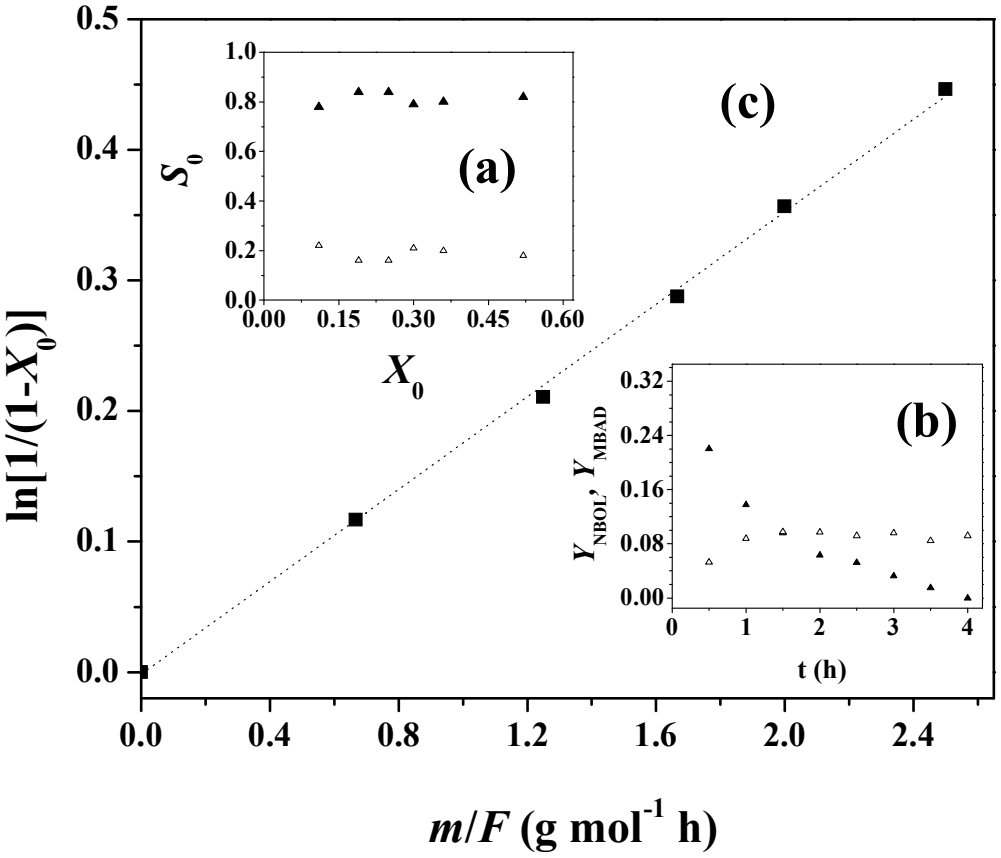

Figure 8.6: (a) Initial selectivity (S_0) to 4-aminobenzaldehyde (▲) and 4-nitrobenzyl alcohol (△) with fractional 4-nitrobenzaldehyde conversion (X_0) over Au/Al_2O_3-1 at 443 K; (b) yield of 4-nitrobenzyl alcohol (Y_{NBOL}, △) and 4-aminobenzaldehyde (Y_{MBAD}, ▲) as a function of time on-stream; (c) pseudo-first order kinetic plot.

The generation of 4-nitrobenzyl alcohol indicates a critical contribution due to Al_2O_3. Results in Chapter 7 demonstrated selective hydrogenation of benzaldehyde to benzyl alcohol over Au/Al_2O_3 [8.31]. Reduction of the carbonyl function is known to occur via a nucleophilic mechanism [8.91] where C=O polarisation renders the oxygen susceptible to attack with hydrogen transfer to generate the alcohol [8.92]. Benzaldehyde interaction with the support can be ionic (*e.g.* on Mn_3O_4) or bridging (*e.g.* on Al_2O_3), the latter leading to the formation of a surface benzoate, which is an intermediate for alcohol formation. FTIR measurements have established that the benzoate results from benzaldehyde adsorption at Al^{3+} sites [8.93]. Lewis acidity is then a critical requirement, which we characterised by FTIR analysis using pyridine as an established probe molecule [8.94].

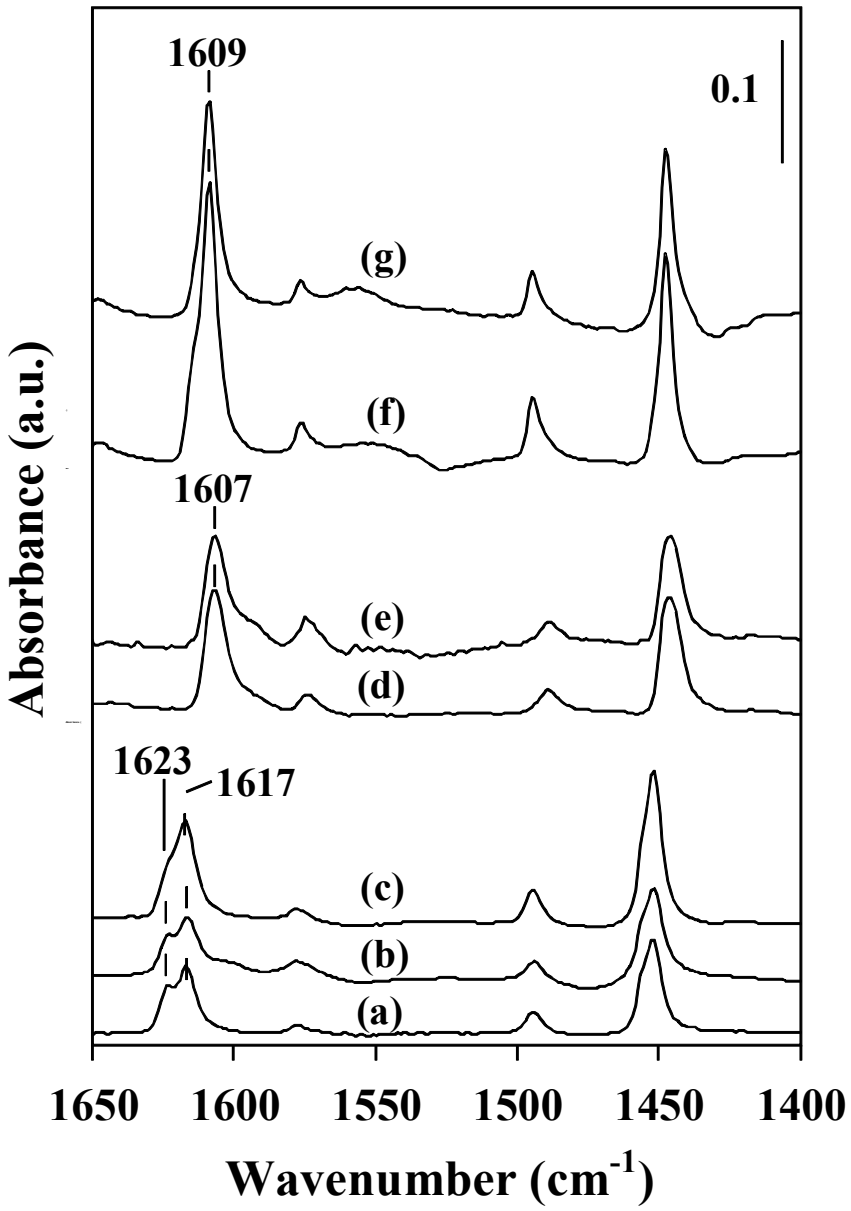

Figure 8.7: FTIR spectrum of pyridine adsorbed on (a) Al_2O_3, (b) Au/Al_2O_3-1, (c) Au/Al_2O_3-2, (d) ZrO_2, (e) Au/ZrO_2, (f) TiO_2 and (g) Au/TiO_2, following outgas treatment at 423 K.

When pyridine is bonded to metal oxide surface sites, the frequency of the modes of ring-breathing vibrations (νCCN) are increased. The interaction of the nitrogen lone pair with oxide Lewis acid sites is associated with a ν_{8a} and ν_{19b} bands position in the range 1445-1460 cm^{-1} and 1600-1633 cm^{-1}, respectively, where a higher frequency of ν_{8a} reflects stronger acidity [8.94]. The νCCN spectrum (following outgas at 423 K) is presented **Figure 8.7**; band positions and acid site concentrations are given

in **Table 8.3**. The ZrO_2 and TiO_2 supports present a peak at 1608 ± 1 cm^{-1}, close to that reported previously (1603-1608 cm^{-1} [8.94,8.95]), suggesting equivalent Lewis acid strength. In contrast, Al_2O_3 exhibits a principal peak at 1617 cm^{-1} with a shoulder at a higher frequency (1623 cm^{-1}) that are associated with Al^{3+} sites in octahedral and tetrahedral symmetries, respectively [8.94]. The occurrence of a higher ν_{8a} frequency for Al_2O_3 is indicative of stronger Lewis acidity than ZrO_2 and TiO_2, which can be attributed to the smaller Al ionic radius [8.96]. There is a measurable increase in acid site concentration that follows the order $TiO_2 > ZrO_2 > Al_2O_3$. The number of acid sites associated with oxide supports is dependent on synthesis method, bulk crystal structure, exposed planes on the surface, pretreatment conditions as well as the method of analysis and a direct comparison with the literature is difficult [8.97,8.98]. It is however worth noting that the occurrence of oxygen vacancies due to the partial reduction of TiO_2 enhances pyridine interaction [8.98], which can account, at least in part, for the higher site concentration recorded in **Table 8.3**. The introduction of Au to the supports did not significantly affect acid strength or concentration in the case of Au/ZrO_2, Au/TiO_2 or Au/Al_2O_3-1. The conversion of 4-nitrobenzaldehyde to 4-nitrobenzyl alcohol over Au/Al_2O_3-1 can then be linked to strong surface Lewis acidity that contributes to the formation of a surface benzoate, which is reduced by hydrogen supplied from Au sites.

Table 8.3: Wavelength(s) of the ν_{8a} vibration and Lewis acid sites titrated from pyridine adsorption on the supports and supported Au as determined by FTIR analysis with outgas treatment at 423 K.

	ν_{8a} (cm^{-1})	Acid sites (μmol g^{-1})
Au/ZrO_2	1607	41[a] (43[b])
Au/TiO_2	1609	48[a] (52[b])
Au/Al_2O_3-1	1617, 1623	40[a] (35[b])
Au/Al_2O_3-2	1617, 1623	55[a] (35[b])

[a]catalyst
[b]support

Reaction over Au/Al_2O_3-1 was accompanied by a temporal variation of 4-aminobenzaldehyde and 4-nitrobenzyl alcohol yields, as shown in **Figure 8.6(b)**. The yield of 4-aminobenzaldehyde (Y_{MBAD}) declined with time on-stream while the yield of 4-nitrobenzyl alcohol (Y_{NBOL}) showed an initial increase to attain a steady state (at $t > 1$

h). This response suggests a time dependent deactivation of sites responsible for -NO_2 reduction as observed for Au/ZrO_2 (**Figure 8.3(b)**). 4-Nitrobenzaldehyde consumption followed pseudo-first order kinetics as confirmed by the linear relationship presented in **Figure 8.6(c)** with a *TOF* (**Table 8.2**) close to (but measurably higher than) Au/TiO_2 and appreciably greater than that recorded for Au/ZrO_2. This response is consistent with an activity dependence on Au particle size, where smaller Au particles (≤ 5 nm) show higher intrinsic efficiency.

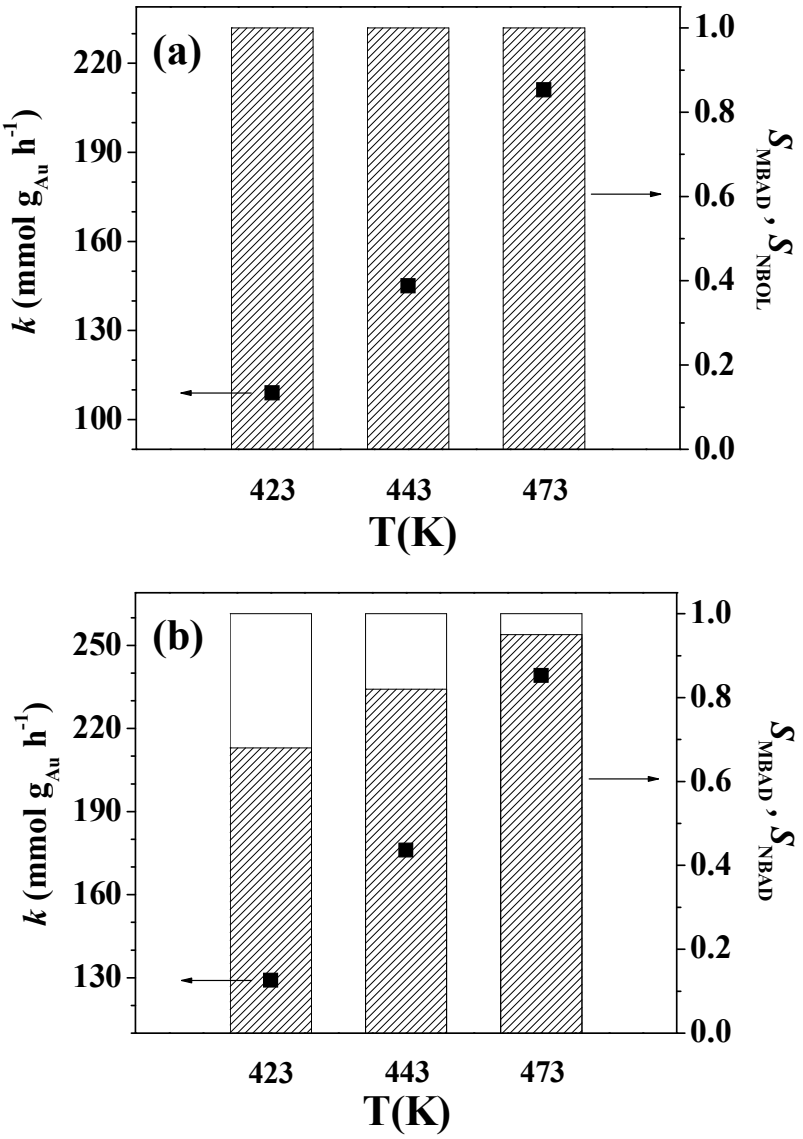

Figure 8.8: Rate constant (*k*) and initial selectivity (at $X_0 \approx 0.3$) to 4-aminobenzaldehyde (S_{MBAD}, hatched bars) and 4-nitrobenzyl alcohol (S_{NBOL}, open bars) as a function of temperature for the conversion of 4-nitrobenzaldehyde over (a) Au/TiO_2 and (b) Au/Al_2O_3-1.

The effect of reaction temperature (423-473 K) on the activity/selectivity delivered by (**a**) Au/TiO_2 and (**b**) Au/Al_2O_3-1 was considered and the results are presented in **Figure 8.8**. Full selectivity to 4-aminobenzaldehyde was retained over Au/TiO_2 at each temperature with an accompanying increase in selective hydrogenation rate with increasing temperature. In contrast, Au/Al_2O_3-1 exhibited a temperature dependent selectivity where 4-nitrobenzyl alcohol was favoured by decreasing temperature, suggesting different activation energies for $-NO_2$ and C=O reduction.

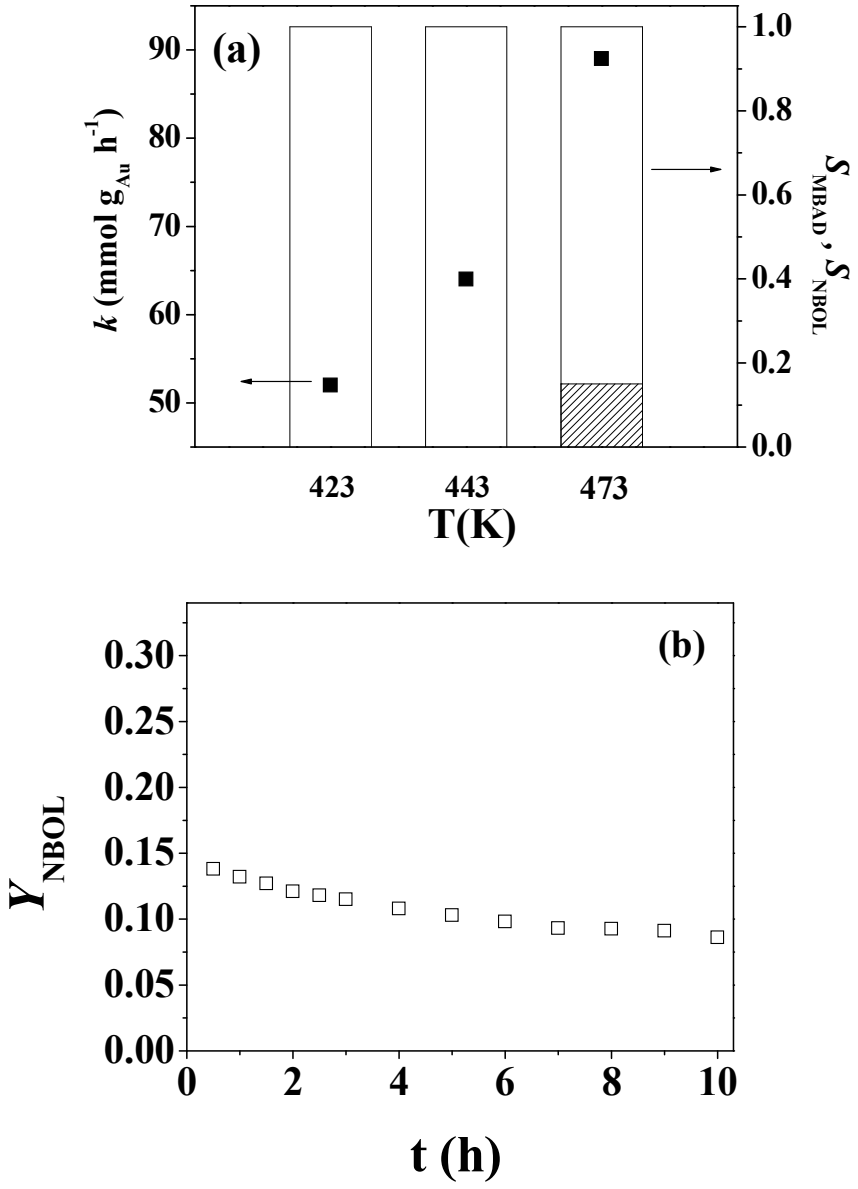

Figure 8.9: (a) Rate constant (k) and initial selectivity (at $X_0 \approx 0.3$) to 4-aminobenzaldehyde (S_{MBAD}, hatched bars) and 4-nitrobenzyl alcohol (S_{NBOL}, open bars) as a function of temperature for the conversion of 4-nitrobenzaldehyde over Au/Al_2O_3-2. (b) Representative (m/F = 2.8 g_{Au} mol^{-1} h, T = 443 K) yield of 4-nitrobenzyl alcohol (Y_{NBOL}) with time on-stream.

Hydrogenation of 4-nitrobenzaldehyde over Au/Al_2O_3-2 in the temperature range 423-473 K generated the results presented **Figure 8.9(a)**. In contrast to Au/Al_2O_3-1, reaction over Au/Al_2O_3-2 was 100% selective to 4-nitrobenzyl alcohol (at 423-443 K). The alcohol yield showed an initial temporal decline to attain a steady state after *ca.* 7 h on-stream (**Figure 8.9(b)**). On the basis of FTIR measurement (**Figure 8.7**), the Lewis acid strength of Au/Al_2O_3-2 was equivalent to that of Au/Al_2O_3-1. The increased number of acid sites on Au/Al_2O_3-2 (**Table 8.3**) can be ascribed to a higher residual Cl content [8.99], which is a feature of catalysts prepared by impregnation (using $HAuCl_4$ as precursor) relative to deposition-precipitation [8.87]. Reaction exclusivity to 4-nitrobenzyl alcohol over Au/Al_2O_3-2 can be attributed to the action of surface acidity resulting in benzoate formation in tandem with larger Au size. In the hydrogenation of acrolein [8.38,8.39], increased selectivity to allyl alcohol (to the detriment of C=C hydrogenation) was associated with an increase in Au size (from 4 to 8 nm). The number of low coordination Au sites is known to decrease at lower Au dispersion [8.85], limiting catalytic effectiveness in $-NO_2$ reduction, which must apply to Au/Al_2O_3-2. As in the case of Au/Al_2O_3-1, formation of the aminobenzaldehyde (selective $-NO_2$ reduction) over Au/Al_2O_3-2 was favoured by a higher reaction temperature (**Figure 8.9(a)**). The lower Au dispersion for Au/Al_2O_3-2 was accompanied by an appreciably lower *TOF* than that recorded for Au/Al_2O_3-1 (**Table 8.2**).

Reaction selectivity was probed further by examining the hydrogenation of benzaldehyde and nitrobenzene over Au/Al_2O_3-2 and Au/ZrO_2, which were chosen as they exhibit similar Au size but different surface acidity. Benzaldehyde and nitrobenzene hydrogenation delivered benzyl alcohol and aniline, respectively, as the only products over both catalysts. Both reactions are exothermic (calculated with HSC Chemistry, Version 5.0) ΔH_{423K} = -67 kJ mol^{-1} (benzaldehyde) and -469 kJ mol^{-1} (nitrobenzene)), exhibiting negative free energies where nitrobenzene→aniline (ΔG_{443K} = -442 kJ mol^{-1}) is more thermodynamically favourable than benzaldehyde→benzyl alcohol (ΔG_{443K} = -18 kJ mol^{-1}). Selectivity to 4-nitrobenzyl alcohol over Au/Al_2O_3-2 is consistent with the significantly higher rate of benzyl alcohol formation relative to aniline, as recorded in **Table 8.4**. This can be attributed to a predominant contribution due to support Lewis acidity that promotes C=O activation. In contrast, reaction over Au/ZrO_2, which exhibits weak Lewis acidity, resulted in a measurably higher nitrobenzene hydrogenation rate relative to benzaldehyde. In this case, the more thermodynamically facile $-NO_2$ reduction is preferred, which can account for the

observed selective 4-nitrobenzaldehyde→4-aminobenzaldehyde step. A higher reaction rate was obtained for the hydrogenation of 4-nitrobenzaldehyde relative to benzaldehyde and nitrobenzene over both catalysts, suggesting an activating inductive effect due the presence of the second electronegative group on the benzene ring.

Table 8.4: Rate constants for the hydrogenation of 4-nitrobenzaldehyde, benzaldehyde and nitrobenzene over Au/ZrO_2 and Au/Al_2O_3-2 at 443 K.

	4-Nitrobenzaldehyde feed (mmol g_{Au} h^{-1})	Benzaldehyde feed (mmol g_{Au} h^{-1})	Nitrobenzene feed (mmol g_{Au} h^{-1})
Au/ZrO_2	71	35	44
Au/Al_2O_3-2	64	43	22

8.4 Conclusion

A dependence of the catalytic response in the gas phase hydrogenation of 4-nitrobenzaldehyde over supported Au on metal particle size and support properties (notably in terms of Lewis acidity) was established in this Chapter. The preparation of a ZrO_2 support by precipitation of $ZrOCl_2$ with ammonia in basic medium generates a mixture of tetragonal and monoclinic phases (determined by XRD) with pH_{PZC} = 7.4. The incorporation of Au by deposition-precipitation increased the monoclinic ZrO_2 content where TPR served to reduce Au^{3+} to Au^0 with a mean particle size of 7.0 nm with evidence (from XPS) of electron transfer from the support and greater H_2 release (during TPD) relative to chemisorption that is ascribed to the involvement of spillover hydrogen. The hydrogenation of 4-nitrobenzaldehyde over Au/ZrO_2 generated 4-aminobenzaldehyde as sole product. An equivalent synthesis and activation of Au/TiO_2 resulted in a narrower distribution of smaller Au particles (mean = 4.7 nm) that again exhibited 100% selectivity with respect to $–NO_2$ reduction with an elevated *TOF* relative to Au/ZrO_2, which can be attributed to the contribution of a greater number of lower coordination Au sites. In contrast, reaction over Au/Al_2O_3 generated 4-nitrobenzyl alcohol due to stronger surface Lewis acidity (as demonstrated by FTIR analysis following pyridine adsorption), which favours the formation of an intermediate benzoate that is reduced to the alcohol; the selectivity was enhanced with decreasing Au size and lower reaction temperature.

8.5 References

[8.1] B. Nair, *Final report on the safety assessment of benzyl alcohol, benzoic acid, and sodium benzoate*, Int. J. Toxicol. 20 (2001) 23-50.

[8.2] H.-U. Blaser, H. Steiner and M. Studer, *Selective catalytic hydrogenation of fonctionalized nitroarenes: an update*, ChemCatChem 1 (2009) 210-221.

[8.3] P. T. Anastas, M. M. Kirchhoff and T. C. Williamson, *Catalysis as a foundational pillar of green chemistry*, Appl. Catal. A: General 221 (2001) 3-13.

[8.4] R. A. Sheldon and R. S. Downing, *Heterogeneous catalytic transformations for environmentally friendly production*, Appl. Catal. A: General 189 (1999) 163-183.

[8.5] P. Maki-Arvela, J. Hajek, T. Salmi and D. Y. Murzin, *Chemoselective hydrogenation of carbonyl compounds over heterogeneous catalysts*, Appl. Catal. A: General 292 (2005) 1-49.

[8.6] A. Corma and P. Serna, *Chemoselective hydrogenation of nitro compounds with supported gold catalysts*, Science 313 (2006) 332-332.

[8.7] A. K. Pahari and B. S. Chauhan, *Engineering Chemistry*, Laxmi Publications, New Delhi, 2006, pp. 95-97.

[8.8] A. Indra, N. Maity, P. Maity, S. Bhaduri and G. K. Lahiri, *Control of chemoselectivity in hydrogenations of substituted nitro- and cyano-aromatics by cluster-derived ruthenium nanocatalysts*, J. Catal. 284 (2011) 176-183.

[8.9] A. Corma, C. Gonzalez-Arellano, M. Iglesias and F. Sanchez, *Gold complexes as catalysts: Chemoselective hydrogenation of nitroarenes*, Appl. Catal. A: General 356 (2009) 99-102.

[8.10] S. G. Xu, X. L. Xi, J. Shi and S. K. Cao, *A homogeneous catalyst made of poly(4-vinylpyridine-co-N-vinylpyrrolidone)-Pd(0) complex for hydrogenation of aromatic nitro compounds*, J. Mol. Catal. A: Chemical 160 (2000) 287-292.

[8.11] S. K. Cao, S. L. Xu and S. G. Xu, *Hydrogenation of nitroaromatics containing a carbonyl group catalyzed by the palladium complex of MgO-supported melamino-formaldehyde polymer*, Polym. Adv. Technol. 10 (1999) 43-47.

[8.12] S. K. Mohapatra, S. U. Sonavane, R. V. Jayaram and P. Selvam, *Heterogeneous catalytic transfer hydrogenation of aromatic nitro and carbonyl compounds over cobalt(II) substituted hexagonal mesoporous aluminophosphate molecular sieves*, Tetrahedron Lett. 43 (2002) 8527-8529.

[8.13] L. Liu, B. Qiao, Y. Ma, J. Zhang and Y. Deng, *Ferric hydroxide supported gold subnano clusters or quantum dots: enhanced catalytic performance in chemoselective hydrogenation*, Dalton Trans. 19 (2008) 2542-2548.

[8.14] L. Q. Liu, B. T. Qiao, Z. J. Chen, J. Zhang and Y. Q. Deng, *Novel chemoselective hydrogenation of aromatic nitro compounds over ferric hydroxide supported nanocluster gold in the presence of CO and H_2O*, Chem. Commun. (2009) 653-655.

[8.15] A. Corma, P. Serna, P. Concepcion and J. J. Calvino, *Transforming nonselective into chemoselective metal catalysts for the hydrogenation of substituted nitroaromatics*, J. Am. Chem. Soc. 130 (2008) 8748-8753.

[8.16] A. P. Phillips and A. Maggiolo, *Catalytic hydrogenation of nitrobenzyl alcohols and nitrobenzaldehydes*, J. Org. Chem. 15 (1950) 659-661.

[8.17] J. Kijenski, M. Glinski, R. Wisniewski and S. Murghani, *Selective Hydrogenation of Aromatic and Aliphatic Nitro-Compounds by Hydrogen Transfer over MgO in Heterogeneous Catalysis and Fine Chemicals II*, M. Guisnet, J. Barrault, C. Bouchoule, D. Duprez, G. Pérot, R. Maurel, C. Montassier (Eds), Elsevier, Amsterdam, 1991, pp. 169-176.

[8.18] V. Pandarus, R. Ciriminna, F. Beland and M. Pagliaro, *Selective hydrogenation of functionalized nitroarenes under mild conditions*, Catal. Sci. Tech. 1 (2011) 1616-1623.

[8.19] A. Corma and P. Serna, *Preparation of substituted anilines from nitro compounds by using supported gold catalysts*, Nat. Protoc. 1 (2006) 2590-2595.

[8.20] F. Cárdenas-Lizana, S. Gómez-Quero and M. A. Keane, *Ultra-selective gas phase catalytic hydrogenation of aromatic nitro compounds over Au/Al_2O_3*, Catal. Commun. 9 (2008) 475-481.

[8.21] F. Cárdenas-Lizana, S. Gómez-Quero, N. Perret and M. A. Keane, *Support effects in the selective gas phase hydrogenation of p-chloronitrobenzene over gold*, Gold Bull. 42 (2009) 124-132.

[8.22] J. E. Bailie and G. J. Hutchings, *Promotion by sulfur of gold catalysts for crotyl alcohol formation from crotonaldehyde hydrogenation*, Chem. Commun. (1999) 2151-2152.

[8.23] C. Milone, M. L. Tropeano, G. Gulino, G. Neri, R. Ingoglia and S. Galvagno, *Selective liquid phase hydrogenation of citral on Au/Fe_2O_3 catalysts*, J. Chem. Soc., Chem. Commun. (2002) 869-869.

[8.24] C. Milone, R. Ingoglia, A. Pistone, G. Neri, F. Frusteri and S. Galvagno, *Selective hydrogenation of α, β-unsaturated ketones to α, β-unsaturated alcohols on gold-supported catalysts*, J. Catal. 222 (2004) 348-356.

[8.25] C. Milone, R. Ingoglia, L. Schipilliti, C. Crisafulli, G. Neri and S. Galvagno, *Selective hydrogenation of α,β-unsaturated ketone to α,β-unsaturated alcohol on gold-supported iron oxide catalysts: Role of the support*, J. Catal. 236 (2005) 80-90.

[8.26] C. Milone, C. Crisafulli, R. Ingoglia, L. Schipilliti and S. Galvagno, *A comparative study on the selective hydrogenation of α,β unsaturated aldehyde and ketone to unsaturated alcohols on Au supported catalysts*, Catal. Today 122 (2007) 341.

[8.27] M. Okumura, T. Akita and M. Haruta, *Hydrogenation of 1,3-butadiene and of crotonaldehyde over highly dispersed Au catalysts*, Catal. Today 74 (2002) 265-269.

[8.28] R. Zanella, C. Louis, S. Giorgio and R. Touroude, *Crotonaldehyde hydrogenation by gold supported on TiO_2: Structure sensitivity and mechanism*, J. Catal. 223 (2004) 328-339.

[8.29] B. Campo, C. Petit and M. A. Volpe, *Hydrogenation of crotonaldehyde on different Au/CeO_2 catalysts*, J. Catal. 254 (2008) 71-78.

[8.30] J. Lenz, B. C. Campo, M. Alvarez and M. A. Volpe, *Liquid phase hydrogenation of alpha,beta-unsaturated aldehydes over gold supported on iron oxides*, J. Catal. 267 (2009) 50-56.

[8.31] N. Perret, F. Cárdenas-Lizana and M. A. Keane, *Selective hydrogenation of benzaldehyde to benzyl alcohol over Au/Al_2O_3*, Catal. Commun. 16 (2011) 159–164.

[8.32] L. McEwan, M. Julius, S. Roberts and J.C.Q. Fletcher, *A Review of the use of gold catalysts in selective hydrogenation reactions*, Gold Bull. 43 (2010) 298-306.

[8.33] E. Bus, R. Prins and J. A. van Bokhoven, *Origin of the cluster-size effect in the hydrogenation of cinnamaldehyde over supported Au catalysts*, Catal. Commun. 8 (2007) 1397-1402.

[8.34] F. Cárdenas-Lizana, S. Gómez-Quero and M. A. Keane, *Exclusive production of chloroaniline from chloronitrobenzene over Au/TiO_2 and Au/Al_2O_3*, ChemSusChem 1 (2008) 215-221.

[8.35] F. Cárdenas-Lizana, S. Gómez-Quero, N. Perret and M. A. Keane, *Gold catalysis at the gas–solid interface: role of the support in determining activity and selectivity in the hydrogenation of m-dinitrobenzene*, Catal. Sci. Tech. 1 (2011) 652-661

[8.36] K. Shimizu, Y. Miyamoto, T. Kawasaki, T. Tanji, Y. Tai and A. Satsuma, *Chemoselective Hydrogenation of Nitroaromatics by Supported Gold Catalysts: Mechanistic Reasons of Size- and Support-Dependent Activity and Selectivity*, J. Phys. Chem. C 113 (2009) 17803-17810.

[8.37] S. Schimpf, M. Lucas, C. Mohr, U. Rodemerck, A. Brückner, J. Radnik, H. Hofmeister and P. Claus, *Supported gold nanoparticles: in-depth catalyst characterization and application in hydrogenation and oxidation reactions.*, Catal. Today 72 (2002) 63-78.

[8.38] C. Mohr, H. Hofmeister and P. Claus, *The influence of real structure of gold catalysts in the partial hydrogenation of acrolein*, J. Catal. 213 (2003) 86-94.

[8.39] P. Claus, A. Brückner, C. Mohr and H. Hofmeister, *Supported gold nanoparticles from quantum dot to mesoscopic size scale: Effect of electronic and structural properties on catalytic hydrogenation of conjugated functional groups*, J. Am. Chem. Soc. 122 (2000) 11430-11439.

[8.40] J. A. Peck, C. D. Tait, B. I. Swanson and G. E. Brown, *Speciation of aqueous gold(III) chlorides from ultraviolet/visible absorption and Raman/resonance Raman spectroscopies*, Geochim. Cosmochim. Acta 55 (1991) 671-676.

[8.41] I. Dobrosz, K. Jiratova, V. Pitchon and J. M. Rynkowski, *Effect of the preparation of supported gold particles on the catalytic activity in CO oxidation reaction*, J. Mol. Catal. A: Chemical 234 (2005) 187-197.

[8.42] H. S. Oh, J. H. Yang, C. K. Costello, Y. M. Wang, S. R. Bare, H. H. Kung and M. C. Kung, *Selective catalytic oxidation of CO: Effect of chloride on supported Au catalysts*, J. Catal. 210 (2002) 375-386.

[8.43] R. Zanella and C. Louis, *Influence of the conditions of thermal treatments and of storage on the size of the gold particles in Au/TiO_2 samples*, Catal. Today 107 (2005) 768-777.

[8.44] J. Vakros, C. Kordulis and A. Lycourghiotis, *Potentiometric mass titrations: a quick scan for determining the point of zero charge*, Chem. Commun. 17 (2002) 1980-1981.

[8.45] C. A. Emeis, *Determination of integrated molar extinction coefficients for infrared-absorption bands of pyridine adsorbed on solid acid catalysts*, J. Catal. 141 (1993) 347-354.

[8.46] H. Toraya, M. Yoshimura and S. Somiya, *Calibration curve quantitative-analysis of the monoclinic-tetragonal ZrO_2 system by X-Ray-Diffraction*, J. Am. Ceram. Soc. 67 (1984) C119-C121.

[8.47] J. J. F. Scholten, A. P. Pijpers and A. M. L. Hustings, *Surface characterization of supported and nonsupported hydrogenation catalysts*, Catal. Rev. Sci. Eng. 27 (1985) 151-206.

[8.48] M.A. Keane, *Gas phase hydrogenation/hydrogenolysis of benzaldehyde and o-tolualdehyde over Ni/SiO_2*, J. Mol. Catal. A: Chemical 118 (1997) 261-269.

[8.49] R. Srinivasan and B. H. Davis, *Zirconia: A Review of Super Ceramic in Materials Synthesis and Characterization*, Plenum Press, New York, 1997.

[8.50] B. H. Davis, *Effect of pH on crystal phase of ZrO_2 precipitated from solution and calcined at 600°C*, J. Am. Ceram. Soc. 67 (1984) C168-C169.

[8.51] S. S. Jada and N. G. Peletis, *Study of pH influence on phase composition and mean crystallite size of pure ZrO_2*, J. Mater. Sci. Lett. 8 (1989) 243-246.

[8.52] G. K. Chuah, S. Jaenicke, S. A. Cheong and K. S. Chan, *The influence of preparation conditions on the surface area of zirconia*, Appl. Catal. A: General 145 (1996) 267-284.

[8.53] K. Tanabe and T. Yamaguchi, *Acid-base bifunctional catalysis by ZrO_2 and its mixed oxides*, Catal. Today 20 (1994) 185-198.

[8.54] X. Zhang, H. Shi and B.-Q. Xu, *Vital roles of hydroxyl groups and gold oxidation states in Au/ZrO_2 catalysts for 1,3-butadiene hydrogenation*, J. Catal. 279 (2011) 75-87.

[8.55] J. W. Geus and A. J. van Dillen, *Preparation of Supported Catalysts by Deposition-Precipitation* in Preparation of Solid Catalysts, Ertl G, Knözinger H, Weitkamp J (Eds), Wiley-VCH, Weinheim, 1999, pp. 460-486.

[8.56] S. Ardizzone and C. L. Bianchi, *Electrochemical features of zirconia polymorphs. The interplay between structure and surface OH species*, J. Electroanal. Chem. 465 (1999) 136-141.

[8.57] S. Ardizzone, M. G. Cattania and P. Lugo, *Interfacial electrostatic behavior of oxides-Correlations with structural and surface parameters of the phase*, Electrochim. Acta 39 (1994) 1509-1517.

[8.58] F. Moreau, G. C. Bond and A. O. Taylor, *Gold on titania catalysts for the oxidation of carbon monoxide: control of pH during preparation with various gold contents*, J. Catal. 231 (2005) 105-114.

[8.59] S. B. Xie, E. Iglesia and A. T. Bell, *Water-assisted tetragonal-to-monoclinic phase transformation of ZrO_2 at low temperatures*, Chem. Mater. 12 (2000) 2442-2447.

[8.60] F. B. Noronha, E. C. Fendley, R. R. Soares, W. E. Alvarez and D. E. Resasco, *Correlation between catalytic activity and support reducibility in the CO_2 reforming of methane over $Pt/Ce_xZr_{1-x}O_2$ catalysts*, Chem. Eng. J. 82 (2001) 21-31.

[8.61] D. L. Hoang and H. Lieske, *Effect of Hydrogen Treatments on ZrO_2 and Pt/ZrO_2 Catalysts*, Catal. Lett. 27 (1994) 33-42.

[8.62] X. Zhang, H. Shi and B. Q. Xu, *Catalysis by gold: Isolated surface Au^{3+} ions are active sites for selective hydrogenation of 1,3-butadiene over Au/ZrO_2 catalysts*, Angew. Chem. Int. Ed. 44 (2005) 7132-7135.

[8.63] G. Bond, C. Louis and D. T. Thompson, *Catalysis by Gold in Catalytic Science Series*, G. J. Hutchings (Ed.), Imperial College Press, London, 2006, pp. 150-153.

[8.64] R. Radnik, C. Mohr and P. Claus, *On the origin of binding energy shifts of core levels of supported gold nanoparticles and dependence of pretreatment and material synthesis*, Phys. Chem. Chem. Phys. 5 (2003) 172-177.

[8.65] N. Kruse and S. Chenakin, *XPS characterization of Au/TiO_2 catalysts: Binding energy assessment and irradiation effects*, Appl. Catal. A: General 391 (2011) 367-376.

[8.66] R. A. Koeppel, A. Baiker, C. Schild and A. Wokaun, *Carbon dioxide hydrogenation over Au/ZrO_2 catalysts from amorphous precursors: Catalytic reaction mechanism*, J. Chem. Soc., Faraday Trans. 87 (1991) 2821-2828.

[8.67] P. Claus, H. Hofmeister and C. Mohr, *Identification of active sites and influence of real structure of gold catalysts in the selective hydrogenation of acrolein to allyl alcohol*, Gold Bull. 37 (2004) 181-186.

[8.68] M. Boronat, P. Concepcion, A. Corma, S. Gonzalez, F. Illas and P. Serna, *A molecular mechanism for the chemoselective hydrogenation of substituted nitroaromatics with nanoparticles of gold on TiO_2 catalysts: A cooperative*

effect between gold and the support, J. Am. Chem. Soc. 129 (2007) 16230-16237.

[8.69] M. Boronat, F. Illas and A. Corma, *Active Sites for H_2 Adsorption and Activation in Au/TiO_2 and the Role of the Support*, J. Phys. Chem. A 113 (2009) 3750-3757.

[8.70] K. D. Jung and A. T. Bell, *Role of hydrogen spillover in methanol synthesis over Cu/ZrO_2*, J. Catal. 193 (2000) 207-223.

[8.71] C. M. Lu, Y. M. Lin and I. Wang, *Naphthalene hydrogenation over Pt/TiO_2-ZrO_2 and the behavior of strong metal-support interaction (SMSI)*, Appl. Catal. A: General 198 (2000) 223-234.

[8.72] Y. Hao, R. Liu, X. Meng, H. Cheng and F. Zhao, *Deactivation of Au/TiO_2 catalyst in the hydrogenation of o-chloronitrobenzene in the presence of CO_2*, J. Mol. Catal. A: Chemical 335 (2011) 183-188.

[8.73] P. Sangeetha, P. Seetharamulu, K. Shanthi, S. Narayanan and K. S. Rama Rao, *Studies on Mg-Al oxide hydrotalcite supported Pd catalysts for vapor phase hydrogenation of nitrobenzene*, J. Mol. Catal. A: Chemical 273 (2007) 244-249.

[8.74] C. A. Koutstaal and V. Ponec, *New Aspects of the Selective Reduction of Aromatic Carboxylic Acids to Aldehydes in Science and Technology in Catalysis 1994*, Y. Izumi, H. Arai, M. Iwamoto (Eds.), Elsevier, Amsterdam, 1995, pp. 105-110.

[8.75] V. Idakiev, T. Tabakova, Z.-Y. Yuan and B.-L. Sub, *Gold catalysts supported on mesoporous titania for low-temperature water–gas shift reaction*, Appl. Catal. A: General 270 (2004) 135-141.

[8.76] G. L. Haller and D. E. Resasco, *Metal Support Interaction - Group-Viii Metals and Reducible Oxides*, Adv. Catal. 36 (1989) 173-235.

[8.77] T. Sekiya, T. Yagisawa and S. Kurita, *Annealing of anatase titanium dioxide under hydrogen atmosphere*, J. Ceram. Soc. Jpn. 109 (2001) 672-675.

[8.78] A. Zwijnenburg, A. Goossens, W. G. Sloof, M. W. J. Craje, A. M. van der Kraan, L. J. de Jongh, M. Makkee and J. A. Moulijn, *XPS and Mossbauer characterization of Au/TiO_2 propene epoxidation catalysts*, J. Phys. Chem. B 106 (2002) 9853-9862.

[8.79] D. A. Panayotov and J. T. Yates, *Spectroscopic detection of hydrogen atom spillover from au nanoparticles supported on TiO_2: Use of conduction band electrons*, J. Phys. Chem. C 111 (2007) 2959-2964.

[8.80] D. A. Panayotov, S. P. Burrows, J. T. Yates, Jr. and J. R. Morris, *Mechanistic Studies of Hydrogen Dissociation and Spillover on Au/TiO_2: IR Spectroscopy of Coadsorbed CO and H-Donated Electrons*, J. Phys. Chem. C 115 (2011) 22400-22408.

[8.81] S. Lin and M. A. Vannice, *Gold dispersed on TiO_2 and SiO_2: Adsorption properties and catalytic behavior in hydrogenation reactions*, Catal. Lett. 10 (1991) 47-62.

[8.82] F. Cárdenas-Lizana, Z. M. de Pedro, S. Gómez-Quero and M. A. Keane, *Gas phase hydrogenation of nitroarenes: A comparison of the catalytic action of titania supported gold and silver*, J. Mol. Catal. A: Chemical 326 (2010) 48-54.

[8.83] M. A. Keane and R. Larsson, *Isokinetic behavior in the gas phase hydrogenation of nitroarenes over Au/TiO_2: application of the selective energy transfer model*, React. Kinet. Mech. Catal. 106 (2012) 267-288.

[8.84] A. Corma, P. Concepcion and P. Serna, *A different reaction pathway for the reduction of aromatic nitro compounds on gold catalysts*, Angew. Chem. Int. Ed. 46 (2007) 7266-7269.

[8.85] T. V. W. Janssens, B. S. Clausen, B. Hvolbaek, H. Falsig, C. H. Christensen, T. Bligaard and J. K. Norskov, *Insights into the reactivity of supported Au nanoparticles: combining theory and experiments*, Top. Catal. 44 (2007) 15-26.

[8.86] G. K. Bethke and H. H. Kung, *Selective CO oxidation in a hydrogen-rich stream over Au/gamma-Al_2O_3 catalysts*, Appl. Catal. A: General 194 (2000) 43-53.

[8.87] F. Cárdenas-Lizana, S. Gómez-Quero, A. Hugon, L. Delannoy, C. Louis and M. A. Keane, *Pd-promoted selective gas phase hydrogenation of p-chloronitrobenzene over alumina supported Au*, J. Catal. 262 (2009) 235-243.

[8.88] F. Ahmed, M. K. Alam, A. Suzuki, M. Koyama, H. Tsuboi, N. Hatakeyama, A. Endou, H. Takaba, C. A. Del Carpio, M. Kubo and A. Miyamoto, *Dynamics of Hydrogen Spillover on Pt/gamma-Al_2O_3 Catalyst Surface: A Quantum Chemical Molecular Dynamics Study*, J. Phys. Chem. C 113 (2009) 15676-15683.

[8.89] G. M. Veith, A. R. Lupini, S. J. Pennycook, G. W. Ownby and N. J. Dudney, *Nanoparticles of gold on gamma-Al_2O_3 produced by dc magnetron sputtering*, J. Catal. 231 (2005) 151-158.

[8.90] S. Arrii, F. Morfin, A. J. Renouprez and J. L. Rousset, *Oxidation of CO on gold supported catalysts prepared by laser vaporization: Direct evidence of support contribution*, J. Am. Chem. Soc. 126 (2004) 1199-1205.

[8.91] A. Saadi, Z. Rassoul and M.M. Bettahar, *Gas phase hydrogenation of benzaldehyde over supported copper catalysts*, J. Mol. Catal. A: Chemical 164 (2000) 205-216.

[8.92] K. Lanasri, A. Saddi, K. Bachari, D. Halliche and O. Cherifi, *Gas phase hydrogenation of benzaldehyde over supported copper catalysts. Effect of copper loading*, Stud. Surf. Sci. Catal. 174 (2008) 1279-1282.

[8.93] C. A. Koutstaal, P. Angevaare and V. Ponec, *Surface chemistry of benzoyl compounds on oxides, an FT-IR study*, J. Catal. 143 (1993) 573-582.

[8.94] M. I. Zaki, M. A. Hasan, F. A. Al-Sagheer and L. Pasupulety, *In situ FTIR spectra of pyridine adsorbed on SiO_2-Al_2O_3, TiO_2, ZrO_2 and CeO_2: general considerations for the identification of acid sites on surfaces of finely divided metal oxides*, Colloids Surf., A 190 (2001) 261-274.

[8.95] T. Onfroy, G. Clet, S. B. Bukallah, D. M. Hercules and M. Houalla, *Development of the acidity of zirconia-supported niobia catalysts*, Catal. Lett. 89 (2003) 15-19.

[8.96] A. Gutiérrez-Alejandre, J. Ramírez and G. Busca, *A vibrational and spectroscopic study of WO_3/TiO_2-Al_2O_3 catalyst precursors*, Langmuir 14 (1998) 630-639.

[8.97] K. I. Hadjiivanov and G. N. Vayssilov, *Characterization of oxide surfaces and zeolites by carbon monoxide as an IR probe molecule* Adv. Catal. 47 (2002) 307-511.

[8.98] I. X. Green, C. Buda, Z. Zhang, M. Neurock and J. T. Yates, *IR Spectroscopic Measurement of Diffusion Kinetics of Chemisorbed Pyridine through TiO_2 Particles*, J. Phys. Chem. C 114 (2010) 16649-16659.

[8.99] L. F. Sharanda, A. P. Shimansky, T. V. Kulik and A. A. Chuiko, *Study of acid-base surface properties of pyrogenic gamma-aluminium oxide*, Colloids Surf., A 105 (1995) 167-172.

Chapter 9

Selective Hydrogenation of Benzoic acid over Au Supported on CeO_2 and $Ce_{0.62}Zr_{0.38}O_2$: Formation of Benzyl Alcohol

The results Chapter 7 and Chapter 8 demonstrated the viability of Au supported as catalysts in the hydrogenation of benzaldehyde and nitrobenzaldehyde as an alternative route to aromatic alcohol. In this Chapter, the formation of benzyl alcohol from benzoic acid is considered over Au supported on reducible support.

9.1 Introduction

Increasing sustainability demands are now placed on chemical production to improve catalytic selectivity in order to minimise by-product formation, circumvent separation/purification unit operations and avoid costly clean up and disposal. This requires a fundamental understanding of reaction mechanisms and catalyst structure/performance relationships. Benzoic acid, the reactant considered in this Chapter, is an inexpensive feedstock [9.1] that can be hydrogenated to benzaldehyde [9.2] or benzyl alcohol [9.3,9.4] as important commercial products. Reaction over a range of oxide catalysts, including CeO_2 [9.5-8], ZrO_2 [9.1,9.7,9.9-11], MgO [9.7], ZnO [9.1,9.7,9.12], TiO_2 [9.11], HfO_2 [9.11] and MoO_x [9.13,9.14] in gas phase operation (P = 1 atm, T = 473-773 K) has resulted in the formation of benzaldehyde, benzyl alcohol, toluene, benzene and benzophenone (**Figure 9.1**).

Infrared studies suggest a dissociative adsorption of benzoic acid to form a benzoate with coordination between the carboxylic oxygen(s) and cationic metal site(s) [9.10,9.15-18]. In the presence of surface oxygen vacancies, hydrogenation proceeds *via* a redox Mars and van Krevelen (MvK) mechanism [9.1,9.7,9.8,9.11,9.19]. Interaction with isolated oxygen vacancies results in the removal of one oxygen atom from the carboxyl function with the formation of benzaldehyde (step I, **Figure 9.1**) [9.18]. Surface hydrogen can react with this oxygen to form water, regenerating the active site [9.1,9.7]. In the presence of twin vacancies, benzoic acid adsorbs through both oxygens with reduction to produce toluene (step II) [9.20,9.21]. Toluene can also be generated on a surface that bears excess vacancies *via* consecutive reduction of benzaldehyde (step

III) [9.22,9.23]. The steady-state concentration of oxygen vacancies is a critical factor that controls selectivity *via* steps I-III [9.11]. This concentration is influenced by solvents/additives [9.1,9.7,9.11] but is largely determined by the reducibility of the oxide where redox properties [9.22,9.23], metal-oxygen bond strength [9.11], H_2 partial pressure [9.22] and activation conditions [9.6] are crucial variables. Reducible oxides (such as Co_3O_4) exhibit a high oxygen vacancy density and promote the generation of toluene [9.7,9.11] where use of solvents or additives that possess an affinity for these sites (*e.g.* CO_2 or polar compounds such as water) favours benzaldehyde formation [9.1,9.11].

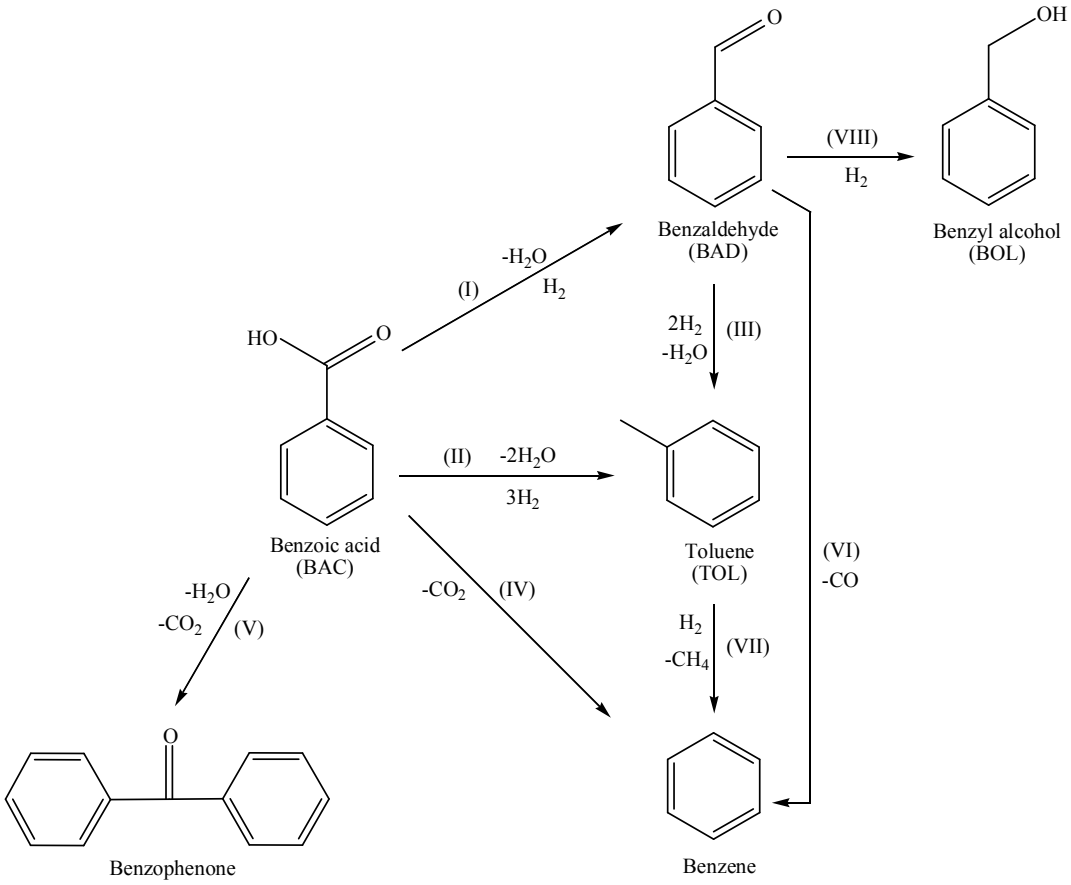

Figure 9.1: Reaction pathway reported in the literature for the gas phase hydrogenation of benzoic acid over oxide catalysts.

Adsorption on surfaces that do not bear oxygen vacancies is accompanied by scission of the acidic function [9.9,9.18,9.21] with the formation of benzene (step IV) and/or benzophenone (step V). Decarboxylation of benzoic acid is favoured at high temperature (> 673 K) and low surface hydrogen coverage [9.1] but this step is slow relative to deoxygenation at oxygen vacancies (MvK mechanism) [9.22]. Benzene can also result from a decarbonylation of benzaldehyde (step VI) [9.22] or hydrogenolysis of toluene (step VII) [9.18]. Hydrogenation of benzaldehyde to benzyl alcohol (step VIII) has been observed at low temperatures (< 630 K) [9.7,9.8,9.12,9.22].

Catalyst acidity/basicity can alter the affinity of the surface for reactant and products and influence selectivity. Benzoic acid is a stronger acid and carboxylate benzoates are better ligands than benzaldehyde or benzyl alcohol [9.17,9.22]. Surface basicity enhances adsorption of benzoic acid but inhibits interaction with benzaldehyde while acidity favours the consecutive (hydrogenation/hydrogenolysis/MvK) reaction of benzaldehyde [9.12,9.17,9.20,9.22]. However, on a strong basic oxide, such as MgO [9.7], carboxylate benzoates are strongly bound to the surface and decarboxylation (to benzene or benzophenone) can result.

The activation of H_2 *via* dissociative adsorption on oxides (such as ZrO_2) has been shown to be rate determining [9.9]. While the incorporation of noble metals can facilitate hydrogen dissociation and influence reactivity, only one study report the gas phase hydrogenation of benzoic acid over supported metals (Cu and Pt on ZrO_2) where the increase in H_2 uptake resulted in preferential hydrogenation (particularly in the case of Pt) of the aromatic ring with the formation of methyl-cyclohexane and cyclohexane-carboxylic acid [9.11]. Gold is known to exhibit lower capacity for H_2 adsorption relative to Pt [9.24-26] and has been used to promote selective C=O hydrogenation of aldehydes [9.27-30] and ketones [9.31,9.32]. In Chapter 7, supported Au promoted the sole formation of benzyl alcohol in the hydrogenation of benzaldehyde.

The literature dealing with benzyl alcohol generation from benzoic acid is limited and the possibility of a direct hydrogenation (single step) has not been investigated in any detail. The facility for oxygen vacancy formation [9.6,9.33] and amphoteric surface properties [9.18] of ZrO_2 [9.1,9.7,9.9,9.10] and CeO_2 [9.5,9.6,9.8] should serve to promote benzoic acid→benzaldehyde with secondary formation of benzyl alcohol, toluene and benzene. The addition of a metal, such as Au, can favour hydrogenation (step VIII) due to increased surface hydrogen. Gold supported on CeO_2 and a mixed

oxide ($Ce_{0.62}Zr_{0.38}O_2$) has exhibited activity in the hydrogenation of *p*-chloronitrobenzene [9.34] and crotonaldehyde [9.28]. In this Chapter, the catalytic action of these systems are considered in the hydrogenation of benzoic acid directed at the selective formation of benzyl alcohol where the role of reaction temperature and solvent carrier are examined.

9.2 Experimental

9.2.1 Catalyst Preparation

$Au/Ce_{0.62}Zr_{0.38}O_2$ (Au/CZ) and Au/CeO_2 were prepared by deposition-precipitation. An aqueous solution of $HAuCl_4$ (Alfa Aesar) served as precursor and the oxide supports (CZ) and CeO_2) were obtained from Grace Davison. A known mass (*ca.* 15 g) of the support was added to 800 cm^3 deionised water, the suspension stirred and heated to 333 K, the $HAuCl_4$ solution (0.0032 M) introduced at a fixed flow rate (3 cm^3 min^{-1}) and the pH adjusted to 8 with an aqueous Na_2CO_3 solution (0.05 M). After ageing for 1 h, the solution was cooled to ambient temperature, filtered and the resultant solid washed with deionised water until there was no evidence of chloride ions and dried at 383 K for 12 h. The samples were calcined in a flow of 5% v/v O_2/He at 523 K, which was maintained for 1 h with a further contact (1 h) in flowing He and subsequent cooling to 298 K. The samples were sieved to 75 μm mean particle diameter and stored in the dark under He. The Au content was measured by inductively coupled plasma-optical emission spectrometry (ICP-OES, Vista-PRO, Varian Inc.) from the diluted extract in aqua regia.

9.2.2 Catalyst Characterisation

BET surface area, total pore volume and pore size distribution were determined by volumetric adsorption of N_2 at 77 K. Carbon monoxide adsorption isotherms were measured at 308 K (P_{CO} = 1.33×10^4 Pa) and used to determine Au mean particle size (*d*) as described in detail elsewhere [9.35]. Temperature programmed reduction (TPR) and temperature programmed desorption (TPD) were determined using the commercial CHEM-BET 3000 (Quantachrome) unit. The samples were loaded into a U-shaped Quartz cell (10 cm×3.76 mm i.d.) and heated in 17 cm^3 min^{-1} (Brooks mass flow controlled) 5% v/v H_2/N_2 at 5 K min^{-1} to 573 K. The effluent gas passed through a liquid N_2 trap and changes in H_2 consumption were monitored by TCD with data

acquisition/ manipulation using the TPR Win^{TM} software. The samples were maintained at the final temperature in a constant flow of H_2/N_2 until return of the signal to baseline, swept with 65 cm^3 min^{-1} N_2 for 1.5 h and cooled to room temperature. Hydrogen chemisorption was conducted using a pulse (10 μl) titration procedure followed by TPD in N_2 (65 cm^3 min^{-1}) at 50 K min^{-1} to 973 K with an isothermal hold until the signal returned to the baseline. Ammonia chemisorption by pulse (1 ml) titration was also conducted with TPD in N_2 (180 cm^3 min^{-1}) at 10 K min^{-1} to 873 K. The degree of support reduction was determined with respect to oxygen storage capacity (OSC) where the sample was reduced in 50 cm^3 min^{-1} H_2 at 5 K min^{-1} to 573 K, which was maintained for 1h, swept with 65 cm^3 min^{-1} N_2 for 1.5 h, cooled to 523 K and subjected to a pulse (50 μl) O_2 titration. It has been demonstrated previously that there is a negligible contribution from Au to the total O_2 adsorbed [9.36] and the degree of Ce^{4+} reduction was determined from O_2 uptake.

Powder X-ray diffractograms were recorded using a Bruker/Siemens D500 incident X-ray diffractometer using Cu Kα radiation. The samples were scanned at a rate of 0.02º $step^{-1}$ over the range $5º \leq 2\theta \leq 85º$. Diffractograms were identified using the JCPDS-ICDD reference standards (CeO_2 (43-1002), monoclinic (37-1484) or tetragonal (50-1089) ZrO_2 and Au (04-0784)). The oxide crystal size (d_{hkl}) was estimated using the Scherrer equation

$$d_{hkl} = \frac{K \times \lambda}{\beta \times \cos\theta} \tag{9.1}$$

where $K = 0.9$, λ is the incident radiation wavelength (1.5056 Å), β is the peak width at half the maximum intensity and θ represents the diffraction angle corresponding to the main plane of CeO_2 and CZ ($2\theta = 28.5$-$29.0°$).

The supported Au particle size distribution was measured by High Angle Annular Dark Field-Scanning Transmission Electron Microscopy (HAADF-STEM). Images were recorded using a JEOL2010-F microscope with 0.19 nm spatial resolution under Scherzer defocus conditions. HAADF-STEM images were obtained with an electron probe (0.5 nm diameter) at a diffraction camera length of 10 cm. This imaging mode provides contrast that is directly related to the average atomic number (Z) in the region under the electron beam. X-ray photoelectron spectroscopy (XPS) analysis was performed on a Kratos Axis Ultra DLD unit equipped with a catalytic cell, allowing transfer of the pretreated samples to the analytical chamber under anaerobic conditions.

Spectra were recorded using monochromatised AlK_α radiation (1486.6 eV) at an x-ray source power = 60 W. Surface charging effects were compensated for using the Kratos coaxial neutralization system. A 20 eV pass energy was used to collect the spectra where the energy resolution corresponded to a full-width at half the maximum intensity (1.1 eV) of the Au $4f_{7/2}$ peak. The Ce $3d_{3/2}$ and $3d_{5/2}$ signals for cerium (III) and (IV) were fitted and Ce^{3+} (%) were calculated based on the integrated peak area ratios of the total area corresponding to Ce^{3+} with respect to the total area of the entire spectrum.

9.2.3 Catalysis Procedure

The four samples (CeO_2, CZ, Au/CeO_2 and Au/CZ) were reduced (at 5 K min^{-1}) in 50 cm^3 min^{-1} H_2 at 573 K for 1 h prior to catalysis. Reactions were carried out at 523-573 K and 1 atm *in situ* in a fixed bed vertical continuous flow glass reactor (l = 600 mm; i.d. = 15 mm). The catalytic reactor and operating conditions to ensure negligible heat/mass transport limitations have been fully described elsewhere [9.37] but some features, pertinent to this study, are given below. A layer of borosilicate glass beads served as preheating zone, ensuring that the benzoic acid (or benzaldehyde) reactant was vaporised and reached reaction temperature before contacting the catalyst. Isothermal conditions (± 1 K) were ensured by diluting the catalyst bed with ground glass (75 μm); the ground glass was mixed thoroughly with catalyst before insertion into the reactor. The reaction temperature was continuously monitored using a thermocouple inserted in a thermowell within the catalyst bed.

Benzoic acid (or benzaldehyde) as an aqueous or ethanolic solution was delivered at a fixed calibrated flow rate to the reactor *via* a glass/teflon air-tight syringe and teflon line using a microprocessor controlled infusion pump (Model 100 kd Scientific). A co-current flow in ultra pure H_2 (< 1% v/v organic in H_2) was maintained at a GHSV = 1.7×10^4 h^{-1} with an inlet reactant molar flow (F) = 2.5-8.4×10^{-5} mol h^{-1}. The molar Au to inlet organic feed rate (n/F) ratio spanned the range 0.03-0.28 h. Product composition was determined using a Perkin-Elmer Auto System XL gas chromatograph equipped with a programmed split/splitless injector and a flame ionization detector, employing a DB-1 50 m×0.20 mm i.d., 0.33 μm film thickness capillary column (J&W Scientific). Benzoic acid (Fluka, ≥ 99% w/w purity), benzaldehyde (Fluka, ≥ 98% w/w purity) and ethanol (Sigma Aldrich, ≥ 99% v/v) were used as received without further purification.

Repeated reactions with different samples from the same batch of catalyst delivered a product composition that was reproducible to within ± 6%.

9.3 Characterisation Measurements

9.3.1 BET and pore size distributions

Catalyst textural properties in term of surface area, pore volume, crystal size and crystallographic phase are important as they can impact on redox behaviour [9.38]. Critical characteristics of the supports (CeO_2 and CZ) and catalysts (Au/CeO_2 and Au/CZ) are presented **Table 9.1**. The CZ support presents a surface area (67 m^2 g^{-1}) which falls within the range (15-128 m^2 g^{-1}) reported in the literature for mixed oxides [9.39-41]. The CeO_2 support exhibits an appreciably higher surface area and the pore size distribution presented in **Figure 9.2** reveals pore diameters in the range 20-100 Å with a mean value of 46 Å. In contrast, the CZ support shows a broader bimodal distribution of larger pores (17-2300 Å, mean = 173 Å) with a greater total pore volume (0.31 cm^3 g^{-1}, **Table 9.1**).

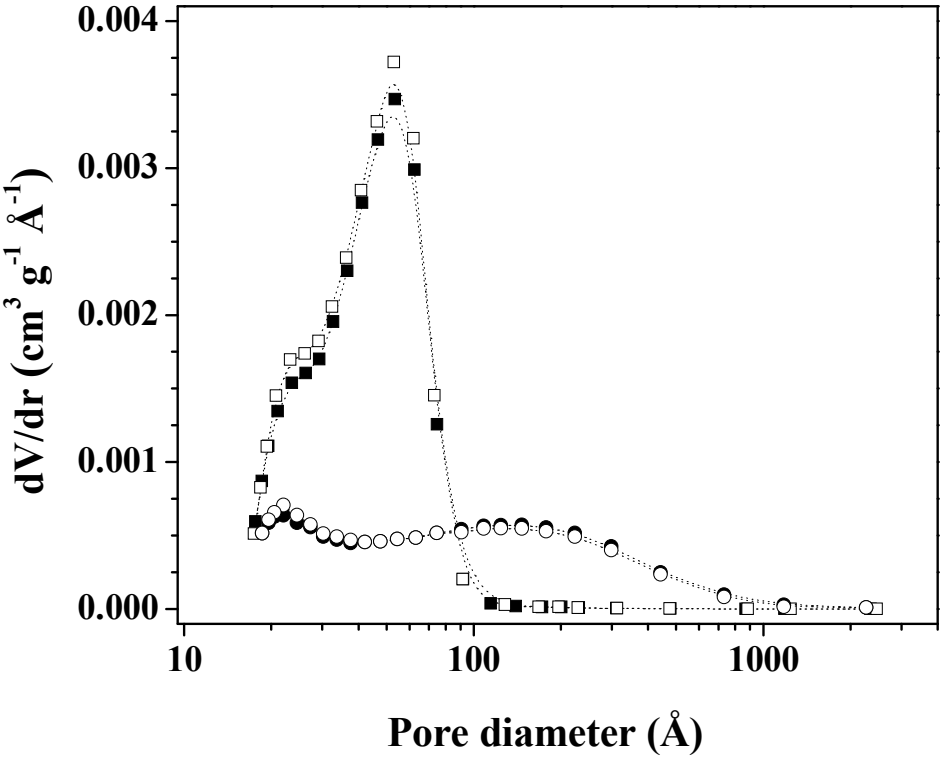

Figure 9.2: Pore size distributions for CeO_2 (□), CZ (○), Au/CeO_2 (■) and Au/CZ (●).

Table 9.1: BET surface area, mean pore diameter, total pore volume, crystal spacing (d_{111}) with lattice parameter (a) and crystal size (d_{hkl}), Au loading, CO uptake (CO/Au), mean Au particle size, temperature programmed reduction maxima (T_{max}) with H_2 and NH_3 consumed/released during TPR/TPD, oxygen capacity storage (OSC, expressed in terms of % Ce^{3+}) and XPS binding energy (BE) of Au $4f_{7/2}$ peak.

		Au/CeO_2	Au/CZ
BET ($m^2\ g^{-1}$)		108[a] (113[b])	67[a] (67[b])
Mean pore diameter (Å)		47[a] (46[b])	177[a] (173[b])
Total pore volume ($cm^3\ g^{-1}$)		0.15[a] (0.16[b])	0.29[a] (0.31[b])
XRD	d_{111} spacing (Å)	3.13[a, b]	3.07[a, b]
	Lattice parameter: a (Å)[c]	5.41[a, b]	5.34[a, b]
	Crystal size d_{hkl} (nm)[d]	10[a, b]	6[a, b]
Au (wt%)		3.0	2.3
CO/Au ($mol_{CO}\ mol_{Au}^{-1}$)[e]		0.31	0.31
Au mean particle size (d, nm)		1.4[e]; 2.0[f]	1.4[e]; 1.5[f]
TPR[a]	T_{max} (K)	420	420
	H_2 consumed ($mmol_{H2}\ g_{Au}^{-1}$)	18.1	22.4
H_2 TPD[a]	T_{max} (K)	817	822
	H_2 released ($mmol_{H2}\ g_{Au}^{-1}$)	6.3	5.5
NH_3 TPD	T_{max} (K)	410[a] (420[b])	379, 521[a] (387, 537)[b]
	NH_3 released ($mmol\ g^{-1}$)	0.31[a] (0.32[b])	0.39[a] (0.34[b])
OSC (% Ce^{3+})[a]		2[g], 7[h]	34[g], 31[h]
XPS BE : Au $4f_{7/2}$(eV)		84.7	84.3

[a]supported Au; [b]support; [c]based on *Fm*3*m* space group; [d]from Scherrer equation; [e]calculated from CO isotherms; [f]obtained from STEM analysis;
[g]from oxygen pulse titration; [h]from XPS analysis

The average pore diameter for CeO_2-ZrO_2 has been shown to increase (from 30 to 250 Å) with decreasing surface area (from 111 to 15 $m^2\ g^{-1}$) [9.39] and volumes in the range 0.11-0.33 $cm^3\ g^{-1}$ have been reported [9.39,9.42]. The larger pores and bimodal distribution in CZ confer a hierarchical and stable pore network [9.43], which contribute

to enhanced thermal stability [9.38]. The incorporation of Au did not result in any significant modification to the pore size characteristics or total surface area.

9.3.2 XRD

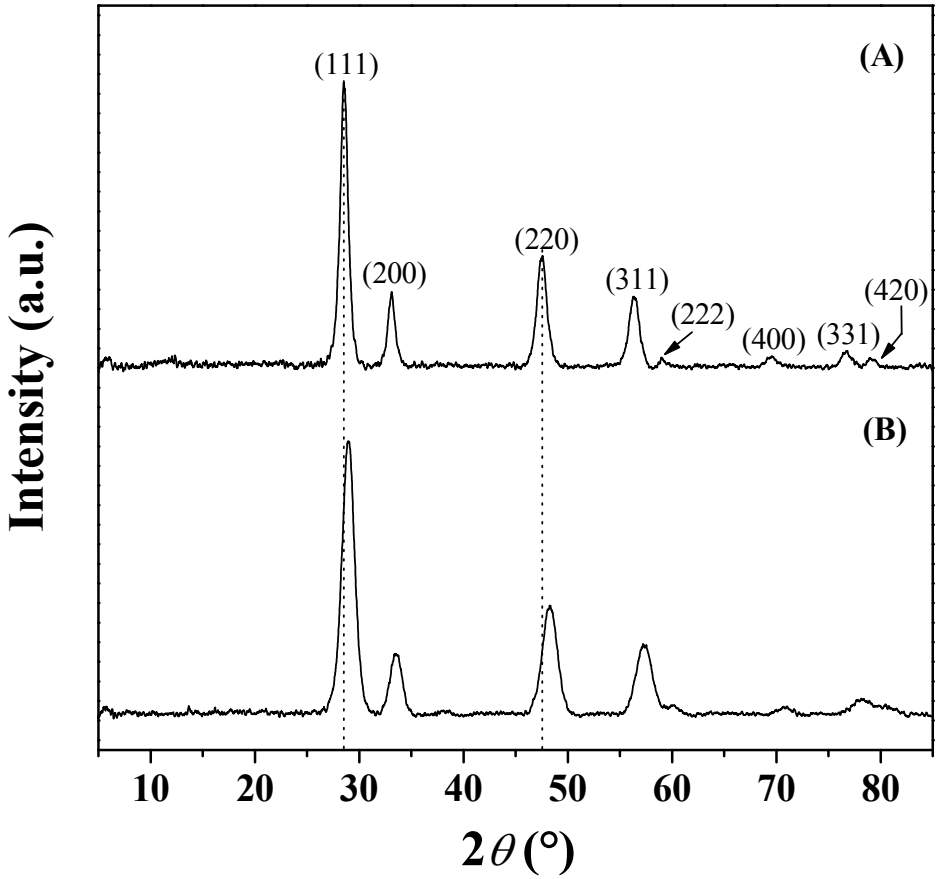

Figure 9.3: XRD patterns for (A) Au/CeO_2 and (B) Au/CZ. Note: the main planes associated with CeO_2 (reference standard 43-1002) are identified in (A).

The XRD pattern for Au/CeO_2 (**Figure 9.3(A)**) presents eight peaks in the range 2θ = 28°-79° that can be associated with the main planes of CeO_2 (JCPDS-ICDD reference standard 43-1002). The absence of any signal due to supported Au, notably at 38.2° ((111) plane of Au), suggests that the Au particles are well dispersed (particle size < 5 nm) and not detectable by XRD. The pattern for CeO_2 (not shown) coincides with that recorded for Au/CeO_2. Ceria exhibits a cubic-fluorite structure (space group $Fm3m$) and the lattice parameter (**Table 9.1**) is in agreement with the JCPDS reference (a = 5.41 Å). The XRD pattern of CZ (not shown) is identical to that recorded for Au/CZ (**Figure 9.3(B)**) and exhibited a response similar to CeO_2 with no detectable signals due

to ZrO_2. Studies of the structural properties and phase composition of $Ce_xZr_{1-x}O_2$ (with $0.2 < x < 0.8$) [9.44-46] have revealed that the solid formed is not thermodynamically stable due to the difference in the ionic radius of Zr^{4+} (0.84 Å) and Ce^{4+} (0.97 Å) and associated crystallographic structures (monoclinic or tetragonal ZrO_2 and cubic-fluorite CeO_2). A decrease in Ce content from 0.8 to 0.5 can result in two tetragonal phases (*t′* and *t″*) with a $P4_2/nmc$ structure [9.46]. The metastable *t″* phase has been reported for $Ce_xZr_{1-x}O_2$ with $0.5 < x < 0.8$ and is characterised by a lattice parameter $c/a = 1$ [9.44,9.45] while the *t′* phase has been reported for *x* in the range 0.4-0.6 (and c/a = 1.001-1.02) [9.38,9.47]; the predominant phase is dependent on method of synthesis and crystal size [9.48]. The XRD results (**Figure 9.3**, **Table 9.1**) for CZ and Au/CZ relative to CeO_2 and Au/CeO_2 show a shift to higher 2θ (by 0.5-1.5°) with a decrease in d_{111} spacing (from 3.13 to 3.07 Å), lattice parameter (from 5.41 to 5.34 Å) and crystal size (from 10 to 6 nm) that is in agreement with the reported XRD analysis of $Ce_xZr_{1-x}O_2$ with a *t″* structure [9.49-51]. These changes can be attributed to the incorporation of Zr in the framework resulting in a shortening of Ce-O bond length with a decrease in the lattice parameter where values in the range 5.30-5.36 Å have been recorded for $Ce_xZr_{1-x}O_2$ ($0.6 < x < 0.7$) [9.44,9.47,9.52].

9.3.3 Carbon monoxide adsorption isotherms and HAADF-STEM

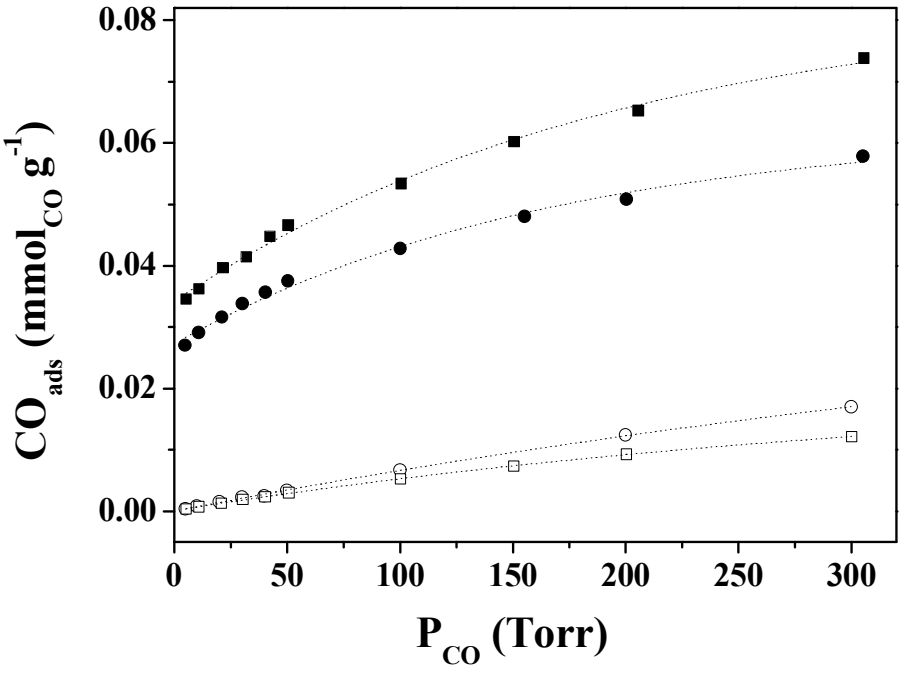

Figure 9.4: Carbon monoxide adsorption isotherms (at 308 K) for CeO_2 (□), CZ (○), Au/CeO_2 (■) and Au/CZ (●).

The occurrence of nano-crystals (d_{hkl} < 15 nm, **Table 9.1**) is significant as crystalline ceria at the nano-scale is known to favour the formation of a well dispersed metal phase [9.53]. In an earlier FTIR study of CO adsorption on Au/CZ [9.54], the occurrence of zero valent Au following calcination of Au/CZ under the conditions used in this study was established. Carbon monoxide adsorption isotherms are presented in **Figure 9.4** where the CO/Au ratios given in **Table 9.1** were determined from the difference in CO uptake recorded for the supported Au and bare support. Previous work has demonstrated [9.35] that Au dispersion can be related to CO/Au and used to determine Au particle size. The resultant mean Au size (d) is the same (1.4 nm, **Table 9.1**) on CeO_2 and CZ. Representative HAADF-STEM images (**Figure 9.5(A)**) and associated Au size distributions (**Figure 9.5(B)**) reveal Au particles < 5 nm with a mean value (1.5-2 nm) that agrees with the CO adsorption measurements. Gold on CZ is characterised by a narrower size distribution than Au/CeO_2. Gold particle size is critical in hydrogenation applications where significant activity is only observed for particles < 10 nm with enhanced rates for smaller particles (1-4 nm) due to an increase in low coordination edge and corner sites [9.55].

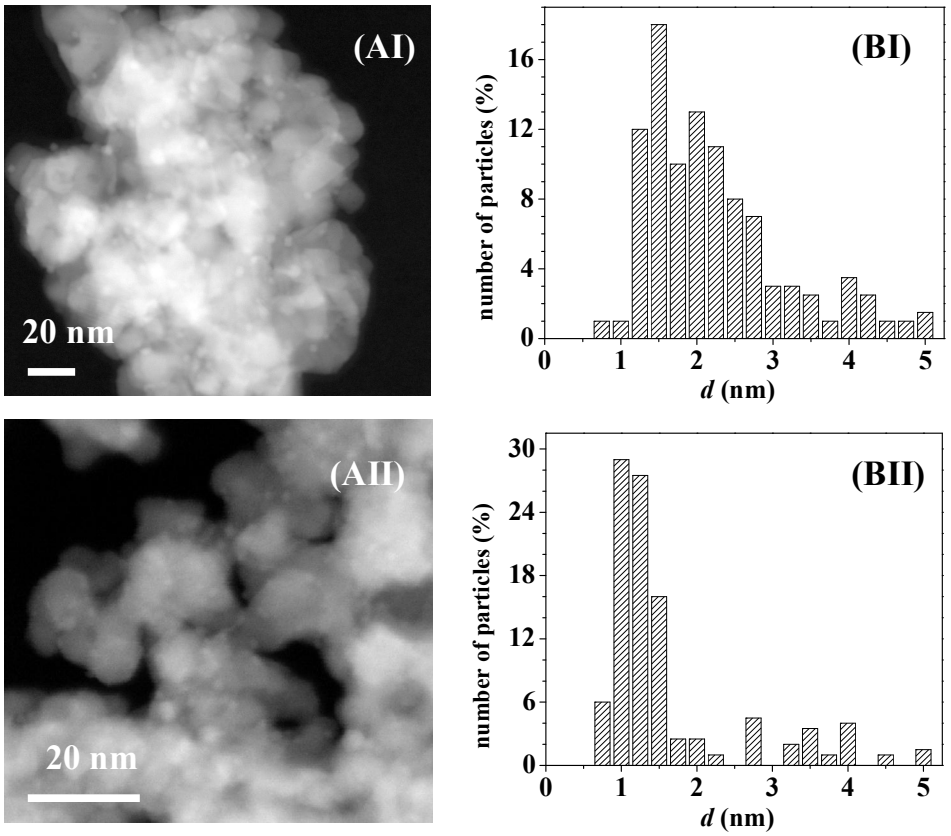

Figure 9.5: (A) Representative STEM images and (B) associated Au particle size distributions for (I) Au/CeO_2 and (II) Au/CZ.

9.3.4 TPR, OSC and H_2 TPD measurements

Temperature programmed reduction (TPR) profiles are presented in **Figure 9.6(A)** where the final temperature (573 K) matched that used in the activation step prior to catalysis. There was no measurable H_2 consumption in the treatment of CeO_2 or CZ, suggesting that the supports were not reduced under these conditions. Indeed, published TPR analyses [9.28,9.56] have established H_2 consumption by CeO_2 at higher temperatures (670-800 K) that was attributed to surface reduction whereas bulk transformation required temperatures > 970 K. Moreover, reduction of $Ce_xZr_{1-x}O_2$ (x = 0.5-0.8) has only been observed at temperatures in excess of 700 K with a maximum H_2 consumption at *ca.* 850 K [9.35,9.42]. The incorporation of Au on both supports resulted in a positive TPR signal at 420 K that can be ascribed to a partial reduction of both supports with the occurrence of H_2 spillover, *i.e.* dissociation on Au with diffusion of atomic H across the metal/support interface [9.35]. The spillover phenomenon is important in hydrogenation reactions, providing a surface reservoir of reactive hydrogen that can contribute to increased reaction rate [9.57]. Reduction of the support leading to the creation of oxygen vacancies is significant in this application as these vacancies can participate in the reaction (*via* the MvK mechanism) [9.33]. The TPR step can then result in (a) incorporation of chemisorbed hydrogen (reversible) and/or (b) formation of oxygen vacancies (irreversible) with the generation of water and Ce^{3+} to accommodate charge balance [9.58]. Reduction of CeO_2 and $Ce_xZr_{1-x}O_2$ is limited by hydrogen adsorption on the surface [9.59], which is facilitated by Au as has been proposed for Au/CeO_2 [9.28,9.56,9.60], $Au/Ce_{0.62}Zr_{0.38}O_2$ [9.35], $Au/CeZrO_4$ [9.61] and Au/Ce-Zr [9.62].

The measurement of oxygen storage capacity (OSC) *post*-TPR provides a measure of the degree of support reduction [9.42]. Previous FTIR [9.63] analysis has confirmed that the reduction of $Ce_xZr_{1-x}O_2$ generates Ce^{3+} sites with no evidence for the reduction of Zr^{4+}. We accordingly relate the O_2 consumed in the OSC analysis to Ce^{3+} oxidation and the data given in **Table 9.1** establish a higher degree of Au/CZ reduction compared with Au/CeO_2, which is consistent with the literature [9.42,9.45,9.47]. The smaller Zr cannot accommodate 8 atoms in its coordination sphere, resulting in the smaller lattice parameter for CZ (**Table 9.1**), which favours migration of oxygen from tetrahedral to octahedral sites [9.64]. The increase in oxygen mobility in the lattice facilitates formation of oxygen vacancies [9.59]. The H_2 TPD profiles for Au/CeO_2 and

Au/CZ are given in **Figure 9.6(B)** and characterised by signals at T_{max} = 820 ± 3 K; there was no detectable H_2 release from the bare supports. Hydrogen desorbed (**Table 9.1**) from Au/CeO_2 was measurably higher, suggesting a greater reversible surface hydrogen component relative to Au/CZ, which exhibited increased support reduction ($Ce^{4+} \rightarrow Ce^{3+}$) during TPR.

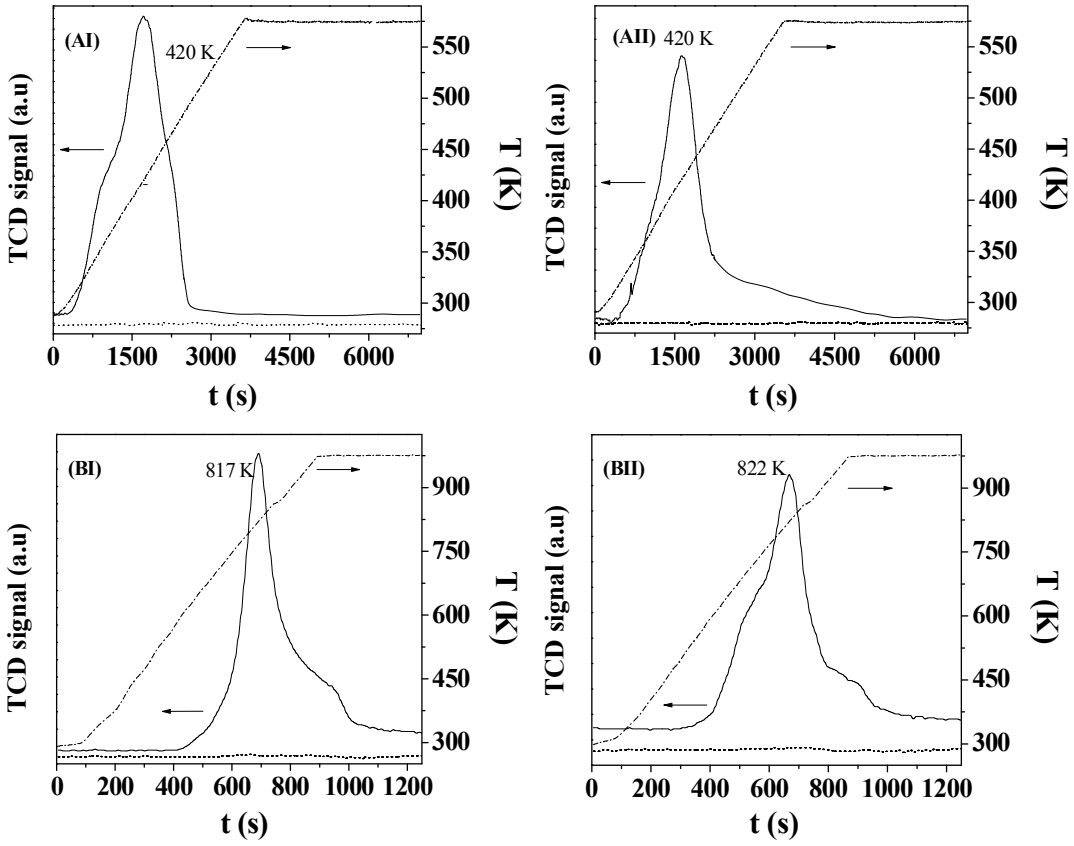

Figure 9.6: (A) Temperature programmed reduction (TPR) and (B) H_2 temperature programmed desorption (TPD) profiles (with the associated temperature ramp) generated for the support (dotted lines) and supported Au (solid lines) systems: (I) CeO_2 and Au/CeO_2; (II) CZ and Au/CZ.

9.3.5 NH_3 TPD

Surface acidity has been shown to play a significant role in benzoic acid hydrogenation, affecting adsorption/desorption of benzoic acid and benzaldehyde [9.12,9.20,9.22]. Ammonia TPD measurements were conducted to evaluate total acid site concentration and strength [9.65]. The TPD profiles are presented in **Figure 9.7** and the associated temperature for maximum release (T_{max}) and total NH_3 desorbed are recorded in **Table 9.1**. The CeO_2 support exhibited desorption over the 320-620 K range that can be attributed to surface hydroxyl groups and weak Lewis acidity (Ce^{4+}) where

the T_{max} and NH_3 released are in reasonable agreement with the literature (T_{max} = 390-470 K; 0.10-0.25 mmol NH_3 g^{-1}) [9.66,9.67]. The TPD profile for CZ presents two desorption peaks at 387 K and 537 K, which coincide with that reported previously (T_{max} = 398 and 580 K) for $Ce_{0.5}Zr_{0.5}O_2$ [9.62], suggesting a range of acid strength. Ammonia release from CZ falls within that (0.18-0.45 mmol NH_3 g^{-1}) recorded elsewhere [9.62,9.66].

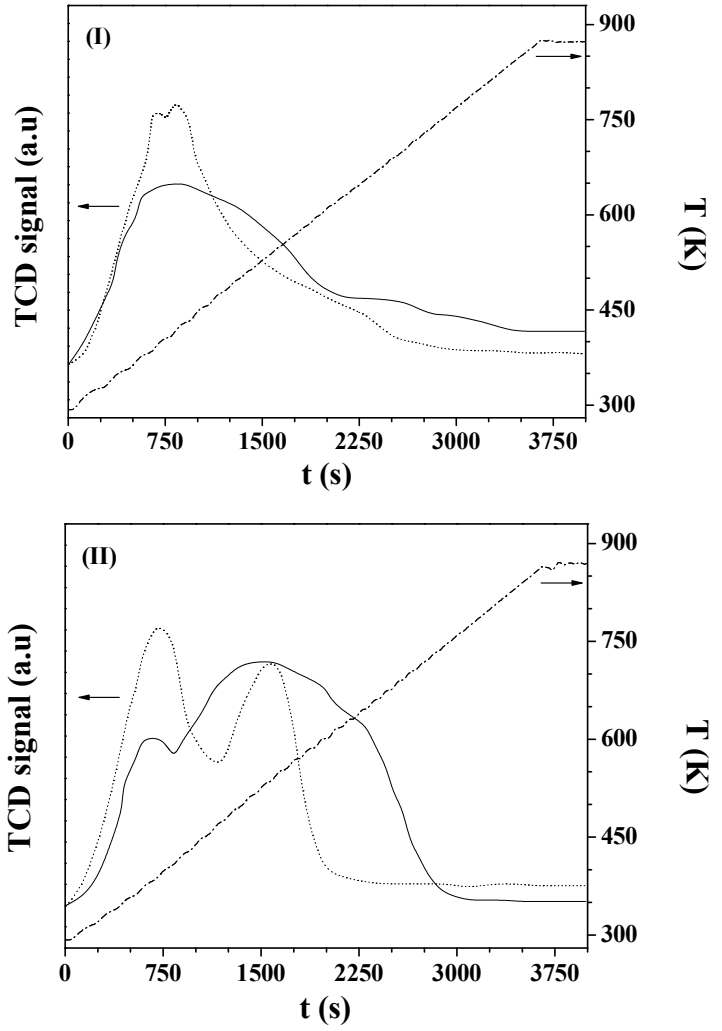

Figure 9.7: Ammonia TPD profiles (with associated temperature ramp) generated for the support (dotted lines) and supported Au (solid lines) systems: (I) CeO_2 and Au/CeO_2; (II) CZ and Au/CZ.

Both CeO_2 and CZ have been characterised as weak Lewis acids where the inclusion of Zr increases the number of acid sites [9.66] and strength [9.68]. This is consistent with the measurably higher NH_3 release from CZ (**Table 9.1**) and occurrence of the higher temperature (T_{max} = 537 K) desorption (**Figure 9.7(II)**). Peaks with a maximal temperature in the range 530-600 K have been reported in the literature for

Lewis acid sites on ZrO_2, *i.e.* Zr^{4+} [9.69,9.70]. The low and high temperature peaks may then coincide with desorption from Ce^{4+} and Zr^{4+}, respectively. A decrease in acid strength has been reported [9.62] for Au and Pt supported on Ce-Zr mixed oxides, which may be reflected in the shift of T_{max} for Au/CZ relative to CZ (**Table 9.1**). Inclusion of Au with CZ is accompanied by a marked decrease in intensity of the lower temperature desorption peak. The decrease in acid strength and intensity of the lower peak can be attributed to Ce^{4+} reduction to Ce^{3+}, as demonstrated by OSC measurements.

9.3.6 XPS

Partial reduction of CZ was also determined by XPS where the calculated % Ce^{3+} is in good agreement with that obtained from OSC analysis (**Table 9.1**). The XPS profiles over (**A**) the Ce 3*p* and (**B**) Au 4*f* binding energy (BE) range are presented in **Figure 9.8**. The Ce profiles present up ten 3*p* signal components where the peaks denoted v_0, v, v', v'' and v''' correspond to the spin-orbit split of the Ce $3d_{5/2}$ core hole while the peaks designated as u_0, u, u', u'' and u''' represent the Ce $3d_{3/2}$ contribution [9.6,9.71,9.72]. The peaks due to Ce $3d^{10}$ $4f^0$ O $2p^6$ (u'''; v'''), Ce $3d^9$ $4f^1$ O $2p^5$ (u''; v'') and Ce $3d^9$ $4f^2$ O $2p^4$ (u; v) electronic states result from Ce^{4+} while Ce^{3+} is associated with $3d^9$ $4f^1$ O $2p^6$ (u'; v') and $3d^9$ $4f^2$ O $2p^5$ (u_0; v_0) electronic states. The profile of Au/CeO_2 (**Figure 9.8(AI)**) exhibits the six peaks attributed to Ce^{4+} and the contribution due to Ce^{3+} (u'; v') is small, which is consistent with the low degree of reduction of the support (<10%). In contrast, Au/CZ exhibits four peaks due to Ce^{3+} (u'; v'; u_0; v_0) that can be linked to the significant level of Ce^{4+} reduction. The higher Au $4f_{7/2}$ BE for Au/CeO_2 (84.7 eV, **Table 9.1**) and Au/CZ (84.3 eV) relative to the Au reference (84.0 eV [9.73]) suggest the formation of surface $Au^{\delta+}$. Charge transfer, Au-support interaction and Au coordination number are known to influence Au $4f_{7/2}$ BE [9.54]. Density functional calculations [9.74] have established charge transfer between Au and Ce cations where Au^+ results from strong interaction with one or two (bridging) surface oxygen atoms while adsorption on other sites (*e.g.* O-Ce and Ce cations) are weaker and associated with Au^0 [9.74]. We can note that the most stable sites for Au on ZrO_2 are the bridging positions on an oxygen and Zr, which results in a relatively weak interaction with limited charge transfer [9.75]. As both catalysts exhibit similar Au particle size, the difference in BE can be related to support interactions.

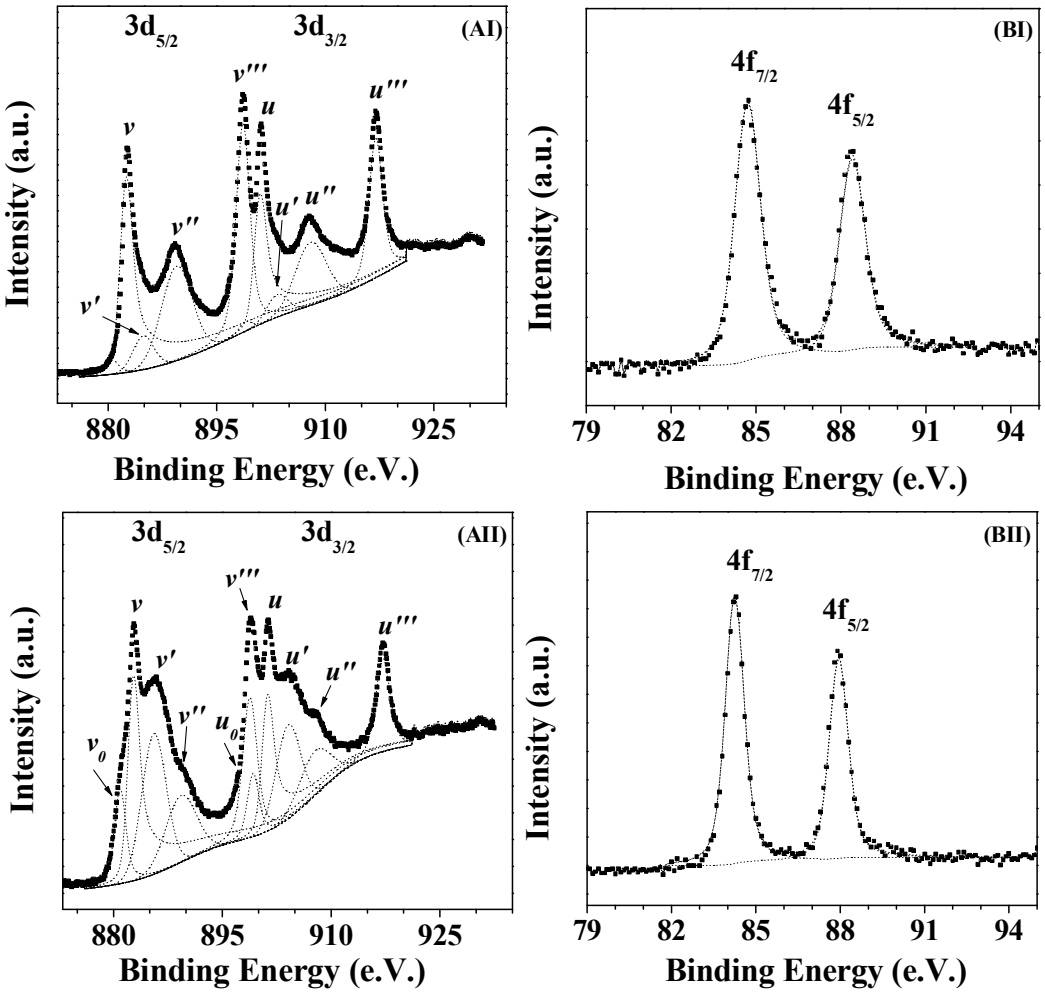

Figure 9.8: XPS spectra over (A) Ce 3*p* and (B) Au 4*f* regions for (I) Au/CeO_2 and (II) Au/CZ; raw data are given by ■ where lines represent the fits.

9.4 Catalytic Results

Reactions operated under thermodynamic control favour pathways with lower enthalpies and higher negative Gibbs free energies. Taking the reaction network given in **Figure 9.1**, the stoichiometric requirement (with respect to H_2) for each step and associated changes in reaction enthalpy (ΔH_{298K}) and Gibbs free energy (ΔG_{298K}) [9.76] are presented in **Table 9.2**. Formation of benzaldehyde *via* path I is endothermic (positive ΔH_{298K}) whereas all the other steps are exothermic with paths (II) and (VI) releasing the greatest heat. The ΔG_{298K} values provide valuable information and serve as an indicator of possible thermodynamic limitations: reaction can occur spontaneously where $\Delta G_{298K} < 0$. It can be seen from the entries in **Table 9.2** that benzaldehyde is a

thermodynamically unfavourable product while the formation of benzyl alcohol, toluene and benzene are favoured ($\Delta G_{298K} << 0$).

Table 9.2: Stoichiometric requirements for reactions given in Figure 9.1 with associated changes in enthalpy (ΔH) and Gibbs free energy (ΔG) of formation. *Note*: All the compounds are in gas state.

Product (path)	Stoichiometry[a]	Reaction	ΔH_{298K} ($kJmol^{-1}$)	ΔG_{298K} ($kJmol^{-1}$)
Benzaldehyde (I)	1	$C_7O_2H_6 + H_2 \leftrightarrow C_7OH_6 + H_2O$	8.3	6.5
Toluene (II)	3	$C_7O_2H_6 + 3H_2 \leftrightarrow C_7H_8 + 2H_2O$	-143.5	-124.1
Toluene (I+III)	3	$C_7O_2H_6 + H_2 \leftrightarrow C_7OH_6 + H_2O$	8.3	6.5
		$C_7OH_6 + 2H_2 \leftrightarrow C_7H_8 + H_2O$	-101.3	-82.1
Benzyl alcohol (I+VIII)	2	$C_7O_2H_6 + H_2 \leftrightarrow C_7OH_6 + H_2O$	8.3	6.5
		$C_7OH_6 + H_2 \leftrightarrow C_7OH_8$	-50.6	-48.5
Benzene (II+VII)	4	$C_7O_2H_6 + 3H_2 \leftrightarrow C_7H_8 + 2H_2O$	-143.5	-124.1
		$C_7H_8 + H_2 \leftrightarrow C_6H_6 + CH_4$	-41.9	-43.5
Benzene (I+III+VII)	4	$C_7O_2H_6 + H_2 \leftrightarrow C_7OH_6 + H_2O$	8.3	6.5
		$C_7OH_6 + 2H_2 \leftrightarrow C_7H_8 + H_2O$	-101.3	-82.1
		$C_7H_8 + H_2 \leftrightarrow C_6H_6 + CH_4$	-41.9	-43.5
Benzene (IV)	-	$C_7O_2H_6 \leftrightarrow C_6H_6 + CO_2$	-20.4	-54.3
Benzene (I+VI)	4	$C_7O_2H_6 + H_2 \leftrightarrow C_7OH_6 + H_2O$	8.3	6.5
		$C_7OH_6 \leftrightarrow C_6H_6 + CO$	-193.7	-174.1
Benzophenone (V)	-	$2C_7O_2H_6 \leftrightarrow C_{13}OH_{10} + H_2O + CO_2$	-121.1	-[b]

[a]with respect to H_2
[b]no reference ΔG value available for this step

Passage of benzoic acid over the supports alone, *i.e.* in the absence of Au, did not result in any detectable conversion. Taking an overview of the literature, a range of oxides (ZnO, ZrO_2, CeO_2, PbO) have shown activity for reaction at 523-573 K [9.7,9.8,9.12,9.22] with benzaldehyde and toluene as principal products and low selectivity to benzyl alcohol (S < 0.1). We can attribute the lack of hydrogenation/hydrogenolysis activity observed in this study for CeO_2 and CZ to the low activation temperature (573 K) employed. Indeed, under these activation conditions, TPR and TPD analysis have revealed insignificant support reduction with no measurable hydrogen uptake/release on/from the bare supports. Conversion of benzoic acid can then be attributed to contributions due to the supported Au phase. Reaction of

aqueous solutions of benzoic acid over Au/CeO_2 and Au/CZ generated benzaldehyde and benzyl alcohol as the only products with no detectable toluene, benzene or benzophenone formation. This response is far removed from the product distribution that would result under thermodynamic control. Formation of benzene and benzophenone has been observed at higher temperatures (> 673 K) and longer contact time [9.22] over strongly basic catalysts (such as MgO [9.7]) or at low H_2 surface coverage [9.21], conditions that are removed from those which prevail in this study. Moreover, aromatic ring reduction, with formation of methyl-cyclohexane or cyclohexane-carboxylic acid, was not observed in contrast to reaction over Cu and Pt supported on ZrO_2 [9.11].

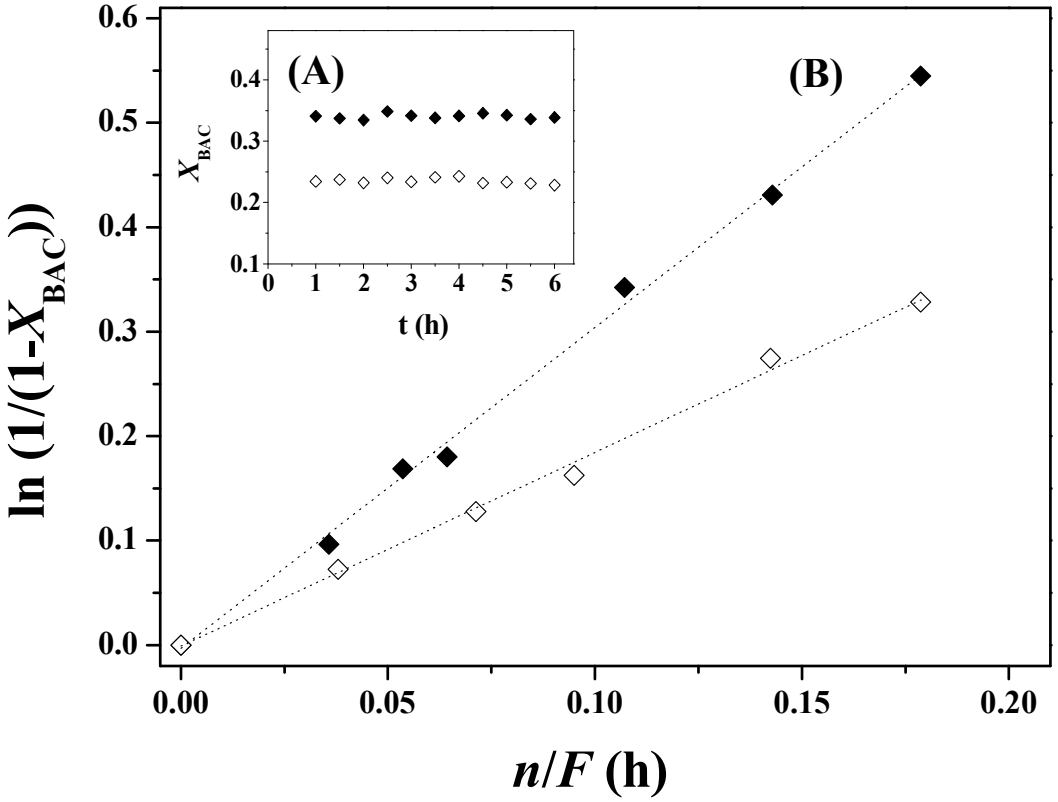

Figure 9.9: (A) Variation of aqueous benzoic acid fractional conversion (X_{BAC}) with time-on-stream over Au/CeO_2 (◇) and Au/CZ (◆) (n/F = 0.14 h; T = 573 K); (B) Pseudo-first order kinetic plots.

The temporal dependence of benzoic acid fractional conversion (X_{BAC}) over Au/CeO_2 and Au/CZ is shown in **Figure 9.9(A)** where a time invariant (for up to 6 h on-stream) response is in evidence. This is significant as the catalysts that have been

used to promote gas phase benzoic acid hydrogenation (including CeO_2) have exhibited loss of activity [9.5,9.6], which was attributed to coke deposition [9.5] and associated with toluene and benzene formation [9.6]. Applicability of a pseudo-first order kinetic treatment can be tested using the relationship [9.77]

$$\ln(1-X_{\mathrm{BAC}})^{-1} = k_{\mathrm{BAC}}\left(\frac{n}{F}\right) \tag{9.2}$$

where n/F (h) represents the molar ratio of Au in the catalyst bed to benzoic acid inlet flow rate. The linear relationship between $\ln(1\text{-}X_{\mathrm{BAC}})^{-1}$ and n/F, shown in **Figure 9.9(B)**, confirms adherence to pseudo-first order behaviour and the associated rate constants (k_{BAC}) are given in **Table 9.3**. An increase in reaction temperature (from 523 to 573 K) served to raise the rate where higher k_{BAC} values were recorded for Au/CZ relative to Au/CeO_2. Hydrogenation activity and selectivity over supported Au have been shown to depend on: (a) Au particle size and morphology [9.36,9.78,9.79]; (b) surface hydrogen [9.80]; (c) nature of the support in terms of reducibility (oxygen vacancy site density), acid-base properties and interaction at the metal interface [9.32,9.81]. As both catalysts show an equivalent Au size (**Table 9.1** and **Figure 9.5**), contributions due to the first factor can be excluded. While TPD results have exhibited a measurably greater H_2 release from Au/CeO_2, the difference was not significant and did not translate into increased rate. For the hydrogenation of benzoic acid, Cheng *et al.* [9.23] attributed the increase in activity after incorporating Mn on CeO_2/Al_2O_3 to enhanced support reducibility. The greater degree of Ce^{4+} reduction exhibited by Au/CZ (from OSC) with formation of oxygen vacancies must play a critical role in delivering higher rate by activating benzoic acid for reaction.

The variation of benzaldehyde (S_{BAD}) and benzyl alcohol (S_{BOL}) selectivities as a function of conversion (X_{BAC}) are shown in **Figure 9.10(I)** for reaction over Au/CeO_2 at 523 K **(AI)** and 573 K **(BI)** and Au/CZ at 523 K **(CI)** and 573 K **(DI)**. In common with conversion, product selectivity was constant with time on-stream. It can be seen that benzyl alcohol selectivity increased with conversion over both catalysts and was favoured by a lower reaction temperature. At 523 K, Au/CZ exhibited higher S_{BOL} relative to Au/CeO_2 and the reverse trend holds for reaction at 573 K where Au/CZ delivered lower S_{BOL}.

Table 9.3: Pseudo-first order rate constant and rate constant ratios (k_2/k_1 and k_3/k_1, see Figure 9.11 and eqns 9.6-9.8) obtained from the fit of Eqn (9.11) for the hydrogenation of aqueous and ethanolic benzoic acid (k_{BAC}) and aqueous benzaldehyde (k_{BAD}) solutions at 523 and 573 K.

Catalyst	T (K)	k_{BAC} aqueous feed (h^{-1})	k_2/k_1	k_3/k_1	k_{BAD} aqueous feed (h^{-1})	k_{BAC} ethanolic feed (h^{-1})
Au/CeO_2	523	0.3	3.2	3.0	6.9	-
	573	1.8	6.8	0.3	2.2	5.4
Au/CZ	523	0.5	13.1	0.7	6.0	-
	573	3.1	1.8	1.0	2.4	10.6

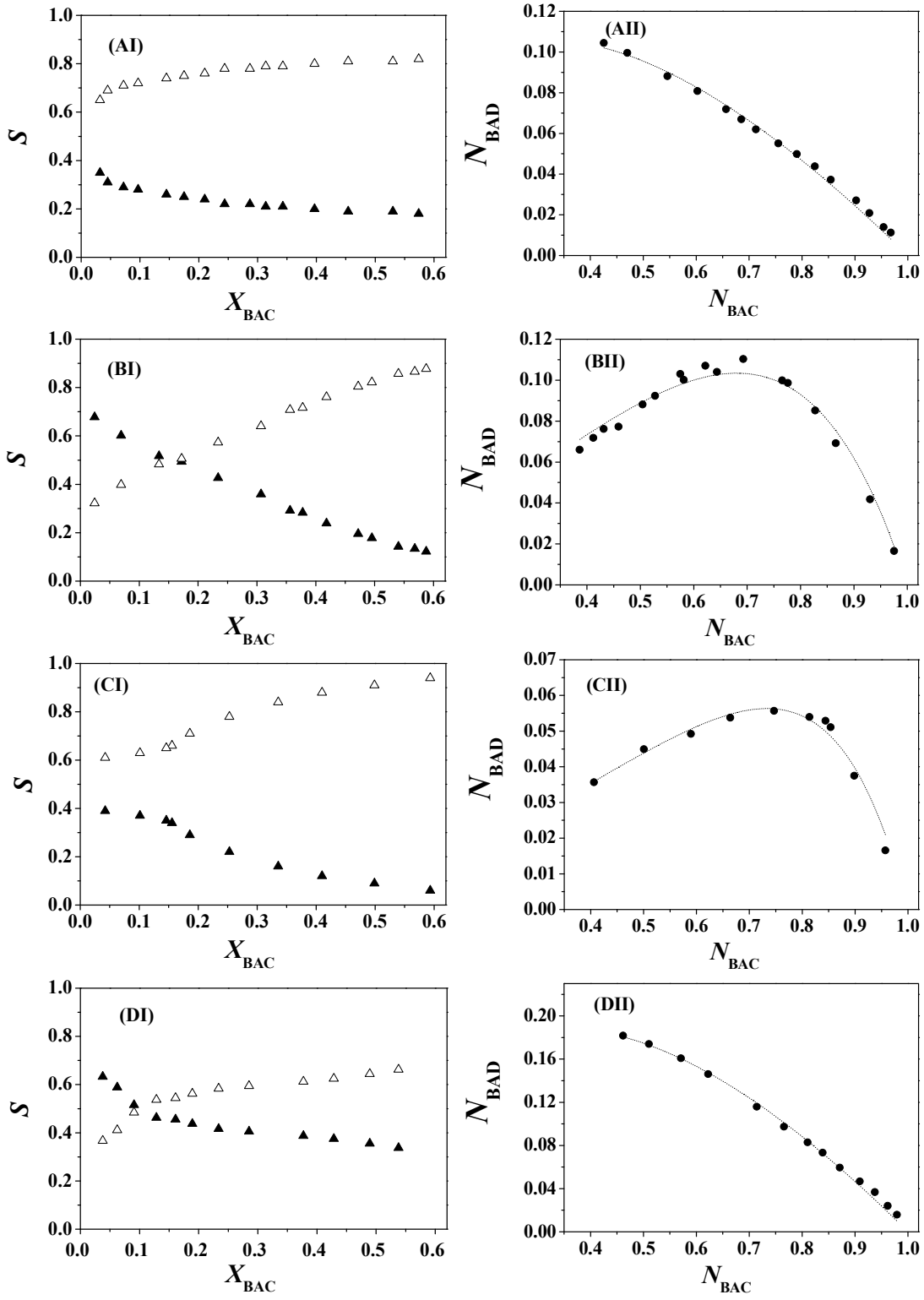

Figure 9.10: Hydrogenation of aqueous benzoic acid over Au/CeO_2 at 523 K (A) and 573 K (B) and Au/CZ at 523 K (C) and 573 K (D): (I) Variation of selectivity (*S*) to benzaldehyde (▲) and benzyl alcohol (Δ) with benzoic acid fractional conversion (X_{BAC}); (II) Variation of benzaldehyde molar fraction (N_{BAD}) with benzoic acid molar fraction (N_{BAC}).

The production of benzyl alcohol over oxides is known to proceed in a stepwise manner with the reduction of benzoic acid to benzaldehyde (path I, **Figure 9.1**) and subsequent hydrogenation to the alcohol (path VIII) [9.7,9.22]. In addition to the stepwise conversion, we also consider here the possibility of a direct hydrogenation of benzoic acid to benzyl alcohol. The consecutive/parallel steps are given below (see **Figure 9.11**),

$$BAC + H_2 \xrightarrow{k_1} BAD + H_2O \tag{9.3}$$

$$BAD + H_2 \xrightarrow{k_2} BOL + H_2O \tag{9.4}$$

$$BAC + 2H_2 \xrightarrow{k_3} BOL + H_2O \tag{9.5}$$

and

$$\frac{dN_{\mathrm{BAC}}}{d\left(n/F_{\mathrm{BAC}}\right)} = -\left(k_1 + k_3\right) \times N_{\mathrm{BAC}} \tag{9.6}$$

$$\frac{dN_{\mathrm{BAD}}}{d\left(n/F_{\mathrm{BAC}}\right)} = k_1 \times N_{\mathrm{BAC}} - k_2 \times N_{\mathrm{BAD}} \tag{9.7}$$

$$\frac{dN_{\mathrm{BOL}}}{d\left(n/F_{\mathrm{BAC}}\right)} = k_2 \times N_{\mathrm{BAD}} + k_3 \times N_{\mathrm{BAC}} \tag{9.8}$$

where N_i represents the molar fraction of the ith compound and k_j is the pseudo-first order rate constant of step j; BAD and BOL represent benzaldehyde and benzyl alcohol, respectively.

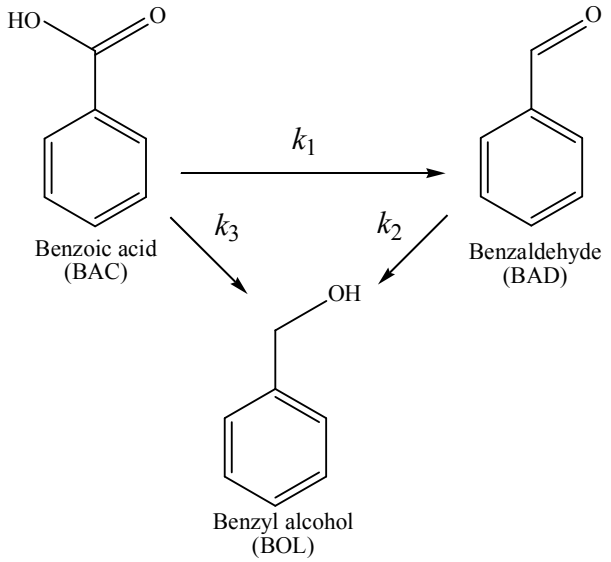

Figure 9.11: Possible consecutive/parallel steps (k_1, k_2 and k_3) associated with the conversion of benzoic acid to benzyl alcohol.

From a combination of Eqns (9.6) and (9.7)

$$\frac{dN_{\mathrm{BAD}}}{dN_{\mathrm{BAC}}} = -L + M \times \left(\frac{N_{\mathrm{BAD}}}{N_{\mathrm{BAC}}} \right) \tag{9.9}$$

$$\text{with} \qquad L = \frac{k_1}{k_1 + k_3} \quad \therefore \quad M = \frac{k_2}{k_1 + k_3} \tag{9.10}$$

which, when integrated gives

$$N_{\mathrm{BAD}} = \frac{L}{1-M} \times \left({N_{\mathrm{BAC}}}^{M} - N_{\mathrm{BAC}} \right) + C \tag{9.11}$$

where C is a constant and the values of L and M can be determined by non-linear fitting; L and M are given by

$$\frac{k_3}{k_1} = \frac{1-L}{L} \quad \therefore \quad \frac{k_2}{k_1} = \frac{M}{L} \tag{9.12}$$

The applicability of this parallel/consecutive model can be assessed from the plots presented **Figure 9.10(II)**; related rate constant ratios (k_2/k_1 and k_3/k_1) are given **Table 9.3**. A ratio $k_3/k_1 < 1$ is indicative of a stepwise formation of benzyl alcohol (*via* benzaldehyde) where $k_2/k_1 > 1$ favours alcohol formation. In contrast, $k_3/k_1 > 1$ can be associated with a direct hydrogenation of benzoic acid to benzyl alcohol, which is the case for Au/CeO_2 at 523 K. Given the limited support reduction observed for Au/CeO_2, any contribution due to oxygen vacancies coverage in the direct formation of benzyl alcohol over Au/CeO_2 is minor. Benzoic acid can adsorb to form a surface benzoate where the carboxyl oxygen coordinates to surface cationic sites [9.10,9.15]. A bidentate coordination with one (chelating) or two (bridging) points of attachment has been proposed for benzoic acid adsorption on oxides [9.82]. The role of the metal/support interface can be critical in determining product distribution. Indeed, contributions due to the occurrence of defects, degree of coordination and electronic state of Au (neutral, positive or negatively charged) have been proposed to influence the catalytic response [9.83]. XPS analysis has revealed the occurrence of electron transfer to the support where the formation of $Au^{\delta+}$ facilitates interaction with anionic species and bidentate

adsorption of benzoic acid as been reported for Au (111) [9.84]. Moreover, NH_3 TPD analysis has established surface acidity, most likely due to Ce^{4+}. Therefore, we envisage a two point attachment of benzoic acid on Au/CeO_2 that generates a bridging bidentate benzoate *via* interaction with Ce^{4+} and $Au^{\delta+}$ sites as shown in **Figure 9.12(A)**. Addition of surface hydrogen generates the alcohol in a single step.

Reaction over Au/CZ at 523 K shows a contribution due to both concerted and stepwise pathways where the stepwise conversion is preferred ($k_3/k_1 = 0.7$). Given the higher density of oxygen vacancies on Au/CZ, this can be attributed to a MvK mechanism with benzoic acid activation at a vacancy site and reaction with surface hydrogen to generate benzaldehyde (**Figure 9.12(B)**). Surface hydrogen can react with the oxygen that filled the vacancy to form water, regenerating the active site [9.8]. The surface benzaldehyde as a reactive intermediate can, in turn, be converted to benzyl alcohol *via* nucleophilic attack of C=O, which does not required the involvement of oxygen vacancies [9.85]. Infrared analysis has demonstrated the formation of an intermediate chemisorbed at a cationic metal site [9.10], which can react with surface hydrogen to give benzyl alcohol that desorbs into the gas phase (see **Figure 9.12(C)**).

A one step benzoic acid → benzyl alcohol transformation over Au/CZ can result from carboxyl oxygen interaction with $Au^{\delta+}$ in close proximity to an oxygen vacancy that serves to activate the second reactant oxygen (**Figure 9.12(D)**). Oxygen interaction with the support vacancy facilitates C-O scission while hydrogen addition at the gold site generates the alcohol. The interaction of Au with oxygen vacancies at the metal/support has been shown to play a crucial role in the catalytic response of Au/CeO_2 [9.86]. The presence of gold facilitate reduction to Ce^{3+} and oxygen vacancies are most likely created close to the support interface with metal nanoparticles [9.87]. The surface mechanisms proposed (**A** and **D**) for the direct formation of benzyl alcohol require the participation of Au sites that bear a partial positive charge, as confirmed by XPS. Mechanism (**D**) involves synergism between $Au^{\delta+}$ and oxygen vacancies, which is facilitated by Au/CZ as it exhibits higher OSC and the well dispersed (from STEM analysis) Au phase ensures the occurrence of Au in close proximity to these vacancies. While a concerted surface reaction can proceed *via* both mechanisms, proposal (**A**) should predominate on Au/CeO_2 given the higher relative Ce^{4+} content (from NH_3 TPD and OSC analysis) and lesser oxygen vacancy formation.

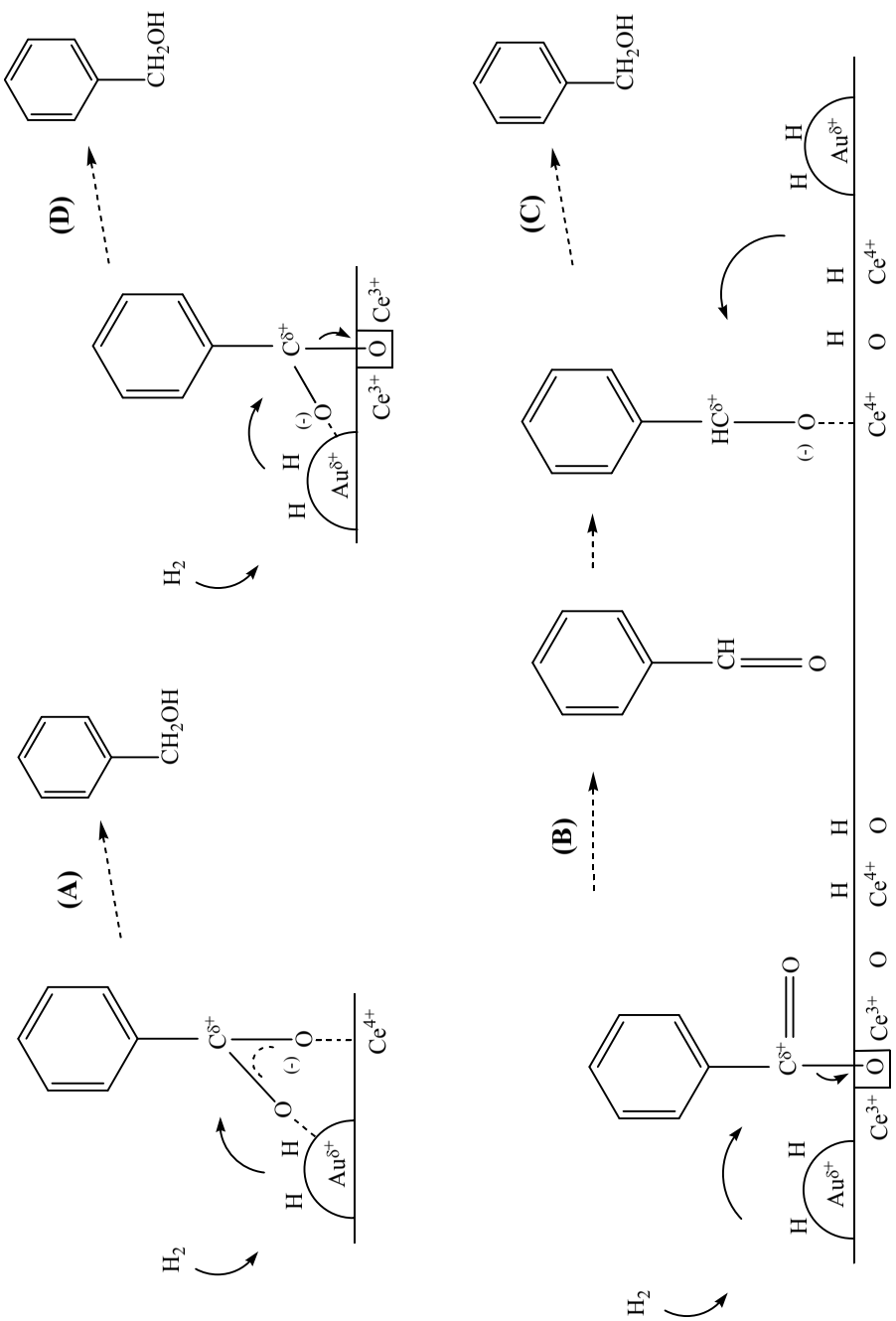

Figure 9.12: Schematic showing possible benzoic acid/surface interaction(s) leading to reaction: (A) one step generation of benzyl alcohol *via* bidentate attachment at $Au^{\delta+}$ and support Ce^{4+} sites; stepwise route involving (B) benzoic acid adsorption at an oxygen vacancy with surface hydrogen addition to give benzaldehyde as a reactive intermediate that is (C) activated at a Ce^{4+} site; (D) concerted activation of the carboxyl function at an oxygen vacancy and $Au^{\delta+}$ with hydrogen addition.

An increase in reaction temperature over Au/CZ favoured the concerted reaction with a rate equivalency for both pathways ($k_3/k_1 = 1$). The relative rate of the sequential benzoic acid and benzaldehyde hydrogenation showed a marked response to temperature (k_2/k_1 decreasing from 13.1 to 1.8). In order to probe this effect, the hydrogenation of benzaldehyde was examined and the results (k_{BAD}) are included in **Table 9.3**. The conversion of the benzaldehyde feed delivered similar rate constants for Au/CeO_2 and Au/CZ where benzyl alcohol was the sole product with no detectable toluene formation. This response suggests that the difference in surface acidity or number of oxygen vacancies does not affect C=O reduction to C-OH to any significant extent and benzaldehyde conversion in the stepwise mechanism (**C**) must proceed over equivalent active sites on both catalysts. The significantly higher rate of benzaldehyde hydrogenation relative to benzoic acid conversion over Au/CeO_2 and Au/CZ at 523 K is consistent with the observed $k_2/k_1 > 1$. The lower k_{BAD} recorded at the higher temperature suggests benzaldehyde desorption from the surface that serves to lower rate and limits the sequential pathway, which is evident for reaction over Au/CZ (lowered k_2/k_1, increased k_3/k_1). In contrast, an increase in reaction temperature to 573 K favours stepwise conversion ($k_3/k_1 < 1$) over Au/CeO_2. This suggests that the relative contribution of the reactive benzoate (**Figure 9.12(A)**) to the overall surface mechanism is lower at the higher reaction temperature. The rate of benzaldehyde hydrogenation (k_{BAD}) exceeds that for the acid (k_{BAC}), which facilitates stepwise conversion to the alcohol. As expected for a sequential reaction, the selectivity/conversion plot (**Figure 9.10(BI)**) shows a crossing point (at $X_{BAC} \approx 0.17$) and selectivity to the alcohol increases with conversion. The highest selectivity to benzyl alcohol ($S = 0.94$) was achieved for reaction over Au/CZ at 523 K and can be associated with a favoured stepwise route with high associated k_2/k_1.

Contacting reducible oxides, such as CeO_2 [9.88,9.89] and ZrO_2 [9.1,9.11], with water vapour can occlude oxygen vacancies. A significant decrease in the conversion of benzoic acid to benzaldehyde [9.1] or toluene [9.11] has been observed after addition of water. Even at low coverage and pressure, H_2O dissociates readily where the resultant OH group fills an oxygen vacancy and the H atom binds to a bridging O site [9.90], leading to a reoxidation of the surface [9.91]. Consequently, adsorption and dissociation of water on the reducible supports can consume oxygen vacancies. In order to check for a possible contribution due to a solvent effect, the hydrogenation of ethanolic benzoic

acid solutions was examined at 573 K and the resultant selectivity/conversion responses are presented **Figure 9.13**.

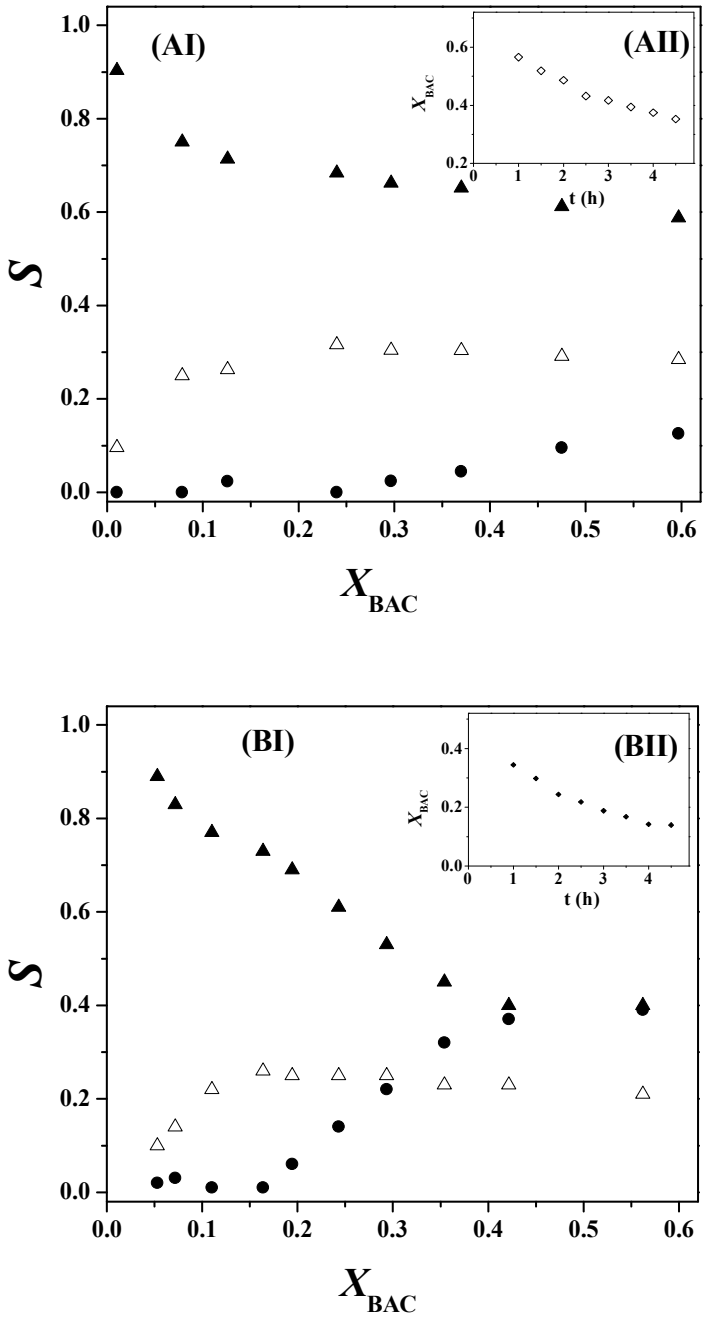

Figure 9.13: (I) Selectivity (*S*) to benzaldehyde (▲), benzyl alcohol (Δ) and toluene (●) as a function of the fractional conversion of benzoic in ethanolic solutions (X_{BAC}); (II) Variation X_{BAC} with time-on-stream; (A) reaction over Au/CeO_2; (B) reaction over Au/CZ; T = 573 K.

In addition to benzaldehyde and benzyl alcohol, the formation of toluene was recorded over both catalysts. Toluene can be generated (i) directly *via* deoxygenation of benzoic acid (step (II), **Figure 9.1**) or (ii) from consecutive the reaction of benzaldehyde (step (III), **Figure 9.1**) [9.22]. Both reactions have been proposed to occur through a MvK mechanism and require (i) twin or (ii) excess oxygen vacancies. We can attribute the higher (by a factor 3) rate constants (k_{BAC}, **Table 9.3**) and the formation of toluene to the increase in available oxygen vacancies in the ethanol carrier. Reaction over Au/CeO_2 (**Figure 9.13(AI)**) resulted in a significant increase in selectivity to benzaldehyde (in ethanol relative to water), which can be attributed to the contribution of oxygen vacancies, favouring the stepwise mechanism. Conversion of ethanolic benzoic acid over Au/CZ (**Figure 9.13(BI)**) generated appreciable levels of toluene where selectivity converges with that for benzaldehyde at $X_{BAC} > 0.4$. Given the invariance of selectivity to the alcohol with conversion, we can conclude that toluene formation occurs mainly *via* the consecutive reaction of benzaldehyde. The higher selectivity to toluene exhibited by Au/CZ compared with Au/CeO_2 can be attributed to the greater oxygen vacancy site density associated with CZ. In contrast to the conversion of the aqueous feed, a temporal decline in activity was observed for the conversion of benzoic acid in ethanol (**Figure 9.13(AII)** and **9.13(BII)**, which can be linked to toluene formation and associated coking [9.12].

9.5 Conclusion

This is the first reported application of supported Au catalysts to promote the gas phase hydrogenation of benzoic acid where we establish differences in catalytic response for Au/CeO_2 and Au/CZ. Gold incorporation by deposition-precipitation generated nanosized Au particles (< 5 nm) with an equivalent mean size (*ca.* 2 nm) on both supports, as determined by CO chemisorption and STEM analysis. The presence of Au facilitated support reduction, particularly in the case of CZ, to create oxygen vacancies (with reduction of Ce^{4+} to Ce^{3+} quantified by OSC measurements) and provided a supply of surface hydrogen. XPS results establish the occurrence of $Au^{\delta+}$ resulting from electron transfer and strong interaction with the support while differences in surface acidity were demonstrated by NH_3 TPD.

The gas phase hydrogenation of aqueous benzoic acid solutions generated benzaldehyde and benzyl alcohol as the sole products. Kinetic analysis has revealed that

the formation of benzyl alcohol can proceed in a stepwise manner, *via* formation of benzaldehyde as a reactive intermediate, or in a single step (*i.e.* direct hydrogenation of benzoic acid). A higher overall rate of benzoic acid conversion was achieved with Au/CZ and can be attributed to the action of oxygen vacancies to activate the carboxyl function for hydrogen attack. A concerted hydrogenation was favoured over Au/CeO_2 at 523 K, which we attribute to a two point interaction with surface Ce^{4+} and $Au^{\delta+}$ sites to generate a reactive benzoate where surface hydrogen addition produces the alcohol. Reaction over Au/CZ at the same temperature followed both sequential and concerted routes with preferential stepwise conversion where benzaldehyde is generated *via* an MvK mechanism and subsequently converted to the alcohol through surface interaction with Ce^{4+}. An increase in reaction temperature (to 573 K) resulted in a slight shift in favour of a single step conversion of benzoic acid to benzyl alcohol over Au/CZ. This is facilitated by activation of a carboxyl oxygen at a support vacancy and polarisation of the second oxygen at an $Au^{\delta+}$ site. A switch from water to ethanol as carrier increased availability of surface oxygen vacancies with an enhancement in overall reaction rate, the occurrence of toluene as a significant product and higher selectivity to benzaldehyde.

9.6 References

[9.1] M. W. de Lange, J. G. van Ommen and L. Lefferts, *Deoxygenation of benzoic acid on metal oxides. 1. The selective pathway to benzaldehyde*, Appl. Catal. A: General 220 (2001) 41-49.

[9.2] *Kirk-Othmer Encyclopedia of Chemical Technology*, 5th Edition, A. Seidel (Ed.), John Wiley, Hoboken, 2007, pp. 590-596.

[9.3] B. Nair, *Final report on the safety assessment of benzyl alcohol, benzoic acid, and sodium benzoate*, Int. J. Toxicol. 20 (2001) 23-50.

[9.4] *SIDS Initial Assessment report for 13th SIAM, OECD SIDS, Benzoates, CAS N° 65-85-0, 532-32-1, 582-25-2, 100-51-6*, UNEP publications, 2001, pp. 9-10.

[9.5] M. Chong, D.-G. Cheng, L. Liu, F. Chen and X. Zhan, *Deactivation of CeO_2 catalyst in the hydrogenation of benzoic acid to benzaldehyde*, Catal. Lett. 114 (2007) 198-201.

[9.6] D.-G. Cheng, M. Chong, F. Chen and X. Zhan, *XPS characterization of CeO_2 catalyst for hydrogenation of benzoic acid to benzaldehyde*, Catal. Lett. 120 (2008) 82-85.

[9.7] Y. Sakata, C. A. Koutstaal and V. Ponec, *Selectivity problems in the catalytic deoxygenation of benzoic acid*, J. Catal. 169 (1997) 13-21.

[9.8] Y. Sakata and V. Ponec, *Reduction of benzoic acid on CeO_2 and, the effect of additives*, Appl. Catal. A: General 166 (1998) 173-184.

[9.9] T. Yokoyama and N. Yamagata, *Hydrogenation of carboxylic acids to the corresponding aldehydes*, Appl. Catal. A: General 221 (2001) 227-239.

[9.10] J. Kondo, N. Ding, K. Maruya, K. Domen, T. Yokoyama, N. Fujita and T. Maki, *Infrared study of hydrogenation of benzoic acid to benzaldehyde on ZrO_2 catalysts*, Bull. Chem. Soc. Jpn. 66 (1993) 3085-3090.

[9.11] C. A. Koutstaal and V. Ponec, *New Aspects of the Selective Reduction of Aromatic Carboxylic Acids to Aldehydes in Science and Technology in Catalysis 1994*, Y. Izumi, H. Arai, M. Iwamoto (Eds.), Elsevier, Amsterdam, 1995, pp. 105-110.

[9.12] W. F. Hölderich and J. Tjoe, *Direct hydrogenation of aromatic carboxylic acids to their corresponding aldehydes with zinc oxide catalysts*, Appl. Catal. A: General 184 (1999) 257-264.

[9.13] F. Dury and E. M. Gaigneaux, *The deoxygenation of benzoic acid as a probe reaction to determine the impact of superficial oxygen vacancies (isolated or twin) on the oxidation performances of Mo-based oxide catalysts*, Catal. Today 117 (2006) 46-52.

[9.14] F. Dury, S. Meixner, D. Clément and E. M. Gaigneaux, *Coupling the deoxygenation of benzoic acid with the oxidation of propylene on a Co molybdate catalyst*, J. Mol. Catal. A: Chemical 237 (2005) 9-16.

[9.15] A. Aboulayt, A. Chambellan, M. Marzin, J. Saussey, F. Mauge, J. C. Lavalley, C. Mercier and R. Jacquot, *Study of the hydrogenation of methyl benzoate to benzaldehyde on various metal-oxides*, Stud. Surf. Sci. Catal. 78 (1993) 131-138.

[9.16] C. A. Koutstaal, P. Angevaare and V. Ponec, *Surface chemistry of benzoyl compounds on oxides, an FT-IR study*, J. Catal. 143 (1993) 573-582.

[9.17] C. A. Koutstaal and V. Ponec, *FT-IR study on the adsorption of benzoic acid and its derivatives on transition metal oxides*, Appl. Surf. Sci. 70-71 (1993) 206-210.

[9.18] T. Yokoyama, T. Setoyama, N. Fujita, M. Nakajima, T. Maki and K. Fujii, *Novel direct hydrogenation process of aromatic carboxylic-acids to the*

corresponding aldehydes with zirconia catalyst, Appl. Catal. A: General 88 (1992) 149-161.

[9.19] C. Doornkamp and V. Ponec, *The universal character of the Mars and Van Krevelen mechanism*, J. Mol. Catal. A: Chemical 162 (2000) 19-32.

[9.20] A. M. Chen, H. L. Xu, Y. H. Yue, W. M. Hua, S. Wei and G. Zi, *Hydrogenation of methyl benzoate to benzaldehyde over manganese oxide catalysts prepared from Mg/Mn/Al hydrotalcite-like compounds*, Appl. Catal. A: General 274 (2004) 101-109.

[9.21] F. Dury, V. Misplon and E. M. Gaigneaux, *Probing the reduction state of Mo oxide catalysts by the deoxygenation of carboxylic acid*, Catal. Today 91-92 (2004) 111-116.

[9.22] M. W. de Lange, J. G. van Ommen and L. Lefferts, *Deoxygenation of benzoic acid on metal oxides. 2. Formation of by products*, Appl. Catal. A: General 231 (2002) 17-26.

[9.23] D. G. Cheng, C. Y. Hou, F. Q. Chen and X. L. Zhan, *Effect of manganese and potassium addition on CeO_2-Al_2O_3 catalyst for hydrogenation of benzoic acid to benzaldehyde*, J. Rare Earths 27 (2009) 723-727.

[9.24] P. Claus, *Heterogeneously catalysed hydrogenation using gold catalysts*, Appl. Catal. A: General 291 (2005) 222-229.

[9.25] G. C. Bond and D. T. Thompson, *Catalysis by gold*, Catal. Rev. Sci. Eng. 41 (1999) 319-388.

[9.26] C. Kartusch and J. A. van Bokhoven, *Hydrogenation over gold catalysts: The interaction of gold with hydrogen*, Gold Bull. 42 (2009) 343-347.

[9.27] J. E. Bailie and G. J. Hutchings, *Promotion by sulfur of gold catalysts for crotyl alcohol formation from crotonaldehyde hydrogenation*, Chem. Commun. (1999) 2151-2152.

[9.28] B. Campo, C. Petit and M. A. Volpe, *Hydrogenation of crotonaldehyde on different Au/CeO_2 catalysts*, J. Catal. 254 (2008) 71-78.

[9.29] B. Campo, G. Santori, C. Petit and M. Volpe, *Liquid phase hydrogenation of crotonaldehyde over Au/CeO_2 catalysts*, Appl. Catal. A: General 359 (2009) 79-83.

[9.30] P. Claus, H. Hofmeister and C. Mohr, *Identification of active sites and influence of real structure of gold catalysts in the selective hydrogenation of acrolein to allyl alcohol*, Gold Bull. 37 (2004) 181-186.

[9.31] C. Milone, R. Ingoglia, L. Schipilliti, C. Crisafulli, G. Neri and S. Galvagno, *Selective hydrogenation of α,β-unsaturated ketone to α,β-unsaturated alcohol on gold-supported iron oxide catalysts: Role of the support*, J. Catal. 236 (2005) 80-90.

[9.32] C. Milone, C. Crisafulli, R. Ingoglia, L. Schipilliti and S. Galvagno, *A comparative study on the selective hydrogenation of α,β unsaturated aldehyde and ketone to unsaturated alcohols on Au supported catalysts*, Catal. Today 122 (2007) 341.

[9.33] C. T. Campbell and C. H. F. Peden, *Chemistry - Oxygen vacancies and catalysis on ceria surfaces*, Science 309 (2005) 713-714.

[9.34] X. Wang, N. Perret, J. J. Delgado, G. Blanco, X. Chen, C. M. Olmos, S. Bernal and M. A. Keane, *Reducible Support Effects in the Gas Phase Hydrogenation of p-Chloronitrobenzene over Gold*, manuscript in preparation (2012)

[9.35] S. E. Collins, J. M. Cíes, E. del Río, M. López-Haro, S. Trasobares, J. J. Calvino, J. M. Pintado and S. Bernal, *Hydrogen interaction with a ceria-zirconia supported gold catalyst. Influence of CO co-adsorption and pretreatment conditions*, J. Phys. Chem. C 111 (2007) 14371-14379.

[9.36] G. Bond, C. Louis and D. T. Thompson, *Catalysis by Gold in Catalytic Science Series*, G. J. Hutchings (Ed.), Imperial College Press, London, 2006, pp. 150-153.

[9.37] G. Tavoularis and M. A. Keane, *The gas phase hydrodechlorination of chlorobenzene over nickel/silica*, J. Chem. Technol. Biotechnol. 74 (1999) 60-70.

[9.38] R. Di Monte and J. Kaspar, *Nanostructured CeO_2-ZrO_2 mixed oxides*, J. Mater. Chem. 15 (2005) 633-648.

[9.39] G. Colon, M. Pijolat, F. Valdivieso, H. Vidal, J. Kaspar, E. Finocchio, M. Daturi, C. Binet, J. C. Lavalley, R. T. Baker and S. Bernal, *Surface and structural characterization of $Ce_xZr_{1-x}O_2$ CEZIRENCAT mixed oxides as potential three-way catalyst promoters*, J. Chem. Soc., Faraday Trans. 94 (1998) 3717-3726.

[9.40] I. Atribak, A. Bueno-Lopez, A. Garcia-Garcia and B. Azambre, *Contributions of surface and bulk heterogeneities to the NO oxidation activities of ceria-zirconia catalysts with composition $Ce_{0.76}Zr_{0.24}O_2$ prepared by different methods*, Phys. Chem. Chem. Phys. 12 (2010) 13770-13779.

[9.41] Y. Madier, C. Descorme, A. M. Le Govic and D. Duprez, *Oxygen mobility in CeO_2 and $Ce_xZr_{1-x}O_2$ compounds: Study by CO transient oxidation and $^{18}O/^{16}O$ isotopic exchange*, J. Phys. Chem. B 103 (1999) 10999-11006.

[9.42] H. Vidal, J. Kaspar, M. Pijolat, G. Colon, S. Bernal, A. Cordon, V. Perrichon and F. Fally, *Redox behavior of CeO_2-ZrO_2 mixed oxides I. Influence of redox treatments on high surface area catalysts*, Appl. Catal. B: Environmental 27 (2000) 49-63.

[9.43] J. H. Sun, Z. P. Shan, T. Maschmeyer, J. A. Moulijn and M. O. Coppens, *Synthesis of tailored bimodal mesoporous materials with independent control of the dual pore size distribution*, Chem. Commun. (2001) 2670-2671.

[9.44] G. Vlaic, R. Di Monte, P. Fornasiero, E. Fonda, J. Kaspar and M. Graziani, *Redox property-local structure relationships in the ph-loaded CeO_2-ZrO_2 mixed oxides*, J. Catal. 182 (1999) 378-389.

[9.45] J. Kaspar, P. Fornasiero and M. Graziani, *Use of CeO_2-based oxides in the three-way catalysis*, Catal. Today 50 (1999) 285-298.

[9.46] M. Yashima, H. Arashi, M. Kakihana and M. Yoshimura, *Raman-scattering study of cubic-tetragonal phase-transition in $Zr_{1-x}Ce_xO_2$ solid-solution*, J. Am. Ceram. Soc. 77 (1994) 1067-1071.

[9.47] P. Fornasiero, R. Dimonte, G. R. Rao, J. Kaspar, S. Meriani, A. Trovarelli and M. Graziani, *Rh-loaded CeO_2-ZrO_2 solid-solutions as highly efficient oxygen exchangers-dependence of the reduction behavior and the oxygen storage capacity on the structural-properties*, J. Catal. 151 (1995) 168-177.

[9.48] A. Trovarelli, M. Boaro, E. Rocchini, C. de Leitenburg and G. Dolcetti, *Some recent developments in the characterization of ceria-based catalysts*, J. Alloys Compd. 323 (2001) 584-591.

[9.49] C. E. Hori, H. Permana, K. Y. S. Ng, A. Brenner, K. More, K. M. Rahmoeller and D. Belton, *Thermal stability of oxygen storage properties in a mixed CeO_2-ZrO_2 system*, Appl. Catal. B: Environmental 16 (1998) 105-117.

[9.50] J. Kaspar, P. Fornasiero, G. Baiducci, R. Di Monte, N. Hickey and V. Sergo, *Effect of ZrO_2 content on textural and structural properties of CeO_2-ZrO_2 solid solutions made by citrate complexation route*, Inorg. Chim. Acta 349 (2003) 217-226.

[9.51] M. H. Yao, R. J. Baird, F. W. Kunz and T. E. Hoost, *An XRD and TEM investigation of the structure of alumina-supported ceria-zirconia*, J. Catal. 166 (1997) 67-74.

[9.52] B. Azambre, I. Atribak, A. Bueno-Lopez and A. Garcia-Garcia, *Probing the Surface of Ceria-Zirconia Catalysts Using NO_x Adsorption/Desorption: A First Step Toward the Investigation of Crystallite Heterogeneity*, J. Phys. Chem. C 114 (2010) 13300-13312.

[9.53] Q. Fu, W. L. Deng, H. Saltsburg and M. Flytzani-Stephanopoulos, *Activity and stability of low-content gold-cerium oxide catalysts for the water-gas shift reaction*, Appl. Catal. B: Environmental 56 (2005) 57-68.

[9.54] J. M. Cies, E. del Rio, M. Lopez-Haro, J. J. Delgado, G. Blanco, S. Collins, J. J. Calvino and S. Bernal, *Fully Reversible Metal Deactivation Effects in Gold/Ceria-Zirconia Catalysts: Role of the Redox State of the Support*, Angew. Chem., Int. Ed. 49 (2010) 9744-9748.

[9.55] Z. P. Liu, P. Hu and A. Alavi, *Catalytic role of gold in gold-based catalysts: A density functional theory study on the CO oxidation on gold*, J. Am. Chem. Soc. 124 (2002) 14770-14779.

[9.56] S. Scire, S. Minico, C. Crisafulli, C. Satriano and A. Pistone, *Catalytic combustion of volatile organic compounds on gold/cerium oxide catalysts*, Appl. Catal. B: Environmental 40 (2003) 43-49.

[9.57] W. C. Conner and J. L. Falconer, *Spillover in heterogeneous catalysis*, Chem. Rev. 95 (1995) 759-788.

[9.58] N. Hickey, P. Fornasiero, J. Kaspar, J. M. Gatica and S. Bernal, *Effects of the nature of the reducing agent on the transient redox behavior of $NM/Ce_{0.68}Zr_{0.32}O_2$ (NM = Pt, Pd, and Rh)*, J. Catal. 200 (2001) 181-193.

[9.59] R. Di Monte and J. Kaspar, *On the role of oxygen storage in three-way catalysis*, Top. Catal. 28 (2004) 47-57.

[9.60] F. Cárdenas-Lizana, S. Gómez-Quero, N. Perret and M. A. Keane, *Gold catalysis at the gas–solid interface: role of the support in determining activity and selectivity in the hydrogenation of m-dinitrobenzene*, Catal. Sci. Tech. 1 (2011) 652-661

[9.61] A. A. Fonseca, J. M. Fisher, D. Ozkaya, M. D. Shannon and D. Thompsett, *Ceria-zirconia supported Au as highly active low temperature Water-gas shift catalysts*, Top. Catal. 44 (2007) 223-235.

[9.62] J. Gaálová, P. Topka, L. Kaluza and O. Solcova, *Gold versus platinum on ceria–zirconia mixed oxides in oxidation of ethanol and toluene*, Catal. Today 175 (2011) 231-237.

[9.63] M. Daturi, E. Finocchio, C. Binet, J. C. Lavalley, F. Fally, V. Perrichon, H. Vidal, N. Hickey and J. Kaspar, *Reduction of high surface area CeO_2-ZrO_2 mixed oxides*, J. Phys. Chem. B 104 (2000) 9186-9194.

[9.64] E. Mamontov, T. Egami, R. Brezny, M. Koranne and S. Tyagi, *Lattice defects and oxygen storage capacity of nanocrystalline ceria and ceria-zirconia*, J. Phys. Chem. B 104 (2000) 11110-11116.

[9.65] B. T. Loveless, A. Gyanani and D. S. Muggli, *Discrepancy between TPD- and FTIR-based measurements of Bronsted and Lewis acidity for sulfated zirconia*, Appl. Catal. B: Environmental 84 (2008) 591-597.

[9.66] S. Bhogeswararao and D. Srinivas, *Chemoselective Hydrogenation of Cinnamaldehyde over Pd/CeO_2-ZrO_2 Catalysts*, Catal. Lett. 140 (2012) 55-64.

[9.67] E. S. Ranganathan, S. K. Bej and L. T. Thompson, *Methanol steam reforming over Pd/ZnO and Pd/CeO_2 catalysts*, Appl. Catal. A: General 289 (2005) 153-162.

[9.68] M. G. Cutrufello, I. Ferino, V. Solinas, A. Primavera, A. Trovarelli, A. Auroux and C. Picciau, *Acid-base properties and catalytic activity of nanophase ceria-zirconia catalysts for 4-methylpentan-2-ol dehydration*, Phys. Chem. Chem. Phys. 1 (1999) 3369-3375.

[9.69] V. R. Choudhary and A. J. Karkamkar, *Temperature-programmed desorption of water and ammonia on sulphated zirconia catalysts for measuring their strong acidity and acidity distribution*, Proc. Ind. Aca. Sci.-Chem. Sci. 115 (2003) 281-286.

[9.70] R. Barthos, F. Lonyi, G. Onyestyak and J. Valyon, *An NH_3-TPD and -FR study on the acidity of sulfated zirconia*, Solid State Ionics 141 (2001) 253-258.

[9.71] E. Beche, P. Charvin, D. Perarnau, S. Abanades and G. Flamant, *Ce 3d XPS investigation of cerium oxides and mixed cerium oxide ($Ce_xTi_yO_z$)*, Surface and Interface Analysis 40 (2008) 264-267.

[9.72] D. I. Kondarides and X. E. Verykios, *Effect of chlorine on the chemisorptive properties of Rh/CeO_2 catalysts studied by XPS and temperature programmed desorption techniques*, J. Catal. 174 (1998) 52-64.

[9.73] M. P. Seah, L. S. Gilmore and G. Beamson, *XPS: Binding energy calibration of electron spectrometers 5 - Re-evaluation of the reference energies*, Surf. Interface Anal. 26 (1998) 642-649.

[9.74] N. C. Hernandez, R. Grau-Crespo, N. H. de Leeuw and J. F. Sanz, *Electronic charge transfer between ceria surfaces and gold adatoms: a GGA plus U investigation*, Phys. Chem. Chem. Phys. 11 (2009) 5246-5252.

[9.75] R. Grau-Crespo, N. C. Hernandez, J. F. Sanz and N. H. de Leeuw, *Theoretical investigation of the deposition of Cu, Ag, and Au atoms on the ZrO_2(111) surface*, J. Phys. Chem. C 111 (2007) 10448-10454.

[9.76] D. R. Stull, E. F. Westrum and G. C. Sinke, *The Chemical Thermodynamics of Organic Compounds*, John Wiley, New York, 1969.

[9.77] M. A. Keane, G. Pina and G. Tavoularis, *The catalytic hydrodechlorination of mono-, di- and trichlorobenzenes over supported nickel*, Appl. Catal. B: Environmental 48 (2004) 275-286.

[9.78] L. McEwan, M. Julius, S. Roberts and J.C.Q. Fletcher, *A Review of the use of gold catalysts in selective hydrogenation reactions*, Gold Bull. 43 (2010) 298-306.

[9.79] F. Cárdenas-Lizana, S. Gómez-Quero, N. Perret and M. A. Keane, *Support effects in the selective gas phase hydrogenation of p-chloronitrobenzene over gold*, Gold Bull. 42 (2009) 124-132.

[9.80] P. Serna, P. Concepcion and A. Corma, *Design of highly active and chemoselective bimetallic gold-platinum hydrogenation catalysts through kinetic and isotopic studies*, J. Catal. 265 (2009) 19-25.

[9.81] F. Cárdenas-Lizana, S. Gómez-Quero and M. A. Keane, *Exclusive production of chloroaniline from chloronitrobenzene over Au/TiO_2 and Au/Al_2O_3*, ChemSusChem 1 (2008) 215-221.

[9.82] K. D. Dobson and A. J. McQuillan, *In situ infrared spectroscopic analysis of the adsorption of aromatic carboxylic acids to TiO_2, ZrO_2, Al_2O_3, and Ta_2O_5 from aqueous solutions*, Spectrochim. Acta, Part A 56 (2000) 557-565.

[9.83] C. T. Campbell, *The active site in nanopaticle gold catalysis*, Science 306 (2004) 234-235.

[9.84] Y. Ikezawa, R. Sekiguchi and T. Kitazume, *Adsorption of benzoic acid on Au(111) and Au(110) electrodes in acidic media by IRAS*, Electrochim. Acta 46 (2000) 731-736.

[9.85] K. Lanasri, A. Saddi, K. Bachari, D. Halliche and O. Cherifi, *Gas phase hydrogenation of benzaldehyde over supported copper catalysts. Effect of copper loading*, Stud. Surf. Sci. Catal. 174 (2008) 1279-1282.

[9.86] J. A. Rodriguez, M. Perez, J. Evans, G. Liu and J. Hrbek, *Reaction of SO_2 with $Au/CeO_2(111)$: Importance of O vacancies in the activation of gold*, J. Chem. Phys. 122 (2005)

[9.87] K. Qian, S. Lv, X. Xiao, H. Sun, J. Lu, M. Luo and W. Huang, *Influences of CeO_2 microstructures on the structure and activity of $Au/CeO_2/SiO_2$ catalysts in CO oxidation*, J. Mol. Catal. A: Chemical 306 (2009) 40-47.

[9.88] M. Fronzi, S. Piccinin, B. Delley, E. Traversa and C. Stampfl, *Water adsorption on the stoichiometric and reduced CeO_2 (111) surface: a first-principles investigation*, Phys. Chem. Chem. Phys. 11 (2009) 9188-9199.

[9.89] M. Molinari, S. C. Parker, D. C. Sayle and M. S. Islam, *Water adsorption and its effect on the stability of low index stoichiometric and reduced surfaces of ceria*, J. Phys. Chem. C 116 (2012) 7073-7082.

[9.90] G. Ketteler, S. Yamamoto, H. Bluhm, K. Andersson, D. E. Starr, D. F. Ogletree, H. Ogasawara, A. Nilsson and M. Salmeron, *The nature of water nucleation sites on $TiO_2(110)$ surfaces revealed by ambient pressure X-ray photoelectron spectroscopy*, J. Phys. Chem. C 111 (2007) 8278-8282.

[9.91] S. Kumar and P. K. Schelling, *Density functional theory study of water adsorption at reduced and stoichiometric ceria (111) surfaces*, J. Chem. Phys. 125 (2006)

Chapter 10
Summary and Future Work

The main objective of this research project was the enhancement of catalytic processes (in term of selectivity and activity) through optimisation of the catalysts and control of the reaction conditions. The results presented in this PhD thesis demonstrate the viability of Au supported on molybdenum nitride and carbide as catalyst for the gas phase hydrogenation of nitroarenes. Moreover, the work has demonstrated new catalytic processes based on supported Au for the synthesis of an aromatic alcohol via the hydrogenation of an aldehyde and carboxylic acid feed. All the reactions were conducted under relatively mild reaction conditions (393-573 K, 1 atm) in continuous flow gas phase operation. The results can be applied to develop cleaner alternative routes in the production of a range of amines and alcohols as products of commercial importance in the fine chemical sector. The main findings are highlighted in this Chapter and future research directions are proposed.

10.1 General Conclusions

The results establish the formation of β-Mo_2N by temperature programmed treatment of MoO_3 in N_2/H_2 *via* a stepwise reduction $MoO_3 \rightarrow MoO_2 \rightarrow Mo$. This is followed by a subsequent nitridation $Mo \rightarrow \beta$-Mo_2N, to generate catalytic material that exhibits reaction exclusivity in -NO_2 reduction. The catalytic action of Mo_2N, Mo_2C and Fe_3Mo_3N were demonstrated to promote the selective nitro reduction in the continuous gas phase hydrogenation of nitro compounds. Hydrogen adsorption/dissociation was shown to be the limiting factor over the binary compounds under the experimental conditions employed.

In the hydrogenation of *p*-chloronitrobenzene, the incorporation of Au with Mo_2N and Mo_2C served to increase H_2 uptake with a higher rate relative to the bare support and 100% selectivity to the target product, *i.e. p*-chloroaniline. Moreover, Au supported on Mo nitride and carbide outperformed benchmark Au/Al_2O_3 catalysts. Under the same reaction conditions, the addition of Pd or incorporation of Co with Mo nitride promoted hydrodechlorination (non-selective reaction) that is attributed to a strong interaction of the aromatic ring with the surface. Rate invariance with respect to surface area and a dependence on crystallographic phase was demonstrated for Mo

nitride. The higher specific activity of β- relative to γ-phase was attributed to higher surface H_2 content that was correlated to increased availability of nitrogen deficient sites.

The results for the gas phase hydrogenation of *m*-dinitrobenzene established that the exclusive formation of the partially reduced *m*-nitroaniline was achieved over Mo_2C at low conversions. Catalytic performance (in term of activity and selectivity) was enhanced with the incorporation of gold where Au/Al_2O_3 was non-selective under similar conditions. This difference in selectivity was attributed to the specific interaction of the reactant with Mo_2C and/or at the metal-support interface associated, which favours formation of *m*-nitroaniline. A switch from $-NO_2$ to C=O reduction over Mo compounds was probed in the hydrogenation of benzaldehyde where toluene formation was linked to C=O activation for hydrogenolytic attack.

The reduction of C=O group was further investigated in the hydrogenation of benzaldehyde, 4-nitrobenzaldehyde and benzoic acid. Au/Al_2O_3 exhibited 100% selectivity to benzyl alcohol in the conversion of benzaldehyde where two benchmark catalysts (Pd/Al_2O_3 and Ni/Al_2O_3) promoted hydrogenolysis to toluene. In the presence of the $-NO_2$ group (hydrogenation of 4-nitrobenzaldehyde), reaction over Au/Al_2O_3 resulted in the selective reduction of C=O group with formation of 4-nitrobenzyl alcohol. Selectivity to the alcohol was attributed to stronger surface Lewis acidity present on the surface and was enhanced with increasing Au size and lower reaction temperature. In contrast, Au/ZrO_2 and Au/TiO_2 demonstrated exclusive reduction of $-NO_2$. Adsorption/activation of the organic reactant was the limiting factor with activity related to the number of low coordination Au sites. The hydrogenation of benzoic acid to benzyl alcohol can occur through a stepwise manner with formation of a benzaldehyde intermediate. The possibility of a direct one step route over Au supported on CeO_2 and $Ce_{0.62}Zr_{0.38}O_2$ was examined and the reaction pathway correlated with surface properties, notably Au size, support reducibility/oxygen vacancy formation and acidity where the metal/support interface is critical.

10.2 Future Directions

10.2.1 Preparation of bimetallic Pd-Au/Mo_2C by a colloidal method

The results **Chapter 4** showed that Mo_2C was active and selective in the hydrogenation of *p*-chloronitrobenzene to *p*-chloroaniline. After addition of Au, the

selectivity was maintained and the system delivered higher hydrogenation rates relative to the reference Au/Al_2O_3 and Mo_2C. Exclusive selectivity eliminates waste by-products but industrial application necessitates higher activity than achieved in this study. The catalytic system can be improved by the use of promoters.

In a previous collaboration [10.1] between this laboratory and Dr. Catherine Louis (Laboratoire de Réactivité de Surface, Université Pierre et Marie Curie, Paris), oxide supported Au-Pd nano-particles were prepared by deposition-precipitation and found to exhibit ultra-selective in the conversion of *p*-chloronitrobenzene to *p*-chloroaniline. The selectivity was attributed to a surface Pd-Au synergism that activated the $-NO_2$ function for hydrogen attack. The Au/Pd ratio was critical where *p*-chloroaniline was the sole product at Au/Pd $\geq$ 20; higher Pd content increased rate but promoted the formation of nitrobenzene (hydrodechlorination). Moreover, the supported $Au\text{-}Pd/Al_2O_3$ prepared by deposition precipitation exhibited Au/Pd surface ratios that differed from the nominal values.

Colloidal methods show promise in catalyst synthesis [10.2] and involve the combination of the metal salt precursor with a stabilizing (polyvinylalcohol), addition of a reducing agent ($NaBH_4$) with the introduction of the support. The stabilizing agent prevents undesired agglomeration and promotes the formation of well dispersed Au particles. Supported Au-Pd nanoalloy with well defined size, shape and composition can be generated with this method. Therefore, a Au-Pd phase, with varying Au/Pd ratios, supported on Mo_2C can be synthesised and used in the hydrogenation of nitro compounds. This future study would set out to (i) improve the method of synthesis of supported Au-Pd catalysts at the nanoscale, (ii) use for the first time Mo_2C as a support for bimetallic particles and (iii) enhance selective hydrogenation rates relative to results obtained in C**hapter 4** due to the addition of Pd.

10.2.2 Further investigation of benzoic acid hydrogenation

By adjusting experimental conditions in term of temperature and solvent (**Chapter 9**), high selectivity to benzyl alcohol (S = 0.96) was achieved over $Au/Ce_{0.62}Zr_{0.38}O_2$. The incorporation of Zr served to increase the reducibility of the support and generate oxygen vacancy sites. A decrease in temperature favoured the

stepwise route over $Au/Ce_{0.62}Zr_{0.38}O_2$. It would be interesting to investigate further the possibility of achieving 100% selectivity to the alcohol and increase overall activity.

Metal particle size can affect selectivity where increased selectivity to the alcohol (to the detriment of C=C hydrogenation) with an increase in Au size (from 4 to 8 nm) has been reported in the literature [10.3]. This tendency was also observed in **Chapter 8**. In the same manner, it is likely that an increase in Au particles size would affect selectivity in the conversion of benzoic acid by promoting the stepwise route. Indeed, active sites for the direct route involved the metal/support interface and may be promoted by Au sites of low coordination, *i.e.* high dispersion.

An increase in oxygen storage capacity was associated with an increase in activity. However, increase in oxygen vacancy site density resulted in the formation of toluene. The impact of oxygen vacancy density on the catalytic response is still not well understood. This can be investigated by using solvents or promoters/inhibitors which exhibit different affinity with oxygen vacancies (*e.g.* CO_2 [10.4]) or $Ce_xZr_{1-x}O_2$ supports with different composition ($0 \leq x \leq 1$).

Carboxylic acids serve as inexpensive feedstock so their use as reactant is economically attractive. The catalytic system which was developed **Chapter 9** may be exploited for the formation of other aldehyde and alcohol products of industrial interest. Pestman *et al.* [10.5] investigated the formation of acetaldehyde from acetic acid where Pt supported on reducible supports (*e.g.* Fe_2O_3, TiO_2) exhibited promising results as the ketonization reaction was suppressed and high selectivity to the aldehyde (up to 85%) was achieved. However, by-products resulting from decomposition, *i.e.* CO_2 and CH_4, were still obtained. The mechanism proposed involved the oxygen vacancies (MvK mechanism) on the oxide, the activation of H_2 on Pt and transfer of H to the oxide *via* H_2-spillover. The hydrogenation of benzoic acid in **Chapter 9** presented a similar reaction mechanism but benzene (from decomposition) or benzophenone (from ketonization) formation was not detected. Hence, the hydrogenation of acetic acid over $Au/Ce_xZr_{1-x}O_2$ may generate only aldehyde and alcohol and circumvent ketonization or decomposition by-products and the formation of acetaldehyde and ethanol can be optimised.

10.2.3 Ternary nitride

The hydrogenation of nitrobenzene and *p*-chloronitrobenzene over Fe_3Mo_3N (**Chapter 5**) gave promising results in term of exclusive formation of aniline and *p*-chloroaniline, respectively. The work to date has mainly focused on improving synthesis method/optimising parameters in order to obtain the pure phase and the use of this material for hydrogenation reaction is limited [10.6]. One drawback of this material is the low surface area recorded in the literature ($\leq$18 m^2 g^{-1} [10.7-9]), which limits its industrial application as catalyst. While a few studies [10.10-12] have dealt with the synthesis of Mo_2N with high surface area, there is a dearth of literature dealing with ternary compounds.

In the synthesis of Mo binary nitrides, a decrease in temperature ramp rate and an increase in gas space velocity (GHSV) serve to enhance surface area [10.10-12]. Indeed, low surface area has been attributed to sintering, which results from water released during reduction [10.12]. The synthesis mechanism for ternary Mo nitride has not been investigated to any extent and the same phenomena may occur during the nitridation of $FeMoO_4$. A GHSV of 40000 h^{-1} and temperature ramp up to 5.4 K min^{-1} was employed in the preparation method used **Chapter 5**, while, for Mo_2N, high surface area are achieved with GHSV of 150000 h^{-1} and temperature ramp rate $\leq$ 1 K min^{-1}. Therefore, further work should focus on studying the effect of GHSV and temperature ramp on the surface area of ternary Fe_3Mo_3N.

Any variation in synthesis procedure may still result in a relatively low surface area. An alternative solution is the deposition of Fe_3Mo_3N on a support. Indeed, incorporation of Mo_2N on Al_2O_3 has already been studied [10.13,10.14]; the synthesis consist on impregnation of Al_2O_3 with an aqueous solution of $(NH_4)_6Mo_7O_{24}$ followed by a temperature programmed nitridation in NH_3. There is no available literature on the synthesis of supported Fe_3Mo_3N, albeit Ni_2Mo_3N and Co_3Mo_3N supported on Al_2O_3 have been synthesised [10.15]. Based on these studies, a method involving impregnation of the precursor followed by nitridation can be developed.

10.3 References

[10.1] F. Cárdenas-Lizana, S. Gómez-Quero, A. Hugon, L. Delannoy, C. Louis and M. A. Keane, *Pd-promoted selective gas phase hydrogenation of p-chloronitrobenzene over alumina supported Au*, J. Catal. 262 (2009) 235-243.

[10.2] J. A. Lopez-Sanchez, N. Dimitratos, C. Hammond, Gemma L. Brett, L. Kesavan, S. White, P. Miedziak, R. Tiruvalam, R. L. Jenkins, A. F. Carley, D. Knight, C. J. Kiely and G. J. Hutchings, *Facile removal of stabilizer-ligands from supported gold nanoparticles*, Nature Chemistry 3 (2011) 551-556.

[10.3] T. V. W. Janssens, B. S. Clausen, B. Hvolbaek, H. Falsig, C. H. Christensen, T. Bligaard and J. K. Norskov, *Insights into the reactivity of supported Au nanoparticles: combining theory and experiments*, Top. Catal. 44 (2007) 15-26.

[10.4] M. W. de Lange, J. G. van Ommen and L. Lefferts, *Deoxygenation of benzoic acid on metal oxides. 2. Formation of by products*, Appl. Catal. A: General 231 (2002) 17-26.

[10.5] R. Pestman, R. M. Koster, J. A. Z. Pieterse and V. Ponec, *Reactions of carboxylic acids on oxides .1. Selective hydrogenation of acetic acid to acetaldehyde*, J. Catal. 168 (1997) 255-264.

[10.6] D. S. Bem, C. P. Gibson and H. C. Z. Loye, *Synthesis of intermetallic nitrides by solid-state precursor reduction*, Chem. Mater. 5 (1993) 397-399.

[10.7] C. J. H. Jacobsen, *Novel class of ammonia synthesis catalysts*, Chem. Commun. (2000) 1057-1058.

[10.8] R. Kojima and K. Aika, *Cobalt molybdenum bimetallic nitride catalysts for ammonia synthesis - Part 1. Preparation and characterization*, Appl. Catal. A: General 215 (2001) 149-160.

[10.9] R. N. Panda and N. S. Gajbhiye, *Electronic and magnetic properties of Fe_3Mo_3N*, J. Alloys Compd. 256 (1997) 102-107.

[10.10] E. J. Markel, S. E. Burdick, M. E. Leaphart and K L. Roberts, *Synthesis, characterization, and thiophene desulfurization activity of unsupported gamma-Mo_2N macrocrystalline catalysts*, J. Catal. 182 (1999) 136-147.

[10.11] J.-G. Choi, R. L. Curl and L. T. Thompson, *Molybdenum nitride catalysts I. Influence of the synthesis factors on structural properties*, J. Catal. 146 (1994) 218-227.

[10.12] R. S. Wise and E. J. Markel, *Synthesis of high surface area molybdenum nitride in mixtures of nitrogen and hydrogen*, J. Catal. 145 (1994) 344-355.

[10.13] Z. L. Wu, C. Li, Z. B. Wei, P. L. Ying and Q. Xin, *FT-IR spectroscopic studies of thiophene adsorption and reactions on Mo_2N/gamma-Al_2O_3 catalysts*, J. Phys. Chem. B 106 (2002) 979-987.

[10.14] Z. L. Wu, C. Li, P. L. Ying, Z. B. Wei and Q. Xin, *Low-temperature isomerization of 1-butene on Mo_2N/gamma-Al_2O_3 catalyst studied by in situ FT-IR spectroscopy*, J. Phys. Chem. B 105 (2001) 9183-9190.

[10.15] S. Korlann, B. Diaz and M. E. Bussell, *Synthesis of bulk and alumina-supported bimetallic carbide and nitride catalysts*, Chem. Mater. 14 (2002) 4049-4058.